

Nanoliter-Droplet Thermophoresis for Biomedical Applications



Dissertation

zur Erlangung des Grades
Doktor der Naturwissenschaften (Dr. rer. nat.)

der Fakultät für Physik
der Ludwig-Maximilians-Universität München

vorgelegt von
Susanne Anja Irene Seidel
aus Selb

München, Juni 2014

Erstgutachter: Prof. Dr. Dieter Braun

Zweitgutachter: Prof. Dr. Joachim Rädler

Mündliche Prüfung am 01. August 2014

Table of Contents

Summary	1
Zusammenfassung	3
1 Introduction: Biomolecular Interaction	5
1.1 Relevance.....	5
1.2 Analysis	5
2 Background: Biomolecule Thermophoresis	7
2.1 Thermophoresis	7
2.2 All-optical Measurement	8
2.3 Binding Quantification	9
3 Thermophoresis in Nanoliter-Droplets	11
3.1 Sample Preparation	11
3.2 Inverted Microscopic Setup	11
3.3 Local Heating in Experiment and Simulation.....	12
3.4 Aptamer Quantification	14
3.5 Discussion.....	16
4 Thermophoretic Protein Studies	19
4.1 Protein-Protein Binding in Cell Lysate: TEM1-BLIP	19
4.2 Protein-Peptide Binding With Two Phases: AMA1-RON2	20
4.3 Protein-Small Molecule Binding Without Labeling	23
4.3.1 Glutamate Receptor iGluR2	23
4.3.2 MAP Kinase p38 α	24
4.4 Discussion.....	25
5 Thermophoretic Immunoassays	27
5.1 Antibody Characterization.....	27
5.1.1 Towards a Therapeutic Antibody For Granulomatosis With Polyangiitis.....	27
5.1.2 MCPR3-7 Affinity and Selectivity	28
5.1.3 Interference with PR3- α 1PI Complex Formation	28
5.2 Quantitative In Vitro Diagnostics	30
5.2.1 Autoantibodies as Biomarkers for Dilated Cardiomyopathy.....	30
5.2.2 Affinity and Specificity of the Tracer COR1.....	31
5.2.3 Autocompetition Assay	32
5.2.4 Quantification of Affinity and Concentration.....	32
5.3 Discussion.....	35
6 Conclusion and Outlook	37
7 References	39
8 Danksagung	45
9 Associated Publications	47

Summary

Specific interactions of biomolecules are central to cellular processes, drug discovery and immunodiagnosics. Such biological binding events are quantifiable via thermophoresis, the directed molecule movement driven by a temperature gradient. Biomolecule thermophoresis can be induced by infrared laser heating and analyzed using fluorescence. The objective of this thesis was to enhance and optimize these all-optical measurements, regarding instrumentation, assay design and biomedical applications.

In the first part, a novel measurement device and approach are presented, which cut down sample consumption 50-fold compared to established capillary thermophoresis. Instead of capillaries, analysis was performed in 10 nl-sample droplets transferred into standard 1536-well plates with a non-contact liquid handler (Labcyte). To prevent evaporation, the aqueous sample droplets were stabilized in an oil-surfactant mix. Temperature induced effects in this water-in-oil system were experimentally characterized and the results agreed with numerical simulation. The system's applicability for biomolecular interaction analysis was confirmed with a DNA aptamer. The achieved miniaturization and the easy-to-handle multi-well plate format promote automated high-throughput screens. Besides aptamers, proteins should also be measurable very well when judging from the application depth of capillary measurements.

This versatility of protein investigation via capillary thermophoresis is demonstrated in the second part. Successful experiments were not only conducted in diverse liquids including crude cell lysate, but also for binding partners with a broad range of molecular weight ratios. Affinities between protein and protein, protein and peptide, as well as protein and small molecule were determined with high accuracy. Further flexibility arises from the herein presented label free approach which utilizes protein intrinsic UV fluorescence. It is caused by aromatic amino acids with tryptophan being the major intrinsic fluorophore. This approach exempts from the need to attach a dye, which saves time and excludes labeling artifacts.

The wide variety of proteins that can be analyzed with thermophoresis also includes antibodies. Two applications of such thermophoretic immunoassays are introduced in the third part. Firstly, the therapeutically interesting antibody MCPR3-7 was assessed. MCPR3-7 binds proteinase 3 (PR3), the major autoimmune target in granulomatosis with polyangiitis. Thermophoresis allowed to quantify MCPR3-7's affinity and selectivity for different PR3 forms. In addition, it revealed that the antibody interferes with the complexation of PR3 and α 1-proteinase inhibitor (α 1PI). Secondly, a diagnostic autocompetition assay is described, which directly determines affinity and concentration of disease related biomarkers. It was applied for autoantibodies against the cardiac β 1-adrenoceptor found in patients suffering from dilated cardiomyopathy. To detect these autoantibodies, the small peptide COR1 mimicking the adrenoceptor's dominant epitope served as an artificial antigen. This tracer was labeled with a red-fluorescent dye, which ensured selectivity for measurements directly in untreated human blood serum. The results prove that thermophoresis is a valuable tool to characterize antibodies including those of diagnostic value and those with a therapeutic potential.

Taken together, the presented innovations in assay design and the novel nl-droplet approach can be expected to considerably widen the application spectrum of thermophoresis in fundamental research, industrial drug discovery and clinical laboratory diagnostics.

Zusammenfassung

Spezifische Interaktionen von Biomolekülen sind von zentraler Bedeutung für zelluläre Prozesse, die Entwicklung neuer Medikamente und die Immundiagnostik. Solche biologischen Bindungsvorgänge lassen sich mittels Thermophorese, der gerichteten Molekülbewegung entlang eines Temperaturgradienten, quantifizieren. Die Thermophorese von Biomolekülen kann durch Infrarotlaser-Heizen induziert und mittels Fluoreszenz analysiert werden. Die Weiterentwicklung dieses optischen Verfahrens bezüglich des Messinstruments, des Versuchsdesigns und der biomedizinischen Anwendungen war das Ziel der vorliegenden Dissertation.

Im ersten Teil wird eine neuartige Technik vorgestellt, die den Probenverbrauch verglichen mit etablierten Kapillarmessungen um den Faktor 50 verkleinert. Statt in Kapillaren wurde in 10 nl-großen Probentropfen gemessen, die mit einem kontaktfreien Liquid-Handler (Labcyte) in eine 1536-Well-Platte übertragen wurden. Zum Schutz vor Verdunstung wurden die Tropfen in eine Öl-Tensid-Schicht transferiert. Temperaturinduzierte Effekte in diesem Wasser-in-Öl-System wurden experimentell charakterisiert, wobei die Ergebnisse durch numerischen Simulationen bestätigt wurden. Dass sich die Methode für biomolekulare Interaktionstests eignet, wurde anhand eines DNA-Aptamers belegt. Die Miniaturisierung und die einfache Handhabung der Multi-Well-Platten ermöglichen automatisierte Hochdurchsatz-Screens. Neben Aptameren sollten sich auch Proteine sehr gut untersuchen lassen, wenn man von einer ähnlichen Anwendungsbreite wie bei Kapillarmessungen ausgeht.

Auf derartige Proteinuntersuchungen mittels Kapillarthermophorese wird im zweiten Teil eingegangen. Analysen wurden nicht nur in diversen Puffern und sogar in rohem Zelllysate durchgeführt, sondern auch mit unterschiedlichsten Bindungspartnern. So wurden Affinitäten zwischen Protein und Protein, Protein und Peptid, sowie Protein und niedermolekularer Verbindung mit hoher Genauigkeit bestimmt. Thermophoresetests gewinnen durch das in dieser Arbeit präsentierte, markierungsfreie Verfahren zusätzlich an Flexibilität. Es basiert auf der intrinsischen UV-Fluoreszenz von Proteinen, die auf aromatische Aminosäuren, hauptsächlich Tryptophan, zurückzuführen ist. Somit müssen Proteine nicht mehr mit Fluoreszenzfarbstoffen markiert werden, was Zeit spart und Artefakte ausschließt.

Der dritte Teil behandelt die Quantifizierung von Antikörpern. Thermophoretische Immunoassays wurden für zwei biomedizinische Fragestellungen eingesetzt. Zunächst wurde der aus therapeutischer Sicht interessante Antikörper MCPR3-7 untersucht. Er ist gegen Proteinase 3 (PR3) gerichtet, das Hauptepitop autoimmuner Antikörper bei der granulomatösen Polyangiitis. Mithilfe der Thermophorese wurde sowohl die Affinität von MCPR3-7 für verschiedene PR3-Formen quantifiziert, als auch gezeigt, dass der Antikörper die Komplexbildung von PR3 und α 1-Proteinaseinhibitor (α 1PI) stört. Ferner wird ein diagnostisches Autokompetitionsverfahren vorgestellt, das gleichzeitig die Affinität und die Konzentration von Biomarkern in humanem Blutserum quantifiziert. Autoantikörper gegen den kardialen β 1-Adrenozeptor, die mit der dilatativen Kardiomyopathie assoziiert sind, wurden mithilfe des kurzen Peptides COR1 analysiert, das das dominante Epitop nachstellt. Die Ergebnisse belegen, dass die Thermophorese ein wertvolles Werkzeug für die Antikörpercharakterisierung ist.

Zusammengefasst lassen die vorgestellten Neuerungen eine umfangreiche Erweiterung des Anwendungsspektrums der Biomolekülthermophorese in der Grundlagenforschung, der industriellen Wirkstoffsuche und der klinischen Labordiagnostik erwarten.

1 Introduction: Biomolecular Interaction

1.1 Relevance

Cellular processes are mainly based on molecular recognition and interaction, e.g. between cell surface receptors and ligands, enzymes and substrates, transcription factors and DNA, or antibodies and antigens. Elucidating these biological binding events is essential to understand physiological and pathological mechanisms on a molecular level.^{1,2}

This understanding allows to identify novel target structures for pharmacological treatment.^{3,4} By testing the binding of a disease specific target to large libraries of chemical compounds, candidate medications are discovered. In fact, molecular interaction does not only drive the development of medications, but also represents their mechanism of action. The effect of a pharmaceutical drug relies on its interaction with one or a few specific cellular targets. The vast majority of today's drugs target proteins: cell surface receptors (60%), ion channels, or enzymes.⁵

Biomolecule interaction is also utilized in clinical laboratory diagnostics. Immuno-diagnostics rely on the interaction of antibodies and antigens. These protein biomarkers report on a patient's status regarding e.g. viral or bacterial infections, vaccine response, allergies, or autoimmune diseases.⁶⁻⁹ Depending on the type of condition, specific antigens or antibodies can be detected in different body fluids, often in blood serum or plasma.¹⁰

1.2 Analysis

The above considerations demonstrate the central role of biomolecular interaction analysis in fundamental life science research, industrial drug discovery and clinical diagnostics. Accordingly, biomolecule binding is routinely studied with a variety of methods.

Classical biochemical methods are straightforward to perform and comparably low in cost and effort. They include antibody-based techniques such as enzyme linked immunosorbent assays (ELISA).¹¹ In basic ELISAs, surface-attached antibodies capture antigens within the test sample. The captured antigens bind to secondary antibodies, which carry an enzyme, catalyzing a detectable color reaction. ELISAs are highly popular, especially in serological diagnostics. However, they are typically limited to semiquantitative analysis due to several steps, which influence the result in a hardly predictable way. These include initial strong sample dilution, washing steps, enzymatic signal amplification, and normalization to a standard curve.

Just like ELISA, surface plasmon resonance (SPR) relies on immobilizing one of the binding partners to a surface.^{12,13} SPR is, however, a biophysical technique that allows for absolute quantification of association and dissociation rates and affinities of a binding event. Thus, the method is widely used in pharmaceutical compound screening. In SPR, the target biomolecule is tethered to a thin noble metal film on top of a glass prism, which is illuminated by a polarized light source. Light at the resonance angle is absorbed by the metal electrons, which induces surface plasmons. When the metal-attached biomolecules bind to a compound, the resonance angle is measurably shifted. Complications for kinetic SPR measurements include mass transport and rebinding.^{14,15} An additional disadvantage of

surface-bound techniques like SPR and ELISA is their often time-consuming design and preparation. Furthermore, surface immobilization may affect the bound molecules' dynamics and thus alter the binding event.¹⁶

Such surface artifacts can be excluded for techniques, in which both binding partners are present in free solution. The probably most accepted free-solution method is isothermal titration calorimetry (ITC).¹⁷ In ITC, the heat change upon binding is measured. To achieve this, a thermally conducting sample cell surrounded by an adiabatic jacket is filled with a constant amount of the biomolecule of interest. The binding partner is then titrated into the sample cell, which leads to a heat increase (exothermic binding reaction) or decrease (endothermic). The temperature difference in the sample cell is measured relative to a reference cell filled with buffer or water. To generate a sufficiently strong heat signal, relatively high sample amounts are required. If enough sample is available, ITC gives direct access to affinity, stoichiometry and thermodynamic parameters.^{18,19}

The main advantages of ITC, SPR and ELISA are combined in a recent biophysical technique: thermophoretic binding quantification, also referred to as microscale thermophoresis (MST).^{20,21} MST benefits from its low sample consumption, its free solution format, its flexible and simple assay design and its ability to quantify binding events absolutely and directly.

This thesis introduces key innovations in thermophoretic binding quantification, which comprise automation-friendly, nanoliter-volume measurements (chapter 3) and versatile protein assays including label free studies (chapter 4). In addition, thermophoresis was utilized for antibody characterization and a quantitative diagnostic assay (chapter 5). Before these new developments are addressed, the theoretical background and the measurement principle of biomolecule thermophoresis are outlined (chapter 2).

2 Background: Biomolecule Thermophoresis

2.1 Thermophoresis

Thermophoresis is the directed molecule movement along a temperature gradient. For liquids, this effect was initially described by Carl Ludwig in 1856, and further characterized by Charles Soret in 1879.^{22,23} In a locally heated solution, thermophoresis depicts a molecular flux j_{DT} , which is directly proportional to the temperature gradient ∇T with the proportionality constant D_T , the thermal diffusion coefficient:

$$j_{DT} = -cD_T\nabla T. \quad 1$$

Here, c denotes the molecule concentration. This thermophoretic flux is counteracted by mass diffusion j_D with the diffusion coefficient D :

$$j_D = -D\nabla c. \quad 2$$

In steady state, thermophoresis and backdiffusion compensate: $j = j_{DT} + j_D = 0$. For small temperature gradients this leads to:

$$\frac{dc}{c} = -\frac{D_T}{D}dT = -S_TdT. \quad 3$$

The Soret coefficient $S_T = D_T/D$ determines the thermophoretically induced change in concentration.

To predict thermophoresis in solution, several models are still under debate. Among these different theories, Duhr and Braun suggested a thermodynamic approach to derive S_T and experimentally proved it e.g. for DNA.^{24,25} This approach considers thermophoresis along moderate temperature gradients ($\nabla T < [aS_T]^{-1}$ with the molecule radius a) as a local equilibrium system. This allows to relate S_T with the temperature derivative of the Gibbs free enthalpy G :

$$S_T = \frac{1}{kT} \frac{dG}{dT} = -\frac{S}{kT}. \quad 4$$

Following equation 4, S_T is determined by the entropy S of the solute-solvent system. Contributions to S from solute-solute interactions are negligible for highly dilute solutions. Only solute-solvent interactions have to be considered, which are the hydration entropy S_{hyd} and the ionic shielding entropy S_{is} . S_{is} is calculated from the temperature derivative of Gibbs free enthalpy, which can be depicted as the electric energy stored in a capacitor consisting of the molecule's surface and the surrounding ion cloud.²⁶ Based on these contributions, S_T can be expressed as:

$$S_T = -\frac{S}{kT} = -\frac{S_{hyd} + S_{is}}{kT} = \frac{A}{kT} \left(-s_{hyd} + \frac{\beta\sigma_{eff}^2}{4\epsilon\epsilon_0 T} \lambda_{DH} \right) \quad 5$$

with:

- s_{hyd} : hydration entropy per molecule surface area A
- kT : thermal energy
- σ_{eff} : effective charge per molecule surface area A
- ε and ε_0 : relative permittivity of water and vacuum permittivity
- λ_{DH} : Debye length given by the solution's salt concentration
- β : factor describing the temperature dependence of ε and λ_{DH}
 $\beta \equiv 1 - (T/\varepsilon)(d\varepsilon/dT)$.

Equation 5 applies for all measurements in this thesis, as they were performed under highly dilute conditions and in moderate temperature gradients. These conditions, in the first place, guarantee biomolecule stability throughout analysis. Equation 5 illustrates that under constant buffer conditions S_T probes various molecular properties including size, charge, hydration entropy, and conformation. These parameters typically differ between an unbound biomolecule and its bound complex with a ligand. Thus, thermophoresis discriminates bound and unbound state, which qualifies it for biomolecular interaction analysis.^{20,21}

2.2 All-optical Measurement

For all measurements in this thesis, thermophoresis was induced with an infrared (IR) laser, as Figure 1A shows. The focused IR radiation with a wavelength of 1480 nm is absorbed by the sample buffer's water molecules to create a localized temperature gradient.^{20,21} Typically, a volume of 2 nl is heated by 1-10 K. The resultant thermophoretic molecule motion leads to a concentration change in the heat spot. This change was detected via fluorescence. For this, the biomolecules either were equipped with a fluorescent label or fluorescent fusion protein, or they exhibited a sufficient intrinsic UV fluorescence. Fluorescence was excited with a light emitting diode (LED) of a suitable wavelength and recorded with a photomultiplier tube (PMT) or a charge coupled device (CCD) camera.

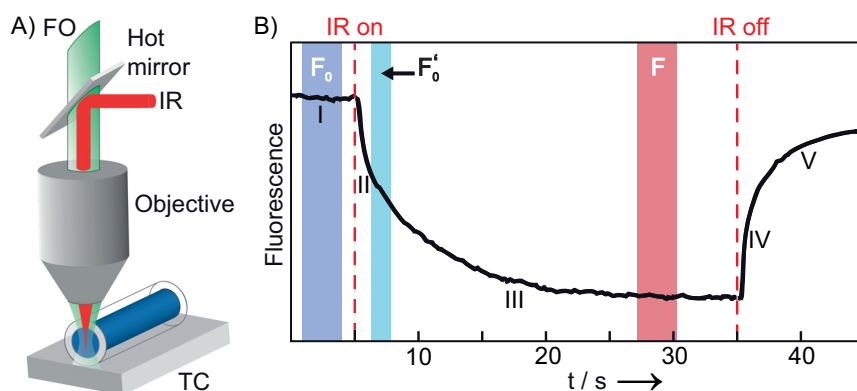


Figure 1. Biomolecule thermophoresis studies. (A) All-optical measurement. A focused infrared laser (IR) induces thermophoresis in a biomolecule solution. The molecule motion in the heat spot is detected via fluorescence excited with an LED and recorded with a fluorescence observation (FO). A thermoelectric cooler (TC) provides a constant basis temperature. (B) Fluorescence time trace. When turning on the IR ($t=5$ s), the initial fluorescence (I) decreases due to the fluorophore's temperature response (FTR, II) and thermophoretic depletion (III). When turning off the IR ($t=35$ s), the fluorescence recovers due to FTR (IV) and backdiffusion (V).

Figure 1B shows a schematic fluorescence time trace, which results from a series of separable processes. Before heating, the initial fluorescence (region I in Figure 1B) is recorded. Turning on the IR-laser ($t=5$ s) leads to an abrupt change in fluorescence intensity (region II), caused by the inherent temperature dependence of the fluorophore.²⁷ This temperature response is sensitive to the fluorophore's local environment and thus to ligand-binding in close proximity or to conformational changes.²⁸ The fluorophore's temperature response (FTR) occurs on a 100 ms timescale. Hence, it can easily be distinguished from the subsequent diffusion limited thermophoresis, which for the measured large biomolecules last several seconds (region III). Thermophoresis creates a concentration gradient of the fluorescent molecules leading to a slow change in the recorded fluorescence. Finally, fluorescence intensity reaches the steady state plateau, in which thermophoresis is counterbalanced by ordinary diffusion. Immediately after the heating laser is turned off ($t=35$ s), the fluorescence recovers due to the FTR (region IV), and backdiffusion driven by pure mass diffusion (region V).

2.3 Binding Quantification

As explained in the previous chapter, the biomolecules' fluorescence was recorded to measure the concentration change due to thermophoresis. This concentration change is described by equation 3 in chapter 7, which after integration yields:

$$\frac{c}{c_0} = \exp(-S_T \Delta T) \cong 1 - S_T \Delta T. \quad 6$$

In this exponential steady state distribution, the concentration after heating c is normalized to the concentration without heating c_0 . The normalized concentration can be approximated by linearization for small temperature and concentration changes, as they are used in biomolecule thermophoresis. To extract this concentration change from the fluorescence time trace in Figure 1B, the fluorescence after thermophoresis F is normalized to the fluorescence before thermophoresis, but after the fluorophore's temperature response (FTR) F'_0 :

$$F'_{norm} = \frac{F}{F'_0} \cong 1 - S_T \Delta T. \quad 7$$

As mentioned in chapter 2.2, FTR is often influenced by binding event. When the binding-induced change in FTR and in thermophoresis have an amplitude with the same sign, they add up to an enhanced binding signal. For this combined analysis, the fluorescence after thermophoresis F is normalized to the fluorescence before heating F_0 , with $\delta F / \delta T$ denoting the contribution of FTR:

$$F_{norm} = \frac{F}{F_0} \cong 1 + \left(\frac{\delta F}{\delta T} - S_T \right) \Delta T. \quad 8$$

To quantify biomolecule interaction, a binding partner A is titrated against a constant concentration of partner B , whose fluorescence is observed. Consequently, the ratio of unbound B and bound complex AB gradually changes. Due to equation 4, B and AB can be expected to differ in S_T . Thus, titration leads to a stepwise change in the ensemble averaged

S_T , which corresponds to the bound fraction x . As the fluorescence signal linearly reports S_T , F_{norm} is directly fit to a suitable description of the binding process.

In many cases, a simple model according to the mass action law well describes the binding event of two partners A and B forming the complex AB : $A + B \rightleftharpoons AB$. The affinity of this reaction is quantified by the equilibrium dissociation constant K_D

$$K_D = \frac{[A]_{free}[B]_{free}}{[AB]} = \frac{([A] - [AB])([B] - [AB])}{[AB]}. \quad 9$$

$[A]_{free}$ and $[B]_{free}$ denote the free concentrations of the binding partners, $[AB]$ the concentration of the bound complex. The unknown free concentrations of A and B can be expressed using the total, initial concentrations $[A]$ and $[B]$. The bound fraction x is then given by the following equation, in which K_D is the single free fit parameter:

$$x = \frac{[AB]}{[B]} = \frac{[A] + [B] + K_D - \sqrt{([A] + [B] + K_D)^2 - 4[A][B]}}{2[B]}. \quad 10$$

Many biological binding processes show cooperativity, which means that for a macromolecule with several binding sites, binding of one ligand molecule affects the K_D of subsequent binding events. An empirical description of cooperativity was originally formulated by Hill for oxygen binding to hemoglobin.²⁹ According to the Hill equation, the fraction of occupied sites x_{sites} is given by:

$$x_{sites} = \frac{1}{1 + \left(\frac{EC_{50}}{[A]}\right)^n}. \quad 11$$

EC_{50} denotes the ligand concentration occupying half of the binding sites, which is the apparent dissociation constant. The dimensionless Hill coefficient n quantifies the cooperativity. A Hill coefficient greater than one indicates positive cooperativity, where binding of one ligand molecule increases the affinity for further ligands. The opposite case of a Hill coefficient less than one reports negative cooperativity: binding of a ligand molecule reduces the affinity for further ligands. A Hill coefficient of one denotes independent binding without cooperativity.

Hill proposed his equation as purely empirical and disavowed a physical interpretation of n .²⁹ Only for extreme positive cooperativity, n accurately estimates the number of binding sites, as then n molecules bind in an all-or-non fashion without intermediate states. Typically, this cannot be assumed and instead n only provides a lower limit of the number of sites.³⁰ For hemoglobin, for instance, n is about 2.7, though the number of oxygen binding sites is four.^{29,31}

3 Thermophoresis in Nanoliter-Droplets

Microscale thermophoresis (MST) has been commercialized successfully and received well by the life science community. In standard MST, biomolecule solutions are analyzed in individual glass capillaries (see Figure 1A). Filling is achieved through capillary action, before the samples are put onto a temperature controlled tray on a translation stage. This allows for sequential analysis of 16 capillaries equivalent to one binding curve (NanoTemper Monolith NT.115). Recently, a medium-throughput MST instrument became available, which uses 24-capillary-chips (Monolith NT.Automated). It allows to analyze 96 samples equivalent to six binding curves at a time.

All available MST instruments are based on capillaries, which entails certain disadvantages. This includes the sample consumption, which with at least 0.5 μl per capillary is unnecessarily high compared to the measurement volume of 2 nl. A further disadvantage is the difficult handling of glass capillaries. Individual capillaries in particular, but also capillary-chips complicate the implementation into automation platforms, which are typically based solely on multi-well plates. Both drawbacks especially hamper thermophoresis applications in high throughput screening, e.g. in drug discovery or laboratory diagnostics. Thus, a 1536-well plate based, nanoliter-volume approach was developed, which is introduced in the following.

3.1 Sample Preparation

To miniaturize thermophoresis measurements, samples were prepared with a non-contact liquid handling system available commercially (Labcyte ECHO 550). The system delivers 2.5 nl-portions with a deviation from the target volume of less than 2% for aqueous buffers.³² The samples are delivered from multi-well source plates into destination plates via acoustic droplet ejection (Figure 2A).³³ To protect the nl-samples from evaporation, they were transferred into standard microbiology mineral oil mixed with a surfactant blend according to Tawfik and Griffiths.³⁴ For the measurements presented below, four or eight 2.5 nl-portions were transferred resulting in 10 nl- (270 μm) or 20 nl-samples (340 μm). Deflection by the oil reduced the transfer's positional accuracy. Thus, to coalesce individual portions, destination plates with funnel-shaped wells were used and mildly centrifuged after transfer ($\leq 500\times g$ to avoid droplet damage). This optimized protocol reproducibly yielded nl-samples that were stable for several hours (Figure 2A, inset). Hence, multiple thermophoretic binding assays were possible (10 min each).

3.2 Inverted Microscopic Setup

The nl-samples inside the multi-well plates were analyzed on a newly constructed microscopic setup (Figure 2B). As in the capillary instrument described in chapter 2.2, thermophoresis was induced and analyzed all-optically. A key difference to the capillary device is the nl-setup's inverted configuration, which allowed the sample plate to stay upright to prevent oil dripping. The plate was fixed to guarantee, that the droplets retained their exact position inside the well. Sequential measurement of multiple droplets was achieved by mounting the optical parts onto translation stages in all three directions.

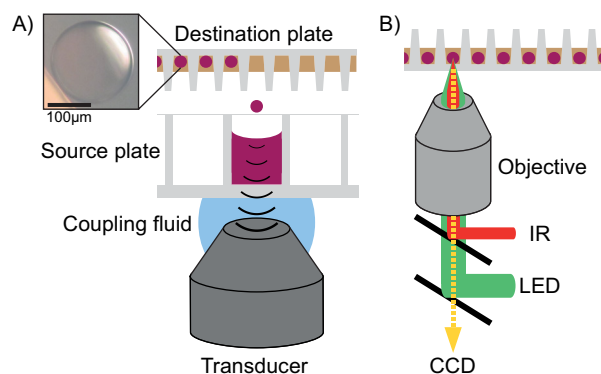


Figure 2 Nanoliter-droplet production and analysis. (A) Sample Preparation. A destination plate is positioned upside down above a source plate containing a sample stock (purple). An acoustic pulse focused to the sample surface leads to the formation of a 2.5 nl-droplet traveling into the destination well. Droplets are transferred into an oil-surfactant layer (brown) to prevent evaporation. Inset: Droplets were stable for several hours. 5 nl, 50% human serum/ 50% PBS. (B) Inverted microscopic setup. A focused IR laser locally heats the droplet center inducing thermophoresis which is analyzed via fluorescence (LED: light emitting diode; CCD: charge-coupled device camera). Sequential droplet analysis is achieved by moving the optical parts on translation stages.

3.3 Local Heating in Experiment and Simulation

The system of locally heated, aqueous nl-droplets in an oil surrounding was characterized extensively. The radial temperature profile in a 20 nl-droplet's central horizontal plane was obtained, utilizing the temperature response of the fluorescent dye Alexa 647 (Figure 3A). The central heat spot warmed up by $\Delta T_c = 11$ K, the droplet periphery by $\Delta T_p = 4$ K. A Lorentz fit yielded an FWHM of 120 μm . In the following, ΔT denotes the average temperature increase in the central (30×30) μm area.

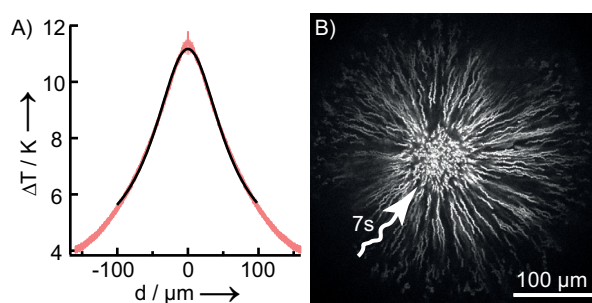


Figure 3 Local heating of 20 nl-droplets. (A) Radial temperature profile in the central horizontal plane (red). The temperature increased by $\Delta T_c = 11$ K in the center and by $\Delta T_p = 4$ K in the droplet's periphery. A Lorentz fit (black) revealed FWHM = 120 μm . (B) Flow profile of fluorescent polystyrene beads ($d = 1.0$ μm) integrated over 7 s during laser heating ($\Delta T = 15$ K). The beads moved toward the heat spot and out of focus with a peak velocity of 15 $\mu\text{m/s}$.

Heating induced convective flows, which were visualized with fluorescent polystyrene beads. The beads moved toward the central heat spot and out of focus, with peak velocities of 5-10 $\mu\text{m/s}$ for $\Delta T = 6$ K and 15 $\mu\text{m/s}$ for $\Delta T = 15$ K. Figure 3B is an integration over 7 s of heating in a 20 nl-droplet. The flows were further characterized with a full numerical simulation considering diffusion, convection, thermophoresis, and the temperature dependence of the dye. The simulation verified that the observed inward flow can be

attributed to Marangoni convection (Figure 4). This type of convection is caused by temperature-induced differences in interfacial tension. In our case, local heating decreased the interfacial tension between water and oil at the top and bottom of the droplet, triggering Marangoni fluid flow along the interface. Due to the cylindrical symmetry, toroidal vortices arose in the upper and lower droplet hemisphere. The simulation (Figure 4) shows the tori's cross section in a vertical cut. The dashed line marks the horizontal plane, where the flow is directed inward in the upper and lower vortex. This agrees with the experimental observation in this plane (Figure 3B).

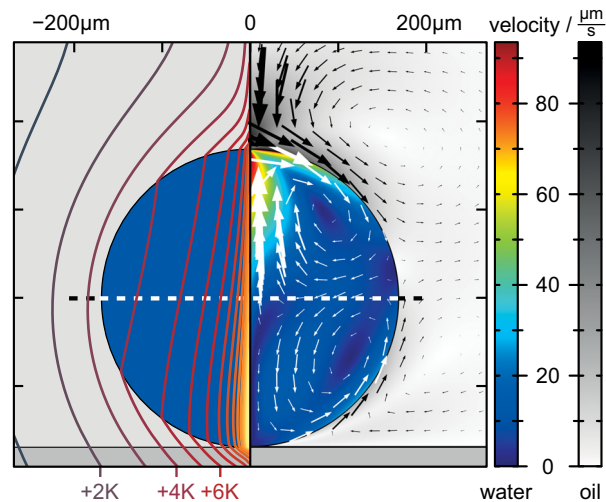


Figure 4 Numerical simulation of temperature and flow fields in a vertical cut through a 20 nl-droplet after 0.2 s of heating. Left: Isotherms indicate the temperature increase. Right: The central horizontal plane (dashed) comprises the boundary of two toroidal flow vortices. The vortices are driven by Marangoni convection at the water-oil interface and have already reached the steady state.

After flow field analysis, fluorescence time traces in 20 nl-Alexa 647 samples were recorded (Figure 5). The experimental curves were reproducible and confirmed by simulation. In both, experimental and simulated traces, the typical series of events can be identified in agreement with standard capillary measurements (see Figure 1). Heating decreases the fluorescence intensity due to the fluorophore's temperature response (FTR) and thermophoretic molecule depletion. Thermophoresis and backdiffusion equilibrate within a few seconds. When heating is turned off, fluorescence recovers due to FTR and backdiffusion. To assess the contributions to the fluorescence signal, simulations excluding Marangoni convection or thermophoresis were performed (Figure 5B). Neglecting Marangoni convection lead to differences in the flow fields, but only slightly affected the fluorescence signal. In contrast, neglecting thermophoresis from the simulation significantly changed the time traces. This demonstrates that thermophoresis prevailed against the convective flows.

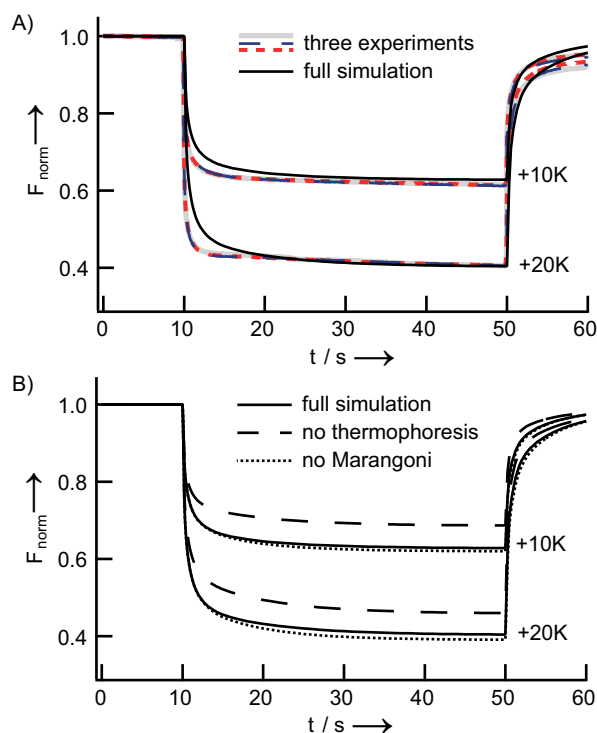


Figure 5 Fluorescence time traces from 20 nl-droplets. (A) Measurements of three Alexa 647-samples (grey, blue, red) overlap with minor deviations demonstrating the low batch-to-batch variation. Experiments and simulation (black) agree well. After the IR laser is turned on ($t=10$ s), the fluorescence decreases due to FTR and thermophoretic depletion. Thermophoresis and backdiffusion equilibrate within a few seconds. After heating ($t=50$ s), F_{norm} recovers due to FTR and isothermal backdiffusion. A larger ΔT enhances FTR and thermophoresis. (B) Simulated contributions to the decrease in F_{norm} . Neglecting Marangoni convection led to a negligible change of 0.008 (dotted); neglecting thermophoresis led to a change of 0.06 (dashed).

3.4 Aptamer Quantification

The applicability of nl-droplet thermophoresis for biomolecular interaction studies was evaluated with a well characterized aptamer. Aptamers have been discovered more than 20 years ago.^{35,36} Owing to their three-dimensional conformation, these single stranded oligonucleotides bind various biomedically relevant targets including proteins and small molecules.^{37,38} Just like antibodies, aptamers show high specificity and affinity. At the same time, these nucleic acid based ligands are superior to protein based ligands in production costs, storage conditions, and chemical modifiability.³⁸ *In vivo*, their small size facilitates good delivery to the target tissue, whereas no immunogenicity and low toxicity have been reported.^{38,39} These benefits and the first marketed aptamer drug demonstrate the high potential of aptamers.⁴⁰

A 25mer DNA aptamer that binds adenosine and its phosphorylated analogues was analyzed.⁴¹ This aptamer has previously been studied extensively.^{20,42} For nl-interaction studies, a constant concentration of fluorescently labeled aptamer ($c=2 \mu\text{M}$) was added to a serial dilution of adenosine 5' monophosphate (AMP). AMP- and aptamer-droplets were coalesced by mild centrifugation (see above). Subsequently, the short diffusion times through the small 10 nl- or 20 nl-samples guaranteed complete mixing within minutes. As measured in these nl-samples, FTR and thermophoretic depletion of free aptamer

significantly differed from its bound complex with AMP. After a combined analysis of FTR and thermophoresis, the signal was fit to the Hill equation (see chapter 2.3). The fit revealed $EC_{50} = (116 \pm 14) \mu\text{M}$ in 10 nl-samples and $EC_{50} = (104 \pm 10) \mu\text{M}$ in 20 nl-samples for measurements in the original selection buffer (Figure 6A).⁴¹ Both values agree with each other and the literature value of $(87 \pm 5) \mu\text{M}$ from capillary thermophoresis.²⁰ The revealed Hill coefficients of $n = 1.2 \pm 0.1$ (10 nl) and $n = 1.9 \pm 0.3$ (20 nl) indicate cooperative binding, which is consistent with the previously reported tertiary structure of the complex (Figure 6C).⁴³ Moreover, the Hill coefficients only slightly deviate from each other and confirm the literature value ($n = 1.4$).²⁰ As a control, a DNA oligonucleotide with the same length as the aptamer but two point mutations was analyzed. The dinucleotide mutant's AMP-affinity was reduced 200-fold ($EC_{50} \cong 20 \text{ mM}$), which demonstrates the binding signal's specificity.

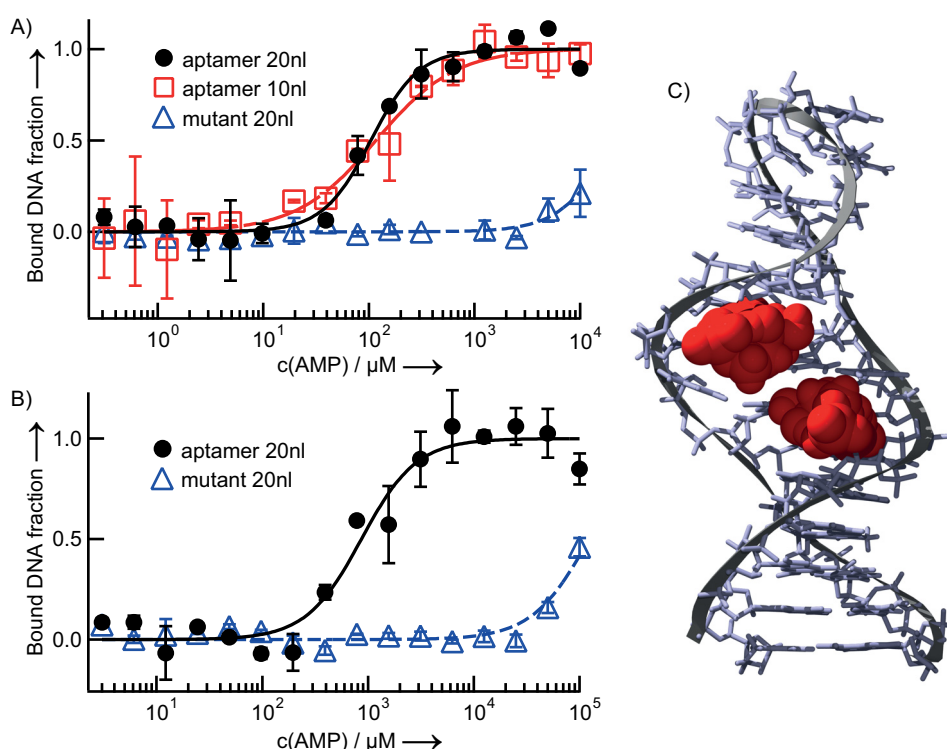


Figure 6 Nanoliter thermophoresis quantifies aptamer binding. The specific signal change in FTR and thermophoresis upon AMP titration to labeled aptamer was fit to the Hill equation. Mean values of at least two individual nl-samples; error bars: standard deviation. (A) Selection buffer. The fit revealed $EC_{50} = (116 \pm 14) \mu\text{M}$ and $n = 1.9 \pm 0.3$ in 10 nl (red squares) and $EC_{50} = (104 \pm 10) \mu\text{M}$ and $n = 1.2 \pm 0.1$ in 20 nl (black circles). A dinucleotide mutant showed a 200-fold increased $EC_{50} \cong 20 \text{ mM}$ (blue triangles). (B) PBS. $EC_{50} = (0.90 \pm 0.13) \text{ mM}$ was found (black circles), confirming the aptamer's buffer dependence. The mutant showed a 130-fold increased $EC_{50} \cong 0.12 \text{ M}$ (blue triangles). (C) Determined Hill coefficients agree with the reported tertiary structure (NDB code 1AW4): an aptamer (grey) binds two AMP molecules (red).⁴³

AMP-aptamer affinity has been reported to depend on the buffer,²⁰ which was analyzed via nl-thermophoresis. In PBS, an EC_{50} of $(0.90 \pm 0.13) \text{ mM}$ was found (Figure 6B), corresponding to a 10-fold affinity reduction compared to selection buffer. This reduction could be expected, as the aptamer has originally been evolved in and thus optimized for its selection buffer.^{41,44} The crucial difference between the buffers is their Mg^{2+} content: the selection buffer contained 5 mM MgCl_2 , while PBS without Mg^{2+} was used. It was exactly

this MgCl_2 reduction from 5 to 0 mM that has been reported to significantly reduce AMP-aptamer retention in affinity chromatography.⁴² Mg^{2+} affects the binding, as it stabilizes the aptamer-DNA and also neutralizes AMP's phosphate group, which reduces repulsion to phosphates in the aptamer backbone.⁴⁵ Unlike the affinity, the Hill coefficient was unaffected by the buffer; it was $n=1.6\pm 0.4$ in PBS. The mutant control's affinity was reduced 130-fold ($\text{EC}_{50}\cong 0.12$ M) compared to the aptamer.

3.5 Discussion

The successful aptamer quantification validates the applicability of nl-droplet thermophoresis for bimolecular interaction analysis. Compared to capillary thermophoresis, sample consumption was reduced by a factor of 50. This implies an enormous potential for high-throughput screens, which are further promoted by the automation-friendly 1536-well plate format.

To achieve automation, a droplet search algorithm has to be implemented into the control software, as this search is up to now done manually. Owing to the standardized plates with low variations in dimensions, automatic positioning into a specific well is already used in many commercial instruments as e.g. the nl-liquid handler. For the nl-thermophoresis instrument, positioning presents a major challenge, as the exact location of the droplet inside the well needs to be found. Currently, the variations in droplet placement are rather high due to deflection by the oil and centrifugation. Additionally, a subset of droplets (10-20%) is typically damaged during preparation and cannot be included into analysis. Thus, the preparation protocol needs to be optimized. Deflection could be reduced by decreasing the thickness of the oil layer. To this end, a low volume oil dispenser would have to be used, as the required oil volumes below 0.5 μl cannot reliably be pipetted manually.

When calculating the total volume consumption, the dead volume of the liquid handler has to be taken into account. To date, two source plate types are available for the transfer of aqueous solutions on the Labcyte ECHO 550 liquid handler. Both have a dead volume of approximately 25%. It is 3 μl from a maximum of 12 μl in 384-well low dead volume plates (384LDV) and 15 μl from a maximum of 65 μl in 384-well polypropylene plates (384PP). The transfer protocol should thus be designed carefully to ensure that the full working volume range of the source plate is exploited. If the stability of the sample is high enough, the dead volume might even be reused after transfer. The drawback of requiring a dead volume is outweighed by the advantages of the liquid handler, which include its high accuracy (see chapter 3.1). As a further benefit, the contact-free nl-transfer exempts from washing steps and minimizes cross contaminations. After transfer, the sample does not touch the well surface, but forms a surfactant surrounded droplet inside the oil. This should significantly reduce unspecific surface adhesion of biomolecules ("sticking"), an often encountered challenge in capillary thermophoresis. The elimination of sticking represents a major benefit, even if surfactant and oil might have to be optimized for different sample types.

Aptamer analysis is likely to gain in importance, now that the comprehensive aptamer patent portfolio is starting to expire.⁴⁶ This might well facilitate commercial aptamer applications. Additionally, nl-thermophoresis is a highly attractive analysis tool for other types of samples. Sample preparation is unlikely to be limiting, as the liquid handler can be deployed

for various solution types. We e.g. produced stable nl-droplets of 50% human blood serum (Figure 2A, inset). In the current nl-thermophoresis instrument the lowest detectable fluorophore concentration inside droplets is approximately 500 nM. Thus, K_{DS} in the high nanomolar range can be determined exactly. To allow for the quantification of higher affinities, the sensitivity of the instrument needs to be improved. This should be possible by optimizing the optics, e.g. by using a photomultiplier tube (PMT), which is more sensitive than the employed CCD camera. In addition, further LED/filter combinations would enable measurements of different fluorophores. With these optimizations, a similar versatility as for capillary thermophoresis can be expected. This flexibility of capillary measurements is demonstrated in the following chapters.

4 Thermophoretic Protein Studies

Proteins are involved in most biomolecular interactions, as they fulfill various cellular functions. Due to these diverse roles, proteins have highly variable properties. As a result for their analysis, they often require very specific assay adjustments. Moreover, for distinct proteins, interactions with very different molecule classes can be of interest. How this need for flexibility is met by capillary thermophoresis, will be shown in the following, structured according to the protein's binding partner.

4.1 Protein-Protein Binding in Cell Lysate: TEM1-BLIP

The β -lactamase TEM1 is the most widespread bacterial resistance enzyme to β -lactam antibiotics like penicillins. The binding of TEM1 to the β -lactamase inhibitory protein BLIP is a well characterized model system for protein-protein interaction. For this interaction, the contribution of individual amino acids has previously been studied using site-specific mutations.⁴⁷⁻⁵⁰ Three mutations of TEM1 and BLIP that have been reported to significantly affect the binding affinity were analyzed with capillary thermophoresis.

For a first set of experiments, wild-type TEM1 (wt-TEM1) was labeled with the red fluorescent dye NT647 via crosslinker reactive groups. Binding of labeled TEM1 to wild-type BLIP (wt-BLIP) and two BLIP mutants with tryptophan-to-alanine substitutions at position 112 or 150 (p.W112A-BLIP, p.W150A-BLIP) was quantified. A fit to equation 10 revealed $K_D = (3.8 \pm 0.8)$ nM for the wt-interaction (Figure 7A). Both alanine substitutions within BLIP reduced the TEM-affinity to $K_D = (0.5 \pm 0.1)$ μ M for p.W112A-BLIP and $K_D = (1.7 \pm 0.4)$ μ M for p.W150A-BLIP (Figure 7B and C). These values agree excellently with the literature values determined by SPR (wt: (3.2 ± 0.6) nM, p.W112A: (0.36 ± 0.06) μ M, p.W150A: (3.8 ± 0.6) μ M).^{47,48} In addition, the thermophoresis signal seems to contain further information on the binding event. Upon binding of wt-BLIP and p.W112A-BLIP to TEM1, the complex shows an increased depletion compared to unbound TEM1 (negative slope in Figure 7A and B). Binding of p.W150A-BLIP has the opposite effect (Figure 7C). This p.W150A mutation has been reported to induce a pronounced conformational rearrangement of BLIP, defects in geometrical shape complementarity to TEM1 and trapping of additional water molecules in the TEM1-BLIP interface.⁴⁹ This decreases the enthalpic driving force for binding and likely causes the differences in thermophoresis.

For a second set of experiments, wt-BLIP was labeled with the yellow fluorescent fusion protein Ypet. Binding of labeled BLIP to wt-TEM1 and a TEM1-mutant with an arginine-to-alanine substitution (p.R243A-TEM1) was quantified. For the interaction of the wt-proteins $K_D = (4.8 \pm 1.7)$ nM was found (Figure 7D). This reproduces the SPR literature value of (3.5 ± 0.5) nM.⁵⁰ It also agrees with the result measured via the reversed assay design (Figure 7A). The p.R243A-TEM1 mutant's affinity for BLIP was reduced to $K_D = (0.19 \pm 0.05)$ μ M, which agrees with literature.⁵¹ All TEM-BLIP measurements presented so far were conducted in buffer. A buffer, however, does not resemble the highly crowded, intracellular environment. Thus, the interaction of Ypet-wt-BLIP and wt-TEM1 was also quantified in mammalian cell lysate. Under these close to *in vivo* conditions, thermophoresis revealed $K_D = (10 \pm 4)$ nM. This demonstrates, that even in cell lysate, thermophoresis quantifies protein-protein interactions with high selectivity and sensitivity.

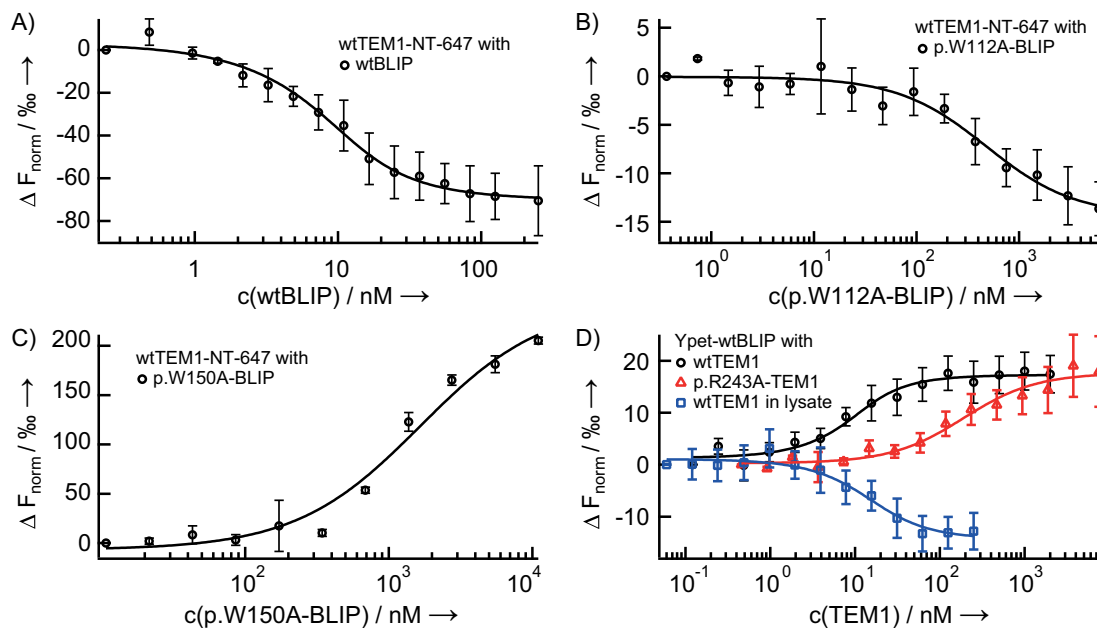


Figure 7 Thermophoresis quantifies TEM1-BLIP binding. (A) Wt-BLIP-titration to wt-TEM1-NT647 yielded $K_D = (3.8 \pm 0.8)$ nM. (B) The p.W112A-mutation in BLIP reduced its TEM1-affinity to $K_D = (0.5 \pm 0.1)$ μM . (C) p.W150A-BLIP bound TEM1 with an even lower affinity of $K_D = 1.7 \pm 0.4$ μM . (D) Wt-TEM1-titration to the fusion protein Ypet-wt-BLIP yielded $K_D = (4.8 \pm 1.7)$ nM (black circles). Mutated p.R243A-TEM1 showed a lower affinity of $K_D = (0.19 \pm 0.05)$ μM (red triangles). In cell lysate, Ypet-wt-BLIP and wt-TEM1 bound with $K_D = (10 \pm 4)$ nM. This demonstrates the applicability of thermophoresis for measurements in cell lysate. Notably, the sign of the signal amplitude changed in lysate due to differences in pH, ionic strength etc.

4.2 Protein-Peptide Binding With Two Phases: AMA1-RON2

The binding of two proteins of the malaria-causing parasite *Plasmodium falciparum* plays a key role during red blood cell invasion: apical membrane antigen 1 (AMA1) and rophtry neck protein 2 (RON2).⁵² This qualifies the AMA1-RON2 interaction as a potential drug target. RON2 contains a highly conserved region with two fully conserved cysteine residues which are critical for AMA1-binding.⁵³ This conserved RON2 region was used as a peptide (4.3 kDa) to quantify its interaction with AMA1 (66 kDa) via thermophoresis.

Firstly, the binding of labeled RON2-FITC to titrated AMA1 was assessed thermophoretically, yielding $K_D = (28 \pm 2)$ nM (Figure 8A). Secondly, the assay was reversed and the binding of labeled AMA1-NT647 to titrated RON2 was analyzed. This assay revealed a biphasic binding event (Figure 8B). The high affinity binding was superimposed by an additional low affinity binding. Individual fits of each binding event to equation 10 yielded $K_D = (62 \pm 16)$ nM and $K_D' = (1.4 \pm 0.2)$ μM . In addition, a model for two serial binding events with different K_D s was used to fit all data points simultaneously:

$$F(A) = M \left(\frac{[A] + [B] + K_D - \sqrt{([A] + [B] + K_D)^2 - 4[A][B]}}{2[B]} \right) + t - M \left(\frac{[A] + [B] + K_D' - \sqrt{([A] + [B] + K_D')^2 - 4[A][B]}}{2[B]} \right) + t'. \quad 12$$

For both binding events, the fit assumes an identical amplitude M but, as the data suggests, with an opposite sign. t denotes the binding curve's y-offset. Fitting to this serial binding model revealed $K_D = (81 \pm 21)$ nM and $K_D' = (1.2 \pm 0.1)$ μ M (Figure 8B, inset). The high affinity K_D slightly varies for the different assay designs. This is likely due to a limited fit accuracy for the biphasic signal, as either less data points (two individual fits) or a more complex fit function (serial binding) were used. Despite this limitation, both experiments yield high affinity K_D s in the double-digit nM range, demonstrating the assay reversibility of thermophoresis studies. In addition, this example evidences the importance of performing titration assays both ways around: while AMA1-titration precisely quantifies the K_D , only the RON2-titration revealed the second, low-affinity binding event.

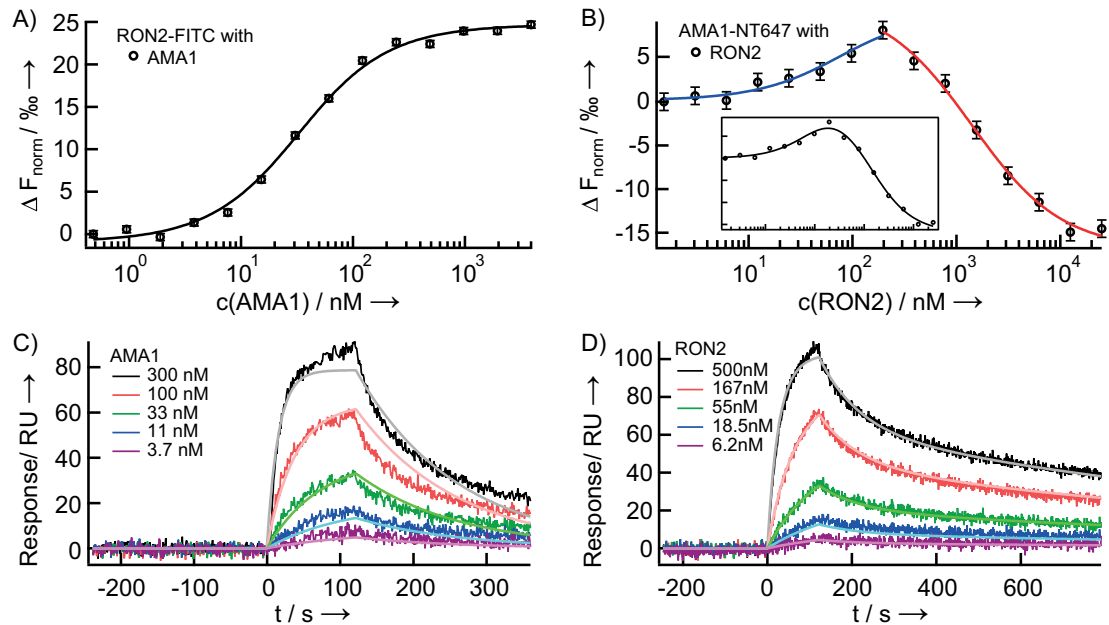


Figure 8 AMA1-RON2 binding in thermophoresis and SPR. (A) Thermophoresis: AMA1-titration to RON2-FITC yielded $K_D = (28 \pm 3)$ nM. (B) RON2-titration to AMA1-NT647 revealed a biphasic event. Fitting both phases separately revealed $K_D = (62 \pm 16)$ nM for the high affinity phase (blue) and $K_D' = (1.4 \pm 0.2)$ μ M for the low affinity phase (red). Inset: All data points were fit to a serial binding model assuming two binding events. This yielded $K_D = (81 \pm 21)$ nM and $K_D' = (1.2 \pm 0.1)$ μ M. (C) SPR: AMA1-titration to immobilized RON2 yielded $K_D = (13 \pm 1)$ nM. (D) RON2-titration to immobilized AMA1 yielded $K_D = (38.3 \pm 0.4)$ nM. A heterogeneous ligand model fit the dissociation phase best, indicating a biphasic event as observed in thermophoresis. 1 RU = 1 SPR response unit $\cong 1$ pg/mm².

To evaluate the thermophoresis results, comparative SPR-measurements were conducted. In SPR, AMA1-titration against immobilized RON2 yielded $K_D = (13 \pm 1)$ nM (Figure 8C). RON2-titration against immobilized AMA1 revealed $K_D = (38.3 \pm 0.4)$ nM (Figure 8D). These affinities are slightly higher than those found in thermophoresis analysis, which agrees with the reported tendency of SPR to overestimate affinities due to surface artifacts.⁵⁴ In SPR, the

dissociation phase of the RON2-titration was best fit by a heterogeneous ligand model. This indicates a second low-affinity binding event, just like thermophoresis did (Figure 8B).

The second binding event was only detected when RON2 was neither labeled (thermophoresis) nor immobilized (SPR). Unlabeled, immobilization-free RON2 might not only be present in the cyclized form with a closed disulfide bond, but also in a linear form with reduced cysteines. While the cyclized form binds with a high affinity, the linear form might bind with a lower affinity, resulting in the second binding phase. Labeling or tethering seems to prevent RON2 from assuming the linear form.

4.3 Protein-Small Molecule Binding Without Labeling

As demonstrated in the previous and following chapters, attached fluorescent dyes or fused fluorescent proteins enable highly sensitive thermophoresis studies. These attached fluorophores also provide high selectivity, which allows for measurements in complex bioliquids like cell lysate (chapter 4.1) or blood serum (chapter 5.2). However, fluorescent tags come along with certain disadvantages. Attaching modifications to a biomolecule can significantly alter its properties, with e.g. membrane proteins being particularly sensitive. Possible consequences include changes in affinity or even protein precipitation. In addition, unspecific binding to the attached fluorophore can lead to false positive results. Apart from these influences on the binding event, labeling procedures and the often required purification steps are time and sample consuming.

A solution to this is label free thermophoresis analysis, which is introduced in the following. Label free thermophoresis utilizes the intrinsic UV fluorescence of proteins, arising from the aromatic amino acids tyrosine, phenylalanine and tryptophan (Trp), with the latter being the dominant intrinsic fluorophore. For these measurements in the UV range, the capillary setup (Figure 1B) was equipped with a 285 nm LED, a quartz objective and a photomultiplier tube (PMT). Photon counting PMTs are more sensitive than CCD cameras, especially in the 350 nm emission regime used for label free thermophoresis. Samples were measured in fused silica capillaries with low background UV fluorescence. Concerning the sample itself, optimal results are obtained, when only one binding partner exhibits UV fluorescence. This is the case for most protein-small molecule interactions. Small molecules typically do not show UV fluorescence. In contrast, the majority of proteins contains enough Trp residues to exhibit a UV fluorescence signal sufficient for label free thermophoresis.

4.3.1 Glutamate Receptor iGluR2

In the mammalian central nervous system, ionotropic glutamate receptors (iGluR) play the key role in fast excitatory synaptic transmission.⁵⁵ The binding of the various iGluR subtypes to their ligands is in the focus of ongoing research.⁵⁶

Via label free thermophoresis, the interaction of the AMPA receptor subunit iGluR2 (activated by α -amino-3-hydroxy-5-methyl-4-isoxazolepropionic acid) was studied. To this end, the soluble ligand binding domain (LBD; 29.2 kDa) was used, which was generated by fusing iGluR2's two discontinuous extracellular fragments S1 and S2. The iGluR2-LBD contains 4 Trp. A concentration of 2 μ M exhibited a sufficient UV fluorescence intensity without significant bleaching. Thermophoresis revealed $K_D = (835 \pm 43)$ nM for the natural agonist glutamate (147.13 Da; Figure 9). This reproduces the literature value of 821 nM.⁵⁷ Azobenzene glutamate (glu-azo; 367.15 Da), a photoswitchable agonist allowing for remote control of neuronal excitability, bound the iGluR2-LBD with $K_D = (19 \pm 5)$ μ M (Figure 9).⁵⁸ Thermophoresis confirmed the finding that glu-azo also binds iGluR2, though designed as a kainate receptor ligand.⁵⁹ When the iGluR2-LBD was pre-incubated with a saturating glutamate concentration (500 μ M), glu-azo titration did not influence thermophoresis. This proves the specificity of the glu-azo signal. It also shows that both agonists compete for the same binding site. The label free measurement for glu-azo was verified using labeled iGluR2-LBD, as shown in the supporting information of the associated publication 3 (chapter 9). The measured K_D of (22 ± 8) μ M did not significantly deviate from the label free analysis, which demonstrates that the latter was not disturbed by autofluorescence.

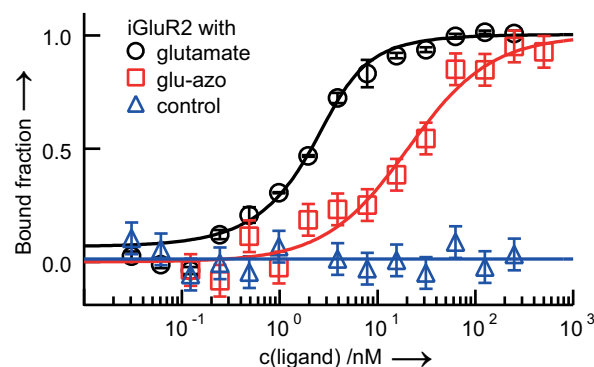


Figure 9 Label free thermophoresis quantifies ligand binding to membrane receptors. The glutamate receptor subunit iGluR2-LBD bound glutamate with $K_D = (835 \pm 43)$ nM (black circles) and glu-azo with $K_D = (19 \pm 5)$ μ M (red squares). Pre-incubation of iGluR2 with a saturating amount of glutamate prevented glu-azo binding, which demonstrates that both agonists compete for the same binding site (blue triangles).

4.3.2 MAP Kinase p38 α

P38 is a mitogen-activated protein kinase (MAP kinase) responding to stress. The isoform p38 α is considered the key subtype in cytokine synthesis during inflammatory response. Thus, potent inhibitors of p38 α promote the development of novel treatments for inflammatory diseases.⁶⁰

Three small molecule inhibitors of p38 α (59.5 kDa) were analyzed. The kinase contains 5 Trp residues, so that a concentration of 100 nM was sufficient for label free thermophoresis. Figure 10 shows, that p38 α bound the inhibitor SB202190 (331 Da) with $K_D = (48 \pm 21)$ nM reproducing the literature value of 37 nM.⁶¹ PD169316 (360 Da) and SB239063 (368 Da) showed upper K_D limits of 33 nM and 20 nM. This lies in a similar range as reported IC_{50} values of 130 nM (PD169316) and 44 nM (SB239063).^{62,63} Thermally denatured p38 α did not show binding, thus proving specificity.

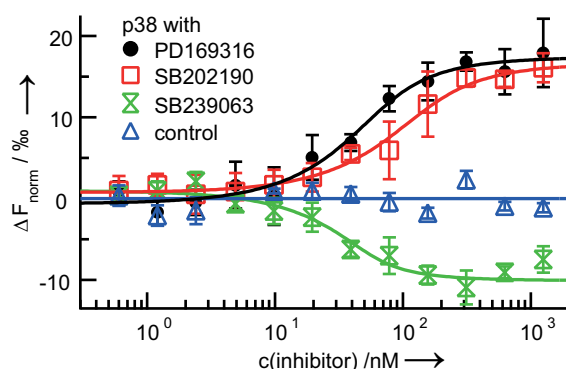


Figure 10 Label free analysis of small molecule MAP kinase inhibitors. SB202190 bound with $K_D = (48 \pm 21)$ nM (red squares). PD169316 (black circles) and SB239063 (green triangles) showed upper K_D limits of 33 nM and 20 nM. Thermally denatured p38 α did not bind (blue triangles). Corresponding to structural differences, the binding of SB202190 and PD169316 had the opposite effect on thermophoresis compared to SB239063.

Remarkably, the thermophoretic signal contained further information on the ligands. Upon binding of SB202190 and PD169316 to p38 α , the complex showed a reduced thermophoretic depletion compared to the unbound kinase, represented by the positive slope of the binding curve. Binding of SB239063 had the opposite effect (Figure 10). These differences are likely

related to the inhibitors' structure. Apart from a single functional group SB202190 (4-(4-Fluorophenyl)-2-(4-hydroxyphenyl)-5-(4-pyridyl)-1H-imidazol) and PD169316 (4-(4-Fluorophenyl)-2-(4-nitrophenyl)-5-(4-pyridyl)-1H-imidazole) are identical in structure. In contrast, the structure of the second generation inhibitor SB239063 (*trans*-1-(4-Hydroxycyclohexyl)-4-(4-fluorophenyl)-5-(2-methoxypyridimidin-4-yl)-imidazole) differs significantly.

4.4 Discussion

Capillary thermophoresis showed a broad application range for protein analysis. In addition to protein-protein interactions, protein binding to peptides and small molecules was readily accessible despite the high molecular weight ratio. Such studies are possible, as thermophoresis is extremely sensitive to binding induced changes not only in size, but also in charge, hydration shell, and conformation (see equation 5). This is a major advantage over SPR and fluorescence polarization,⁶⁴ which rely on size changes alone, or dynamic light scattering, which is limited to a maximum twofold difference of the binding partners' hydrodynamic radii.⁶⁵ The applicability of thermophoresis is further enhanced, as measurements can be performed in various liquids. Buffer and additives may be chosen freely, which allows to stabilize different protein types in solution. Thermophoresis was even measured in crude cell lysate, which resembles close to *in vivo* conditions. This might even exempt from protein isolation, as a fusion construct of a cellular and a fluorescent protein like Ypet should directly be measurable in lysate without purification. Alternatively, certain peptide sequence tags allow for site-specific dye coupling in lysate. Sample volumes and concentrations obtained by such protein purification free approaches should suit the requirements of thermophoresis experiments very well.

On the other hand, binding in buffer was quantified label free utilizing protein intrinsic UV fluorescence. As the binding partners were not attached to a label or surface, their molecular properties were not altered and mobility was not restricted. Thus, native binding affinities were revealed. To get a suitable UV fluorescence signal, proteins with two Trp residues can be used in concentrations down to 100 nM, enabling accurate quantification of K_{DS} down to 50 nM. High affinity interactions with lower K_{DS} are still detected, but not precisely quantified. The fit then only yields an upper K_D limit (see chapter 4.3.2). To realistically evaluate the applicability of Trp based thermophoresis, the average Trp content of proteins has to be considered. According to the minimum redundancy protein database Swiss-Prot (release statistics of May 2014), the percentage of Trp residues in all sequences (>0.5 M) is 1.09 and the average number of amino acids in a sequences is 355.⁶⁶ This yields an average of 3.9 Trp per protein. It demonstrates that label free thermophoresis will be utilizable for the majority of proteins, and in many cases also for protein subdomains as e.g. the ligand binding domain of iGluR2 (see chapter 4.3.1). Ideally, the ligands should not exhibit UV fluorescence. As mentioned above, this holds true for most small molecules, which account for the majority of today's pharmaceuticals. If both binding partners show a similar UV fluorescence, the contribution of the titrated fluorescent ligand to the thermophoresis signal needs to be quantified in control experiments and then subtracted.

As discussed in chapter 3, the drawbacks of capillary thermophoresis include unspecific surface adhesion of biomolecules ("sticking"). Sticking can often be reduced with hydrophilic or hydrophobic capillary coatings and with buffer additives like detergents or

bovine serum albumin. Possible artefacts through coatings and additives need to be excluded in control experiments. Additional disadvantages of capillary analysis are the unnecessarily high sample consumption and the difficult handling. Nanoliter-droplet thermophoresis analysis in multi-well plates (chapter 3) overcomes these limitations, yet its applicability for protein measurements remains to be tested.

Despite the discussed limitations, the above experiments demonstrate that capillary thermophoresis is highly adaptable to the diverse requirements of different proteins. This includes antibodies, a protein class with a high medical relevance, whose thermophoretic analysis is discussed in the following chapters.

5 Thermophoretic Immunoassays

Immunoassays are bioanalytical tests that are based on the interaction of antibodies and antigens. Either of these two binding partners can be the analyte, while the other one serves as a tracer. As mentioned in chapter 1.2, the ELISA is a well established immunoassay format, but as a biochemical method only allows for semiquantitative analysis. The required surface immobilization of the tracer in ELISAs is an additional drawback, which is also discussed in chapter 1.2. In contrast, immunoassays based on thermophoresis allow for absolute quantification in free solution. These thermophoretic immunoassays were applied for antibody characterization and *in vitro* diagnostics. The latter application introduces an autocompetitive assay to simultaneously quantify affinity and concentration in untreated human blood serum.

5.1 Antibody Characterization

5.1.1 Towards a Therapeutic Antibody For Granulomatosis With Polyangiitis

Granulomatosis with polyangiitis (GPA) is a rare, chronic form of systemic vasculitis that mainly affects small and medium sized blood vessels. The resultant tissue damage can lead to lethal organ failure especially of lung and kidney, so that GPA patients require long-term immunosuppression. It is widely accepted that GPA represents an autoimmune disease, caused by antineutrophil cytoplasmic antibodies (ANCA).

The major autoimmune target for ANCA in GPA is proteinase 3 (PR3) bound to the plasma membrane of a subset of resting neutrophils.^{67,68} Neutrophils, which represent the most abundant type of mammalian white blood cells, play a key role in innate immune response. To this end, they express the antimicrobial serine protease PR3. Just like other protease enzymes, PR3 degrades proteins and peptides. To prevent tissue damage, protease activity is regulated by an initial activation step, in which the enzyme's conformation is changed from an inactive zymogen form into an active mature form. In addition, protease activity is controlled by inhibitors, as for example α_1 -proteinase inhibitor (α_1 PI).⁶⁹ PR3 is stored in neutrophil granules in an active, mature conformation. A small amount is expressed on neutrophil membranes and recognized by ANCAs. It is not yet clear if this membrane-associated PR3 assumes the active mature conformation (active PR3), the inactive zymogen form (pro-PR3) or both. *In vitro* ANCAs have been reported to activate neutrophils and induce their degranulation leading to endothelial damage.⁷⁰ This would be a possible explanation for the extensive blood vessel damage in GPA.⁷¹ In addition, GPA has been associated with a point-mutation in the α_1 PI allele (Z-allele), which decreases both, α_1 PI's blood levels and protease affinity.^{72,73}

As a starting point for future GPA treatment, the monoclonal antibody (moAB) MCPR3-7 with specificity close to PR3's active site was developed. MCPR3-7 binding properties were characterized via thermophoresis.

5.1.2 MCPR3-7 Affinity and Selectivity

Thermophoresis revealed a very high binding affinity of NT647-labeled MCPR3-7 to pro-PR3: $K_D \leq 10$ nM (Figure 11A). In addition, MCPR3-7's affinity to mature PR3 was measured. To conserve PR3 in a mature conformation, it was pre-treated with the covalent inhibitor chloromethylketone AAPF (CMK). This mature PR3-CMK did not show binding to MCPR3-7, clearly indicating that the antibody selectively recognizes PR3's inactive conformation.

For active PR3, however, MCPR3-7 indeed showed binding, yet with $K_D = (0.4 \pm 0.2)$ μ M (Figure 11B) corresponding to an approximately 40-fold lower affinity than for pro-PR3. This is probably due to a reversible allosteric switch from the active form of PR3 to a more zymogen-like conformation, which is recognized by MCPR3-7. As this switch is not possible for PR3-CMK, it was not bound by MCPR3-7.

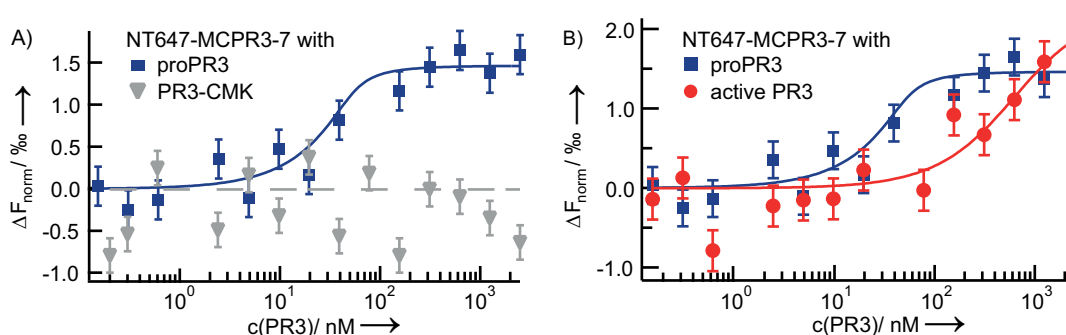


Figure 11 MCPR3-7 binding affinity and selectivity. (A) Thermophoresis revealed a high affinity of MCPR3-7 to pro-PR3 ($K_D \leq 10$ nM; blue rectangles). By contrast, MCPR3-7 did not bind the mature conformation of PR3-CMK (gray triangles). (B) Active PR3 was bound with a 40-fold weaker affinity than pro-PR3: $K_D = (0.4 \pm 0.2)$ μ M (red circles). This is probably due to a reversible allosteric switch from the active to a more zymogen-like conformation.

5.1.3 Interference with PR3- α 1PI Complex Formation

We tested the effect of MCPR3-7 on the canonical complex formation of mature but catalytically inactive PR3 (PR3-S195A) with its inhibitor α 1PI. In this regard, MCPR3-7 was compared to the anti-PR3 moAB CLB-12.8 available commercially. The binding of α 1PI to PR3 was quantified in the presence and absence of moABs. To this end, PR3 and moABs or buffer were preincubated for one hour before adding NT647-labeled α 1PI at a final concentration of 0.88 μ M.

PR3 and α 1PI bound with $K_D = (1.9 \pm 1.1)$ μ M in absence of moABs (Figure 12). In the competition experiments, it was not possible to use saturating amounts of MCPR3-7 as this antibody could not be concentrated to very high levels. Instead, a relatively low final MCPR3-7 concentration of 0.57 μ M was used. Thus, not only MCPR3-7-PR3 complexes but also free PR3 was present in solution. This reduced the putative overall effect of the antibody on the binding curve and lead to a more complex binding behavior. The thermophoresis signal corresponds to the binding of α 1PI to free PR3 and MCPR3-7-bound PR3 which is most likely characterized by two different K_D s. The data could not be fit to a more complex binding model as saturation was not reached in the binding curve. We thus chose the simple model according to equation 10, which revealed an apparent K_D of (5.6 ± 1.0) μ M (Figure 12). Taking into account the rather high K_D of α 1PI and residual free PR3 (1.9 μ M), the actual

affinity of α 1PI to the MCPR3-7-PR3 complex can be expected to be even lower than the measured apparent affinity ($5.6 \mu\text{M}$).

In contrast to this pronounced impact of MCPR3-7, preincubation of PR3 with CLB-12.8 did not affect PR3's affinity to α 1PI. The fitted binding curves overlay and the K_D of (1.8 ± 0.8) μM does not significantly differ (without moABs: (1.9 ± 1.1) μM). The PR3-affinity is expected to be much higher for CLB-12.8 than for MCPR3-7. We, however, added the same concentration of both moABs. Thus, a much higher amount of CLB-12.8-PR3 complexes than MCPR3-7-PR3 complexes were present in our preincubated solutions. Nevertheless, CLB-12.8 did not show any effect on the canonical PR3- α 1PI complexation. This indicates that MCPR3-7 binding changes the conformation of active PR3, which interferes with the canonical complex formation with α 1PI, whereas CLB-12.8 does not.

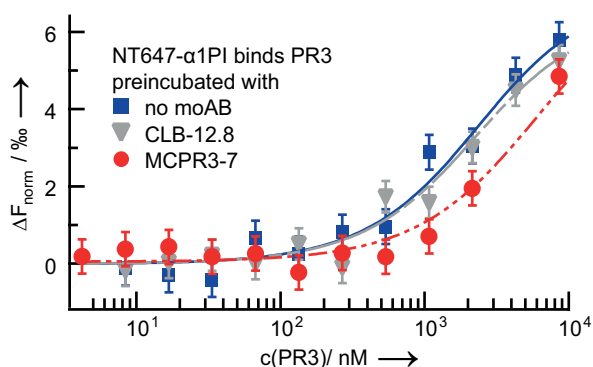


Figure 12 Interference of moABs with canonical PR3- α 1PI complex formation. In absence of moABs, catalytically inactive PR3 and α 1PI bound with $K_D = (1.9 \pm 1.1) \mu\text{M}$ (blue rectangles). Preincubation with MCPR3-7 shifted the binding curve to the right corresponding to a 3-fold decrease in the apparent affinity to α 1PI ($K_D = (5.6 \pm 1.0) \mu\text{M}$; red circles). By contrast, preincubation with CLB-12.8 did not significantly affect the affinity ($K_D = (1.8 \pm 0.8) \mu\text{M}$; gray triangles).

5.2 Quantitative In Vitro Diagnostics

5.2.1 Autoantibodies as Biomarkers for Dilated Cardiomyopathy

Dilated cardiomyopathy (DCM) is a nonischemic heart muscle disease which is characterized by dilation and impaired contraction of the left or both ventricles. With a prevalence of one in 2500 individuals, DCM belongs to the main causes of severe heart defects.^{74,75} Moreover, it is a major reason for heart transplantations.⁷⁶ Besides genetic, toxic and infectious factors, autoimmune reactions are discussed as a cause of DCM. In a notable number of DCM patients, increased concentrations of autoantibodies against several cardiac antigens were found, with the β 1-adrenergic receptor (β 1-AR) representing the major autoimmune target (Figure 13A).⁷⁷⁻⁷⁹ Agonist-like antibodies against β 1-AR were associated with severe ventricular arrhythmia.^{78,80-82} These autoantibodies were found in 30-95% of DCM patients and 0-13% of unaffected controls.^{83,84} It is widely accepted that in many patients suffering from heart failure, a chronic adrenergic overexcitation plays a harmful role.⁸⁵ Permanent β 1-AR stimulation due to elevated catecholamine levels in combination with autoantibodies could change the Ca^{2+} homeostasis of cardiomyocytes. This would result in metabolic and electrophysiological disturbances which are responsible for tachyarrhythmia and sudden death.⁸⁶ It was also shown that anti- β 1-AR-antibodies increase the activity of cAMP-dependent protein kinase (PKA).⁸⁷

Therefore, anti- β 1-AR-antibodies are a highly relevant serological DCM biomarker. Up to now, however, DCM serology is routinely done with ELISAs, which do not allow for quantitative analysis (see chapter 1.2). We thus developed a fully quantitative thermophoretic assay for serological diagnostics of anti- β 1-AR-antibodies. The peptide COR1 with the sequence ADEAR RCYND PKCSD FVQ (Figure 13B) served as a tracer.^{88,89} COR1 mimics the dominant epitope of anti- β 1-AR-antibodies (*ARRCYND*), which is located on β 1-AR's second extracellular loop. Thus, the peptide serves as an artificial antigen. It was labeled with the red fluorescent dye D2 (Figure 13C), as serum exhibits a very low background fluorescence at the red end of the spectrum.

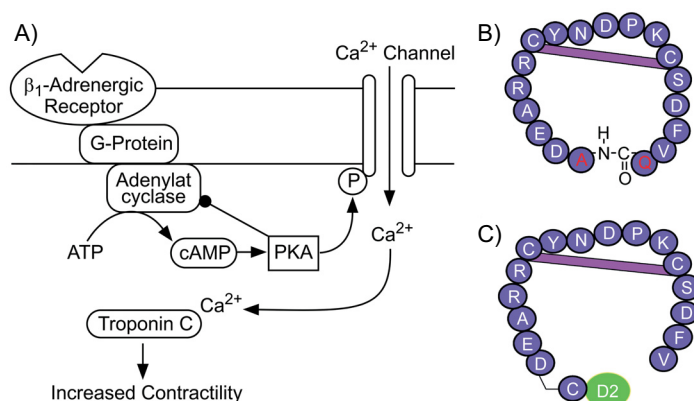


Figure 13 Target signaling pathway in DCM. (A) β 1-AR activation. An adenylat cyclase produces cAMP, which activates PKA to phosphorylate Ca^{2+} channels. The resultant Ca^{2+} influx increases the myocard's contractility. (B) The 18-mer peptide COR1 mimics the dominant autoimmune epitope on β 1-AR's second extracellular loop. (C) Labeled COR1 was used as a tracer to quantify anti- β 1-AR-antibodies via thermophoresis.

5.2.2 Affinity and Specificity of the Tracer COR1

Prior to the diagnostic assay, we tested the affinity of D2-labeled COR1 for monoclonal and polyclonal antibodies, which were generated against β 1-AR's complete second extracellular domain (ARAES DEARR CYNDP KCCDF VTNRQ). Measurements were performed in PBS and 50% human serum. We included into the fit to equation 10 that each antibody is capable of binding two peptides. For moAB ($c = 100$ nM) the fit revealed $K_D = (101 \pm 17)$ nM in PBS and $K_D = (136 \pm 32)$ nM in serum (Figure 14A, B). For poAB ($c = 20$ nM) we found $K_D = (70 \pm 11)$ nM in PBS and $K_D = (66 \pm 25)$ nM in serum (Figure 14C, D). All K_D s are in a similar range of 70-140 nM. COR1 showed a slightly higher affinity for poAB than for moAB whereas measurements in buffer and serum did not significantly differ. It should be noted that differences in thermophoresis mostly stems from the size increase upon binding of the large antibody (150 kDa) to the much smaller COR1 (3 kDa). Binding of another COR1 to the second antibody arm did not measurably influence thermophoresis, as a two state model was sufficient to describe the binding curves.

An unspecific moAB against E-cadherin served as a control. While the control did not bind, binding was reproduced for the specific moAB ($K_D = (74 \pm 10)$ nM; Figure 14E). The twofold K_D reduction compared to Figure 14 likely occurred, as different serum stocks were used. To exclude unspecific antibody interactions with the dye D2, COR1 was instead labeled with fluorescein (Figure 14F). COR1-fluorescein bound specific poAB with $K_D = (265 \pm 25)$ nM, but did not show binding to the E-cadherin antibody. The slightly reduced affinity for COR1-fluorescein might result from the required fluorescence correction, which is detailed in the supporting information of the associated publication 5 (chapter 9).

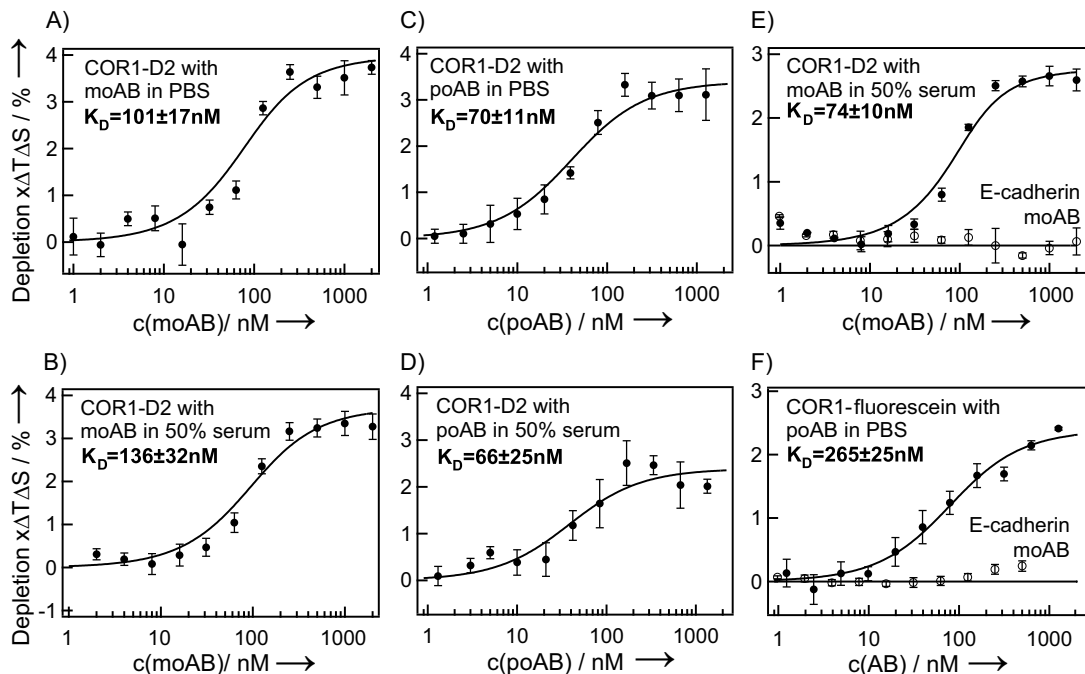


Figure 14 Affinity of labeled COR1 to moAB and poAB in PBS and 50% human serum. (A, B) For moAB the fit revealed $K_D = (101 \pm 17)$ nM in PBS and $K_D = (136 \pm 32)$ nM in serum. (C, D) For poAB we found $K_D = (70 \pm 11)$ nM in PBS and $K_D = (66 \pm 25)$ nM in serum. (E) The specificity of the serum measurements was confirmed with an unspecific moAB against E-cadherin, for which no binding was detected. (F) Measurements with COR1 labeled with fluorescein instead of D2 showed the same specific binding signal, yet with a slightly lower affinity.

5.2.3 Autocompetition Assay

In the assays described so far, one binding partner was titrated against a constant concentration of the other, fluorescent partner. This is not possible for diagnostic assays in serum. The serum contains the first binding partner, here the anti- β 1-AR-antibody. However, serum dilution would result in artifacts, as it leads to a change in various properties which influence thermophoresis (e.g. pH, protein content). Hence, the concentration of the serum containing the anti- β 1-AR-antibodies was kept constant. On the other hand, diluting the labeled COR1 would lead to bleaching artifacts and was thus also kept constant. Instead, unlabeled COR1 was titrated. It competes with labeled COR1 for antibody-binding, which leads to a decreasing thermophoresis signal along the titration curve.

In this autocompetition assay, the fraction of occupied COR1 is given by the mass action law just as in a simple binding assay. It has to be tested though, if labeled and unlabeled tracers differ in affinity. If a more complex model assuming two different K_D s does not describe the data better, it can be assumed that the two tracer species have the same affinity. This was the case for COR1, as shown later in Figure 16 (inset). Hence, the simple model according to equation 10 was used. In contrast to the description in chapter 2.3, A now denotes the partner whose concentration is kept constant (antibody in serum). B denotes the total tracer concentration, which includes the constant concentration of labeled tracer plus the titrated concentration of unlabeled tracer (COR1). Figure 15 shows that antibody affinity and concentration have a different influence on the binding curve. An increasing antibody concentration shifts the curve to the right along the COR1 concentration axis (Figure 15A). By contrast, an alteration of the K_D changes the curve's amplitude (Figure 15B). The amplitude reports the fraction of bound labeled COR1. A higher fraction of labeled COR1 is antibody-bound when the antibody's K_D is lower (higher affinity). Thus, antibody affinity and concentration can be fit independently.

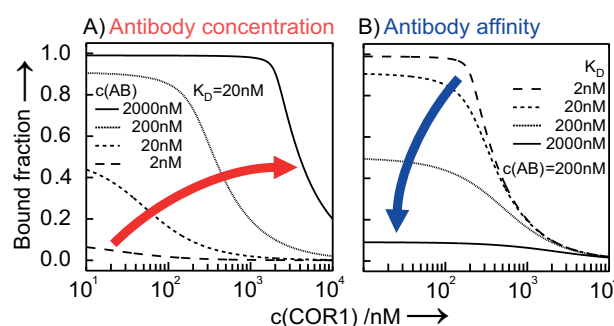


Figure 15 Antibody concentration and K_D inferred independently. The fraction of antibody-bound fluorescent COR1 is plotted against the total COR1-concentration according to equation 10. (A) A change of the antibody concentration shifts the binding curve along the COR1 concentration axis. (B) A K_D change modulates the curve's amplitude.

5.2.4 Quantification of Affinity and Concentration

We tested the autocompetition assay by spiking poAB to final concentrations of 2 nM, 20 nM, 80 nM, and 200 nM into 50% human serum. Using labeled COR1 in a constant concentration of 20 nM, a fit to equation 10 reported poAB concentrations of (0.9 ± 1.5) nM, (26 ± 3.4) nM, (108 ± 19) nM, and (176 ± 21) nM (Figure 16). This confirms the pipetted concentrations within statistical errors. In addition, the fit revealed $K_D = (74 \pm 11)$ nM, which

agrees with the K_D measured in the simple binding assay (66 nM, Figure 14D). The K_D was again considered as per antibody molecule. The thermophoretic depletion amplitude $\Delta T\Delta S$ was fit globally, but held constant for all four concentrations. Baselines $\Delta T S_{COR1}$ were fit individually for each curve as they showed a minor variability of 0.5%. We measured poAB concentrations down to 2 nM. At such low concentrations, significant errors arise as the thermophoretic depletion amplitude approaches the instrument's error. Apart from this small concentration, all poAB affinities and concentrations were measured with errors around 20%.

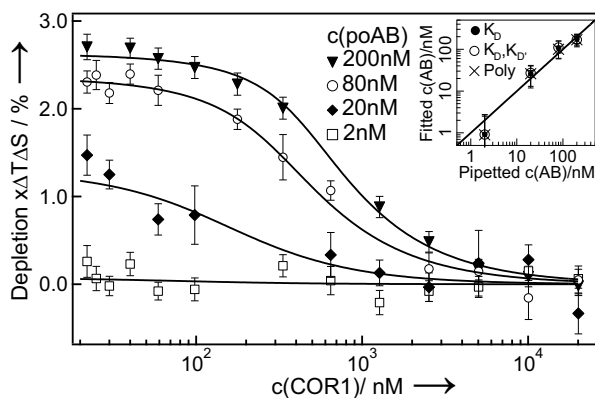


Figure 16 Autocompetition assay reproduces pipetted poAB concentrations. In 50% human serum with poABs, the total COR1 concentration was increased by adding unlabeled COR1 to 20 nM labeled COR1. Thermophoresis only reports the depletion of the labeled species. Unlabeled COR1 competes with labeled COR1 for poAB binding, thus reducing the thermophoretic depletion signal. Added poAB concentrations of 2 nM, 20 nM, 80 nM and 200 nM were reproduced, well within the pipetting errors, as (0.9 ± 1.5) nM, (26 ± 3.4) nM, (108 ± 19) nM, and (176 ± 21) nM. Independently, $K_D = (74 \pm 11)$ nM was inferred. Inset: more complex binding models (label dependent affinity, polyclonal binding) failed to better describe the data, which confirms the simple binding assumption.

In the inset of Figure 16, the pipetted poAB concentrations are plotted against fit values for three different binding models. This includes the simple binding model with one K_D (equation 10), label dependent affinity with differing K_D s for labeled and unlabeled COR1, and polyclonal binding assuming two different antibody subpopulations. The latter two models are detailed in the supporting information of the associated publication 5 (chapter 9). The label dependent model revealed very similar antibody concentrations of (0.9 ± 1.8) nM, (27 ± 14) nM, (110 ± 49) nM, and (170 ± 55) nM. Moreover, it reported statistically indistinguishable K_D s for labeled COR1 ($K_D = (76 \pm 73)$ nM) and unlabeled COR1 ($K_D' = (74 \pm 25)$ nM). This confirms that both COR1 species had the same affinity. The polyclonal model, assuming half more affine (K_D) and half less affine (K_D') antibodies, did not statistically distinguish between these two affinities ($K_D = (73 \pm 3)$ nM, $K_D' = (74 \pm 4)$ nM). Determined poAB concentrations were again very similar ((0.9 ± 1.6) nM, (26 ± 5) nM, (100 ± 19) nM, and (170 ± 32) nM). Hence, both more complex models failed to better describe the data, so that using the simple model is valid.

To reliably fit both, antibody concentration and affinity without prior knowledge, two autocompetition assays were combined, one in 50% serum and one in a mild dilution down to 10% (Figure 17). The global fit assumed an identical, unknown K_D and a common depletion amplitude $\Delta T\Delta S$, considering the 5-fold poAB dilution. The fit revealed a poAB concentration of (187 ± 26) nM and $K_D = (73 \pm 18)$ nM. This reproduces the pipetted

concentration of 200 nM with an error of 13% and the previously measured K_D of 66 nM (see Figure 14) with an error of 25%. Figure 17 shows that a 4-fold reduction of poAB concentration or K_D would lead to a significantly differing response, even though the depletion amplitude $\Delta T\Delta S$ was treated as a free fit parameter.

Taken together, our measurements demonstrate that thermophoresis allows to simultaneously quantify both, antibody affinity and concentration under close to *in vivo* conditions in 50% human serum.

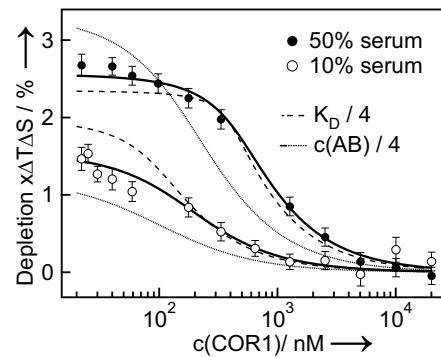


Figure 17 Combined autocompetition assays in 50% and 10% human serum quantify poAB concentration and affinity. The global fit revealed a poAB concentration of (187 ± 26) nM and $K_D = (73 \pm 18)$ nM. Theoretical predictions for a 4-fold reduction of poAB concentration (dotted) or K_D (dashed) significantly differ from the measurements.

5.3 Discussion

Two specific biomedical applications of thermophoresis were introduced. In both cases, antibodies were the biomolecules of interest and thus different types of thermophoretic immunoassays were performed.

Firstly, the antibody MCPR3-7 was characterized. It is directed against proteinase 3 (PR3), the major autoimmune target in granulomatosis with polyangiitis (GPA). Thermophoresis quantified MCPR3-7's affinity and revealed its selectivity for the inactive pro-PR3 form. In addition, thermophoresis elucidated that MCPR3-7-binding impaired PR3 complexation by α_1 -proteinase inhibitor. These experiments added to the understanding of MCPR3-7's allosteric mechanism of action. Antibodies with similar properties and epitope specificity as MCPR3-7 but higher affinity are of high therapeutic interest. In GPA patients, they could block the binding of PR3 to neutrophil membranes and serve as selective PR3 inhibitors and clearers of PR3. This could reduce neutrophil activation by anti-neutrophil cytoplasmic antibodies (ANCA) via membrane-bound PR3 and tissue-damaging effects of secreted PR3. The development of such therapeutic antibodies is greatly promoted by the introduced quantitative thermophoretic immunoassays which complement classical biochemical methods.

Secondly, thermophoresis was applied to serological diagnostics of autoantibodies associated with dilated cardiomyopathy (DCM). The peptide COR1 was used as a tracer. It mimics the dominant autoimmune epitope on the second extracellular loop of the β_1 -adrenoceptor. A global fit of two autocompetition assays in 50% and 10% serum simultaneously quantified antibody affinity and concentration. The relatively low affinity of the tracer COR1 ($K_D=70$ nM) limited the sensitivity to an antibody concentration of approximately 5 nM. However, autoimmune antibodies in DCM patients are expected in the low nanomolar range. Thus, to allow for direct serological screening, the affinity of the tracer has to be enhanced by one order of magnitude. This should be possible by replacing the monomeric COR1 with a dimeric tracer peptide, to which an antibody binds with both of its arms.⁹⁰ The introduced autocompetition approach and the possibility to measure directly in untreated serum qualify thermophoresis a highly promising tool for serological diagnostics.

Taken together, thermophoretic immunoassays allow for fully quantitative studies of antibody-antigen interactions. Absolute quantification of affinity and concentration is achieved, as thermophoresis analysis is free of washing or amplification steps, which might introduce nonlinear characteristics into the detection signal. This represents a major advantage compared to traditionally used ELISAs.

6 Conclusion and Outlook

This thesis introduces key innovations to thermophoretic bioanalytics, regarding measurement device, assay design and specific biomedical applications. An autocompetition assay was successfully used to quantify antibody concentration and affinity, directly in mildly diluted human serum. This assay reproduced pipetted concentrations and the K_D measured beforehand. However, the affinity of the tracer COR1 was too low to resolve the very small autoimmune antibody concentrations expected in DCM patient sera. This demonstrates the central role of the tracer design in thermophoretic serology. Firstly, the affinity needs to be high enough to resolve the concentration range of the biomarker of interest. Secondly, tracers need to have a high stability, specificity and fluorescence intensity in blood serum, as it was the case for COR1. It has to be guaranteed that the tracer neither reacts with, nor unspecifically binds to serum components. Red fluorescent labels guarantee a specific fluorescence signal in serum, which shows a very low background fluorescence at the red end of the spectrum. With the right tracers, thermophoresis should enable the detection of several types of antibodies or antigens, even in other bodily fluids than blood. The provided fully quantitative picture of the status of disease related biomarkers promotes reliable differential diagnostics and precise therapy monitoring, thus helping to pave the way for personalized medicine.

Apart from diagnostics, thermophoretic immunoassays were also used to characterize the potentially therapeutic antibody MCPR3-7. Here, quantitative thermophoresis measurements and classical biochemical assays complemented each other very well, leading to a comprehensive understanding of MCPR3-7's properties. Such extensive characterizations are especially important for antibodies of therapeutic interest.

Thermophoresis is also applicable for classical drug discovery. It was successfully used to analyze proteins, which represent the majority of today's drug targets. Thermophoretic protein analysis was found to be highly flexible and adaptable. The size ratio of protein and binding partner, for instance, is not limiting. Even the binding of a small molecule compound (below 1 kDa) to a protein (50-150 kDa) was detected with high sensitivity. This is possible as thermophoresis does not only depend on molecular size, but also on various other properties like charge or conformation. Protein-small molecule interactions are highly relevant, as most of today's drugs are small molecules. When applied to drug discovery, thermophoresis could potentially decrease the high failure rates of candidate compounds, as it excludes several common artifacts. Surface artifacts are eliminated, as thermophoresis measurements are performed in free solution. Labeling artifacts can be avoided with label free thermophoresis, which was validated in this thesis. On the other hand, thermophoresis with a fluorescent label was successfully performed in cell lysate and blood serum. Such close to *in vivo* analyses have a much higher predictive value for a compound's behavior inside the body than measurements in simple buffers do. In this context, thermophoretic binding analysis inside living cells represents an attractive extension, but to date has not yet been established.

Another interesting extension of bioanalytical thermophoresis assays is the extraction of additional binding characteristics, beyond affinity and concentration. In several of the protein measurements shown in this thesis, the thermophoresis signal seemed to contain further information on the binding event. This includes conformational changes (TEM1-BLIP), a

second binding event (AMA1-RON2) or structural differences of small molecule ligands (p38 α inhibitors). These findings suggest that thermophoresis could e.g. be used to classify ligands or to exactly determine their binding mechanism. This does not only require extensive comparative thermophoresis studies, but also a detailed theoretical description of thermophoresis. As protein-ligand binding is mainly based on specific non-covalent interactions at the partners' interfaces, a better understanding of the non-ionic contributions to thermophoresis is of special interest.

To elucidate the underlying principles of thermophoresis, high throughput screens (HTS) of different protein classes under various conditions would be highly beneficial. Thermophoretic HTS also promotes applications in fundamental research, diagnostics, or drug discovery. These screens are made possible by the novel capillary-free approach, which was introduced and evaluated in this thesis. Instead of capillaries, thermophoresis was measured in aqueous nl-samples under an optimized oil-surfactant layer in standard 1536 well plates. The major benefits of this approach are the 50-fold sample volume reduction and the easy handling of the multi-well plates. This standard well plate format should allow for an efficient implementation into automated platforms. In one plate, 96 binding curves consisting of 16 samples each can be measured. This significantly enhances the throughput compared to the available capillary instruments, which measure one or six curves at a time. As a further benefit, the water-in-oil system should reduce or even prevent unspecific biomolecule adhesion to the sample container. This can be expected, as the sample does not touch the well surface but forms a surfactant surrounded droplet inside the oil.

In the droplets, diffusive mixing after the nl-transfer was successful. Hence, an assay design in which a stock dilution series of a biomolecule target is tested against a high number of binding partners seems very practical e.g. for drug discovery. For diagnostics, it could be combined with the autocompetition approach. A stock dilution of an unlabelled tracer for the biomarker of interest would then be tested against multiple patient sera, supplemented with a constant amount of labeled tracer.

Preparing the samples with an ECHO 550 liquid handler has several advantages. The highly accurate, nanoliter-volume transfer of a wide variety of possible liquids is performed contact free. This eliminates cross contaminations and also leads to dramatic cost savings as no tips are consumed. However, if the ECHO 550 is not already part of an existing automation platform, the primary costs for the liquid handler are rather high. This could be an obstacle, especially for smaller laboratories. Hence, alternative methods for the preparation of the nl-droplets in oil remain to be explored, e.g. via microfluidics.

Taken together, thermophoresis measurements are a highly flexible tool for bioanalytics in all fields of the life sciences. New application possibilities beyond standard affinity determination in fundamental research are opened up by the innovations presented in this thesis. This includes quantitative high-throughput screening in serological diagnostics. Thermophoretic HTS is also highly attractive for drug discovery, as it can either be performed label free or under close to *in vivo* conditions in bioliquids. Based on the presented results, the application spectrum of thermophoresis can be expected to widen considerably.

7 References

1. **Giancotti FG.** Deregulation of cell signaling in cancer. *FEBS Letters* 588: 2558-2570 (2014).
2. **Alto NM & Orth K.** Subversion of Cell Signaling by Pathogens. *Cold Spring Harbor Perspectives in Biology* 4, a006114 (2012).
3. **Wells JA & McClendon CL.** Reaching for high-hanging fruit in drug discovery at protein–protein interfaces. *Nature* 450, 1001–1009 (2007).
4. **Morra G, Genoni A, Neves MAC, Merz KM, JR & Colombo G.** Molecular recognition and drug-lead identification: what can molecular simulations tell us? *Curr Med Chem* 17, 25–41 (2010).
5. **Christopoulos A.** Allosteric binding sites on cell-surface receptors: novel targets for drug discovery. *Nat Rev Drug Discov* 1, 198–210 (2002).
6. **Cornett JK & Kirn TJ.** Laboratory Diagnosis of HIV in Adults: A Review of Current Methods. *Clinical Infectious Diseases* 57, 712–718 (2013).
7. **Ko SC, Schillie SF, Walker T, Veselsky SL, Nelson NP, Lazaroff J, Crowley S & Dusek C et al.** Hepatitis B vaccine response among infants born to hepatitis B surface antigen-positive women. *Vaccine* 32, 2127–2133 (2014).
8. **Sicherer SH & Wood RA.** Allergy Testing in Childhood: Using Allergen-Specific IgE Tests. *Pediatrics* 129, 193–197 (2011).
9. **Willitzki A, Hiemann R, Peters V, Sack U, Schierack P, Rödiger S, Anderer U & Conrad K et al.** New Platform Technology for Comprehensive Serological Diagnostics of Autoimmune Diseases. *Clinical and Developmental Immunology* 2012, 1–8 (2012).
10. **Rifai N, Gillette MA & Carr SA.** Protein biomarker discovery and validation: the long and uncertain path to clinical utility. *Nat Biotechnol* 24, 971–983 (2006).
11. **Engvall E & Perlmann P.** Enzyme-linked immunosorbent assay (ELISA). Quantitative assay of immunoglobulin G. *Immunochemistry* 8, 871–874 (1971).
12. **Liedberg B, Nylander C & Lunström I.** Surface plasmon resonance for gas detection and biosensing. *Sensors and Actuators* 4, 299–304 (1983).
13. **Cullen D, Brown R & Lowe C.** Detection of immuno-complex formation via surface plasmon resonance on gold-coated diffraction gratings. *Biosensors* 3, 211–225 (1987).
14. **Nguyen B, Tanious FA & Wilson WD.** Biosensor-surface plasmon resonance: quantitative analysis of small molecule-nucleic acid interactions. *Methods* 42, 150–161 (2007).
15. **Schuck P.** Use of surface plasmon resonance to probe the equilibrium and dynamic aspects of interactions between biological macromolecules. *Annu Rev Biophys Biomol Struct* 26, 541–566 (1997).

16. **Baksh MM, Kussrow AK, Mileni M, Finn MG & Bornhop DJ.** Label-free quantification of membrane-ligand interactions using backscattering interferometry. *Nat Biotechnol.* 29, 357–360 (2011).
17. **Wiseman T, Williston S, Brandts JF & Lin L.** Rapid measurement of binding constants and heats of binding using a new titration calorimeter. *Analytical Biochemistry* 179, 131–137 (1989).
18. **Lovatt M, Cooper A & Camilleri P.** Energetics of cyclodextrin-induced dissociation of insulin. *Eur Biophys J* 24, 354–357 (1996).
19. **Ladbury JE & Chowdhry BZ.** Sensing the heat: the application of isothermal titration calorimetry to thermodynamic studies of biomolecular interactions. *Chem Biol* 3, 791–801 (1996).
20. **Baaske P, Wienken CJ, Reineck P, Duhr S & Braun D.** Optical thermophoresis for quantifying the buffer dependence of aptamer binding. *Angew Chem Int Ed Engl.* 49, 2238–2241 (2010).
21. **Wienken CJ, Baaske P, Rothbauer U, Braun D & Duhr S.** Protein-binding assays in biological liquids using microscale thermophoresis. *Nat Comms* 1, 100 (2010).
22. **Ludwig C.** *Sitzungsber. Akad. Wiss. Wien Math.-Naturwiss. Kl.*, 539 (1856).
23. **Soret C.** Sur l'état d'équilibre que prend, au point de vue de sa concentration, une dissolution saline primitivement homogène dont deux parties sont portées à des températures différentes. *Archives des sciences physiques et naturelles [de la] Bibliothèque Universelle* 3, 48 (1879).
24. **Duhr S & Braun D.** Thermophoretic depletion follows Boltzmann distribution. *Phys Rev Lett* 96, 168301 (2006).
25. **Duhr S & Braun D.** Why molecules move along a temperature gradient. *Proc. Natl. Acad. Sci. U.S.A.* 103, 19678–19682 (2006).
26. **Dhont JKG, Wiegand S, Duhr S & Braun D.** Thermodiffusion of charged colloids: single-particle diffusion. *Langmuir* 23, 1674–1683 (2007).
27. **Ross D, Gaitan M & Locascio LE.** Temperature Measurement in Microfluidic Systems Using a Temperature-Dependent Fluorescent Dye. *Anal. Chem.* 73, 4117–4123 (2001).
28. **Royer CA.** Probing protein folding and conformational transitions with fluorescence. *Chem Rev* 106, 1769–1784 (2006).
29. **Hill AV.** The possible effects of the aggregation of the molecules of haemoglobin on its dissociation curves. *J physiol* 40, iv–vii (1910).
30. **Weiss JN.** The Hill equation revisited: uses and misuses. *FASEB J* 11, 835–841 (1997).
31. **Shaanan B.** Structure of human oxyhaemoglobin at 2.1 Å resolution. *J Mol Biol* 171, 31–59 (1983).
32. **Harris D, Mutz M, Sonntag M, Stearns R, Shieh J, Picket S, Ellson R & Olechno J.** Low Nanoliter Acoustic Transfer of Aqueous Fluids with High Precision and Accuracy of Volume Transfer and Positional Placement. *Journal of the Association for Laboratory Automation* 13, 97–102 (2008).

33. **Ellson R, Mutz M, Browning B, Lee, L Jr, Miller M & Papen R.** Transfer of low nanoliter volumes between microplates using focused acoustics – automation considerations. *Journal of the Association for Laboratory Automation* 8, 29–34 (2003).
34. **Tawfik DS & Griffiths AD.** Man-made cell-like compartments for molecular evolution. *Nat Biotechnol* 16, 652–656 (1998).
35. **Tuerk C & Gold L.** Systematic evolution of ligands by exponential enrichment: RNA ligands to bacteriophage T4 DNA polymerase. *Science* 249, 505–510 (1990).
36. **Ellington AD & Szostak JW.** In vitro selection of RNA molecules that bind specific ligands. *Nature* 346, 818–822 (1990).
37. **Keefe AD, Pai S & Ellington A.** Aptamers as therapeutics. *Nat Rev Drug Discov* 9, 537–550 (2010).
38. **Wochner A, Menger M & Rimmle M.** Characterisation of aptamers for therapeutic studies. *Expert Opin Drug Discov* 2, 1205–1224 (2007).
39. **Apte RS, Modi M, Masonson H, Patel M, Whitfield L & Adamis AP.** Pegaptanib 1-year systemic safety results from a safety-pharmacokinetic trial in patients with neovascular age-related macular degeneration. *Ophthalmology* 114, 1702–1712 (2007).
40. **Gragoudas ES, Adamis AP, Cunningham ET, Feinsod M & Guyer DR.** Pegaptanib for Neovascular Age-Related Macular Degeneration. *N Engl J Med* 351, 2805–2816 (2004).
41. **Huizenga DE & Szostak JW.** A DNA aptamer that binds adenosine and ATP. *Biochemistry* 34, 656–665 (1995).
42. **Deng Q, German I, Buchanan D & Kennedy RT.** Retention and separation of adenosine and analogues by affinity chromatography with an aptamer stationary phase. *Anal Chem* 73, 5415–5421 (2001).
43. **Lin CH & Patel DJ.** Structural basis of DNA folding and recognition in an AMP-DNA aptamer complex: distinct architectures but common recognition motifs for DNA and RNA aptamers complexed to AMP. *Chem Biol* 4, 817–832 (1997).
44. **Cho EJ, Lee J & Ellington AD.** Applications of Aptamers as Sensors. *Annual Review of Analytical Chemistry* 2, 241–264 (2009).
45. **Sigel H.** Interactions of metal ions with nucleotides and nucleic acids and their constituents. *Chem. Soc. Rev.* 22, 255 (1993).
46. **Dua P, Kim S & Lee D.** Patents on SELEX and therapeutic aptamers. *Recent Pat DNA Gene Seq* 2, 172–186 (2008).
47. **Albeck S & Schreiber G.** Biophysical Characterization of the Interaction of the β -Lactamase TEM-1 with Its Protein Inhibitor BLIP. *Biochemistry* 38, 11–21 (1999).
48. **Reichmann D, Cohen M, Abramovich R, Dym O, Lim D, Strynadka NCJ & Schreiber G.** Binding hot spots in the TEM1-BLIP interface in light of its modular architecture. *J Mol Biol* 365, 663–679 (2007).
49. **Wang J, Palzkill T & Chow D.** Structural insight into the kinetics and DeltaCp of interactions between TEM-1 beta-lactamase and beta-lactamase inhibitory protein (BLIP). *J Biol Chem* 284, 595–609 (2009).

50. **Phillip Y, Sherman E, Haran G & Schreiber G.** Common crowding agents have only a small effect on protein-protein interactions. *Biophys J* 97, 875–885 (2009).
51. **Reichmann D, Rahat O, Albeck S, Meged R, Dym O & Schreiber G.** The modular architecture of protein-protein binding interfaces. *Proc Natl Acad Sci U S A* 102, 57–62 (2005).
52. **Tyler JS & Boothroyd JC.** The C-terminus of Toxoplasma RON2 provides the crucial link between AMA1 and the host-associated invasion complex. *PLoS Pathog* 7, e1001282 (2011).
53. **Srinivasan P, Beatty WL, Diouf A, Herrera R, Ambroggio X, Moch JK, Tyler JS & Narum DL et al.** Binding of Plasmodium merozoite proteins RON2 and AMA1 triggers commitment to invasion. *Proc Natl Acad Sci U S A* 108, 13275–13280 (2011).
54. **Jecklin MC, Schauer S, Dumelin CE & Zenobi R.** Label-free determination of protein-ligand binding constants using mass spectrometry and validation using surface plasmon resonance and isothermal titration calorimetry. *J Mol Recognit* 22, 319–329 (2009).
55. **Dingledine R, Borges K, Bowie D & Traynelis SF.** The glutamate receptor ion channels. *Pharmacol. Rev.* 51, 7–61 (1999).
56. **Stawski P, Janovjak H & Trauner D.** Pharmacology of ionotropic glutamate receptors: A structural perspective. *Bioorganic & Medicinal Chemistry* 18, 7759–7772 (2010).
57. **Armstrong N, Mayer M & Gouaux E.** Tuning activation of the AMPA-sensitive GluR2 ion channel by genetic adjustment of agonist-induced conformational changes. *Proc Natl Acad Sci U S A* 100, 5736–5741 (2003).
58. **Volgraf M, Gorostiza P, Szobota S, Helix MR, Isacoff EY & Trauner D.** Reversibly Caged Glutamate: A Photochromic Agonist of Ionotropic Glutamate Receptors. *J. Am. Chem. Soc.* 129, 260–261 (2007).
59. **Volgraf, M. I.** Photocontrol of Ionotropic Glutamate Receptors and II. Total Synthesis of Exiguamine A and B. *Bibliobazaar, Llc, [S.l.]*, (2011).
60. **Dominguez C, Powers DA & Tamayo N.** p38 MAP kinase inhibitors: many are made, but few are chosen. *Curr Opin Drug Discov Devel* 8, 421–430 (2005).
61. **Frantz B, Klatt T, Pang M, Parsons J, Rolando A, Williams H, Tocci MJ & O'Keefe SJ et al.** The activation state of p38 mitogen-activated protein kinase determines the efficiency of ATP competition for pyridinylimidazole inhibitor binding. *Biochemistry* 37, 13846–13853 (1998).
62. **Nordin H, Jungnelius M, Karlsson R & Karlsson OP.** Kinetic studies of small molecule interactions with protein kinases using biosensor technology. *Anal. Biochem.* 340, 359–368 (2005).
63. **Barone FC, Irving EA, Ray AM, Lee JC, Kassis S, Kumar S, Badger AM & White RF et al.** SB 239063, a second-generation p38 mitogen-activated protein kinase inhibitor, reduces brain injury and neurological deficits in cerebral focal ischemia. *J. Pharmacol. Exp. Ther.* 296, 312–321 (2001).

64. **Dandliker WB & Feigen GA.** Quantification of the antigen-antibody reaction by the polarization of fluorescence. *Biochem Biophys Res Commun* 5, 299–304 (1961).
65. **Hanlon AD, Larkin MI & Reddick RM.** Free-solution, label-free protein-protein interactions characterized by dynamic light scattering. *Biophys J* 98, 297–304 (2010).
66. **The UniProt Consortium.** Activities at the Universal Protein Resource (UniProt). *Nucleic Acids Research* 42, D191 (2013).
67. **Korkmaz B, Horwitz MS, Jenne DE & Gauthier F.** Neutrophil Elastase, Proteinase 3, and Cathepsin G as Therapeutic Targets in Human Diseases. *Pharmacological Reviews* 62, 726–759 (2010).
68. **Witko-Sarsat V, Cramer EM, Hieblot C, Guichard J, Nusbaum P, Lopez S, Lesavre P & Halbwachs-Mecarelli L.** Presence of proteinase 3 in secretory vesicles: evidence of a novel, highly mobilizable intracellular pool distinct from azurophil granules. *Blood* 94, 2487–2496 (1999).
69. **Pham CTN.** Neutrophil serine proteases: specific regulators of inflammation. *Nat Rev Immunol* 6, 541–550 (2006).
70. **Kallenberg CGM.** Pathogenesis of ANCA-associated vasculitides. *Annals of the Rheumatic Diseases* 70, i59 (2011).
71. **Hoffman GS & Specks U.** Antineutrophil cytoplasmic antibodies. *Arthritis Rheum* 41, 1521–1537 (1998).
72. **Lyons PA, Rayner TF, Trivedi S, Holle JU, Watts RA, Jayne DR, Baslund B & Brenchley P et al.** Genetically Distinct Subsets within ANCA-Associated Vasculitis. *N Engl J Med* 367, 214–223 (2012).
73. **Ogushi F, Fells GA, Hubbard RC, Straus SD & Crystal RG.** Z-type alpha 1-antitrypsin is less competent than M1-type alpha 1-antitrypsin as an inhibitor of neutrophil elastase. *J Clin Invest* 80, 1366–1374 (1987).
74. **Taylor MRG, Carniel E & Mestroni L.** Cardiomyopathy, familial dilated. *Orphanet J Rare Dis* 1, 27 (2006).
75. **Rosamond W, Flegal K, Friday G, Furie K, Go A, Greenlund K, Haase N & Ho M et al.** Heart disease and stroke statistics--2007 update: a report from the American Heart Association Statistics Committee and Stroke Statistics Subcommittee. *Circulation* 115, e69-171 (2007).
76. **Fu M & Matsui S.** Is cardiomyopathy an autoimmune disease? *Keio J Med* 51, 208–212 (2002).
77. **Fu LX, Magnusson Y, Bergh CH, Liljeqvist JA, Waagstein F, Hjalmarson A & Hoebeke J.** Localization of a functional autoimmune epitope on the muscarinic acetylcholine receptor-2 in patients with idiopathic dilated cardiomyopathy. *J. Clin. Invest.* 91, 1964–1968 (1993).
78. **Jahns R, Boivin V, Siegmund C, Inselmann G, Lohse MJ & Boege F.** Autoantibodies activating human beta1-adrenergic receptors are associated with reduced cardiac function in chronic heart failure. *Circulation* 99, 649–654 (1999).

79. **Matsui S, Fu ML, Shimizu M, Fukuoka T, Teraoka K, Takekoshi N, Murakami E & Hjalmarson Å.** Dilated Cardiomyopathy Defines Serum Autoantibodies Against G-Protein-Coupled Cardiovascular Receptors. *Autoimmunity* 21, 85–88 (1995).
80. **Christ T, Schindelhauer S, Wettwer E, Wallukat G & Ravens U.** Interaction between autoantibodies against the β 1-adrenoceptor and isoprenaline in enhancing L-type Ca^{2+} current in rat ventricular myocytes. *Journal of Molecular and Cellular Cardiology* 41, 716–723 (2006).
81. **Iwata M, Yoshikawa T, Baba A, Anzai T, Mitamura H & Ogawa S.** Autoantibodies against the second extracellular loop of beta1-adrenergic receptors predict ventricular tachycardia and sudden death in patients with idiopathic dilated cardiomyopathy. *J Am Coll Cardiol* 37, 418–424 (2001).
82. **Khoynezhad A.** Promising aspects and caveats of studies on anti-apoptotic therapies in patients with heart failure. *European Journal of Heart Failure* 9, 120–123 (2007).
83. **Limas CJ, Goldenberg IF & Limas C.** Assessment of immune modulation of beta-adrenergic pathways in human dilated cardiomyopathy: influence of methodologic factors. *Am Heart J* 123, 967–970 (1992).
84. **Wallukat G, Morwinski M, Kowal K, Forster A, Boewer V & Wollenberger A.** Autoantibodies against the beta-adrenergic receptor in human myocarditis and dilated cardiomyopathy: beta-adrenergic agonism without desensitization. *Eur Heart J* 12, 178–181 (1991).
85. **Francis GS.** Neurohumoral mechanisms involved in congestive heart failure. *Am J Cardiol* 55, 15A-21A (1985).
86. **Wallukat G.** The beta-adrenergic receptors. *Herz* 27, 683–690 (2002).
87. **Krause EG, Bartel S, Beyerdorfer I & Wallukat G.** Activation of cyclic AMP-dependent protein kinase in cardiomyocytes by anti-beta 1-adrenoceptor autoantibodies from patients with idiopathic dilated cardiomyopathy. *Blood Press Suppl* 3, 37–40 (1996).
88. **Holthoff H, Zeibig S, Jahns-Boivin V, Bauer J, Lohse MJ, Kaab S, Clauss S & Jahns R et al.** Detection of Anti- 1-AR Autoantibodies in Heart Failure by a Cell-Based Competition ELISA. *Circulation Research* 111, 675–684 (2012).
89. **MüncH G, Boivin-Jahns V, Holthoff H, Adler K, Lappo M, Truöl S, Degen H & Steiger N et al.** Administration of the cyclic peptide COR-1 in humans (phase I study): ex vivo measurements of anti- β 1 -adrenergic receptor antibody neutralization and of immune parameters. *European Journal of Heart Failure* 14, 1230–1239 (2012).
90. **Randle BJ, Scoltock SJ & Scott DK.** Integrating molecular detection and response to create self-signalling antibodies. *Biochem Biophys Res Commun* 324, 504–510 (2004).

8 Danksagung

Viele Menschen haben dazu beigetragen diese Arbeit zu ermöglichen und die letzten drei Jahre zu einer großartigen Erfahrung zu machen. Ich danke euch allen!

Dieter für sein Vertrauen und seine Unterstützung bei meinem Schritt in die Biophysik; für unglaublich viel Neues, das ich während der Zeit in seiner Gruppe gelernt habe; für alles, was er mir über die Wissenschaft beigebracht hat; für seine außergewöhnlichen Ideen und seine Kreativität, die eine große Inspiration war und ist und für die Laborkatze, die es sicher bald geben wird.

Allen Kollaborationspartnern, besonders der **AG Jenne**, für die interessanten und vielfältigen gemeinsamen Projekte und für die Einblicke in verschiedenste Bereiche der Lebenswissenschaften.

Der AG Braun, all „meinen“ Physikern: **Friederike, Manuel, Matthias & Lorenz, Franziska, Maren, Ferdinand, Shoichi, Zhenya, Natan, Mario, Hubert, Christoph, Andreas, Ulrich und allen anderen** für die beste Arbeitsumgebung, die man sich vorstellen kann; für den wissenschaftlichen Austausch und die gegenseitige Hilfe; für unzählige ideenreiche Diskussionen; für viele zusammen getrunzene, goldene Espresso und für allerlei amüsante Sozialevents.

Christof für seine Antworten auf alle physikalischen Fragen; für all die unterhaltsamen Momente und Stunden im Labor oder außerhalb und fürs Korrekturlesen.

Simon für tolle Simulationen; für mindestens genauso tolle Gespräche bei Tee, Cocktails oder gebratenen Tofuwürfeln und fürs Korrekturlesen.

Niklas für die spannende Möglichkeit, ihn durch seine Masterarbeit zu begleiten und für seine enorme Ausdauer und Genauigkeit beim Messen.

Georg für gemeinsames Schrauben am „Stuffed Rabbit“ und für viel Fett.

Svenja für den angenehmen Einstieg in die Thermophorese und die lustige Zeit miteinander.

Dem **LS Gaub** und dem **LS Rädler** für die gute „Nachbarschaft“, wissenschaftlich wie kollegial.

Den beiden „nicht-physikalischen“ Korrekturleserinnen **Rebecca** und **Noreen**.

Meinen Freunden und **meiner Familie**, besonders meinen Eltern **Irene** und **Heinz** für Motivation, Rückhalt und Anerkennung.

Außerdem danke ich **Peter** für seine Unterstützung inklusive Korrekturlesen; für seine Geduld mit mir, selbst in den stressigsten Momenten und einfach dafür, dass Du an meiner Seite bist!

9 Associated Publications

1. Thermophoresis in nanoliter droplets to quantify aptamer binding.
Seidel SAI, Markwardt NA, Lanzmich SA, Braun D.
Angewandte Chemie Int Ed Engl.
2014 Jul; 53(30): 7948-51. doi: 10.1002/anie.201402514. Epub 2014 Jun.
Figures 1 to 5 adapted with permission. Full article reprinted with permission.
© Wiley-VCH Verlag gGmbH & Co. KGaA, Weinheim.
2. Microscale thermophoresis quantifies biomolecular interactions under previously challenging conditions.
Seidel SAI, Dijkman PM, Lea WA, van den Bogaart G, Jerabek-Willemsen M, Lazic A, Joseph JS, Srinivasan P, Baaske P, Simeonov A, Katritch I, Melo FA, Ladbury JE, Schreiber G, Watts A, Braun D, Duhr S.
Methods.
2013 Mar; 59(3): 301-15. doi:10.1016/j.ymeth.2012.12.005. Epub 2012 Dec. Review.
Figures 1, 2 and 4 adapted with permission. Full article reprinted with permission.
© 2013 Elsevier Inc.
3. Label-free microscale thermophoresis discriminates sites and affinity of protein-ligand binding.
Seidel SAI, Wienken CJ, Geissler S, Jerabek-Willemsen M, Duhr S, Reiter A, Trauner D, Braun D, Baaske P.
Angewandte Chemie Int Ed Engl.
2012 Oct; 51(42):10656-9. doi: 10.1002/anie. 201204268. Epub 2012 Sep.
Figures 2 and 3 adapted with permission. Full article reprinted with permission.
© Wiley-VCH Verlag gGmbH & Co. KGaA, Weinheim.
4. A monoclonal antibody (MCPR3-7) interfering with the activity of proteinase 3 by an allosteric mechanism.
Hinkofer LC, Seidel SAI, Korkmaz B, Silva F, Hummel AM, Braun D, Jenne DE, Specks U.
The Journal of Biological Chemistry.
2013 Sep; 288(37):26635-48. doi: 10.1074/ jbc.M113.495770. Epub 2013 Jul.
Figures 3 and 6 adapted with permission. Full article reprinted with permission.
© 2013 The American Society for Biochemistry and Molecular Biology.
5. Direct detection of antibody concentration and affinity in human serum using microscale thermophoresis.
Lippok S, Seidel SAI, Duhr S, Uhland K, Holthoff HP, Jenne D, and Braun D.
Analytical Chemistry. 2012 Apr; 84(8):3523-30. doi: 10.1021/ac202923j. Epub 2012 Mar.
Figures 1, 3, 4, 5 and 6 adapted with permission. Full article reprinted with permission.
© 2012 American Chemical Society.

Thermophoresis in Nanoliter Droplets to Quantify Aptamer Binding**

Susanne A. I. Seidel, Niklas A. Markwardt, Simon A. Lanzmich, and Dieter Braun*

Abstract: Biomolecule interactions are central to pharmacology and diagnostics. These interactions can be quantified by thermophoresis, the directed molecule movement along a temperature gradient. It is sensitive to binding induced changes in size, charge, or conformation. Established capillary measurements require at least 0.5 μL per sample. We cut down sample consumption by a factor of 50, using 10 nL droplets produced with acoustic droplet robotics (Labcyte). Droplets were stabilized in an oil–surfactant mix and locally heated with an IR laser. Temperature increase, Marangoni flow, and concentration distribution were analyzed by fluorescence microscopy and numerical simulation. In 10 nL droplets, we quantified AMP–aptamer affinity, cooperativity, and buffer dependence. Miniaturization and the 1536-well plate format make the method high-throughput and automation friendly. This promotes innovative applications for diagnostic assays in human serum or label-free drug discovery screening.

Molecular recognition is not only central to cell signaling, but it also represents the functional principle of pharmaceuticals and laboratory diagnostics. A variety of opportunities thus comes along with an in-depth understanding of biological binding events. From this perspective, it is not surprising to see an ever-growing interest in quantitative biomolecule interaction analysis. To this end, the directed movement of molecules along a temperature gradient, referred to as thermophoresis,^[1] has been successfully utilized in the last years.^[2,3] It is highly sensitive to molecular size, charge, and conformation. Based on binding induced changes in at least one of these parameters, affinity and concentration can be quantified, even in complex bioliquids.^[4]

In the well-established microscale thermophoresis (MST) approach, samples are measured in glass capillaries. Capillary MST has been applied for ions, small molecules, nucleic acids,

peptides, proteins, crude cell lysate, and untreated human blood serum.^[4–6] With circa 0.5 μL per capillary filling, the sample consumption is low compared to, for example, isothermal titration calorimetry.^[7] However, the actual measurement volume is significantly smaller: it lies in the range of 2 nL.^[2] The additionally consumed volume becomes essential when working with expensive or rare material such as patient samples. This is especially true if high-throughput analyses need to be performed, for instance, in diagnostics or drug discovery. Throughput and automation of conventional MST are further limited by the complicated handling of glass capillaries.

Therefore, we developed a capillary-free approach to measure thermophoresis in nL droplets under an oil–surfactant layer inside 1536-well plates (Figure 1). The water-in-oil system was experimentally characterized for temperature induced effects. The findings agreed with numerical simulations.

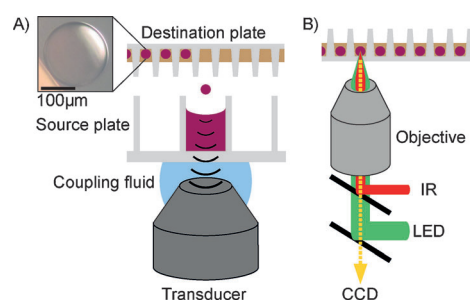


Figure 1. A) Droplet production. The liquid handler positions a destination plate above a source plate with a sample stock (purple). A transducer emits an acoustic pulse focused to the sample surface, whereby a 2.5 nL droplet travels into the destination well. To prevent evaporation, droplets are transferred into an oil–surfactant mix (brown). Inset: Samples were stable for several hours. 5 nL of 1:1 human serum/PBS. B) Inverted microscopic setup. The droplet center is heated with an IR laser. Thermophoresis is monitored by fluorescence (LED: light emitting diode; CCD: charge-coupled device camera).

The applicability of the system for biomolecule interaction studies was evaluated with a well-described nucleic acid aptamer. Aptamers were discovered more than 20 years ago.^[8] Owing to their three-dimensional conformation, these single-stranded oligonucleotides bind to various biomedically relevant targets, including proteins and small molecules.^[9,10] Just like antibodies, aptamers show high specificity and affinity. At the same time, these nucleic acid based ligands are superior to protein based ligands in production costs, storage conditions, and chemical modifiability.^[10] In vivo, their small size facilitates good delivery to the target tissue,

[*] S. A. I. Seidel, N. A. Markwardt, S. A. Lanzmich, Prof. D. Braun Systems Biophysics, Physics Department, NanoSystems Initiative Munich and Center for Nanoscience Ludwig-Maximilians-University Munich Amalienstrasse 54, 80799 Munich (Germany) E-mail: dieter.braun@lmu.de Homepage: <http://www.biosystems.physik.lmu.de>

[**] Financial support through a joint grant (BR2152/2-1) and project A4 within SFB 1032 from the Deutsche Forschungsgemeinschaft (DFG), by the Center for NanoScience (CeNS), and by the Nanosystems Initiative Munich (NIM) is gratefully acknowledged. The authors would like to thank Maximilian Weitz from the group of Friedrich C. Simmel for sharing his knowledge on microemulsions, Georg C. Urtel for support in building the setup and Christof B. Mast for programming support.

Supporting information for this article (including experimental details in Chapter 1) is available on the WWW under <http://dx.doi.org/10.1002/anie.201402514>.

whereas no immunogenicity and low toxicity have been reported.^[10,11] These benefits and the first marketed aptamer drug demonstrate the high potential of aptamers.^[12]

Aptamer binding studies were miniaturized employing a non-contact liquid handling system available commercially (Labcyte). The system delivers 2.5 nL portions from multi-well source plates into destination plates by acoustic droplet ejection (Figure 1 A).^[13] The deviation from the target volume is less than 2% (Supporting Information, Chapter S3a). To prevent evaporation, droplets were transferred into a protective layer of standard microbiology mineral oil supplemented with a surfactant mix according to Tawfik and Griffiths.^[14] For the presented experiments, we transferred four or eight 2.5 nL portions to yield 10 nL (270 μm) or 20 nL samples (340 μm). The positional accuracy of the transfer was reduced owing to deflection by the oil. To coalesce individual portions, destination plates with funnel-shaped wells were mildly centrifuged after transfer (≤ 500 g to avoid droplet damage). With our optimized procedure, we reproducibly obtained nL samples that were stable for several hours (Figure 1 A, inset). This allowed for multiple thermophoretic binding assays (10 min each).

Droplets were measured on a newly constructed microscopic setup (Figure 1 B). Similar to the previously described capillary instrument,^[2,5] thermophoresis was induced and analyzed all-optically. As an essential modification to the capillary setup, an inverted configuration was chosen so that the sample plate stayed upright to avoid oil dripping. While fixing the plate guaranteed that the droplets stayed in place, moving the optical parts allowed sequential measurements.

Before studying biomolecule affinity, we characterized the effects of local heating on aqueous nL droplets under oil. If asymmetrically applied, heating occasionally led to convective flows strong enough to move an entire droplet away from the laser spot. This was prevented by using plates with a small well floor area ($r=0.45$ mm). Utilizing the temperature dependence of the fluorescent dye Alexa 647, the radial temperature profile in the central horizontal plane of a 20 nL droplet was obtained 0.2 s after the IR laser had been turned on (Figure 2 A). For a temperature increase of $\Delta T_c = 11$ K in the heat spot center, the droplet periphery warmed up by $\Delta T_p = 4$ K. A Lorentz fit revealed an FWHM of 120 μm . In

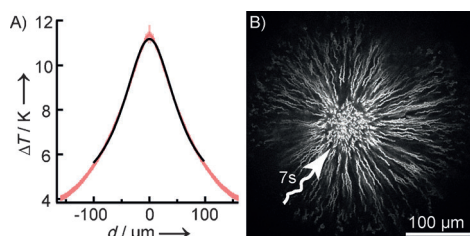


Figure 2. Local heating of 20 nL droplets. A) Radial temperature profile in the central horizontal plane (red). The temperature increased by $\Delta T_c = 11$ K in the center and by $\Delta T_p = 4$ K in the droplet periphery. A Lorentz fit (black) revealed FWHM = 120 μm . B) Flow profile of fluorescent polystyrene beads ($d = 1.0$ μm) integrated over 7 s during heating ($\Delta T = 15$ K). The beads moved toward the heat spot and out of focus with a peak velocity of 15 $\mu\text{m s}^{-1}$.

the following, ΔT denotes the average temperature increase of the central (30 \times 30) μm area.

Convective flows inside 20 nL samples were visualized with fluorescent polystyrene beads. Figure 2 B is integrated over 7 s of heating. The beads moved toward the central heat spot and out of focus, with peak velocities of 5–10 $\mu\text{m s}^{-1}$ for $\Delta T = 6$ K and 15 $\mu\text{m s}^{-1}$ for $\Delta T = 15$ K. To elucidate these flows, we performed full numerical simulations considering diffusion, convection, thermophoresis, and the temperature dependence of the dye. Simulations of 20 nL (Figure 3) and

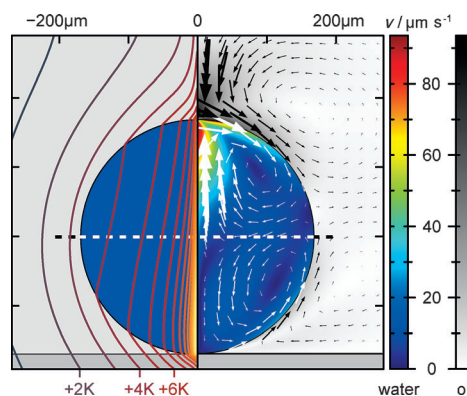


Figure 3. Numerical simulation of temperature and flow fields in a vertical cut through a 20 nL droplet after 0.2 s of heating. Left: Isotherms indicate the temperature increase. Right: The central horizontal plane (dashed) comprises the boundary of two toroidal flow vortices. The vortices are driven by Marangoni convection at the water–oil interface and have already reached the steady state.

10 nL droplets (Supporting Information, Figure S1) verified that the observed inward flow can be explained by Marangoni convection. This type of convection is caused by temperature-induced differences in interfacial tension. In our case, local heating decreased the interfacial tension between water and oil at the top and bottom of the droplet, triggering Marangoni fluid flow along the interface. Owing to the cylindrical symmetry, toroidal vortices arose in the upper and lower droplet hemisphere. Figure 3 shows the cross-sections of the tori in a vertical cut. The dashed line indicates the horizontal plane. Here, the flow is directed inward in the upper and lower vortex, which agrees with the experimental observation in this plane (Figure 2).

After flow field analysis, we recorded fluorescence time traces, the basis for our binding measurements, in 20 nL Alexa 647 samples (Figure 4 A). The experimental curves were highly reproducible and confirmed by simulation. A series of different events was identified in agreement with standard capillary measurements. When the heating laser was turned on, the fluorescence decreased owing to the temperature response (DTR) of the dye and thermophoretic molecule depletion. Thermophoresis and back-diffusion equilibrated within seconds. Subsequent slow warming of the entire sample slightly reduced the dye fluorescence intensity, but did not affect the measurement. When heating was turned off, fluorescence recovered owing to DTR and back-diffusion. A larger ΔT enhanced DTR and thermophoresis in experiment

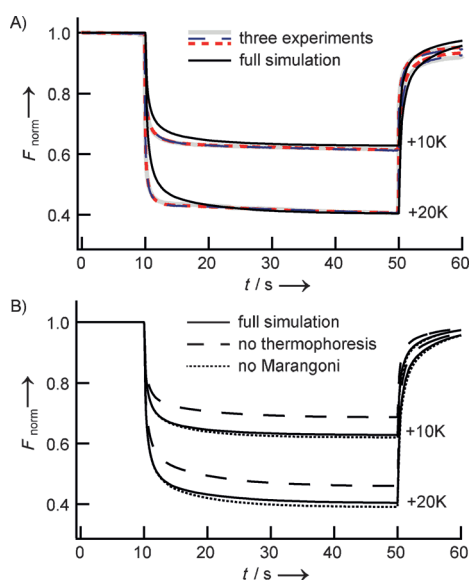


Figure 4. Fluorescence time traces from 20 nL droplets. A) Measurements of three Alexa 647 samples (gray, blue, red) overlap with minor deviations demonstrating the low batch-to-batch variation. Experiments and simulation (black) agree well. After the IR laser is turned on ($t=10$ s), the fluorescence decreases due to the temperature response (DTR) of the dye and thermophoresis. Thermophoresis and back-diffusion equilibrate within seconds. After heating ($t=50$ s), F_{norm} recovers due to DTR and isothermal back-diffusion. A larger ΔT enhances DTR and thermophoresis. B) Simulated contributions to the decrease in F_{norm} . Omitting Marangoni convection led to a negligible change of 0.008 (dotted); omitting thermophoresis changed the signal by 0.06 (dashed).

and simulation (Figure 4A). To assess the contribution of Marangoni convection and thermophoresis, simulations excluding either effect were performed (Figure 4B; implementation details are given in the Supporting Information, Chapter S2a). When neglecting Marangoni convection, the flow fields differed considerably, but the fluorescence signal was only slightly altered. Upon removal of thermophoresis from the simulation, the time traces changed significantly. This demonstrates that thermophoresis prevailed against the convective flows.

Having characterized thermophoresis in nL droplets under oil, we evaluated its applicability for biomolecule interaction studies. We analyzed a 25 mer DNA aptamer that binds adenosine and its phosphorylated analogues.^[15] This aptamer has previously been studied extensively.^[2,16] For nL-scale interaction studies, a constant concentration of fluorescently labeled aptamer ($c=2 \mu\text{M}$) was added to a serial dilution of adenosine-5'-monophosphate (AMP). As mentioned above, mild centrifugation in the funnel-shaped wells reliably coalesced individual AMP and aptamer portions. After coalescence, the concentration of AMP and aptamer equilibrated by diffusion. The short diffusion times through the small 10 nL or 20 nL samples guaranteed complete mixing within minutes. We found diffusive mixing to be as effective as manual premixing.

The mixed samples were locally heated by $\Delta T=6$ K. The resultant thermophoretic depletion of free aptamer significantly differed from its bound complex with AMP (Support-

ing Information, Figure S2). Furthermore, the temperature response of the aptamer dye (DTR) changed upon AMP binding.

The fluorescence after DTR and thermophoresis was divided by the fluorescence before heating as described in the Supporting Information, Figure S2 and previously.^[6] As this relative fluorescence can be approximated as linear to the bound aptamer fraction, it was directly fit to the Hill equation (Supporting Information, Chapter S3c).

Using the original selection buffer according to Huizenga and Szostak,^[15] we found $EC_{50}=(116 \pm 14) \mu\text{M}$ in 10 nL samples and $EC_{50}=(104 \pm 10) \mu\text{M}$ in 20 nL samples (Figure 5A). Both values agree with each other and the literature value of $(87 \pm 5) \mu\text{M}$ from capillary thermophoresis.^[2] The determined Hill coefficients of $n=1.2 \pm 0.1$ (10 nL) and $n=1.9 \pm 0.3$ (20 nL) indicate cooperative binding of more than one AMP, which is consistent with the previously reported tertiary structure of the complex (Figure 5, inset).^[17] Moreover, the Hill coefficients only slightly deviate from each other and confirm the literature value ($n=1.4$).^[2] As a control, we measured a DNA oligonucleotide with the same length as the aptamer but two point mutations. The dinucleotide

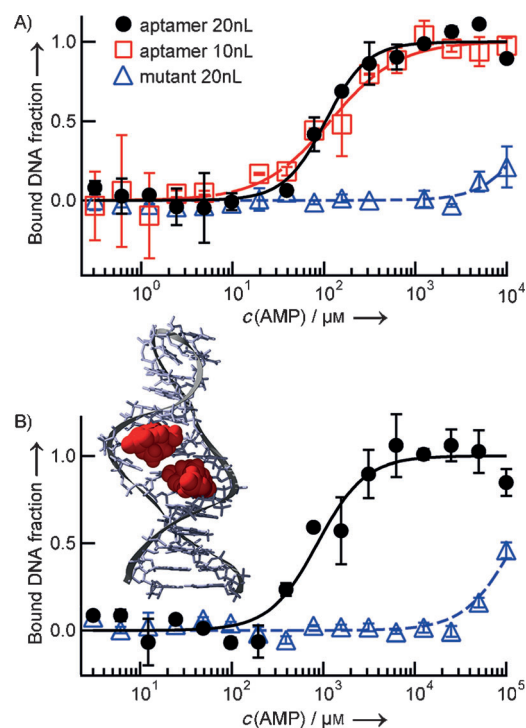


Figure 5. The specific signal change in DTR and thermophoresis upon AMP titration to labeled aptamer was fit to the Hill equation. Mean values of at least two individual nL samples; error bars: standard deviation. A) Selection buffer. The fit revealed $EC_{50}=(116 \pm 14) \mu\text{M}$ and $n=1.9 \pm 0.3$ in 10 nL (red squares) and $EC_{50}=(104 \pm 10) \mu\text{M}$ and $n=1.2 \pm 0.1$ in 20 nL (black circles). A dinucleotide mutant showed a 200-fold increased EC_{50} value of about 20 mM (blue triangles). B) PBS. $EC_{50}=(0.90 \pm 0.13) \text{mM}$ was found (black circles), confirming the buffer dependence of the aptamer ($n=1.6 \pm 0.4$). The mutant showed a 130-fold increased EC_{50} value of about 0.12 M (blue triangles). Inset: Determined Hill coefficients agree with the reported tertiary structure (NDB code 1AW4): an aptamer (gray) binds two AMP molecules (red).^[17]

mutant showed a 200-fold reduced AMP-affinity ($EC_{50} \approx 20$ mM). This demonstrates the specificity of the binding signal.

To quantify the reported buffer dependence of the AMP-aptamer,^[2] binding was measured in PBS (Figure 5B). An EC_{50} of (0.90 ± 0.13) mM was found, corresponding to a 10-fold affinity reduction compared to selection buffer. This reduction is not surprising, as the aptamer has originally been evolved in and thus optimized for its selection buffer.^[15,18] A dominant effect can most likely be ascribed to magnesium ions: while the selection buffer contained 5 mM $MgCl_2$, we used PBS without Mg^{2+} . Mg^{2+} do not only stabilize DNA, but can also neutralize AMP phosphate group and thus reduce repulsion to phosphates in the aptamer backbone.^[19] A reduction of the $MgCl_2$ concentration from 5 to 0 mM has been reported to significantly reduce AMP-aptamer retention in affinity chromatography.^[16] This is in accordance with the EC_{50} differences that we found in nL-thermophoresis. The Hill coefficient was not significantly affected by the buffer; it was $n = 1.6 \pm 0.4$ in PBS. The affinity of the mutant control was reduced 130-fold compared to the aptamer ($EC_{50} \approx 0.12$ M).

The successful quantification of affinity, cooperativity, and buffer dependence confirms the applicability of the presented method for aptamer analysis. This type of study is most likely to gain in importance now that the comprehensive aptamer patent portfolio, which presumably has suppressed many commercial applications, is starting to expire.^[20] Furthermore, nL-thermophoresis is a highly attractive analytical method for other biomolecules including peptides or proteins, and for complex bioliquids such as blood. The suitability for these studies remains to be tested, but can be expected judging from the application depth of capillary thermophoresis.^[4-6] Sample preparation is unlikely to be limiting, as the liquid handler can be deployed for various solution types. We, for example, produced stable nL droplets of 50% human blood serum (Figure 1A, inset) as required for thermophoretic diagnostics. Diffusive mixing after nL transfer was successful. Therefore, an assay design in which a stock dilution series of a biomolecule target is tested against a high number of binding partners seems very practical, for example, for drug discovery. It could also be combined with our previously published diagnostic autocompetition approach.^[4] A stock dilution of an unlabeled tracer for the biomarker of interest would then be tested against multiple patient sera, supplemented with a constant amount of labeled tracer.

Compared to conventional capillary thermophoresis, the volume was reduced 50-fold. This leads to an enormous potential for high-throughput screens, even more so, as the easy-to-handle multi-well plates promote automation.

As a further advantage, the nL transfer is contact-free, which exempts from washing steps and minimizes cross-contaminations. After transfer, the sample is not in direct contact with the well surface, but forms a surfactant surrounded droplet inside the oil. This should significantly reduce nonspecific surface adhesion of biomolecules ("sticking"), an often encountered challenge in capillary thermo-

phoresis.^[6] The elimination of sticking represents a major benefit, even if surfactant and oil might have to be optimized for different sample types.

Considering these advantages, the miniaturization, and the extensive characterization in experiment and simulation, nL droplet thermophoresis promises diverse applications throughout the life sciences.

Received: February 17, 2014

Revised: April 11, 2014

Published online: June 4, 2014

Keywords: analytical methods · binding affinity · high-throughput screening · nanoliter thermophoresis · numerical simulation

- [1] a) C. Ludwig, *Sitzungsber. Akad. Wiss. Wien Math.-Naturwiss. Kl.* **1856**, 539; b) S. Duhr, D. Braun, *Proc. Natl. Acad. Sci. USA* **2006**, *103*, 19678–19682.
- [2] P. Baaske, C. J. Wienken, P. Reineck, S. Duhr, D. Braun, *Angew. Chem.* **2010**, *122*, 2286–2290; *Angew. Chem. Int. Ed.* **2010**, *49*, 2238–2241.
- [3] a) C. J. Wienken, P. Baaske, U. Rothbauer, D. Braun, S. Duhr, *Nat. Commun.* **2010**, *1*, 100; b) L. C. Hinkofer, S. A. I. Seidel, B. Korkmaz, F. Silva, A. M. Hummel, D. Braun, D. E. Jenne, U. Specks, *J. Biol. Chem.* **2013**, *288*, 26635–26648.
- [4] S. Lippok, S. A. I. Seidel, S. Duhr, K. Uhland, H.-P. Holthoff, D. Jenne, D. Braun, *Anal. Chem.* **2012**, *84*, 3523–3530.
- [5] S. A. I. Seidel, C. J. Wienken, S. Geissler, M. Jerabek-Willemsen, S. Duhr, A. Reiter, D. Trauner, D. Braun, P. Baaske, *Angew. Chem.* **2012**, *124*, 10810–10814; *Angew. Chem. Int. Ed.* **2012**, *51*, 10656–10659.
- [6] S. A. I. Seidel, P. M. Dijkman, W. A. Lea, G. van den Bogaart, M. Jerabek-Willemsen, A. Lazic, J. S. Joseph, P. Srinivasan, P. Baaske, A. Simeonov, I. Katritch, F. A. Melo, J. E. Ladbury, G. Schreiber, A. Watts, D. Braun, S. Duhr, *Methods* **2013**, *59*, 301–315.
- [7] T. Wiseman, S. Williston, J. F. Brandts, L.-N. Lin, *Anal. Biochem.* **1989**, *179*, 131–137.
- [8] a) C. Tuerk, L. Gold, *Science* **1990**, *249*, 505–510; b) A. D. Ellington, J. W. Szostak, *Nature* **1990**, *346*, 818–822.
- [9] A. D. Keefe, S. Pai, A. Ellington, *Nat. Rev. Drug Discovery* **2010**, *9*, 537–550.
- [10] A. Wochner, M. Menger, M. Rimmle, *Expert Opin. Drug Discovery* **2007**, *2*, 1205–1224.
- [11] R. S. Apte, M. Modi, H. Masonson, M. Patel, L. Whitfield, A. P. Adamis, *Ophthalmology* **2007**, *114*, 1702–1712.
- [12] E. S. Gragoudas, A. P. Adamis, E. T. Cunningham, M. Feinsod, D. R. Guyer, *N. Engl. J. Med.* **2004**, *351*, 2805–2816.
- [13] R. Ellson, M. Mutz, B. Browning, L. Lee, Jr., M. Miller, R. Papen, *JALA* **2003**, *8*, 29–34.
- [14] D. S. Tawfik, A. D. Griffiths, *Nat. Biotechnol.* **1998**, *16*, 652–656.
- [15] D. E. Huizenga, J. W. Szostak, *Biochemistry* **1995**, *34*, 656–665.
- [16] Q. Deng, I. German, D. Buchanan, R. T. Kennedy, *Anal. Chem.* **2001**, *73*, 5415–5421.
- [17] C. H. Lin, D. J. Patel, *Chem. Biol.* **1997**, *4*, 817–832.
- [18] E. J. Cho, J.-W. Lee, A. D. Ellington, *Annu. Rev. Anal. Chem.* **2009**, *2*, 241–264.
- [19] H. Sigel, *Chem. Soc. Rev.* **1993**, *22*, 255–267.
- [20] P. Dua, S. Kim, D.-K. Lee, *Recent Pat. DNA Gene Sequences* **2008**, *2*, 172–186.

Supporting Information

© Wiley-VCH 2014

69451 Weinheim, Germany

Thermophoresis in Nanoliter Droplets to Quantify Aptamer Binding**

*Susanne A. I. Seidel, Niklas A. Markwardt, Simon A. Lanzmich, and Dieter Braun**

anie_201402514_sm_miscellaneous_information.pdf

Table of contents

1. *Experimental section*
2. *Numerical simulation of locally heated nl-droplets*
 - a. *Excluding Marangoni convection or thermophoresis*
 - b. *Influences from droplet size*
3. *Thermophoresis measurements in nl-droplets*
 - a. *Accuracy of the acoustic droplet production*
 - b. *Raw fluorescence time traces of a binding study*
 - c. *Data analysis in binding studies*

1. *Experimental section*

Nanoliter samples were prepared on an Echo 550 liquid handler (Labcyte Inc, USA). Echo qualified 384-well low dead volume source plates (Labcyte Inc) were filled manually. Air bubbles were avoided via reverse pipetting and centrifugation (2 min, 1000×g) of the source plate. Destination plates (1536-well imp@ct plates, flat bottom; Greiner Bio-One GmbH, Germany) were manually filled with 0.5 µl/ well microbiology mineral oil (Carl Roth GmbH, Germany) with 4.5% (v/v) Span 80, 0.5% (v/v) Tween 80 (Sigma Aldrich Chemie GmbH, Germany). To remove air bubbles, destination plates were centrifuged (2 min, 1000×g). Taking into account oil properties and destination well dimensions, the oil layer was chosen to be thin enough to prevent dripping from the upside-down plate during transfer, but also thick enough to fully incorporate droplets with diameters of approximately 270 or 340 µm (10 or 20 nl). Due to deflection by the oil, droplets tended to not reach the well floor. To sink the droplets, plates were shortly centrifuged (one pulse up to ≤500×g). Typically, two or more individually transferred nl-ports had to be coalesced, which required 5-10 min of centrifugation. To avoid droplet damage, 500×g should not be exceeded.

The nl-thermophoresis setup was built from optomechanical components ordered from Thorlabs GmbH, Germany. A red LED (625 nm, 1600 mA) with an aspheric condenser lens (Thorlabs GmbH) was used for fluorescence excitation. An Ag-coated mirror (AHF Analysentechnik AG, Germany), an infinity-corrected tube lens (Thorlabs GmbH) and a CCD-camera (Stingray F-145B; Allied Vision Technologies GmbH, Germany) were employed for imaging. Cy5-fluorescence filters were ordered from Laser Components GmbH, Germany. Temperature gradients were created with an infrared laser diode (λ=1480 nm, P<500 mW; Fibotec Fiberoptics GmbH, Germany) coupled into the fluorescence light path with a heat-reflecting mirror (NanoTemper Technologies GmbH, Germany) and focused into the fluid with a 20x plan-apochromat objective (NA=0.8; Carl Zeiss AG, Germany). The optical components were mounted onto three orthogonal precision translation stages (Physik Instrumente GmbH, Germany; Edmund Optics Inc., USA).

All measurements were performed at room temperature. The temperature increase was measured utilizing the temperature dependence of the fluorescent dye Alexa 647 (Life Technologies). Flows were visualized with 0.05% (m/v) crimson fluorescent microspheres (d=1.0 µm; Life Technologies, USA) in MilliQ water with 3.25 µM Alexa 647.

Binding assays were performed in selection buffer (20 mM Tris-Cl, 300 mM NaCl, 5 mM MgCl₂, pH 7.6) and in PBS (10 mM Na₂HPO₄, 1 mM KH₂PO₄, 137 mM NaCl, 2.7 mM KCl, pH 7.0). AMP sodium salt (Sigma Aldrich Chemie GmbH) was diluted starting at maximum final concentrations of 10 mM (selection buffer) or 0.1 M (PBS). DNA oligonucleotides (biomers.net GmbH, Germany) with the sequences 5'-Cy5-CCT GGG GGA GTA TTG CGG AGG AAG G-3' (aptamer) or 5'-

Cy5-CCT tGG GGA GTA TTG CGG AtG AAG G-3' (mutant) were added to the AMP-dilution steps manually prior to (PBS) or during nl-droplet transfer (selection buffer) to yield final oligonucleotide concentrations of 2 µM and final droplet volumes of 10 or 20 nl. Fluorescence after thermophoresis was averaged over a (30x30) µm area in the heat spot and normalized to the cold fluorescence. Mean F_{norm} -values of at least two nl-samples from identical stocks were fit to the Hill equation. Error bars represent the standard deviation.

Finite element simulations were done using COMSOL Multiphysics (COMSOL Inc., USA). Flows in the aqueous droplet and the oil were described by cylindrically symmetric incompressible Navier-Stokes equations, combined with equations for thermal convection and conduction, laser absorption, and Marangoni convection at the interface. Molecules inside the droplet are subject to diffusion, convection and thermophoresis. The temperature dependence of the interfacial tension was adjusted to reproduce experimentally measured flow velocities. For the time traces in Fig. 4b, the fluorescence was averaged over a cylindrical volume (d=30 µm) in the droplet center.

2. *Numerical simulation of locally heated nl-droplets*

a. *Excluding Marangoni convection or thermophoresis*

The physics in the aqueous droplet are described by a set of coupled partial differential equations. In addition to the incompressible Navier-Stokes equations, equations for thermal convection and conduction, and laser absorption, two more equations are required. For Marangoni convection, this is

$$\eta^{(i)} \left[r \mathbf{n} \cdot \nabla \left(\frac{\mathbf{t} \cdot \mathbf{v}}{r} \right) \right] = \gamma_T \mathbf{t} \cdot \nabla T,$$

which must hold at the oil-water interface.^[1] \mathbf{n} and \mathbf{t} are the normal and tangential unit vectors, \mathbf{v} is the fluid velocity and r the radial coordinate. $\gamma_T = \partial\gamma/\partial T$ denotes the temperature dependence of the interfacial tension, $\eta^{(i)}$ the viscosity of water or oil on each side of the interface.

The distribution of the solute inside the droplet is described by a convection-diffusion equation, extended by a thermophoresis-term:

$$\frac{\partial c}{\partial t} + \nabla [(-D\nabla - D_T\nabla T + \mathbf{v})c] = 0.$$

D is the diffusion coefficient and D_T the thermodiffusion coefficient. Their ratio is the Soret coefficient $S_T = D_T/D$.

To quantify the respective contributions of Marangoni convection and thermophoresis to the observed fluorescence decrease, two control simulations were performed. In these controls, either the Soret coefficient S_T or the temperature dependence of the interfacial tension γ_T has been set to zero.

In the latter case ($\gamma_T = 0$, “no Marangoni”), the flow fields in the droplet are very different from those in the full simulation. However, the fluorescence time traces are not altered significantly. On the other hand, setting $D_T = 0$ (hence $S_T = 0$, “no thermophoresis”) strongly reduces the magnitude of the fluorescence decrease. Therefore, the Soret coefficient of the solute strongly affects the observed fluorescence time traces. Moreover, this signal is not masked by the convective flows.

b. *Influences from droplet size*

To assess the influence of the droplet size on the thermophoresis measurements, we simulated droplets of two different sizes, 20 nl (340 µm) and 10 nl (270 µm) (Fig. 3 and Fig. S1). The resulting flow fields and temperature distributions were highly similar.

The mean flow velocity was $12 \mu\text{m/s}$ in the 20 nl-droplet and $14 \mu\text{m/s}$ in the 10 nl droplet. The average temperature increase in the measurement volume ($d=30 \mu\text{m}$) was 10 K in the 20 nl-droplet and 11.5 K in the 10 nl-droplet (for the same heating power). These minor differences illustrate that the measurement principle is independent of the droplet size in the relevant range. Therefore, small deviations from the target volumes will not have any considerable effect on the thermophoresis measurements. The differences could even be fully avoided by decreasing the heating power in 10 nl.

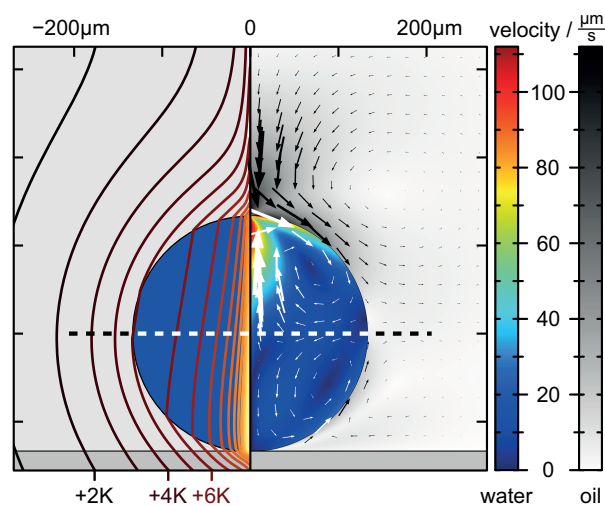


Figure S1. Numerical simulation of temperature and flow fields in a vertical cut through a 10 nl-droplet after 0.2 s of heating. This figure is completely analogous to Fig. 3. In particular, the laser power is the same as for the 20 nl droplet.

3. Thermophoresis measurements in nl-droplets

a. Accuracy of the acoustic droplet production

The accuracy of the Labcyte ECHO 550 liquid handler for aqueous buffers was previously analyzed by Harris et al.^[2] In this systematic analysis, deviations from the expected volume lay below 2% for PBS or TRIS buffer with MgCl_2 for all tested volumes. This high accuracy is achieved, as the liquid handler measures fluid height and properties before transfer and then calibrates automatically.

The transfer volume deviations of $<2\%$ does not affect the nl-thermophoresis measurements, as experiments in both, 20 nl and 10 nl droplets gave consistent results. This corresponds to a volume difference of 50%. In addition, simulations in 20 nl and 10^onl were almost identical in terms of convective flows, temperature distribution, and fluorescence time traces (2b with Fig. S1).

Volume deviations correspond to concentration errors, when mixing two compounds for binding studies. However, a concentration error $<2\%$ is very small compared to e.g. manual pipetting of small μl -volumes.

Taken together, the inaccuracy of the transfer is so small, that it is not critical for our technique. Furthermore, rare outliers in droplet size e.g. due to inaccurate source well filling or oil layer preparation can easily be identified with the optical measurement setup.

b. Raw fluorescence time traces of a binding study

Fig. 2 shows fluorescence time traces of labeled aptamer with and without AMP during a thermophoresis experiment in 20 nl-selection buffer droplets. The heating laser was turned on after 10 s, which led to a fluorescence decrease because of two events.

Firstly, the intensity of the fluorophore decreased due to the temperature increase. Secondly, thermophoretic molecule movement away from the heat spot led to depletion and thus lowered the fluorescence. Both events were influenced, when AMP bound to the aptamer. The temperature response of the fluorophore is sensitive to its local environment. This temperature response is thus influenced by binding in close proximity to the dye or by conformational changes of the aptamer during the binding event. In case of the AMP-aptamer binding, the dye's temperature response was smaller for the unbound aptamer than for the bound complex. Thermophoresis is highly sensitive to binding induced changes of various molecular properties. The thermophoretic depletion was weaker for free aptamer than for its complex with AMP.

Titration of AMP two a constant aptamer amount changed the ratio of bound and unbound aptamer. Thus, the titration steps showed a stepwise change in the dye's temperature response and the thermophoretic depletion.

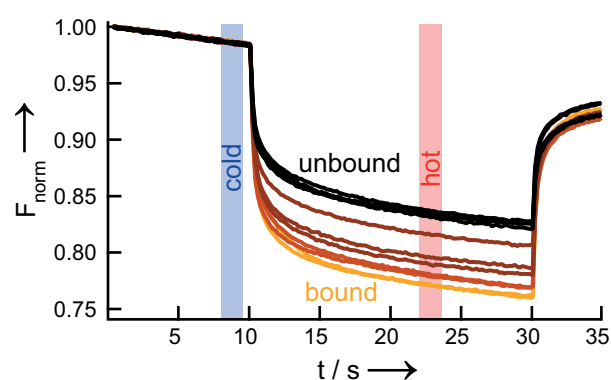


Figure S2. Raw fluorescence time traces of aptamer without and with different concentrations of AMP (20 nl, selection buffer). Unbound aptamer (top, black) shows a smaller temperature response of its fluorophore and a weaker thermophoretic depletion than the bound complex with AMP (bottom, orange). To quantify binding, AMP was titrated against a constant aptamer concentration. This led to a changing ratio of unbound and bound aptamer and thus to a stepwise change of the time traces (middle, brown). The fluorescence after dye response and thermophoresis (hot, red) was divided by the fluorescence before heating (cold, blue). This relative fluorescence was analyzed further (see below).

c. Data analysis in binding studies

Fig. S2 illustrates the first analysis step of the fluorescence time traces: The thermophoresis before heating (cold, blue) was averaged between 8.4 s and 9.5 s, and the fluorescence after heating (hot, red) between 22.4 s and 23.5 s. Afterward, the hot fluorescence was divided by the cold fluorescence, to yield the strength of dye temperature response and thermophoretic depletion. This signal can be approximated as linear to the bound aptamer fraction. It can thus directly be fit to the binding model. As AMP and aptamer have been reported to show cooperative binding, we fit the data to the Hill equation. The Hill equation revealed the EC_{50} and the Hill coefficient.

To obtain the bound fraction, we subtracted $F_{\text{hot}}/F_{\text{cold}}$ of the unbound aptamer as a baseline and normalized the curve to a fully bound plateau of 100%. Finally, the bound fraction was plotted on a linear y-axis against the AMP concentration on a \log_{10} x-axis (see Fig. 5).

[1] F. M. Weinert, D. Braun, *Phys. Rev. Lett.* **2008**, 101, 168301.

[2] D. Harris, M. Mutz, M. Sonntag, R. Stearns, J. Shieh, S. Picket, R. Ellson, J Olechno, *JALA* **2008**, 13, 97–102.



Microscale thermophoresis quantifies biomolecular interactions under previously challenging conditions

Susanne A.I. Seidel^a, Patricia M. Dijkman^b, Wendy A. Lea^c, Geert van den Bogaart^e, Moran Jerabek-Willemsen^j, Ana Lazicⁱ, Jeremiah S. Joseph^f, Prakash Srinivasan^d, Philipp Baaske^j, Anton Simeonov^c, Ilia Katritch^f, Fernando A. Melo^g, John E. Ladbury^g, Gideon Schreiber^h, Anthony Watts^b, Dieter Braun^a, Stefan Duhr^{j,*}

^aSystems Biophysics and Functional Nanosystems, Ludwig-Maximilians-Universität München, Amalienstrasse 54, 80799 Munich, Germany

^bBiomembrane Structure Unit, Department of Biochemistry, University of Oxford, South Parks Road, Oxford, OX1 3QU, UK

^cDivision of Preclinical Innovation, National Center for Advancing Translational Sciences, National Institutes of Health, Bethesda, MD, USA

^dLaboratory of Malaria and Vector Research, National Institute of Allergy and Infectious Diseases, National Institutes of Health, Rockville, MD, USA

^eDepartment of Tumor Immunology, Radboud University Nijmegen Medical Centre, Geert Grooteplein-Zuid 10, 6525 GA Nijmegen, The Netherlands

^fThe Scripps Research Institute, 10550 North Torrey Pines Road, La Jolla, CA 92037, USA

^gDepartment of Biochemistry and Molecular Biology and Center for Biomolecular Structure and Function, University of Texas MD Anderson Cancer Center, Unit 1000, 1515 Holcombe Boulevard, Houston, TX 77030, USA

^hDepartment of Biological Chemistry, Weizmann Institute of Science, Rehovot 76100, Israel

ⁱNanoTemper Technologies, Inc., One Embarcadero Center, Suite 1060, San Francisco, CA 94111, USA

^jNanoTemper Technologies GmbH, Flößergasse 4, 81369 Munich, Germany

ARTICLE INFO

Article history:

Available online 24 December 2012

Communicated by Peter Schuck

Keywords:

Microscale thermophoresis

Binding affinity

Label-free

Bioliquids

Dimerization

Cooperativity

ABSTRACT

Microscale thermophoresis (MST) allows for quantitative analysis of protein interactions in free solution and with low sample consumption. The technique is based on thermophoresis, the directed motion of molecules in temperature gradients. Thermophoresis is highly sensitive to all types of binding-induced changes of molecular properties, be it in size, charge, hydration shell or conformation. In an all-optical approach, an infrared laser is used for local heating, and molecule mobility in the temperature gradient is analyzed via fluorescence. In standard MST one binding partner is fluorescently labeled. However, MST can also be performed label-free by exploiting intrinsic protein UV-fluorescence.

Despite the high molecular weight ratio, the interaction of small molecules and peptides with proteins is readily accessible by MST. Furthermore, MST assays are highly adaptable to fit to the diverse requirements of different biomolecules, such as membrane proteins to be stabilized in solution. The type of buffer and additives can be chosen freely. Measuring is even possible in complex bioliquids like cell lysate allowing close to in vivo conditions without sample purification. Binding modes that are quantifiable via MST include dimerization, cooperativity and competition. Thus, its flexibility in assay design qualifies MST for analysis of biomolecular interactions in complex experimental settings, which we herein demonstrate by addressing typically challenging types of binding events from various fields of life science.

© 2013 Elsevier Inc. All rights reserved.

1. Introduction

1.1. The importance of biomolecular affinity quantification

Binding events involving proteins and other biomolecules play a central role in all fields of life science, from molecular physiology and pathology to diagnostics and pharmacology. Therefore, biomolecular interaction analysis does not only give fundamental in-

sights into the molecular biology of the cell but also paves the way towards improved disease treatment.

Cellular networks for signal transduction are mainly based on the direct interaction of biomolecules. A typical example is the ligand binding-induced activation of cell membrane receptors. It has recently been shown for the fibroblast growth factor receptor (FGFR), that not only interaction with the ligand, but also with a negative regulator is required for proper receptor function: binding of growth factor receptor-bound protein 2 (Grb2) dimers inhibits FGFR activation in absence of extracellular stimuli [1]. Pathological alterations of these signal transduction networks have to be elucidated to understand disease etiology. In infectious diseases, host cell invasion is a critical step that involves specific protein–protein

* Corresponding author. Fax: +49 89 4522895 60.

E-mail addresses: Stefan.duhr@physik.uni-muenchen.de, Stefan.duhr@nanotemper.de (S. Duhr).

URL: <http://www.nanotemper-technologies.com> (S. Duhr).

interactions. For instance, the malaria-causing microorganism *Plasmodium falciparum* invades red blood cells through multiple receptor-ligand interactions. One of the key steps requires injecting parasite rhoptry neck proteins (RONs) [2]. RON2 then functions as a receptor for apical membrane antigen 1 (AMA1) present on the parasite's surface. The interaction of RON2 and AMA1 is therefore of major interest as a potential drug target [3].

In these examples, qualitative binding studies alone would hardly be sufficient. Instead, quantitative analysis not only allows obtaining biologically relevant information but also evaluating it in the context of the corresponding system. Microscale thermophoresis (MST) quantifies biomolecular interactions based on the unique physical principle of thermophoresis not utilized by any other technique. As thermophoresis is influenced by binding-induced changes of various molecular properties, MST distinguishes itself from other biophysical techniques relying on measurable changes in one single parameter. In addition, MST benefits from very low sample consumption and short measurement times. Its highly flexible assay design makes MST a widely applicable approach, even when the system of interest poses challenging conditions. In this work, we place MST in the context of other well-established biochemical and biophysical methods and illustrate how it can be used to quantify interactions that are difficult to quantify by other means. Measurements in cell lysate or in complex buffers as are needed to stabilize GPCRs are shown. In addition to small molecule interactions, homodimerization, binding events comprising multiple constituents and cooperativity are discussed. We furthermore give detailed information on the background of MST and on its experimental implementation.

1.2. Tools for biomolecular binding analysis

The optimal approach to determine binding constants for a given biological system can be selected by considering the specific strengths and weaknesses of the currently available techniques. Biochemical methods are straightforward to perform and comparably low in cost and effort. They include electrophoretic mobility shift assays (EMSA) for the study of protein-nucleic acid interactions and antibody-based techniques such as enzyme linked immunosorbent assays (ELISA) [4,5]. Despite their popularity and application depth, classical biochemical methods are typically limited to semi quantitative interaction analysis [6].

A number of biophysical approaches, including isothermal titration calorimetry, dynamic light scattering, fluorescence polarization and surface plasmon resonance, do allow quantitative binding studies. Isothermal titration calorimetry (ITC) has the advantage of not requiring labeling or tethering. In this calorimetric approach, the heat change upon binding is measured by titrating one binding partner into an adiabatic sample cell, which contains a constant amount of the other binding partner. ITC gives direct access to affinity, stoichiometry and thermodynamic parameters. However, sensitivity is low, requiring relatively high amounts of sample to generate a sufficiently strong heat signal, which can be difficult to achieve for biological samples. Binding affinities from nM to sub-mM can be resolved with low throughput [7–9]. Label-free, free solution binding analysis is also possible via dynamic light scattering (DLS). DLS utilizes the autocorrelation of time-dependent fluctuations in light scattered by biomolecules in solution. The translational diffusion coefficient and thus the hydrodynamic radius (r_H) of the biomolecules are inferred. A binding-induced change in the average particle size can thus be detected. In high-density plate formats, DLS allows for high-throughput measurements of affinities in the low to high micromolar range. The technique, however, relies on a significant difference in the r_H of the unbound partners relative to the complex and is thus limited to binding partners that maximally differ by a factor of two in their

r_H . It has to be taken into account that r_H scales with the cube root of the molecular weight. The sensitivity is thus lower for the binding of two larger proteins compared to the binding of two smaller ones [10,11]. Another free solution method is fluorescence polarization (FP; or fluorescence anisotropy). FP requires fluorescent labeling of one of the binding partners, usually a small molecule ligand, which is then excited with polarized light. Fast rotation of the small ligand causes the emitted light to be depolarized. Binding of a larger protein leads to an increase in size and thus slower rotation. As a result, the emitted light remains polarized to a greater extent. FP allows for fully automated high-throughput analysis. Applicability and sensitivity are limited by the relation of fluorescence lifetime of the dye, the size of the fluoroligand and the molecular weight change upon binding. Fluorescein, a dye frequently used for FP, has a lifetime of 4 ns and is thus only applicable in FP assays in which a ligand of less than several thousand daltons in size is labeled [12,13]. Considering that fluorescein itself has a molecular weight of >300 Da, it seems quite conceivable that labeling alters the ligand's binding behavior.

In contrast to the aforementioned methods, surface plasmon resonance (SPR) is not performed in free solution. Instead, it relies on immobilizing one of the binding partners to a thin noble metal film. Light at the resonance wavelength is used to induce surface plasmons. When a binding partner binds to the immobilized biomolecule layer, the refractive index increases and therefore the resonance frequency changes. The technique allows for real-time determination of on- and off-rates and covers affinities from sub nM to low mM with an intermediate throughput rate. Mass transport as well as rebinding are well-described complications for kinetic measurements [14,15]. Establishing new assays for surface-bound techniques like SPR can be time-consuming. Furthermore, surface immobilization may affect the bound molecules' dynamics and thus alter the binding event [16].

As a solution-based method, microscale thermophoresis avoids such surface artifacts and immobilization procedures. In standard MST, one binding partner is fluorescently labeled [17]. However, protein interactions can also be analyzed using label-free MST which utilizes the intrinsic UV-fluorescence of proteins [18]. MST relies on binding-induced changes in thermophoretic mobility, which depends on several molecular properties, including not only size, but also charge and solvation entropy [19]. Therefore, MST does not require a change in size or mass like FP and SPR and is not limited by the molecular weight ratio of the binding partners like DLS. This does not only lead to a wider applicability but also to a greater flexibility in assay design. Applicability and flexibility are further enhanced by the fact that virtually any type of buffer as well as complex bioliquid can be used.

2. The concept of microscale thermophoresis

2.1. Experimental approach

2.1.1. The MST instrument

Microscale thermophoresis is an all-optical approach to characterize the properties of biomolecules. Visible light is used for fluorescence excitation in the Monolith NT.115 MST instrument, for which three types of LED-filter combinations are available: blue (excitation 460–480 nm, emission 515–530 nm), green (excitation 515–525 nm, emission 560–585 nm) and red (excitation 605–645 nm, emission 680–685 nm). In the Monolith NT.LabelFree instrument an excitation wavelength of 280 nm and an emission of 360 nm are used to, respectively excite and detect the intrinsic UV-fluorescence of proteins. As illustrated in Fig. 1A, an infrared (IR) laser with a wavelength of 1480 nm is coupled into the light path of fluorescence excitation and emission. The IR radiation is

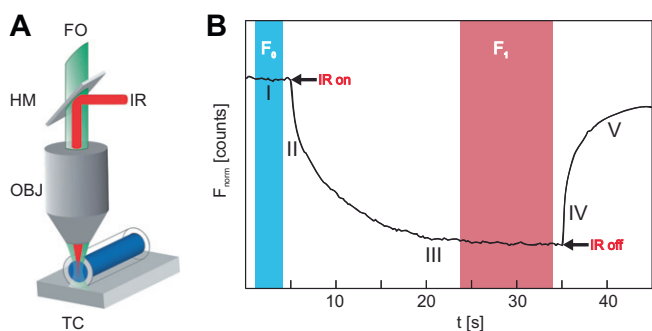


Fig. 1. Microscale thermophoresis. (A) MST setup. The sample solution inside a capillary placed on a temperature-controlled sample tray (TC) is locally heated with an IR-laser (IR), which is coupled into the path of fluorescence excitation and emission with an IR reflecting “hot”-mirror (HM). FO: fluorescence observation; OBJ: objective. (B) Schematic representation of the fluorescence time trace recorded by the MST instrument. A series of processes can be separated from each other: The initial fluorescence (I) drops fast as soon as the heating IR-laser is turned on ($t = 5$ s). This T -jump (II) on a 100 ms timescale depicts the fluorophore’s temperature sensitivity. It can easily be separated from the following diffusion-limited thermophoresis (III) lasting several seconds. Both T -jump and thermophoresis can be influenced by a binding event. Turning off the IR-laser ($t = 35$ s) leads to the inverse T -jump (IV) and the backdiffusion (V). The fluorescence after thermophoresis (F_1) is normalized to the fluorescence F_0 which is either the initial fluorescence (depicted here) or the fluorescence after the T -jump. In the former case shown here, thermophoresis and T -jump are both included in the signal analysis whereas in the latter, only thermophoresis is captured.

focused onto the sample to exactly the spot where fluorescence intensity is measured. The IR radiation is absorbed by the water molecules of the sample buffer to create a temperature gradient. As the coherent laser radiation can be easily focused, the temperature gradient is localized and strong while the overall temperature remains low. The temperature increase has a $1/e$ extension of $25 \mu\text{m}$, and a total volume of 2 nl of the sample is heated by typically 1–6 K, depending on IR-laser power and sample capillary type. The height of the capillaries is tightly regulated to guarantee highly reproducible temperature gradients. The capillaries have a constant inner and outer diameter and are made from highly pure glass. This ensures that a constant amount of laser power is absorbed, that the conductive heat transport through the glass is constant and that no diffraction of laser radiation occurs. Other important capillary properties are discussed separately in Section 2.1.4.

2.1.2. Fluorescent labels

The thermophoretic movement is detected through fluorescence of one of the binding partners, originating either from an attached fluorescent label or fluorescent fusion protein or from protein intrinsic UV-fluorescence.

Crosslinker reactive groups are commonly used for protein labeling. The fluorescent dye is coupled to the crosslinker, which covalently binds to specific functional groups of the protein. For instance, *N*-hydroxysuccinimide (NHS) esters react with primary amines of lysine side chains or at the protein’s *N*-terminus. Coupling to arginine’s guanidino group is possible as well. Alternatively, maleimide dyes can be used to label sulfhydryl groups present in reduced cysteine residues. In both cases, unreacted dye needs to be removed prior to the binding analysis. Biomolecules typically contain more than one of these potential labeling sites. However, the exact position of the fluorescent label is not important for thermophoretic analysis. Furthermore, the presence of labels at random positions adds to MST’s robustness, as it minimizes possible local effects of a label on the binding behavior. Coupling reactions often require a specific pH, but the conditions are normally well-tolerated by most proteins. Besides proteins,

other types of molecules can be fluorescently labeled to study binding interactions (e.g. nucleic acids, sugars, lipids, etc.).

Alternative fluorescent labeling approaches can be used to specifically label the target protein without the need for prior purification. In vitro translation systems allow for the linkage of fluorophore-puromycin conjugates to the C-terminus [20] or the incorporation of “non-natural amino acids”. These amino acids can already carry a fluorescent dye [21] or can be specifically modified after incorporation [22]. In addition, recombinant proteins can be used directly in cell lysate. Either fusions to a fluorescent protein, such as the green fluorescent protein (GFP), can be used or specific peptide sequence tags allowing for site-specific dye coupling. Sample volumes and concentrations obtained by such protein purification-free approaches typically suit the requirements of MST experiments very well.

Fluorescent labels provide high sensitivity such that sub-nM concentrations can be used. They also ensure selectivity for measurements in complex fluids or mixtures of molecules carrying different labels. It is however possible that fluorescent labels influence certain binding interactions. Some biomolecules, such as most membrane proteins (e.g. G protein-coupled receptors), are particularly sensitive to modifications. A solution to this is label-free MST which utilizes intrinsic protein fluorescence in the UV-range, arising from the aromatic amino acids tyrosine, phenylalanine and tryptophan (Trp) with the latter being the dominant intrinsic fluorophore. To get a measurable UV-fluorescence signal in label-free MST, proteins of average Trp-content (2 or more Trp) can typically be used in concentrations as low as 100 nM. A protein concentration of 100 nM allows to precisely quantify $K_{\text{D}} \geq 50$ nM, whereas smaller K_{D} s can still be detected but not accurately quantified [18].

The choice of source of fluorescence should take into account the nature of the liquid in which the MST analysis will be performed. Background fluorescence of the buffer at the fluorophore wavelength should be avoided to obtain a good signal to noise ratio. Therefore, label-free measurements cannot be conducted in complex bioliquids such as concentrated cell lysate or blood serum since these show a high background UV-fluorescence due to their high protein content. Red fluorescent labels are the best choice for measuring in serum as its background fluorescence is very low at the red end of the spectrum. The fluorescence intensity should be high enough to keep the concentration of the non-titrated fluorescent binding partner in the order of the expected K_{D} or below. This ensures maximum resolution and highest precision when determining dissociation constants.

2.1.3. The serial dilution

MST measures equilibrium binding events. For this, the non-fluorescent partner is titrated against a fixed concentration of the fluorescent partner. The initial fluorescence intensity should be constant throughout the serial dilution unless the fluorophore is close to the binding sites or there are problems with aggregation or surface adsorption. To clarify this, the influence of detergents or BSA and a negative control of the protein should be tested. Changes in the fluorescence intensity in label-free MST should be treated carefully, as the non-negligible background fluorescence in the UV-range makes the measurements more susceptible to false-positive signals arising merely from fluorescence changes. Thus, background subtraction and negative controls are very important.

The available monolith series instruments accept up to 16 capillaries for one experiment. The minimal concentration of titrated partner needs to be sufficiently low to measure the thermophoretic movement of the unbound state. The maximal concentration has to be higher than the expected dissociation constant to reach saturation of the fully bound complex. As a rule of thumb this is about 20-fold above the dissociation constant.

2.1.4. Capillaries

Having prepared the serial dilution, the samples are filled into capillaries through capillary action. Sample volumes of less than 4 μl are sufficient resulting in low sample consumption. MST capillaries have precisely defined dimensions with inner diameter variations of less than 1 μm guaranteeing highly reproducible temperature gradients. The temperature gradient and the overall temperature increase also depends on the thickness of the outer layer of glass since its heat conductivity determines the efficiency of heat transport away from the focal IR-laser area. The inner capillary surface greatly influences the quality of the measurement. Standard MST capillaries (NanoTemper Technologies) are physically treated to obtain a highly homogeneous surface and thus a low background signal. Unspecific adsorption of one of the binding partners to the capillary surface is readily detected by the MST device. It can be avoided by using capillaries coated with hydrophilic or hydrophobic polymers or by using buffer additives like detergents or proteins (e.g. BSA). When using BSA for small molecule measurements, control experiments are recommended to rule out unspecific binding of the small molecule to BSA.

2.2. Theoretical background

2.2.1. Thermophoresis

The directed movement of particles in a temperature gradient, thermophoresis, was already described by Carl Ludwig in 1856 [23]. Thermophoresis can be depicted as a molecular flow, which is directly proportional to the temperature gradient with the proportionality constant D_T , the thermal diffusion coefficient:

$$j = -cD_T \text{ grad } T$$

j : molecular flow; c : molecule concentration; D_T : thermal diffusion coefficient; T : temperature.

In steady state this thermophoretic flow is counterbalanced by mass diffusion:

$$j = -D \text{ grad } c$$

D : diffusion coefficient.

The thermophoretically induced change in concentration is then determined by the ratio of D and D_T which is referred to as the Soret coefficient S_T :

$$S_T = \frac{D}{D_T}$$

For a given spatial temperature difference ΔT the steady state concentration change is therefore given by:

$$\frac{c_{\text{hot}}}{c_{\text{cold}}} = \exp(-S_T \Delta T)$$

c_{hot} : molecule concentration in the hot area; c_{cold} : molecule concentration in the cold area.

This thermophoretic depletion depends on the interface between molecule and solvent. Under constant buffer conditions, thermophoresis probes size, charge, solvation entropy and conformation of the molecules. As biomolecular binding events typically affect at least one these parameters, thermophoresis can be used as a flexible tool for biomolecular affinity quantification [19].

2.2.2. MST signal analysis

The MST instrument excites and records fluorescence of the focal IR-laser area within the sample before, during and after the laser is turned on. As thermophoresis is diffusion limited, the spatial restriction of the temperature gradient, achieved by using an IR-laser for heating, allows for short measurement times well below 30 s per sample. The fluorescence time trace, schematically represented in Fig. 1B, displays a series of defined and separable

processes, each of them containing different information on the binding event.

Before heating, the initial fluorescence (region I in Fig. 1B) is recorded. It should be constant for all samples. Minor random variations due to pipetting errors do not influence the result, as a relative fluorescence signal is used. Occasionally, changes of the initial fluorescence occur due to binding close to the fluorophore. Having carefully ruled out artifacts as a possible reason (see Section 2.1.3.), the K_D may already be inferred from these changes in some cases by plotting the initial fluorescence against the concentration of the titrant and fitting to a binding model (see below). Turning on the IR-laser leads to an abrupt change in fluorescence intensity. This so-called temperature jump (T -jump, region II in Fig. 1B) corresponds to the temperature-dependent change of fluorescence, an inherent property of the fluorophore [24]. This temperature dependence is sensitive to the fluorophore's local environment. Thus the T -jump can be influenced by conformational changes or binding in close proximity to the fluorophore [25] which may provide spatial information on the binding site. The T -jump occurs on the same short timescale of several 100 ms as the fast heating by the IR-laser. It can thus easily be separated from the following relatively slow thermophoresis (region III in Fig. 1B) which, as a diffusion-limited process, lasts several seconds. The thermophoretic motion creates a concentration gradient of the fluorescent molecules. Fluorescence intensity reaches a plateau representing the steady state in which thermodiffusion is counterbalanced by mass diffusion. Immediately after the heating laser is turned off, the fluorescence recovery due to the fluorophore's temperature dependence, the inverse T -jump (region IV in Fig. B), indicates cooling of the sample. Finally, backdiffusion (region V in Fig. 1B), driven by pure mass diffusion, leads to the compensating of the concentration gradient.

As mentioned above, relative fluorescence is used to quantify binding via MST:

$$F_{\text{norm}} = \frac{F_1}{F_0}$$

F_{norm} : normalized fluorescence; F_1 : fluorescence after thermodiffusion; F_0 : initial fluorescence or fluorescence after T -jump.

F_1 refers to the fluorescence measured several seconds after the IR-laser has been turned on, when the traces of unbound and bound state can be discriminated. The steady state does not necessarily have to be reached within the time of the experiment [17]. F_0 refers to either the initial fluorescence or the fluorescence after the T -jump which is approximately 1 s after the laser has been turned on. In the former case depicted in Fig. 1B, thermophoresis and T -jump are both included in the signal analysis whereas in the latter, only thermophoresis is captured. When the T -jump is influenced by the binding event, including it leads to a better signal to noise ratio in the resulting binding curve. Analysis of thermophoresis with and without T -jump typically yields the same result. Both processes should, however, not be used for a combined analysis when their binding-induced changes show amplitudes with an opposite sign and would thus cancel each other out.

For small relative temperature and concentration changes as is the case in MST experiments, the above mentioned equation describing the concentration change due to thermophoresis can be approximated by linearization:

$$\frac{c_{\text{hot}}}{c_{\text{cold}}} = \exp(-S_T \Delta T) \approx 1 - S_T \Delta T$$

F_{norm} corresponds to S_T , plus where applicable the additional contribution of the fluorescence change due to the fluorophore's temperature dependence $\delta F/\delta T$:

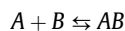
$$F_{\text{norm}} = 1 + \left(\frac{\delta F}{\delta T} - S_T \right) \Delta T$$

Affinity is quantified by analyzing the change in F_{norm} as a function of the concentration of the titrated binding partner. As the thermophoretic movement of bound and unbound state superpose linearly, the fraction bound (FB) is described by:

$$F_{\text{norm}} = (1 - FB)F_{\text{norm, unbound}} + (FB)F_{\text{norm, bound}}$$

FB : fraction bound; $F_{\text{norm, unbound}}$: normalized fluorescence of the unbound state; $F_{\text{norm, bound}}$: normalized fluorescence of the bound state.

In many cases the binding event can be described by a simple model according to the law of mass action. More complex binding modes require different models, e.g. the Hill equation for cooperativity. It would be beyond the scope of this review to discuss different binding models in detail. Thus the often applicable model according to the law of mass action will be described in the following. The binding process of a partner A and a partner B leading to the formation of a complex AB is characterized by:



A: binding partner A; B: binding partner B; AB: bound complex of A and B.

The equilibrium dissociation constant K_D which quantifies the binding affinity is defined as:

$$K_D = \frac{[A]_{\text{free}}[B]_{\text{free}}}{[AB]}$$

K_D : equilibrium dissociation constant; $[A]_{\text{free}}$: concentration of free partner A; $[B]_{\text{free}}$: concentration of free partner B; $[AB]$: concentration of bound complex of A and B.

As the free concentrations are not known, total concentrations are used instead. The total concentration of A and B are defined as:

$$[A] = [A]_{\text{free}} + [AB] \quad \text{and} \quad [B] = [B]_{\text{free}} + [AB]$$

Thus

$$K_D = \frac{[A]_{\text{free}}[B]_{\text{free}}}{[AB]} = \frac{([A] - [AB])([B] - [AB])}{[AB]}$$

In the following, A will represent the titrated partner, B the partner, whose concentration is kept constant and whose fluorescence is read out. To obtain the K_D from the MST data, we solve for the fraction bound of B, FB :

$$FB = \frac{[AB]}{[B]} = \frac{[A] + [B] + K_D - \sqrt{([A] + [B] + K_D)^2 - 4[AB]}}{2[B]}$$

FB is now expressed as a function of the total concentration of A and B with the K_D being the single free parameter. F_{norm} from the MST measurement linearly reports FB and can thus directly be fitted to this equation.

F_{norm} is plotted on a linear y-axis in per mil (‰) against the total concentration of the titrated partner on a log₁₀ x-axis. The advantage of this semi-log plot is, that the binding data can be easily inspected by eye: the curve shows a characteristic s-shape (or mirrored-s-shape) in which the unbound and saturated state build a lower and upper plateau. F_{norm} of the unbound state is revealed by the fit and can be subtracted as a baseline value to yield ΔF_{norm} , as depicted in the figures in this manuscript.

The plots show mean ΔF_{norm} -values resulting from independent repeats of the MST experiment. The error bars on individual data points represent the standard deviation between these repeats. The means are fitted and the resultant K_D -values are given together with an error estimation from the fit. The fitting procedure assumes a Gaussian, symmetric error distribution. Thus the error can reach negative values, if the sensitivity limit determined by the lowest detectable concentration of fluorescent partner is

reached. In these cases, the K_D -values are presented as an upper limit and can also be lower.

2.3. Summary: assay optimization

MST experiments can easily be optimized as any potential problems are immediately revealed during assay design and specific troubleshooting steps are available. Although some points have already been mentioned in the last paragraphs, this section summarizes and details the information on optimization. The list is certainly not exhaustive but can serve as a practical guide for users.

Surface adsorption to reaction tubes, pipette tips or glass capillaries (“Sticking”):

Indications:

- If the capillary scan in the MST-instrument shows asymmetric peaks, peaks with shoulders or double peaks, the labeled material is most likely sticking to the capillary walls. Sometimes it takes several minutes before this is observed, sometimes it is not observable at all even though it is taking place.
- The fluorescence strongly drops along the titration curve as one of the partners or the complex sticks.
- The fluorescence of the sample is much lower than expected when compared to a calibration curve of the dye in the measurement buffer.
- The fluorescence of the same sample decreases much faster over time than would be explained by bleaching.
- The raw data curves of multiple measurements of an identical sample strongly deviate.

Optimization:

- Use low-binding reaction tubes and pipette tips.
- Use capillaries coated with hydrophilic or hydrophobic polymers.
- Use buffer additives like detergents or proteins, e.g. BSA. When testing small molecules, binding to BSA has to be excluded experimentally.

Aggregation:

Indications:

- The raw data curves show bumps or waves.
- The raw data curves of multiple measurements of an identical sample strongly deviate.

Optimization: improve sample stability, quality and homogeneity by

- spinning down the sample before the experiment (e.g. 5 min at 15000 × g) and only using the supernatant;
- using buffer additives like detergents or proteins;
- optimizing the buffer in general (ionic strength, pH, etc.)

Suboptimal fluorescence intensity:

Indications:

- Low signal to noise ratio in fluorescence intensity during the capillary scan and in the raw data curves.
- The upper parts of the peaks in the capillary scan are cut-off or there is no raw data curve but a flat line as the upper limit of the dynamic range of the fluorescence detection is exceeded (2500 counts on the current model of NT.115, see manual).
- The fluorescence of the sample is much higher or lower than expected.

Optimization:

- Test for free dye (high fluorescence intensity) or low labeling efficiency and loss of material (low fluorescence intensity) during the labeling process e.g. by photometrically determining the dye and protein concentration.
- Adjust the LED-power or concentration of the fluorescent binding partner to yield a fluorescence intensity between 200 and 1500 counts. The optimal concentration and LED-setting can be found before the binding measurement by preparing a dilution series of the fluorescent partner in the measurement buffer.

Suboptimal concentration range in the serial dilution:**Indications:**

- No binding is observed.
- The plateau of the unbound state or the saturation of the fully bound state are not reached.

Optimization:

- Optimize the concentration range of the titration, e.g. by using the concentration finder of the Nanotemper-Analysis-Software.
- When the highest possible concentration of one binding partner is below saturation levels (e.g. due to solubility problems) reversing the assay design might be helpful.

Low signal to noise ratio in MST signal amplitude:**Indication:**

- The binding-induced change in the MST signal can barely or not at all be discriminated from the background fluctuation.

Optimization:

- Improve the quality of the sample by optimizing the buffer or spinning down the sample before the experiment (e.g. 5 min at 15000 × g) and only using the supernatant.
- Increase the IR-laser power to use a higher temperature gradient.
- Reverse the assay design.
- Increase the activity of the fluorescent sample.

3. Material and methods**3.1. TEM1-BLIP**

Wt-TEM1 was labeled using the Monolith NT Protein Labeling Kit RED (NanoTemper Technologies) according to the supplied protocol. The concentration of labeled TEM1 or Ypet-wt-BLIP was kept constant at 10 nM. The corresponding unlabeled binding partner was titrated in 1:1 dilutions, with the highest final concentration chosen about 20-fold above the K_D expected from previously published SPR results. Thus the highest final concentrations were 250 nM wt-BLIP, 6 μ M W112A-BLIP and 11 μ M W150A-BLIP for the experiments with wt-TEM-NT647. For the measurements with Ypet-BLIP, maximum concentrations of 2 μ M wt-TEM and 7.5 μ M R243A-TEM were used in buffer, 250 nM TEM in lysate.

A 50 mM Tris-HCl buffer, pH 7.6 containing 150 mM NaCl, 10 mM MgCl₂ and 0.05% Tween-20 was used. For the measurements in cell lysate, 20 × 10⁶ millions 293T cells were lysed in 500 μ l RIPA-buffer and centrifuged at 15,000 × g for 5 min to remove large aggregates and cell debris. Ypet-BLIP was diluted in 200 μ l lysate to a final concentration of 20 nM and mixed with

the TEM1 dilution series in buffer to yield a final Ypet-BLIP concentration of 10 nM in 50% lysate.

Measurements were performed in standard treated capillaries (NanoTemper Technologies) on a Monolith NT.115 system (NanoTemper Technologies) using 50% LED and 80% IR-laser power. Laser on and off times were set at 30 s and 5 s, respectively.

3.2. RON2-AMA1

MST experiments were performed on a Monolith NT.115 system (NanoTemper Technologies) using 100% LED and 20% IR-laser power. Laser on and off times were set at 30 s and 5 s, respectively. Recombinant His-tagged AMA1 (His-AMA1) was expressed in *Pichia* and purified on a nickel column as previously described [3]. The protein was labeled with NT647 (NanoTemper Technologies) and applied at a final concentration of 25 nM. Both unlabeled RON2 peptide and biotinylated RON2 peptide were synthesized by LifeTein LLC (South Plainfield, NJ). A twofold dilution series was prepared for the unlabeled RON2 in DMSO. Subsequently, 0.5 μ l of each dilution point was transferred to 9.5 μ l labeled AMA1-solution, with the final RON2 concentration ranging from 50 μ M to 1.5 nM, thus maintaining the DMSO concentration at 5% constant sample-to-sample. Samples were filled into hydrophilic capillaries (NanoTemper Technologies) for measurement. FITC labeled RON2 peptide was obtained from Peptide 2.0 (Chantilly, VA), further dissolved in DMSO to produce a 20 μ M stock solution and applied at a final concentration of 10 nM. A twofold dilution series was prepared for unlabeled His-AMA1 in PBS and each dilution point was similarly transferred to FITC-RON2 solution. The final concentrations of His-AMA1 ranged from 7.8 μ M to 0.24 nM. Samples were filled into standard treated capillaries (NanoTemper Technologies) for measurement.

SPR experiments were performed on a ProteOn XPR36 system (Bio-Rad, Hercules, CA) at 25 °C using PBS with 0.005% Tween-20 as the running buffer. Immobilization of the His-AMA1 protein was achieved at 30 μ l/min on an HTE chip. Samples of the unlabeled RON2 peptide were prepared at final concentration of 500, 167, 55, 18.5 and 6.2 nM and were injected at 30 μ l/min in each horizontal channel. Association was monitored for 2 min, dissociation for 10 min. In a separate experiment, immobilization of the biotinylated RON2 (b-RON2) peptide was achieved on a NLC chip at 100 μ l/min. Samples of the His-AMA1 protein were prepared at 300, 100, 33, 11 and 3.7 nM and were injected at 30 μ l/min in each horizontal channel. Association was monitored for 2 min, dissociation for 30 min. Kinetic titration data were processed in ProteOn Manager by concatenating the responses of all five analyte concentrations, and by globally fitting to either a simple Langmuir binding model without mass transfer or a heterogeneous ligand model using both buffer blank and interspot as references.

FP experiments were performed on a Viewlux™ high-throughput charge-coupled device (CCD) imager (PerkinElmer, Waltham, MA) using an excitation filter of 480 nm and an emission filter of 540 nm. His-AMA1 was serially diluted in PBS with 0.01% Tween-20 (final concentration: 7.8 μ M to 0.24 nM) and mixed with 20 nM FITC-RON2 peptide (final concentration) in a 384-well Greiner (Monroe, NC) solid bottom assay plate. Plates were read after 5 min incubation at room temperature. For the reverse titration, biotinylated RON2 peptide was serially diluted in the same buffer (final peptide concentration started at 100 nM) and was mixed with 25 nM (final concentration) NT495-His-AMA1.

3.3. GPCR

A fusion construct of the rat neurotensin receptor 1, NTS1B, with N- and C-terminal fusion partners, maltose binding protein

and thioredoxin, respectively, was expressed and purified as described by Attrill et al. [40], with the modification that the ligand affinity column eluate was concentrated using a 1 mL HisTrap Ni²⁺-column (GE Healthcare), and the eluate thereof was diluted in imidazole- and salt-free buffer (50 mM Tris pH 7.4, 0.1% dodecyl maltoside (w/v), 0.01% cholesteryl hemisuccinate (w/v), 10% glycerol (v/v)) to lower the imidazole concentration to ~85 mM and the sodium chloride concentration to ~50 mM in the final sample to allow salt-sensitive ligand binding, giving a final receptor concentration of ~2.5 μ M as determined from A280 and gel electrophoresis against BSA standards. SR48692 was obtained from Sanofi-Aventis and neurotensin was purchased from Sigma Aldrich. A N-terminal cysteine derivative of neurotensin (Alta Bioscience, Birmingham) was labeled with AlexaFluor488 (Sigma Aldrich) by mixing the dye with a threefold excess of the peptide, adjusting the pH to 7 and incubating for 1 h at room temperature. The labeled compound was purified by HPLC using a 20–60% acetonitrile gradient on a semi-preparative C18 column. Labeling and purity were verified by mass spectrometry. Neurotensin-A488 was lyophilised and subsequently stored in 50 mM Tris pH 7.4.

Twofold dilution series starting at 375 nM NTS1B in the standard MST experiments and 2.5 μ M neurotensin as well as 25 μ M SR48692 in the label-free MST experiments were prepared in the following buffer: 50 mM Tris pH 7.4, 0.1% dodecyl maltoside (w/v), 0.01% cholesteryl hemisuccinate (w/v), 10% glycerol (v/v), imidazole 85 mM and sodium chloride 50 mM. Neurotensin-Alexa488 was used at 25 nM, while NTS1B was used at 150 nM. As a control, the SR48692-dilution was tested against a constant concentration of 150 nM thermally denatured NTS1. Due to the fact that concentrations of the receptor in label-free MST experiments were above the K_D , the determined K_D is a lower limit and affinity can be higher. Lowering receptor concentration will increase resolution. Please note, in label-free experiments the detection limit (i.e. minimum concentration of the fluorescent molecule) depends not only on the number of tryptophanes, but also on their respective position in the protein. Typically, concentrations as low as 100 nM can be used [18]. The fit to the quadratic solution of the law of mass action allows to determine even higher affinities than that with high precision.

In the competition experiment, a constant neurotensin concentration of 1 μ M was used and SR48692 was diluted 1:1 starting at 50 μ M. Label-free experiments were performed at 20% LED and 40% IR-laser power, standard MST experiments at 90% LED power and 20% IR-laser power. Laser on and off times were set at 30 and 5 s, respectively.

The A2aR was stored and measured in 50 mM K-HEPES pH 7.5 buffer containing 800 mM KCl, 10% glycerol, 0.05% dodecyl maltoside (w/v) and 0.01% cholesterol hemisuccinate (w/v). The concentration of A2aR was determined by measuring protein peak area in an analytical size exclusion chromatogram, and comparing it with protein standards. For the label-free MST experiments, A2aR was used at a constant concentration of 250 nM when testing theophylline-binding and 500 nM in all other experiments. The ligands were added to the buffers in the required concentrations from a 100 mM stock in DMSO. Twofold dilution series of the ligands were prepared, starting at the following concentrations and resultant maximum DMSO concentrations: 250 μ M for amiloride (2.5% DMSO), 100 μ M for theophylline (0.1% DMSO), 1 mM for caffeine (1% DMSO) and 5 μ M for ZM241385 (0.05% DMSO). For the competition experiments in presence of 250 μ M amiloride, twofold dilution series of caffeine starting at 2 mM and theophylline (2% DMSO) starting at 1 mM (1% DMSO) were used. Prior to measurement, ligands were incubated with protein for 10 min on ice. Experiments were performed at 20% LED and 20% IR-laser power with laser on and off times set at 30 and 5 s, respectively.

3.4. G9a

G9a was labeled with NT495 or NT647 dye (NanoTemper Technologies) and applied at a final concentration of 50 nM in 50 mM Tris-HCl, pH 7.5, with 150 mM NaCl and 0.05% Tween-20. BIX-01294 was obtained from Sigma-Aldrich (St. Louis, MO) and further dissolved in dH₂O to produce a 30 mM stock. A 16-point twofold dilution series (in dH₂O) of BIX-01294 was mixed with G9a solutions to generate a final compound concentration ranging from 500 μ M to 15.3 nM. Peptides corresponding to the first 21 N-terminal amino acids of histone H3 followed by a GG linker and a biotinylated lysine (b-H3(1–21)) were purchased from AnaSpec (Fremont, CA). b-H3(1–21) was similarly diluted in dH₂O and mixed with labeled G9a to generate a final concentration ranging from 183.6 μ M to 5.6 nM. After 15-min incubation at room temperature, samples were filled into standard treated capillaries (NanoTemper Technologies) and MST measurements were performed on a Monolith NT.115 (NanoTemper Technologies) using 100% LED (50% LED for NT647-G9a) and 20% or 40% IR-laser power. Laser on and off times were respectively set at 30 and 5 s. For competition experiments, labeled G9a was pre-mixed with a constant concentration of b-H3(1–21) or S-adenosylmethionine (SAM) and incubated at room temperature for 15-min. Either compound was added at a concentration near its respective K_D (determined using MST for the peptide substrate or based on literature value for SAM [67,69,70]): 2 μ M b-H3(1–21) or 20 μ M SAM. In a separate experiment, either compound was added at a saturating level (15–50-fold above its K_D): 100 μ M b-H3(1–21) or 300 μ M SAM. The same dilution series of BIX-01294 was added to the pre-formed G9a-b-H3(1–21) or G9a-SAM complex, and MST was measured after 15-min incubation at room temperature.

The interaction between G9a and BIX-01294 was also evaluated using a label-free approach. Specifically, a 16-point serial dilution of BIX-01294 was mixed with G9a (final concentration: 2 μ M) with BIX-01294 final concentration ranging from 200 μ M to 6.1 nM. Samples were filled into LabelFree standard treated capillaries (NanoTemper Technologies) and measured on a Monolith NT.LabelFree (NanoTemper Technologies) using 30% LED and 25% IR-laser power. Laser on and off times were also set at 30 and 5 s, respectively.

4. Results and discussion

Studying protein interactions can be challenging in certain cases. Problems arise from high mass ratios of the binding partners as in the case of protein-small molecule interactions. Membrane proteins are experimentally demanding, as they are hard to stabilize in solution. Measuring cooperative and competitive binding modes as well as working in biological liquids instead of simplified buffers can be difficult. In the following we demonstrate that MST is applicable under all mentioned challenging conditions by showing previously unpublished data and highlighting relevant examples from literature.

4.1. Protein–protein interactions

4.1.1. β -Lactamase TEM1 binds its inhibitor BLIP

Protein–protein binding is mainly based on specific non-covalent interactions at the binding partners' interfaces. The contribution of different amino acid residues can be elucidated by quantifying the influence of site-specific mutations. An in this respect well-characterized system is the binding of β -lactamase TEM1 to the β -lactamase inhibitory protein BLIP. Herein, we investigated the binding of TEM1 β -lactamase to BLIP using MST.

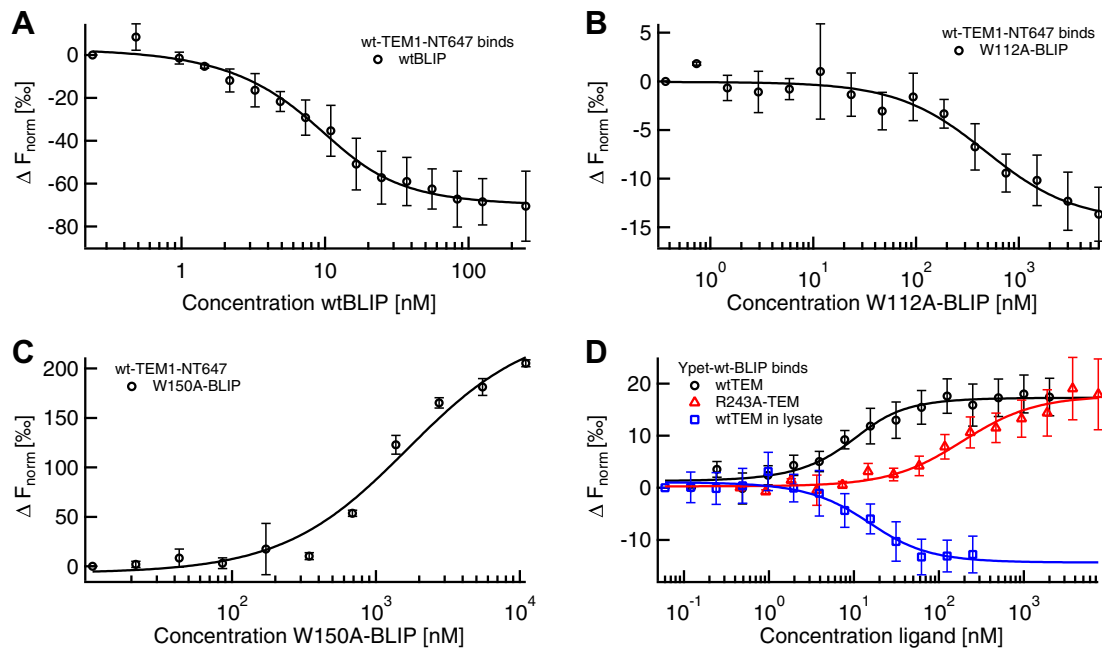


Fig. 2. MST quantifies the TEM1-BLIP interaction in agreement with SPR literature values. (A) By fitting the change in thermophoretic depletion upon titration of wt-BLIP to a constant amount of wt-TEM1 labeled with the fluorescent dye NT647 to the quadratic solution of the mass action law, a binding constant of $K_D = 3.8 \pm 0.8$ nM was determined. (B) The W112A-mutation in BLIP reduces the affinity to TEM1 to 0.5 ± 0.1 μM . (C) W150A-BLIP binds TEM1 with an even lower affinity of $K_D = 1.7 \pm 0.4$ μM . (D) In a reversed assay design, the concentration of the fusion protein Ypet-wt-BLIP was kept constant while titrating in wt-TEM1. In concordance with the binding curve shown in A, a K_D of 4.8 ± 1.7 nM was determined (black circles). Mutated R243A-TEM1 showed a lower affinity of $K_D = 0.19 \pm 0.05$ μM (red triangles). In cell lysate, the K_D between Ypet-wt-BLIP and wt-TEM1 was quantified as 10 ± 4 nM, thus demonstrating the applicability of MST for measurements in complex bioliquids. Notably, the sign of the MST signal amplitude is changed in lysate compared to buffer due to differences in pH, ionic strength etc.

In a first set of experiments, we used a constant concentration of NT647-labeled wild-type TEM1 (wt-TEM1). Binding to wild-type BLIP (wt-BLIP) as well as to two BLIP mutants with substitutions of a tryptophan residue at position 112 or 150 by alanine (W112A-BLIP, W150A-BLIP) was quantified. MST yielded a K_D of 3.8 ± 0.8 nM for the interaction of the wt-proteins (Fig. 2A). As expected, the alanine substitutions within BLIP resulted in reduced affinities for TEM with a K_D of 0.5 ± 0.1 μM in the case of W112A-BLIP and a K_D of 1.7 ± 0.4 μM in the case of W150A-BLIP (Fig. 2B and C). Due to limited sample amounts W150A-BLIP saturation was not fully reached which affects the precision of the fit. Nonetheless, both results are in excellent agreement with the literature values of 3.2 ± 0.6 nM (wt) [26], 0.36 ± 0.06 μM (W112A) and 3.8 ± 0.6 μM (W150A) [27] determined by SPR. Remarkably, the thermophoretic signal seems to contain further information on the binding event. Upon binding of wt-BLIP and W112A-BLIP to TEM1, the complex shows an increased depletion compared to the unbound TEM1, represented by the negative slope of the binding curve (Fig. 2A and B). Binding of W150A-BLIP has the opposite effect (Fig. 2C). As described by Wang et al., the W150A mutation in BLIP leads to a pronounced conformational rearrangement, thus to defects in geometrical shape complementarity to TEM1 and trapping of additional water molecules in the TEM1-BLIP interface. Therefore, the enthalpic driving force for binding decreases [28]. This conformational change likely causes the reversal in sign of the MST-amplitude.

We also used an alternative labeling approach in combination with the reversed titration protocol. The fluorescent fusion protein Ypet-wt-BLIP was kept constant while wt-TEM1 and R243A-TEM1 (substitution of arginine at position 243 to alanine) were titrated (Fig. 2D). For the interaction of the wt-proteins a K_D of 5 ± 2 nM was determined which does not only reproduce the literature value (3.5 ± 0.5 nM, SPR) [29] but also the result measured via the reversed assay design. The R243A-TEM1 mutant showed a reduced

affinity for BLIP ($K_D = 0.19 \pm 0.05$ μM) which is consistent with literature [30]. As measurements in buffer do not resemble the highly crowded, intracellular environment, we also performed MST in mammalian cell lysate. Under these close to in vivo conditions, a K_D of 10 ± 4 nM was determined for the binding of Ypet-wt-BLIP to wt-TEM1. This demonstrates the applicability of MST for affinity quantification of protein-protein interactions, not only in buffer, but also in cell lysate.

4.1.2. Grb2 dimerization

Grb2 is known as an adaptor protein involved in several signal transduction pathways [31]. An additional function has been recently suggested: Grb2 dimers seem to control the activity of the receptor tyrosine kinase FGFR2 in the absence of extracellular stimuli by growth factors [1].

The dimerization of Grb2 was analyzed via MST. Fluorescently labeled Grb2 at a constant concentration of 100 nM was added to a serial dilution of unlabeled Grb2 ranging from 55 nM to 100 μM . A K_D of 0.65 ± 0.08 μM was determined for Grb2 dimerization (Fig. 3). DLS experiments indicate that the dimer is the predominant form from 40 down to 0.4 μM , whereas below that concentration, the monomer was present [1]. The MST result is consistent with DLS, which as discussed in Section 1.2. is most reliable when studying the interaction of small, equally sized molecules as it merely detects changes in the hydrodynamic radius. Also, when measuring dimerization, MST is comparable to DLS in that the twofold size increase is likely to be the major cause of the decrease in thermophoretic mobility. In general, quantification of a dimerization process is not trivial. Although dimerization can also be quantified via a dilution approach in ITC for K_D s in the μM -range [32], the technique is not feasible for higher dimerization affinities. ITC requires minimal protein concentrations in the μM -range to get a measurable heat change [8]. If the dimerization K_D lies in the sub- μM range as for Grb2, nearly all of the

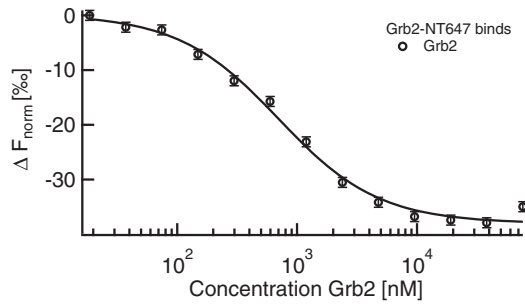


Fig. 3. Grb2 dimerization quantified thermophoretically. Unlabeled Grb2 is titrated to a constant amount of fluorescently labeled Grb2-NT647. Dimerization causes a change in thermophoresis from which a K_D of $0.65 \pm 0.08 \mu\text{M}$ was derived. MST allows the usage of protein concentrations far below this K_D —an obligatory prerequisite for dimerization quantification. Figure adapted with permission from Lin et al. [1].

protein is present as dimers at this lowest detectable concentration (Fig. 3). Thus the monomeric state and the monomer–dimer-transition are not captured and the K_D is not measurable via ITC.

4.2. Protein-peptide interaction: AMA1 and RON2

The invasion of red blood cells by the malaria-causing parasite *Plasmodium falciparum* is critically dependent on the interaction of two parasite proteins, RON2 and AMA1 [3,33,34]. To quantify this interaction, the binding between a short RON2 peptide and AMA1 was extensively characterized using MST, SPR and FP. The RON2 peptide represents a conserved region among all *P. falciparum* isolates with known sequence; in this region, two completely conserved cysteine residues forming a disulfide bridge have been determined to be essential for binding to AMA1, as mutation or alkylation abolished binding [3].

We used two MST-assay designs for the AMA1-RON2 interaction: titration of AMA1 to a constant concentration of RON2-FITC and titration of RON2 to a constant concentration of AMA1-NT647. When titrating AMA1, the MST signal shows a single binding event with a K_D of $28 \pm 2 \text{ nM}$. In contrast, the titration of RON2 yielded an MST signal in which the high affinity binding is superimposed by a second binding event at higher RON2 concentrations. When quantifying the high-affinity binding from these data, we restricted the fit to the first half of data points yielding

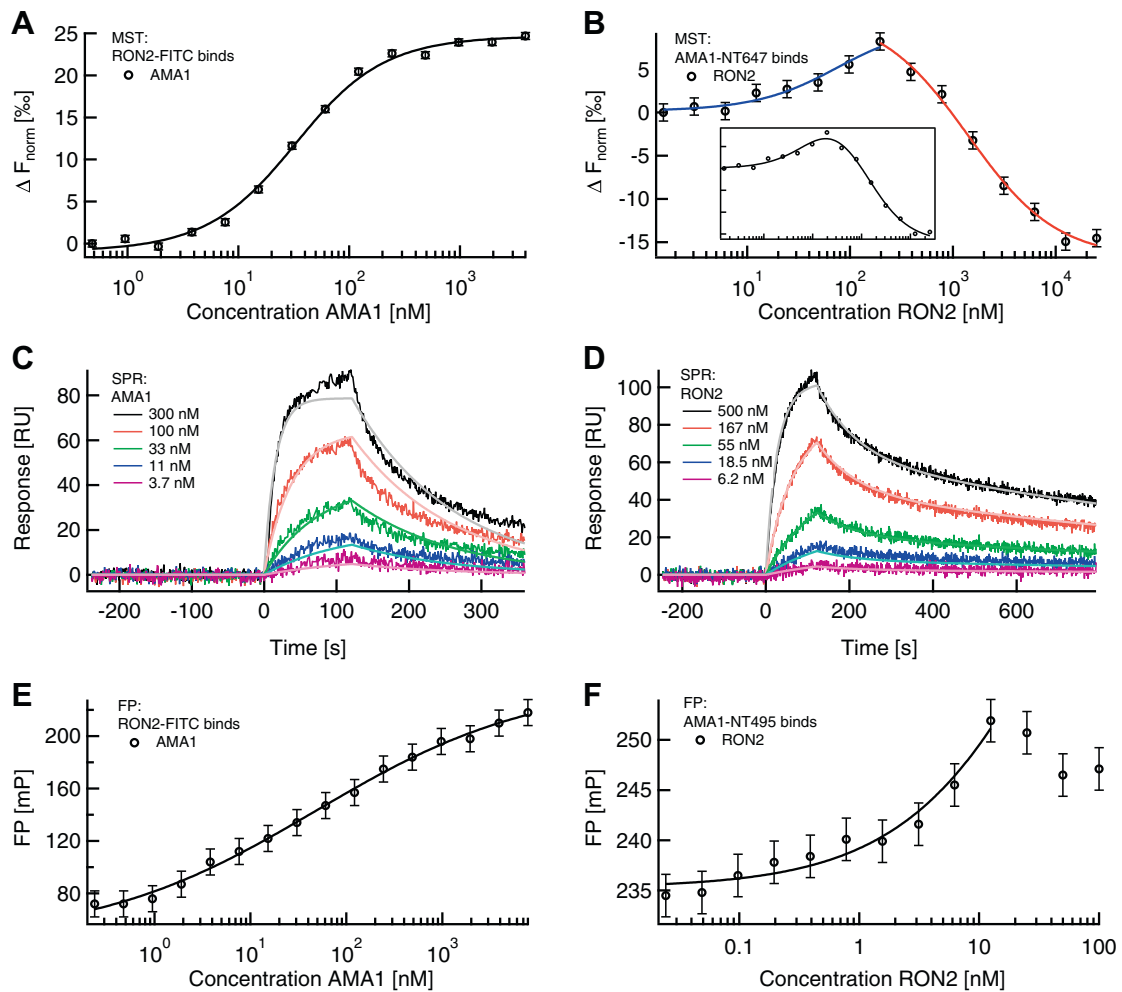


Fig. 4. The AMA1-RON2 binding analyzed via MST, SPR and FP. (A) Titration of the AMA1 protein to a constant amount of RON2-FITC peptide induces a pronounced MST signal change ($K_D = 28 \pm 2 \text{ nM}$). (B) Titrating the peptide (4.3 kDa) to a constant AMA1-NT647 (66 kDa) concentration yielded an MST signal despite the unfavorable size ratio. The signal indicated a biphasic event. Fitting the high affinity phase (blue) reveals a K_D of $62 \pm 16 \text{ nM}$, which is similar to the reverse titration (4A). Fitting the low affinity phase (red) yields a K_D of $1.4 \pm 0.2 \mu\text{M}$, which putatively results from the binding of a non-cyclized RON2 population. Inset: Instead of two independent fits for the two phases, one fit function assuming two binding events is used. This yields similar K_D s of $81 \pm 21 \text{ nM}$ and $1.2 \pm 0.1 \mu\text{M}$. (C) SPR with immobilized RON2 and five different concentrations of AMA1 yields $K_D = 13 \pm 1 \text{ nM}$ confirming MST. (D) Via the reversed SPR assay design, a similar K_D of $38.3 \pm 0.4 \text{ nM}$ is determined. A heterogeneous ligand model fits the dissociation phase best, thus also indicating a biphasic event as observed in MST. (E) FP yields a reliable result when titrating the larger binding partner, AMA1 (EC50 $48 \pm 11 \text{ nM}$). (F) Titrating the small peptide instead reduces the FP signal amplitude significantly. An EC50 of $77.1 \pm 0.2 \text{ nM}$ is estimated from the initial phase (the last three points were omitted because they appeared to represent the onset of a second phase in that range).

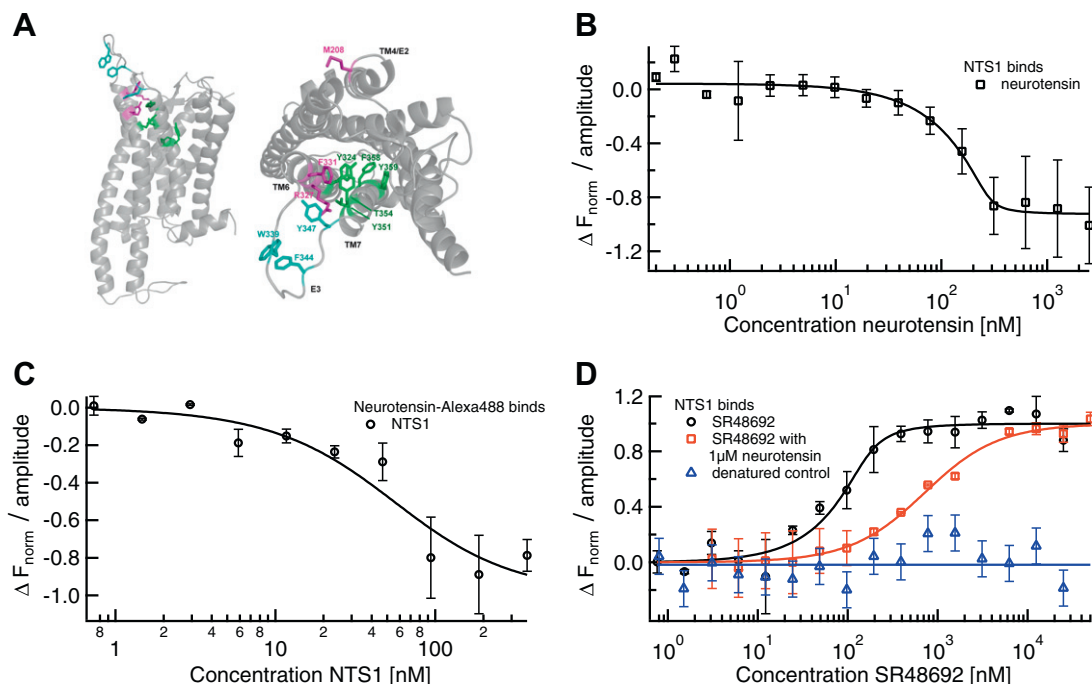


Fig. 5. Label-free MST for quantification of GPCR NTS1B ligand binding. (A) Homology model of neurotensin receptor 1 (NTS1; Satita Tapaneeyakorn, Biomembrane structure unit, University of Oxford) based on rhodopsin for the transmembrane regions and the β -adrenergic receptors for the loop regions viewed from the side (left) and top (right). Residues involved in binding of neurotensin (W339, F344 and Y347, cyan), inverse agonist SR48692 (Y324, Y351, T354, F358 and Y359, green) or both (M208, F331 and R327, magenta), as determined from mutagenesis studies [71], are highlighted. (B) Label-free MST utilizes NTS1B's intrinsic Trp fluorescence to quantify the binding to neurotensin ($K_D \leq 20$ nM). (C) In agreement with other biophysical techniques, MST using fluorescently labeled neurotensin yields a lower affinity ($K_D = 21 \pm 20$ nM). (D) Using label-free MST, a K_D of 15 ± 11 nM for the inverse agonist SR48692 was determined (black circles). Pre-saturating NTS1 with neurotensin right-shifts the K_D for SR48692 to 640 ± 50 nM (red squares). Denatured NTS1B did not show binding to SR48692 thus proving specificity (blue triangles).

a K_D of 62 ± 16 nM. Fitting the low-affinity binding yielded $K_D = 1.4 \pm 0.2$ μ M. We also analyzed all data points with a fit assuming two independent binding events with different K_D s, where we used the simplification that both binding events have the same signal amplitude. This fit yielded K_D s of 81 ± 21 nM and 1.2 ± 0.1 μ M.

The K_D determined for the high-affinity AMA1-RON2 interaction varies for the different MST designs. This is because in case of the biphasic signal, the high-affinity K_D is either determined by fitting less data points or by using a fit function with an additional parameter, the second low-affinity K_D . Despite this limitation, the K_D s for the high-affinity binding lie in the double-digit nanomolar range for both assay designs, which demonstrates the method's reversibility. However, the example also shows the

importance of performing the assay in both ways: while AMA1-titration is needed to precisely quantify the K_D , only the titration of RON2 gave additional information on a second, low-affinity binding event.

In SPR, when AMA1 was titrated against a constant level of immobilized RON2, a K_D of 13 ± 1 nM (Fig. 4C) was found. The reversed assay design of titrating the same RON2 species as used in MST experiments yielded a K_D of 38.3 ± 0.4 nM (Fig. 4D). The dissociation phase in the SPR data was best fit by a heterogeneous ligand model, indicative of the same second, low-affinity binding phase captured in (Fig. 4B and D).

This second binding event could be explained by the fact that the unlabeled RON2 peptide might be present in two forms in solution: one with and one without a disulfide bond, i.e. a cyclized and

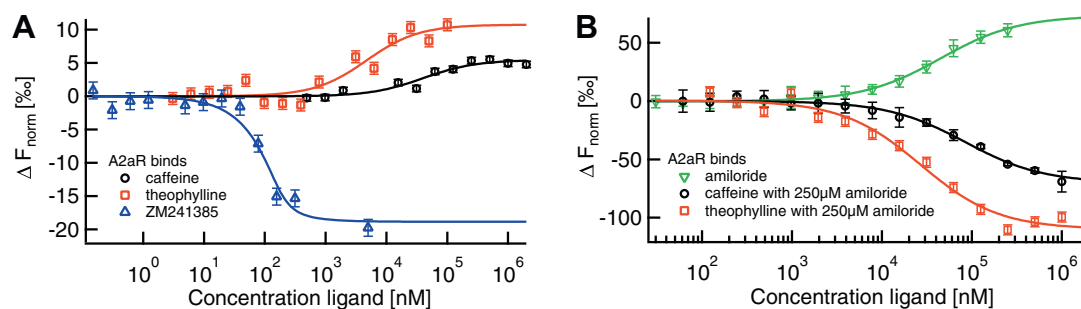


Fig. 6. Label-free MST for quantification of GPCR A2aR ligand binding. (A) Binding of the orthosteric antagonists caffeine ($K_D = 40 \pm 17$ μ M; black circles), theophylline ($K_D = 5 \pm 2$ μ M; red squares) and ZM241385 ($K_D \leq 43$ nM; blue triangles) to A2aR induces a comparably small change in thermophoretic mobility. (B) In contrast, amiloride-binding ($K_D = 52 \pm 7$ μ M; green inverted triangles) leads to a much larger MST signal amplitude, thus indicating conformational changes upon binding. Comparable signal amplitudes were obtained for the binding of caffeine and theophylline in presence of saturating amiloride concentrations, where the apparent affinities were decreased to 84 ± 10 μ M for caffeine and 27 ± 6 μ M for theophylline.

a linear form. As the second binding phase is not present in the reversed assay design (Fig. 4A), the labeled RON2 seems to be homogeneously cyclized.

An EC_{50} of $0.05 \pm 0.01 \mu\text{M}$ was obtained by FP experiments where AMA1 titration was performed against a constant concentration of labeled RON2 as illustrated in Fig. 4E. As expected, the reversed assay design, in which biotinylated RON2 was titrated against a constant level of labeled AMA1, yielded a much smaller FP signal amplitude (Fig. 4F). This is because the FP signal amplitude is largely based on the degree of binding-induced size change. Nevertheless, the observed EC_{50} also lies in the double-digit nanomolar range ($77.1 \pm 0.2 \text{ nM}$).

This AMA1-RON2 case study shows, firstly, that MST can yield K_D data very comparable to that obtained by other well-established biophysical methods, including FP as a solution-based and SPR as a solid-phase technique. All K_D s lie in the double digit nM-range. SPR yielded slightly higher affinities than MST. However, it has previously been described, that due to surface artifacts SPR tends to overestimate the affinity compared to other techniques [35]. Secondly, the experiments also exhibited the ability of MST to detect binding even when the assay was set up in a relatively less favorable manner in terms of size change upon binding: when the larger molecule AMA1 (66 kDa) was labeled and was held constant, titration of the smaller peptide (4.3 kDa) yielded a similar high-affinity binding phase as that obtained in the reverse titration. Thirdly, for this particular system, fluorescent labeling of either binding part-

ner did not adversely affect the binding event, i.e. did not give rise to a significant change in the K_D or assay artifacts such as non-specific binding to the fluorescent label. An interesting and more specific aspect of this system is the observation of a second binding phase that most likely reflects the presence of both, a cyclized and an linear form of the unlabeled RON2 peptide. However, difficulties associated with the production and handling of a fully-reduced/linear peptide precluded us from performing carefully controlled experiments comparing MST and SPR responses derived from fully-cyclized and fully-linear peptide counterparts; thus, the proposed explanation for the observed biphasic behavior remains speculative at this point. Overall, the AMA1-RON2 case study illustrates that MST is a sensitive and versatile biophysical technique for protein-peptide interaction studies. We note that while the RON2 peptide represents a good model system to study the interaction by a range of biophysical techniques without the added encumbrance brought about by the need to produce a second protein, these initial findings need to be further validated through a study using the intact protein pair.

4.3. Analyzing GPCR membrane proteins NTS1 and A2aR

Membrane proteins make up a third of the proteome and constitute the majority of drug targets. Their biological importance notwithstanding, they are extremely challenging to work with. G protein-coupled receptors (GPCR) are the largest class of mem-

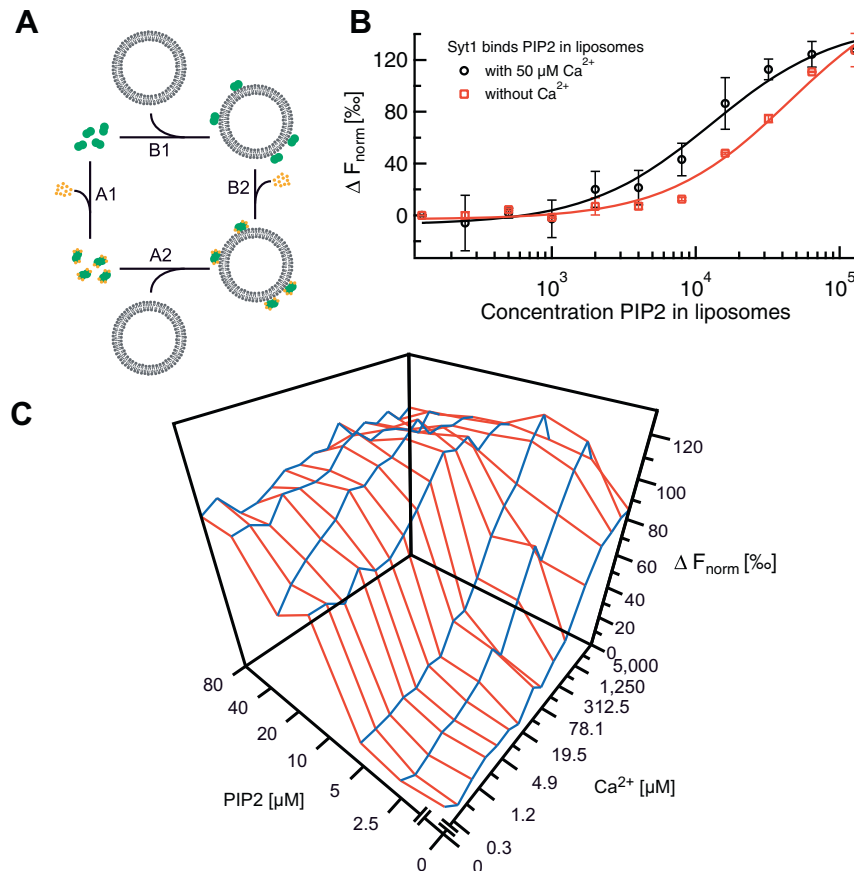


Fig. 7. Lipid and Ca^{2+} -binding to synaptotagmin-1 by MST. (A) Scheme of the binding interactions of synaptotagmin-1 (green) to Ca^{2+} (orange) and liposomes containing PIP2 (grey). Note the two possible binding pathways A1–A2 and B1–B2. (B) Membrane binding as a function of PIP2 incorporated into 100 nm-sized liposomes (5% PIP2 total lipid concentration). The apparent binding constants were 50 ± 10 and $13 \pm 3 \mu\text{M}$ PIP2 in the absence (red squares) and presence (black circles) of $50 \mu\text{M}$ Ca^{2+} , respectively (see [56] for details). (C) Cooperative Ca^{2+} and PIP2 binding to synaptotagmin-1. Ca^{2+} and PIP2 binding affinities could be determined by fitting the blue and red axis of the three dimensional MST curve, respectively. In the presence of saturating concentrations of PIP2, the apparent Ca^{2+} -binding constant decreased from ~ 220 to $3.3 \mu\text{M}$ Ca^{2+} . Accordingly, in the presence of saturating Ca^{2+} concentrations, the apparent PIP2 binding constant decreased from ~ 20 to $<2 \mu\text{M}$ PIP2. Figure adapted with permission from [56].

brane proteins encoded in the human genome [36] and share a common architecture (Fig. 5A): a bundle of seven transmembrane (7TM) helices connected by flexible loop regions. Even though structural data is still scarce it has become apparent that while the 7TM fold is conserved, there is remarkable structural diversity particularly at the extracellular ligand binding side of the proteins [37]. Clearly, a combination of structural knowledge, ligand docking [38,39] and fast and reliable technologies for measurement of ligand binding affinities are necessary and indispensable tools for next generation drug discovery efforts. Typically, ligand binding of GPCRs is studied by radioligand binding assays. However, the availability of radioligands is frequently a limiting factor. MST could provide a good alternative to determining the affinities of ligands without the need for radioligands.

Neurotensin receptor 1 (NTS1) is one of the few class A GPCRs that can be expressed in *E. coli* and purified in a functional, ligand-binding form [40]. Using MST we determined the binding affinity of the tridecapeptide ligand neurotensin for a fusion construct of NTS1, NTS1B [41]. Titrating NTS1B to AlexaFluor488-labeled neurotensin gave a K_D of 21 ± 20 nM (Fig. 5C). Due to limited amounts of NTS1B protein, saturation could not be reached, which affects the precision of the fit. Thus, we also used the reversed protocol yielding $K_D \leq 20$ nM (Fig. 5B). The intrinsic UV-fluorescence of NTS1B was exploited and the ligand was titrated, so that saturation was reached. The MST results are in good agreement with previous SPR data showing a dissociation constant of 1–2 nM for the binding of neurotensin to an NTS1 fusion construct, [42] while slightly lower affinities have previously been found for a fluorescently labeled (TAMRA) neurotensin derivative by fluorescence correlation spectroscopy ($K_D = 7 \pm 3$ nM, Harding, unpublished results), although other fluorophores did not affect the affinity ($K_D = 1.4$ nM for Cy5-neurotensin) [43]. K_D dependence on the choice of fluorophores has previously been observed for other

fluorescent ligand derivatives as well [44]. We also studied binding of a known inverse agonist, SR48692, to NTS1B and obtained a K_D of 15 ± 11 nM using label-free MST (Fig. 5D). This value is in good agreement with the affinities reported in literature obtained for NTS1 in membrane extracts ($K_D \sim 3$ –10 nM [45,46]). A competition assay in which we added SR48692 to receptor pre-saturated with neurotensin ($1 \mu\text{M}$) shifted the dissociation constant more than an order of magnitude ($K_D = 0.64 \pm 0.05 \mu\text{M}$; Fig. 5D), confirming specificity of binding and that both compounds compete for the same binding pocket (Fig. 5A). Non-specific binding was further excluded by performing a control experiment with denatured receptor. Interestingly, binding of the agonist neurotensin has an opposite effect on the thermophoretic depletion compared to binding of the inverse agonist SR48692. This could be due to the different structures of the binding partners, however, considering the small size of both ligands (<2 kDa) compared to the receptor (100 kDa), it could even reflect the different structural effects the agonist and the inverse agonist have on the receptor, with neurotensin promoting conformational changes, while SR48692 locks the receptor in an inactive conformation, giving rise to differences in the hydration shell and thus in the thermophoretic properties of the complex.

As a second type of GPCR, we tested the adenosine A2A receptor (A2aR) expressed and purified as a fusion with apocytochrome b562RIL as previously described [47]. We used label-free MST to analyze the binding of three orthosteric antagonists, caffeine, theophylline and ZM241385, and one allosteric ligand, amiloride. The affinities for these ligands have been previously determined as $K_i = 18 \mu\text{M}$ for caffeine, [48] $K_i = 14 \mu\text{M}$ for theophylline, [49,50] $K_i = 1.2$ nM for ZM241385, [51] and $K_i = 12 \mu\text{M}$ for amiloride (Katritch et al., manuscript in preparation). These K_i values are based on heterologous competition of radioligands and inhibition of biological function and can thus only give an approximate indication

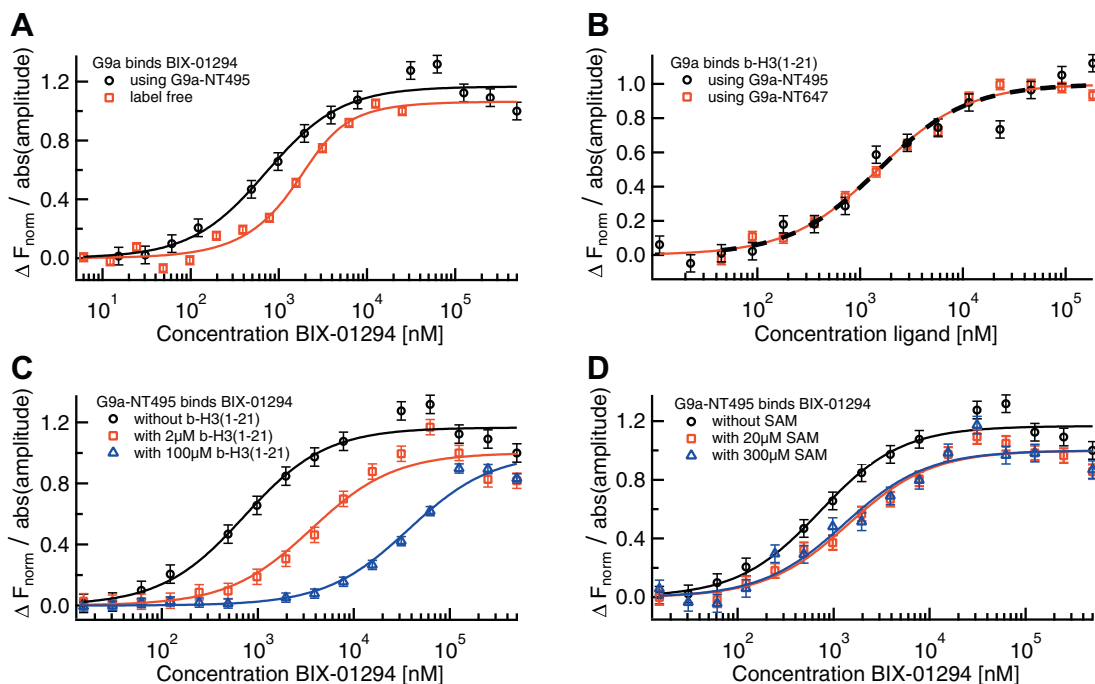


Fig. 8. MST analysis of small molecule binding to G9a. (A) The specific interaction of the small molecule BIX-01294 to G9a was quantified via label-free MST (red squares) as well as standard MST with a NT495-label (black circles), where the results were in excellent agreement with each other ($K_D = 0.7 \pm 0.2 \mu\text{M}$ for both) and confirmed previously reported ITC measurements. (B) The affinity of the peptide b-H3(1-21) to both G9a-NT495 (black circles) and G9a-NT647 (red squares) was quantified via MST yielding identical K_D s ($1.5 \pm 0.4 \mu\text{M}$ for G9a-NT495 and $1.5 \pm 0.2 \mu\text{M}$ for G9a-NT647). (C) Pre-incubating G9a with b-H3(1-21) right-shifted the K_D for BIX-01294 from $0.7 \mu\text{M}$ to $4 \pm 1 \mu\text{M}$ in presence of $2 \mu\text{M}$ (red squares) and to $37 \pm 7 \mu\text{M}$ in presence of $100 \mu\text{M}$ of the peptide (blue triangles) suggesting competition at the histone binding site. (D) In contrast, addition of SAM in concentrations of $20 \mu\text{M}$ ($K_D = 1.4 \pm 0.3 \mu\text{M}$, red squares) and $300 \mu\text{M}$ ($K_D = 1.2 \pm 0.4 \mu\text{M}$, blue triangles) only had a minor effect on the apparent K_D of BIX-01294 to G9a.

of the K_D determined via a direct, biophysical measurement like MST. However, we obtained K_D s that were in good accordance: $40 \pm 17 \mu\text{M}$ for caffeine, $5 \pm 2 \mu\text{M}$ for theophylline, $\leq 43 \text{ nM}$ for ZM241385 and $52 \pm 7 \mu\text{M}$ (Fig. 6A) for amiloride (Fig. 6B). Amiloride was not used at concentrations above $250 \mu\text{M}$ due to solubility problems. This affects the precision of the fit. The signal amplitude for the three orthosteric ligands was low. In contrast amiloride, an allosteric ligand that binds to a different site from caffeine and theophylline [51], induced a strong change in thermophoretic mobility, shown in Fig. 6B. Allosteric ligands are known to alter receptor activity by inducing conformational changes [52]. As amiloride is similar in size to the other tested ligands, the much stronger change in thermophoretic mobility upon binding is likely to be caused by this significant conformational change leading to a reorientation of the receptor's hydration shell. Addition of caffeine and theophylline in presence of saturating amounts of amiloride also had a strong but opposite effect on thermophoresis, indicating non-competitive binding that also produced significant conformational change. Apparent K_D s of $84 \pm 10 \mu\text{M}$ for caffeine and $27 \pm 6 \mu\text{M}$ for theophylline were derived. Hence, label-free MST can also be used to investigate allosteric binding in GPCRs.

This study demonstrates that MST can be used as a quick, sensitive tool to measure binding affinities for difficult systems such as GPCRs which suffer from low expression yields and protein instability. In addition to the pharmaceutical importance of knowing binding affinities, biophysical studies of membrane proteins often require truncations or addition of fusion partners to improve stability and expression, or mutations to facilitate labeling for various techniques. Being able to easily assess the effect of these modifications on the ligand binding capacity to verify the validity of the approach used is invaluable. In comparison to most commonly used techniques, the low sample requirements and the simplicity of the mix-and-read protocol make MST more suited for such routine binding affinity analyses. Compared to alternative techniques such as SPR, MST suffers less from the need for rigorous buffer controls, which can be problematic for membrane proteins in detergent where the exact protein concentration and especially the detergent concentration can be difficult to determine.

4.4. Cooperative binding within the ternary complex: synaptotagmin

Synaptotagmin-1 (syt1) is the main Ca^{2+} -sensor for fast calcium-regulated neurotransmitter release [53]. It binds five Ca^{2+} -ions with affinities ranging from $50 \mu\text{M}$ to 10 mM as measured by NMR and ITC [54,55]. Ca^{2+} -binding was reproduced by MST using hydrophobic capillaries and 2.5 mg/ml BSA in order to overcome association of syt1 with the capillaries. An apparent binding affinity of $210\text{--}230 \mu\text{M}$ was determined by MST [56,57].

Syt1 also binds to membranes containing anionic phospholipids such as phosphatidylinositol 4,5-bisphosphate (PIP2) and this binding is important for its function (Fig. 7A). Binding to PIP2 occurs already in absence of Ca^{2+} as shown by membrane binding co-sedimentation assays in density gradients with a cytoplasmic fragment of syt1 and artificial liposomes [58]. However, precise quantification of membrane binding is limited because co-sedimentation assays do not report binding under equilibrium conditions. This problem was overcome in a recent study where Förster resonance energy transfer (FRET) was measured from syt1 labeled with a donor fluorophore to liposomes tagged with an acceptor fluorophore [59]. Since close proximity between the two fluorophores is required for FRET (typically well below 5 nm), the results of FRET-based assays fundamentally depend on the labeling positions and binding orientations of syt1 to the membrane.

MST does not suffer from these limitations and allows to measure membrane binding under equilibrium conditions irrespective

of the precise labeling of syt1 (Fig. 7B). Indeed, binding of the labeled syt1 to 100 nm -sized PIP2-containing liposomes resulted in a clear change of the MST signal. As apparent from Fig. 7B, the binding strength of syt1 to PIP2-containing liposomes was ~ 5 -fold enhanced in the presence of Ca^{2+} with readily distinguishable K_D -values ($50 \pm 10 \mu\text{M}$ in the absence and $13 \pm 3 \mu\text{M}$ in the presence of Ca^{2+}). The addition of Ca^{2+} was the only change in an otherwise identical MST assay design. Therefore, the change in K_D most likely reflects the influence of Ca^{2+} on the K_D . Similar cooperative Ca^{2+} and PIP2 binding was previously observed with co-sedimentation assays and FRET [55,58]. However, all these assays (including the MST assay shown in Fig. 7B) suffer from the limitation that Ca^{2+} -binding is not directly measured, but only inferred from binding to the liposomes. Thus, in these assays, Ca^{2+} and PIP2 binding cooperativity can only be measured in case syt1 first binds to (sufficient) Ca^{2+} prior to membrane binding (pathway A2–A2 in Fig. 7A) and cannot be distinguished in case syt1 already binds to PIP2 in absence of Ca^{2+} (pathway B1–B2).

In order to measure binding of Ca^{2+} to syt1 under saturating conditions of PIP2, we adapted our MST assay and added PIP2 not incorporated into liposomes but directly to the capillaries. Due to the high charge of PIP2 (between -3 and -5) [59] even brain-isolated PIP2 (i.e. with long acyl chains) is water soluble up to several mM [60] and short chain fatty acid analogs (such as C8-PIP2) have even higher solubilities and micelle concentrations. By direct addition of PIP2 to the capillaries, the full multidimensional binding spectrum of Ca^{2+} and PIP2 could be determined with a single set of MST experiments (Fig. 7C). In the presence of saturating concentrations of PIP2 ($>10 \mu\text{M}$), the apparent binding affinity for Ca^{2+} was increased more than 40-fold [56]. This interplay between Ca^{2+} , PIP2 and syt1 has profound implications for the mechanisms of neurotransmitter release.

4.5. Competitive small molecule binding to histone methyltransferase G9a

The histone methyltransferase (HMT) G9a plays a crucial role in epigenetic regulation and has been implicated in cancer [61]. Thus, G9a inhibitors are expected to exert synergistic effects in epigenetic cancer therapy. A potent new G9a modulator is UNC0321, [62] a BIX-01294 analog. The latter was originally identified as a G9a inhibitor with an IC_{50} ranging from sub- μM (Thioglo assay and AlphaScreen assay) [63] to low μM (DELFI format) [64]. Through an antibody-based time-resolved fluorescence assay, BIX-01294 was found to be the first non-peptidomimetic compound that inhibited G9a in a non-competitive mode versus the methyl donor, S-adenosyl-L-methionine (SAM) [64]. Furthermore, it was confirmed by co-crystallization with G9a-like protein that BIX-01294 acted as a competitive inhibitor for the peptide substrate [65]. Despite the availability of several different assay formats to measure HMT activity [66], direct or competition binding assays for HMTs and their potential inhibitors have been largely limited to FP, ITC or differential scanning fluorimetry (DSF) experiments [63]. Thus, MST could provide further information on the G9a system by assessing the direct interaction between the protein and BIX-01294, the protein and its cognate substrate peptide, and the mode of action of BIX-01294 versus both the peptide and the cofactor.

We firstly evaluated the affinity of BIX-01294 for G9a via MST. We obtained a K_D of $0.7 \pm 0.2 \mu\text{M}$ in both the label-free approach and using NT495-labeled G9a (Fig. 8A), which demonstrates, that the label did not have an influence on the binding. The values are in the same general range established by the enzymatic IC_{50} values for the compound (reported in multiple papers and summarized in Liu et al. 2009 [63] to be between 1.7 and $1.9 \mu\text{M}$) and the ITC-derived K_D of $0.13 \mu\text{M}$ (reported in Liu et al. 2009 [63]). This further

validates both of our MST assays and showcases the ability of MST to detect binding interactions between proteins (G9a; 32.6 kDa) and small molecules (BIX-01294; 490.6 Da) in spite of the extreme size ratio. We subsequently studied the binding of G9a, labeled with either NT495 or NT647, to its cognate peptide substrate, a biotinylated histone peptide (b-H3(1–21)). Both labeled G9a versions yielded identical K_D s, with the former giving a K_D of $1.5 \pm 0.4 \mu\text{M}$ and the latter a K_D of $1.5 \pm 0.2 \mu\text{M}$ (Fig. 8B). These values are in close agreement with the K_M s reported for similar peptide substrates against mammalian G9a [67]. Next, we investigated the mode of inhibitory action of BIX-01294 with respect to either the peptide substrate b-H3(1–21) or the SAM cofactor. Prior to BIX-01294 titration, each component was pre-incubated with NT495-G9a at either a concentration near its respective K_D or at saturating amounts. The results were compared to BIX-01294-G9a binding in absence of the components. As expected, the apparent K_D for BIX-01294 against G9a was reduced upon increasing concentrations of b-H3(1–21), suggesting that the compound was competing with the peptide for binding to the histone binding site (Fig. 8C). In contrast, the addition of increasing concentrations of SAM had little effect on the compound's affinity for G9a (Fig. 8D), indicating that the compound was not competing with SAM. These results are in good agreement with previous enzyme kinetic [64] and co-crystallization studies [65] aimed at elucidating the ligands' mode of action. In summary, the G9a case study demonstrates that MST not only provides enough sensitivity to quantify protein-small molecule interactions but also yields binding affinities that are comparable with those obtained from well-established methods, such as ITC. Moreover, MST has clearly been shown to be able to offer insight on the mode of action of small molecules versus the target protein's native substrate or cofactor.

5. Conclusion

We successfully used MST to quantify the interaction of different proteins with a variety of binding partners. In all cases, the determined K_D s were in agreement with results obtained by other, well-established biophysical techniques for protein interaction analysis. As MST is a capillary based format and binding-induced changes in thermophoretic mobility are detected via fluorescence, μl -volumes and low nM-concentrations are sufficient. This results in small sample consumption and allows direct quantification of high affinity protein dimerization as in the case of Grb2. The measured K_D of $0.7 \mu\text{M}$ lies well below the minimally usable, μM -concentrations for ITC [8]. The monomeric state and monomer-dimer-transition of Grb2 would not be captured and quantification via ITC would not be possible.

The free solution approach of MST avoids immobilization procedures and possible surface artifacts. Labeling artifacts can be excluded entirely by using label-free MST, which only requires a sufficient intrinsic UV-fluorescence of the protein binding partner. In standard MST, the use of different fluorescent labels provides a means of excluding labeling effects as demonstrated for G9a-binding to b-H3(1–21). Additionally, the fluorescent label can be attached to either of the binding partners to test for possible label-dependent changes of the binding behavior as shown in the AMA1-RON2 experiment. This reversibility in assay design results from the fact that thermophoresis is sensitive to various molecular properties and thus, MST, in contrast to DLS, FP and SPR, does not rely on size changes alone and is not limited by the molecular weight ratio of the binding partners. The strongly preferred assay design for SPR and FP, on the other hand, is to measure interactions by titrating the larger binding partner to a constant amount of the smaller one. However, labeling or immobilizing the smaller ligand bears a higher risk of changing its properties, as the label or anchor

is large compared to the ligand. For MST, the reversed assay design of measuring the binding of an unlabeled small molecule to a much bigger, fluorescent protein works equally well, as illustrated by the G9a-BIX-01294 interaction analysis and the label-free GPCR binding studies.

The solution, in which the MST experiment is performed, can be chosen freely to meet the sample's specific buffer requirements. This is invaluable when working with membrane proteins like GPCRs, which typically require strictly optimized buffer conditions and detergents to be stabilized in solution. In addition to buffers with all kinds of additives, proteins embedded in liposomes can be analyzed via MST as well, as demonstrated by the syt1-measurement. MST can also be performed in complex bioliquids such as cell lysate. When combined with the use of fluorescent fusion proteins, as illustrated in the TEM1-BLIP analysis, the fusion protein does not even have to be purified prior to the measurement, but the crude cell extract can directly be used. For the TEM1-BLIP system, the affinities in buffer and lysate were in good agreement. Discrepancies can, however, appear between simple buffers and complex fluids [17]. This demonstrates the importance of analyzing protein interaction in its natural, crowded environment. Apart from cell lysate, MST can also be performed in untreated human blood serum, allowing direct quantification of affinity and concentration of antibodies as disease related biomarkers [68].

In addition, complex binding modes are readily accessible via MST, e.g. competition in the binding of BIX-01294 and b-H3(1–21) to G9a. Furthermore, the cooperative binding of PIP2 and Ca^{2+} to syt1 was quantified via MST. In previous assays, cooperativity had been inferred from Ca^{2+} binding to membranes. Thus, liposomes with low PIP2 content were used, to which syt1 only binds in presence of Ca^{2+} . MST with soluble PIP2 allowed to measure under saturating PIP2 conditions. As a result, PIP2 binding in absence of Ca^{2+} was captured as well, revealing a much higher cooperativity. Due to the low solubility and micelle concentration of PIP2, it would not be possible to perform a comparable assay with a technique requiring higher sample concentrations than MST.

MST provides reliable quantitative information on protein interaction based on a simple protocol, making measurements fast and efficient with low sample consumption. It is sensitive to binding-induced changes in several molecular properties and flexible in assay design. Taken together, this makes MST a highly applicable tool for protein interaction analysis, even for challenging biological systems.

Conflict of interest statement

Ana Lazic is an employee of NanoTemper Technologies Inc., California, USA. Stefan Duhr and Philipp Baaske are founders, Moran Jerabek-Willemsen is an employee of the LMU spin-off company NanoTemper Technologies GmbH, which provides services and devices based on MST.

Acknowledgements

The authors thank Dr. Alan Goddard and Eleanor Healey for making AlexaFluor488-neurotensin. We also thank Dr. Masoud Vedadi (University of Toronto) for provision of the G9a protein. Dr. Mohammed Yousef (Bio-Rad Laboratories) is thanked for his expert advice during the initial chip set up on the ProteOn system. In addition Peter Röttgermann and Christof Mast are thanked for help with figures. The work of S.A.I.S. and D.B. was supported by the Nano Initiative Munich (NIM), the Center for NanoScience (CeNS), the Ludwig Maximilians Universität München (LMU) Initiative Functional Nanosystems and the Deutsche Forschungsgemeinschaft. The work by J.S.J. and I.K. was supported by the

NIH Common Fund's Structural Biology Program Grant P50 GM073197. The work of P.M.D. and A.W. was supported by the Medical Research Council (MRC) grant G0900076 to A.W. The work by P.S., W.A.L., and A.S. was supported in part by the Intramural Research Program of the National Institute of Allergy and Infectious Diseases and the National Center for Advancing Translational Sciences, US National Institutes of Health.

References

- [1] C.-C. Lin, F.A. Melo, R. Ghosh, K.M. Suen, L.J. Stagg, J. Kirkpatrick, S.T. Arold, Z. Ahmed, J.E. Ladbury, *Cell* 149 (2012) 1514–1524.
- [2] S. Besteiro, A. Michelin, J. Poncet, J.-F. Dubremetz, M. Lebrun, *PLoS Pathog.* 5 (2009) e1000309.
- [3] P. Srinivasan, W.L. Beatty, A. Diouf, R. Herrera, X. Ambroggio, J.K. Moch, J.S. Tyler, D.L. Narum, S.K. Pierce, J.C. Boothroyd, J.D. Haynes, L.H. Miller, *Proc. Natl. Acad. Sci. USA* 108 (2011) 13275–13280.
- [4] M.M. Garner, A. Revzin, *Nucl. Acids Res.* 9 (1981) 3047–3060.
- [5] E. Engvall, P. Perlmann, *Immunochemistry* 8 (1971) 871–874.
- [6] L.M. Hellman, M.G. Fried, *Nat. Protoc.* 2 (2007) 1849–1861.
- [7] Thomas Wiseman, Samuel Williston, John F. Brandts, Lung-Nan Lin, *Anal. Biochem.* 179 (1989) 131–137.
- [8] S. Leavitt, E. Freire, *Curr. Opin. Struct. Biol.* 11 (2001) 560–566.
- [9] J.E. Ladbury, B.Z. Chowdhry, *Chem. Biol.* 3 (1996) 791–801.
- [10] S. Fujime, S. Ishiwata, *J. Mol. Biol.* 62 (1971) 251–265.
- [11] A.D. Hanlon, M.I. Larkin, R.M. Reddick, *Biophys. J.* 98 (2010) 297–304.
- [12] W.B. Dandliker, G.A. Feigen, *Biochem. Biophys. Res. Commun.* 5 (1961) 299–304.
- [13] W.A. Lea, A. Simeonov, *Expert Opin. Drug Discov.* 6 (2011) 17–32.
- [14] P. Schuck, *Annu. Rev. Biophys. Biomol. Struct.* 26 (1997) 541–566.
- [15] B. Nguyen, F.A. Tanius, W.D. Wilson, *Methods* 42 (2007) 150–161.
- [16] M.M. Baksh, A.K. Kussrow, M. Mileni, M.G. Finn, D.J. Bornhop, *Nat. Biotechnol.* 29 (2011) 357–360.
- [17] C.J. Wienken, P. Baaske, U. Rothbauer, D. Braun, S. Duhr, *Nat. Commun.* 1 (2010) 100.
- [18] S.A.I. Seidel, C.J. Wienken, S. Geissler, M. Jerabek-Willemsen, S. Duhr, A. Reiter, D. Trauner, D. Braun, P. Baaske, *Angew. Chem. Int. Ed. Engl.* 51 (2012) 10656–10659.
- [19] S. Duhr, D. Braun, *Proc. Natl. Acad. Sci. USA* 103 (2006) 19678–19682.
- [20] Y. Kawahashi, N. Doi, H. Takashima, C. Tsuda, Y. Oishi, R. Oyama, M. Yonezawa, E. Miyamoto-Sato, H. Yanagawa, *Proteomics* 3 (2003) 1236–1243.
- [21] T. Hohsaka, R. Abe, K. Shiraga, M. Sisido, *Nucl. Acids Res. (Suppl.)* (2003) 271–272.
- [22] R. Serwa, I. Wilkening, G. Del Signore, M. Muhlberg, I. Clausnitzer, C. Weise, M. Gerrits, C.P.R. Hackenberger, *Angew. Chem. Int. Ed. Engl.* 48 (2009) 8234–8239.
- [23] C. Ludwig, *Sitzungsber Akad Wiss, Wien Math-Naturwiss Kl.* (1856) 539.
- [24] D. Ross, M. Gaitan, L.E. Locascio, *Anal. Chem.* 73 (2001) 4117–4123.
- [25] C.A. Royer, *Chem. Rev.* 106 (2006) 1769–1784.
- [26] S. Albeck, G. Schreiber, *Biochemistry* 38 (1999) 11–21.
- [27] D. Reichmann, M. Cohen, R. Abramovich, O. Dym, D. Lim, N.C.J. Strynadka, G. Schreiber, *J. Mol. Biol.* 365 (2007) 663–679.
- [28] J. Wang, T. Palzkill, D.-C. Chow, *J. Biol. Chem.* 284 (2009) 595–609.
- [29] Y. Phillip, E. Sherman, G. Haran, G. Schreiber, *Biophys. J.* 97 (2009) 875–885.
- [30] D. Reichmann, O. Rahat, S. Albeck, R. Meged, O. Dym, G. Schreiber, *Proc. Natl. Acad. Sci. USA* 102 (2005) 57–62.
- [31] N. Li, A. Batzer, R. Daly, V. Yajnik, E. Skolnik, P. Chardin, D. Bar-Sagi, B. Margolis, J. Schlessinger, *Nature* 363 (1993) 85–88.
- [32] M. Lovatt, A. Cooper, P. Camilleri, *Eur. Biophys. J.* 24 (1996) 354–357.
- [33] J.S. Tyler, J.C. Boothroyd, *PLoS Pathog.* 7 (2011) e1001282.
- [34] M. Lamarque, S. Besteiro, J. Papoin, M. Roques, B. Vulliez-Le Normand, J. Morlon-Guyot, J.-F. Dubremetz, S. Fauquenoy, S. Tomavo, B.W. Faber, C.H. Kocken, A.W. Thomas, M.J. Boulanger, G.A. Bentley, M. Lebrun, *PLoS Pathog.* 7 (2011) e1001276.
- [35] M.C. Jecklin, S. Schauer, C.E. Dumelin, R. Zenobi, *J. Mol. Recognit.* 22 (2009) 319–329.
- [36] R. Fredriksson, H.B. Schioth, *Mol. Pharmacol.* 67 (2005) 1414–1425.
- [37] V. Katritch, V. Cherezov, R.C. Stevens, *Trends Pharmacol. Sci.* 33 (2012) 17–27.
- [38] M. Michino, E. Abola, C.L.3. Brooks, J.S. Dixon, J. Moulton, R.C. Stevens, *Nat. Rev. Drug Discov.* 8 (2009) 455–463.
- [39] I. Kufareva, M. Rueda, V. Katritch, R.C. Stevens, R. Abagyan, Status of GPCR modeling and docking as reflected by community-wide GPCR Dock 2010 assessment, *Structure* 19 (2011) 1108–1126.
- [40] H. Attrill, P.J. Harding, E. Smith, S. Ross, A. Watts, *Protein Expression Purif.* 64 (2009) 32–38.
- [41] J.F. White, L.B. Trinh, J. Shiloach, R. Grishammer, *FEBS Lett.* 564 (2004) 289–293.
- [42] P.J. Harding, H. Attrill, S. Ross, J.R. Koeppel, A.N. Kapanidis, A. Watts, *Biochem. Soc. Trans.* 35 (2007) 760–763.
- [43] Y. Fang, Y. Hong, B. Webb, J. Lahiri, *MRS Bull.* 31 (2006) 541–545.
- [44] A. Beaudet, D. Nouel, T. Stroth, F. Vandenbulcke, C. Dal-Farra, J.P. Vincent, *Braz. J. Med. Biol. Res.* 31 (1998) 1479–1489.
- [45] D. Gully, M. Canton, R. Boigegrain, F. Jeanjean, J.C. Molimard, M. Poncelet, C. Gueudet, M. Heulme, R. Leyris, A. Brouard, *Proc. Natl. Acad. Sci. USA* 90 (1993) 65–69.
- [46] C. Labbe-Jullie, J.M. Botto, M.V. Mas, J. Chabry, J. Mazella, J.P. Vincent, D. Gully, J.P. Maffrand, P. Kitabgi, *Mol. Pharmacol.* 47 (1995) 1050–1056.
- [47] E. Chun, A.A. Thompson, W. Liu, C.B. Roth, M.T. Griffith, V. Katritch, J. Kunken, F. Xu, V. Cherezov, M.A. Hanson, R.C. Stevens, *Structure* 20 (2012) 967–976.
- [48] K. Ohshita, H. Ishiyama, K. Oyanagi, H. Nakata, J. Kobayashi, *Bioorg. Med. Chem.* 15 (2007) 3235–3240.
- [49] N.P. Peet, G.A. Dickerson, A.H. Abdallah, J.W. Daly, D. Ukena, *J. Med. Chem.* 31 (1988) 2034–2039.
- [50] M.T. Shamim, D. Ukena, W.L. Padgett, J.W. Daly, *J. Med. Chem.* 32 (1989) 1231–1237.
- [51] W. Liu, E. Chun, A.A. Thompson, P. Chubukov, F. Xu, V. Katritch, G.W. Han, C.B. Roth, L.H. Heitman, A.P. IJzerman, V. Cherezov, R.C. Stevens, *Science* 337 (2012) 232–236.
- [52] A. Christopoulos, *Nat. Rev. Drug Discov.* 1 (2002) 198–210.
- [53] E.R. Chapman, *Annu. Rev. Biochem.* 77 (2008) 615–641.
- [54] R. Fernandez-Chacon, A. Konigstorfer, S.H. Gerber, J. Garcia, M.F. Matos, C.F. Stevens, N. Brose, J. Rizo, C. Rosenmund, T.C. Sudhof, *Nature* 410 (2001) 41–49.
- [55] A. Radhakrishnan, A. Stein, R. Jahn, D. Fasshauer, *J. Biol. Chem.* 284 (2009) 25749–25760.
- [56] G. van den Bogaart, K. Meyenberg, U. Diederichsen, R. Jahn, *J. Biol. Chem.* 287 (2012) 16447–16453.
- [57] G. van den Bogaart, S. Thutupalli, J.H. Risselada, K. Meyenberg, M. Holt, D. Riedel, U. Diederichsen, S. Herminghaus, H. Grubmuller, R. Jahn, *Nat. Struct. Mol. Biol.* 18 (2011) 805–812.
- [58] L. Li, O.-H. Shin, J.-S. Rhee, D. Arac, J.-C. Rah, J. Rizo, T. Sudhof, C. Rosenmund, *J. Biol. Chem.* 281 (2006) 15845–15852.
- [59] S. McLaughlin, J. Wang, A. Gambhir, D. Murray, *Annu. Rev. Biophys. Biomol. Struct.* 31 (2002) 151–175.
- [60] A. Chu, E. Stefani, *J. Biol. Chem.* 266 (1991) 7699–7705.
- [61] Y. Shinkai, M. Tachibana, *Genes Dev.* 25 (2011) 781–788.
- [62] F. Liu, X. Chen, A. Allali-Hassani, A.M. Quinn, G.A. Wasney, A. Dong, G. Senisterra, I. Chau, A. Siarheyeva, J.L. Norris, D.B. Kireev, A. Jadhav, J.M. Herold, W.P. Janzen, C.H. Arrowsmith, S.V. Frye, P.J. Brown, A. Simeonov, M. Vedadi, J. Jin, *J. Med. Chem.* 53 (2010) 5844–5857.
- [63] F. Liu, X. Chen, A. Allali-Hassani, A.M. Quinn, G.A. Wasney, A. Dong, D. Barsyte, I. Koziarzdzki, G. Senisterra, I. Chau, A. Siarheyeva, D.B. Kireev, A. Jadhav, J.M. Herold, S.V. Frye, C.H. Arrowsmith, P.J. Brown, A. Simeonov, M. Vedadi, J. Jin, *J. Med. Chem.* 52 (2009) 7950–7953.
- [64] S. Kubicek, R.J. O'Sullivan, E.M. August, E.R. Hickey, Q. Zhang, M.L. Teodoro, S. Rea, K. Mechtler, J.A. Kowalski, C.A. Homon, T.A. Kelly, T. Jenuwein, *Mol. Cell* 25 (2007) 473–481.
- [65] Y. Chang, X. Zhang, J.R. Horton, A.K. Upadhyay, A. Spannhoff, J. Liu, J.P. Snyder, M.T. Bedford, X. Cheng, *Nat. Struct. Mol. Biol.* 16 (2009) 312–317.
- [66] A.M. Quinn, A. Simeonov, *Curr. Chem. Genomics* 5 (2011) 95–105.
- [67] D. Patnaik, H.G. Chin, P.O. Esteve, J. Benner, S.E. Jacobsen, S. Pradhan, *J. Biol. Chem.* 279 (2004) 53248–53258.
- [68] S. Lippok, S.A.I. Seidel, S. Duhr, K. Uhland, H.-P. Holthoff, D. Jenne, D. Braun, *Anal. Chem.* 84 (2012) 3523–3530.
- [69] V. Paquet, M. Roy, L. Pedro, N. Gauthier, A. Labonte, A. Rodenbrock, G. Pinard, L. Beaudet, R. Rodriguez-Suarez, AlphaLISA G9a Histone H3-Lysine N-methyltransferase Assay, Technical Note AlphaLISA #2, PerkinElmer, <www.perkinelmer.com> (2010).
- [70] M. Roy, V. Paquet, L. Pedro, N. Gauthier, A. Labonte, A. Rodenbrock, G. Pinard, L. Beaudet, R. Rodriguez-Suarez, LANCE Ultra G9a Histone H3-Lysine N-methyltransferase Assay, Technical Note U-TRF #36, PerkinElmer <www.perkinelmer.com> (2010).
- [71] P. Kitabgi, *Peptides* 27 (2006) 2461–2468.

Label-Free Microscale Thermophoresis Discriminates Sites and Affinity of Protein–Ligand Binding**

Susanne A. I. Seidel, Christoph J. Wienken, Sandra Geissler, Moran Jerabek-Willemsen, Stefan Duhr, Alwin Reiter, Dirk Trauner, Dieter Braun, and Philipp Baaske*

The analysis of protein binding to small molecules, nucleic acids, and ions not only gives fundamental insights into cellular processes but also paves the way towards improved disease diagnosis and treatment. Herein, we report on a novel label- and preparation-free method to quantify biomolecular interactions and gather additional information on the binding event. The technique is based on the recently developed microscale thermophoresis (MST).

Several approaches to explore biomolecule binding require fluorescent or radioactive labeling.^[1] Other methods, such as surface plasmon resonance (SPR) and quartz crystal microbalance (QCM), rely on surface immobilization.^[2] But the coupling of a protein to a tag or surface may alter or even inhibit the binding event.^[3] Furthermore, the coupling reactions and associated clean-up steps are time consuming and, for some biomolecules, difficult to optimize. This is particularly true for those protein preparations that are typically low in yield or less stable in solution, like membrane receptor systems. A recent solution-based label-free method is the kinetic capillary electrophoresis with mass spectrometry (KCE-MS), which only requires that the binding partners be separable by electrophoresis.^[4] Another method is back-scattering interferometry (BSI), which is limited to proteins displaying detectable changes in the refractive index (RI) upon binding and displays remarkable sensitivity for high-

affinity interactions.^[5] So far, most genuinely label-free studies of protein–ligand interactions have been performed using isothermal titration calorimetry (ITC). ITC provides direct access to the thermodynamic parameters of a binding event but requires considerably high protein concentrations to gain a measurable signal.^[6]

In contrast MST is characterized by low sample consumption. As the name already implies, it is based on thermophoresis, the directed movement of particles in a temperature gradient.^[8,9] A temperature difference ΔT in space leads to a depletion of the solvated biomolecules in the region of elevated temperature, quantified by the Soret coefficient S_T : $c_{\text{hot}}/c_{\text{cold}} = \exp(-S_T \Delta T)$.

This thermophoretic depletion depends on the interface between the molecules and the solvent.^[9] Under constant buffer conditions, thermophoresis probes the size, charge, and solvation entropy of the molecules. The thermophoresis of a protein typically differs significantly from the thermophoresis of a protein–ligand complex as a result of binding-induced changes in size, charge, and solvation energy.^[10,11] Even if a binding event does not significantly change the size or charge of a protein, MST can still detect the binding owing to binding-induced changes in the molecules' solvation entropy. Glutamate binding to ionotropic glutamate receptors (iGluRs), for instance, causes a conformational change observable by MST. Binding leads to a closure of the protein's clamshell-like ligand-binding domain (LBD), inducing receptor activation (Figure 1 B).^[12,13]

The MST setup consists of a fluorescence microscope with a 1480 nm infrared laser coupled into its optical path (Figure 1 A). The laser is focused into the capillaries containing the sample, where it creates a temperature gradient. Up to now the thermophoretic movement has been detected using a fluorescent tag attached to one of the binding partners (standard MST). To avoid the possible drawbacks of labeling we propose the use of intrinsic protein fluorescence. It is mostly caused by the aromatic amino acids phenylalanine, tyrosine, and tryptophan (Trp), with the latter being the dominant intrinsic fluorophore. We used an UV-light-emitting diode for fluorescence excitation and a photomultiplier tube (PMT) to record emission. Especially in the short-wavelength regime around 350 nm used for label-free MST, photon-counting PMTs are more sensitive than the CCD cameras employed for standard MST.

Examples of measured fluorescence signals from label-free MST are shown in Figure 1 B. After the temperature has increased, the fluorescence initially changes rapidly as an inherent property of the fluorophore. This “temperature jump”, which occurs on a timescale of 100 ms, can easily be

[*] S. Geissler, Dr. M. Jerabek-Willemsen, Dr. S. Duhr, Dr. P. Baaske
NanoTemper Technologies GmbH
Flössergasse 4, 81369 Munich (Germany)
E-mail: philipp.baaske@nanotemper.de
Homepage: <http://www.nanotemper.de>

S. A. I. Seidel, Dr. C. J. Wienken, Prof. D. Braun
Systems Biophysics and Functional Nanosystems
Ludwig-Maximilians-Universität München
Amalienstrasse 54, 80799 Munich (Germany)

A. Reiter, Prof. D. Trauner
Department Chemie und Biochemie and Center of Integrated
Protein Science, Ludwig-Maximilians-Universität München
Butenandtstrasse 5–13, Haus F, 81377 Munich (Germany)

[**] We thank the Nanosystems Initiative Munich (NIM) and the Zentrales Innovationsprogramm Mittelstand (ZIM) for financial support of this research. This work was supported by the Federal Ministry of Education and Research (Germany), the Center for NanoScience (CeNS), Center for Integrated Protein Science Munich (CIPSM), and a joint grant from the Deutsche Forschungsgemeinschaft (DFG) and FOR 1279 (Protein Switches as Optogenetic Tools)..



Supporting information for this article is available on the WWW under <http://dx.doi.org/10.1002/anie.201204268>.



Re-use of this article is permitted in accordance with the Terms and Conditions set out at <http://angewandte.org/open>.

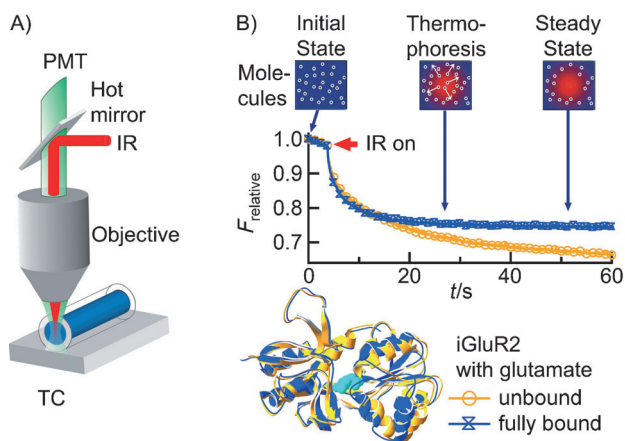


Figure 1. Label-free microscale thermophoresis. A) A capillary containing a protein sample with intrinsic tryptophan fluorescence is placed on a thermoelectric cooler (TC) providing a constant basis temperature. Fluorescence is excited with a UV LED and recorded with a photomultiplier tube (PMT). The solution inside the capillary is locally heated with an IR laser, which is coupled into the fluorescence microscope using an IR-reflecting “hot” mirror. B) The fluorescence of the heated spot is recorded, normalized, and plotted against time. After the IR laser is switched on at $t = 5$ s, the fluorescence decreases as the temperature increases, and the fluorescent protein molecules move away from the heated spot because of thermophoresis. The unbound iGluR2 ligand-binding domain (yellow; PDB code 1FTO) shows stronger thermophoretic depletion than the complex with glutamate (blue; PDB code 1FTJ).^[7] This reflects the conformational change of the protein upon binding.

distinguished from the subsequent rather slow thermodiffusion lasting several seconds.^[11] To infer binding affinity, a titration series is prepared in which the concentration of the ligand is varied while the concentration of the protein is kept constant. For each dilution step, the temperature perturbation is applied and the fluorescence response is recorded. The thermophoretic signal changes stepwise with increasing ligand concentration. This corresponds to the changing ratio of unbound protein to bound complex and reflects the alteration of molecular properties upon binding (Figure 1B). To derive the dissociation constant K_D from the raw data, the fluorescence signals are normalized to the undisturbed situation before heating. Working with these relative signals avoids the difficulties of analyzing absolute fluorescence levels or small alterations in absorption and emission spectra upon binding. As known from standard protein fluorescence spectroscopy, such signals can be complex to interpret, mostly because of the presence of multiple Trp residues or energy transfer between amino acids.^[14] In the following examples, we prove that label-free MST is a valuable tool to study the binding of numerous types of ligands to different protein classes.

In the mammalian central nervous system iGluRs play a key role in fast excitatory synaptic transmission.^[15] The investigation of ligand binding to the various iGluR subtypes is in the focus of ongoing research.^[12] Using label-free MST we analyzed the interaction of the non-NMDA receptor subunits iGluR2 and iGluR6 with different agonists. We used soluble LBD versions generated by fusing the two discontinuous extracellular fragments S1 and S2.

The LBD of the AMPA receptor subunit iGluR2 (29.2 kDa; Figure 1B) contains four tryptophan residues. A solution with a concentration of $2 \mu\text{M}$ exhibited sufficient UV fluorescence intensity without significant bleaching. Analyzing the change in thermophoretic mobility, we found a K_D value of $(835 \pm 43) \text{ nM}$ for the natural agonist glutamate (147.13 Da; Figure 2). This accurately reproduces the liter-

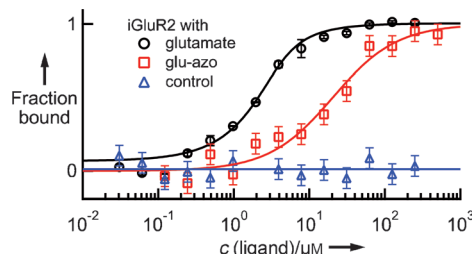


Figure 2. Ligand binding to membrane receptors. Binding curves are derived from the specific change in the thermophoretic mobility upon ligand titration to a constant iGluR2-LBD concentration of $2 \mu\text{M}$. The curves show binding affinities of $(835 \pm 43) \text{ nM}$ for glutamate and $(19 \pm 5) \mu\text{M}$ for glu-azo. The two agonists compete for the same binding site, as preincubation of iGluR2 with a saturating amount of glutamate prevents glu-azo binding (control).

ature value of 821 nM .^[16] Azobenzene glutamate (glu-azo; 367.15 Da), a photoswitchable agonist allowing for remote control of neuronal excitability, binds to the iGluR2-LBD with a K_D value of $(19 \pm 5) \mu\text{M}$ (Figure 2).^[17] MST confirms the finding that glu-azo, designed as a kainate receptor ligand, also binds iGluR2.^[18] Adding glu-azo to iGluR2-LBD preincubated with a saturating amount of glutamate ($500 \mu\text{M}$) did not influence thermophoresis. The result proves the specificity of the glu-azo signal and indicates that both agonists compete for the same binding site. We verified results of the label-free measurement for glu-azo by performing standard MST with labeled iGluR2-LBD (see the Supporting Information, Figure S-1). The measured K_D value of $(22 \pm 8) \mu\text{M}$ does not deviate significantly from the value determined by the label-free analysis. This demonstrates that label-free MST was not disturbed by autofluorescence and that the label did not affect the interaction. We additionally quantified ligand binding to the kainate receptor subunit iGluR6. We used the iGluR6-LBD (4 Trp; 29.3 kDa) in a concentration of $2 \mu\text{M}$. The determined upper limit of 359 nM for the affinity to glutamate is in agreement with the reported K_i value of $(355 \pm 74) \text{ nM}$ (see Figure S-2).^[19] The iGluR6-LBD binds glu-azo with a K_D value of $(3.2 \pm 0.4) \mu\text{M}$ (see Figure S-3).

Label-free MST is sensitive enough to measure the binding of small molecules. Three selective small-molecule inhibitors of p38 α (59.5 kDa) were tested. P38 is a mitogen-activated protein kinase (MAP kinase) responding to stress. The isoform p38 α is considered the key subtype involved in cytokine synthesis during inflammatory response. Thus, potent inhibitors of p38 α might lead to the development of effective novel approaches for the treatment of inflammatory diseases.^[20]

The kinase contains five Trp residues, so that a concentration of 100 nM was sufficient. As shown in Figure 3 p38 α binds the inhibitor SB202190 (331 Da) with a K_D value of

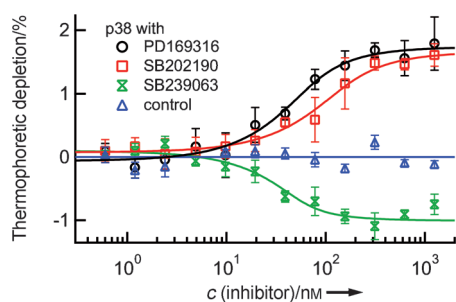


Figure 3. Screening of small-molecule kinase inhibitors. Three selective inhibitors were successfully tested for binding to the nonactivated form of MAP kinase p38 α ($c = 100$ nM). Corresponding to structural differences, the binding of SB202190 and PD169316 has the opposite effect on the thermophoretic movement compared to SB239063. SB202190 binds with a K_D value of (48 ± 21) nM. The upper limits of affinity for PD169316 and SB239063 were determined as 33 nM and 20 nM, respectively. These results are in good agreement with previously reported values. Thermally denatured p38 α did not show binding (control).

(48 ± 21) nM, reproducing the literature value of 37 nM.^[21] The upper limits of affinity for PD169316 (360 Da) and SB239063 (368 Da) were determined to be 33 nM and 20 nM, respectively. This is in good agreement with reported IC_{50} values of 130 nM (PD169316) and 44 nM (SB239063).^[22,23] Nonspecific interactions can be excluded as thermally denatured kinase p38 α did not show binding.

Remarkably, the thermophoretic signal contains further information on the ligands. The complexes formed from SB202190 (and PD169316) to p38 α show less thermal depletion than the unbound kinase, which is represented by the positive slope of the binding curve. The binding of SB239063 has the opposite effect (Figure 3). Apart from a single functional group, the compounds 4-(4-fluorophenyl)-2-(4-hydroxyphenyl)-5-(4-pyridyl)-1*H*-imidazole (SB202190) and 4-(4-fluorophenyl)-2-(4-nitrophenyl)-5-(4-pyridyl)-1*H*-imidazole (PD169316) are identical in structure. The structure of the second-generation inhibitor SB239063 (*trans*-1-(4-hydroxycyclohexyl)-4-(4-fluorophenyl)-5-(2-methoxy-pyridin-4-yl)imidazole), however, differs significantly. These differences are likely to be the cause of the opposite effect on thermophoretic depletion.

Using label-free microscale thermophoresis, we successfully quantified different types of biomolecular binding events which are summarized in Table 1. Affinities reported in the literature were confirmed for all groups of interactions. For the LBD of the membrane receptor iGluR2, we observed that glu-azo binds to the same site as glutamate, yet with a much lower affinity. The affinity of small-molecule binding to the kinase p38 α was measured and we found that structurally different inhibitors had an opposite influence on the thermophoretic depletion. This interesting finding suggests that thermophoresis could be used to not only determine binding strength but also gather additional information on the binding event. Comparative label-free MST studies would be necessary and might be a putative tool to classify novel ligands. The use of label-free MST is, however, not restricted to small-molecule testing. We also demonstrated the applicability for aptamer and ion binding (see the Supporting Information).

Table 1: Protein binding studied by label-free MST.^[a]

Binding event	K_D values from label-free MST	Literature values
<i>iGluR2</i>		
glutamate	(835 ± 43) nM	821 nM ^[16]
glu-azo	(19 ± 5) μ M	–
<i>iGluR6</i>		
glutamate	≤ 359 nM ^[b]	(355 ± 74) nM (K) ^[19]
glu-azo	(3.2 ± 0.4) μ M	–
<i>p38α</i>		
SB202190	(48 ± 21) nM	37 nM ^[21]
PD169316	≤ 33 nM ^[b]	130 nM (IC_{50}) ^[22]
SB239063	≤ 20 nM ^[b]	44 nM (IC_{50}) ^[23]
<i>thrombin</i> ^[c]		
15 mer	(32 ± 15) nM	25 to 100 nM ^[25,26]
29 mer	(133 ± 42) nM	0.5 or 100 nM ^[26,27]
<i>Syt1</i> ^[c]		
Ca ²⁺	(326 ± 26) μ M	50 μ M to 3 mM ^[28]

[a] For all types of biomolecular binding events the measured affinities were in agreement with reported literature values. [b] These affinities represent upper limits. The exact error estimations can be found in the Supporting Information. [c] See the Supporting Information for descriptions, figures, and experimental details.

Label-free MST is particularly suitable for screening approaches as a typical interaction measurement requires only about 50 μ L of a protein solution at a concentration of 0.1–2.0 μ M. Furthermore, the measurement only takes about 5–10 min. This is made possible by the simple “mix-and-read” protocol without laborious sample preparations like surface immobilization or labeling. As the binding partners are not attached to a label or surface, molecular properties are not altered and mobility is not restricted. Thus native binding affinities are measured.

Label-free MST requires a sufficient intrinsic fluorescence signal of the protein, whereas difficulties arise from the UV fluorescence of the ligand and buffer. The UV fluorescence of the buffer, for example, caused by a Trp-containing spectator protein adds to background fluorescence leading to increased noise and a constant offset in the thermophoretic signal, but not to a change in the affinity specified by the binding. If both binding partners show a similar Trp fluorescence, direct quantification with label-free MST is not possible. The contribution of the titrated fluorescent ligand to the measured thermophoresis signal needs to be quantified by control experiments and then subtracted. This corrected thermophoresis signal should make it possible to infer the thermophoretic binding signal. However, most ligands, including the group of small molecules accounting for the majority of today’s pharmaceuticals do not exhibit UV fluorescence.

A protein of average Trp content (≥ 2 Trps) can be used in concentrations down to 100 nM, making it possible to accurately quantify $K_D \geq 50$ nM. Interactions with higher affinities can still be detected qualitatively, but not precisely quantified. If insufficient Trp residues are incorporated, it is possible to introduce Trp by mutation. A conservative exchange of another aromatic amino acid for Trp often does

not affect the molecular properties and protein function.^[24] Alternatively, labeling and standard MST can be chosen, which typically can be used for lower protein concentrations and for the exact determination of affinities in the region of $K_D < 1$ nM.^[9] Considering its practicability and applicability described above, label-free MST should be a promising novel tool to enhance knowledge on protein binding in all fields of life science.

Experimental Section

The setup is based on a Zeiss Axiotech Vario microscope with a 40× quartz objective, numerical aperture 0.8 (Partek GmbH, Muenster, Germany). An UVTOP LED with a center wavelength of 285 nm (Thorlabs GmbH, Dachau, Germany) was used for excitation, a photomultiplier tube (P10PC, ET Enterprises Ltd, Uxbridge, UK) for detection. Fluorescence filters for tryptophan (F36-300) were purchased from AHF-Analysentechnik (Tuebingen, Germany). Fused-silica capillaries from Polymicro Technologies (Phoenix, USA) with different inner diameters and volumes of approximately 500 nL were used. Prior to the measurement, the polyimide coating was removed with an open flame and the capillaries were cleaned with ethanol on the outside. The temperature gradients were created with an IR laser diode (Furukawa FOL1405-RTV-617-1480, $l = 1480$ nm, $k = 320$ μm for water, 320 mW maximum power) purchased from AMS Technologies AG (Munich, Germany). The IR laser beam was coupled into the path of fluorescence light with an IR-reflecting “hot” mirror (NT46-386; Edmund Optics, Barrington, USA) and focused into the fluid with the microscope objective. As measured using the temperature-dependent fluorescence of TAMRA dye, the temperature in the solution was increased by 6 K in the beam center with a $1/e^2$ diameter of 25 μm. All measurements were performed at a capillary basis temperature of 20°C. The capillary basis temperature was controlled with a thermoelectric cooler.

The expression vectors for iGluR2- and iGluR6-LBDs were kindly provided by Mark Mayer. P38α was provided by Krishna Saxena; PD169316, SB202190, and SB239063 were purchased from Sigma Aldrich (Munich, Germany). For the standard MST control, iGluR2-LBD was labeled using the Monolith NT Protein Labeling Kit RED according to the supplied protocol.

Measurements were conducted in the following buffers: iGluR2- and iGluR6-LBD: 10 mM HEPES pH 8.0, 150 mM NaCl, 1 mM EDTA; p38α: 50 mM Tris pH 7.8, 150 mM NaCl, 10 mM MgCl₂, 0.05 % TWEEN20. As a control, p38α was incubated at 95°C for 1 h. All solutions were incubated at room temperature for 1 h after the proteins had been mixed with the different target molecules.

The K_D values were obtained by fitting the fraction of bound proteins to the quadratic solution of the binding reaction equilibrium, derived from the law of mass action, with the K_D being the single free parameter.^[29] The fitting function, number of repetitions, and the explanation of error bars are provided in the Supporting Information.

Received: June 1, 2012

Published online: September 24, 2012

Keywords: analytical methods · binding affinity · label-free methods · microscale thermophoresis · protein conformation

[1] a) Y. Chen, J. D. Müller, S. Y. Tetin, J. D. Tyner, E. Gratton, *Biophys. J.* **2000**, *79*, 1074–1084; b) M. G. Fried, *Electrophoresis* **1989**, *10*, 366–376.

[2] a) L. G. Fägerstam, A. Frostell, R. Karlsson, M. Kullman, A. Larsson, M. Malmqvist, H. Butt, *J. Mol. Recognit.* **1990**, *3*, 208–

214; b) D. G. Myszkka, *Curr. Opin. Biotechnol.* **1997**, *8*, 50–57; c) W. H. King, *Anal. Chem.* **1964**, *36*, 1735–1739.

[3] M. M. Baksh, A. K. Kussrow, M. Mileni, M. G. Finn, D. J. Bornhop, *Nat. Biotechnol.* **2011**, *29*, 357–360.

[4] J. Bao, S. M. Krylova, D. J. Wilson, O. Reinstein, P. E. Johnson, S. N. Krylov, *ChemBioChem* **2011**, *12*, 2551–2554.

[5] D. J. Bornhop, J. C. Latham, A. Kussrow, D. A. Markov, R. D. Jones, H. S. Sorensen, *Science* **2007**, *317*, 1732–1736.

[6] a) S. Leavitt, E. Freire, *Curr. Opin. Struct. Biol.* **2001**, *11*, 560–566; b) R. J. Falconer, B. M. Collins, *J. Mol. Recognit.* **2011**, *24*, 1–16; c) I. Jelesarov, H. R. Bosshard, *J. Mol. Recognit.* **1999**, *12*, 3–18.

[7] N. Armstrong, E. Gouaux, *Neuron* **2000**, *28*, 165–181.

[8] a) C. Ludwig, *Sitzungsber. Akad. Wiss. Wien Math.-Naturwiss. Kl.* **1856**, 539; b) S. Iacopini, R. Piazza, *Europhys. Lett.* **2003**, *63*, 247–253.

[9] S. Duhr, D. Braun, *Proc. Natl. Acad. Sci. USA* **2006**, *103*, 19678–19682.

[10] C. J. Wienken, P. Baaske, U. Rothbauer, D. Braun, S. Duhr, *Nat. Commun.* **2010**, *1*, 100.

[11] P. Baaske, C. J. Wienken, P. Reineck, S. Duhr, D. Braun, *Angew. Chem.* **2010**, *122*, 2286–2290; *Angew. Chem. Int. Ed.* **2010**, *49*, 2238–2241.

[12] P. Stawski, H. Janovjak, D. Trauner, *Bioorg. Med. Chem.* **2010**, *18*, 7759–7772.

[13] M. L. Mayer, *Nature* **2006**, *440*, 456–462.

[14] C. A. Royer, *Chem. Rev.* **2006**, *106*, 1769–1784.

[15] R. Dingleline, K. Borges, D. Bowie, S. F. Traynelis, *Pharmacol. Rev.* **1999**, *51*, 7–61.

[16] N. Armstrong, M. Mayer, E. Gouaux, *Proc. Natl. Acad. Sci. USA* **2003**, *100*, 5736–5741.

[17] M. Volgraf, P. Gorostiza, S. Szobota, M. R. Helix, E. Y. Isacoff, D. Trauner, *J. Am. Chem. Soc.* **2007**, *129*, 260–261.

[18] M. Volgraf, *I. Photocontrol of Ionotropic Glutamate Receptors and II. Total Synthesis of Exiguamine A and B.*, Bibliobazaar, Llc, [S.L.], **2011**.

[19] C. K. Tygesen, J. S. Rasmussen, S. V. Jones, A. Hansen, K. Hansen, P. H. Andersen, *Proc. Natl. Acad. Sci. USA* **1994**, *91*, 13018–13022.

[20] C. Dominguez, D. A. Powers, N. Tamayo, *Curr. Opin. Drug Discovery Dev.* **2005**, *8*, 421–430.

[21] B. Frantz, T. Klatt, M. Pang, J. Parsons, A. Rolando, H. Williams, M. J. Tocci, S. J. O’Keefe, E. A. O’Neill, *Biochemistry* **1998**, *37*, 13846–13853.

[22] H. Nordin, M. Jungnelius, R. Karlsson, O. P. Karlsson, *Anal. Biochem.* **2005**, *340*, 359–368.

[23] F. C. Barone, E. A. Irving, A. M. Ray, J. C. Lee, S. Kassis, S. Kumar, A. M. Badger, R. F. White, M. J. McVey, J. J. Legos, et al., *J. Pharmacol. Exp. Ther.* **2001**, *296*, 312–321.

[24] a) F. Hannemann, A. K. Bera, B. Fischer, M. Lisurek, K. Teuchner, R. Bernhardt, *Biochemistry* **2002**, *41*, 11008–11016; b) M. L. Scalley, Q. Yi, H. Gu, A. McCormack, J. R. Yates, D. Baker, *Biochemistry* **1997**, *36*, 3373–3382.

[25] a) L. C. Bock, L. C. Griffin, J. A. Latham, E. H. Vermaas, J. J. Toole, *Nature* **1992**, *355*, 564–566; b) M. C. R. Buff, F. Schäfer, B. Wulffen, J. Müller, B. Pöttsch, A. Heckel, G. Mayer, *Nucleic Acids Res.* **2010**, *38*, 2111–2118.

[26] D. M. Tasset, M. F. Kubik, W. Steiner, *J. Mol. Biol.* **1997**, *272*, 688–698.

[27] P.-H. Lin, R.-H. Chen, C.-H. Lee, Y. Chang, C.-S. Chen, W.-Y. Chen, *Colloids Surf. B* **2011**, *88*, 552–558.

[28] A. Radhakrishnan, A. Stein, R. Jahn, D. Fasshauer, *J. Biol. Chem.* **2009**, *284*, 25749–25760.

[29] S. Lippok, S. A. I. Seidel, S. Duhr, K. Uhland, H.-P. Holthoff, D. Jenne, D. Braun, *Anal. Chem.* **2012**, *84*, 3523–3530.

Supporting Information

© Wiley-VCH 2012

69451 Weinheim, Germany

Label-Free Microscale Thermophoresis Discriminates Sites and Affinity of Protein–Ligand Binding**

*Susanne A. I. Seidel, Christoph J. Wienken, Sandra Geissler, Moran Jerabek-Willemsen, Stefan Duhr, Alwin Reiter, Dirk Trauner, Dieter Braun, and Philipp Baaske**

anie_201204268_sm_miscellaneous_information.pdf

Table of contents

- 1 Fitting function
- 2 Number of repeats and error bars
- 3 Exact error estimations for values given as an upper limit
- 4 Additional iGluR binding curves
- 5 Additional experiments
 - 5.1 Aptamer binding to thrombin
 - 5.2 Ca^{2+} -ion-binding to synaptotagmin 1
 - 5.3 Additional experimental section

1 Fitting function

To determine the affinity of a ligand L binding to a protein P via label free MST, the total concentration of the ligand c_{L0} is titrated, while the total concentration of the protein c_{P0} is kept constant. For the binding event of L to P, the mass action law reads

$$K_D = \frac{c_L c_P}{c_{LP}} = \frac{(c_{L0} - c_{LP})(c_{P0} - c_{LP})}{c_{LP}}$$

with

- K_D : dissociation constant
- c_L : free ligand concentration
- c_P : free protein concentration
- c_{LP} : concentration of the bound complex
- c_{L0} : total concentration of the ligand and
- c_{P0} : total concentration of the protein.

Solving for the fraction of occupied binder B yields

$$x = \frac{c_{LP}}{c_{P0}} = \frac{c_{L0} + c_{P0} + K_D - \sqrt{(c_{L0} + c_{P0} + K_D)^2 - 4c_{L0}c_{P0}}}{2c_{L0}}$$

2 Number of repeats and error bars

The number of independent repeats was at least 3 for all measurements except for syt1 and iGluR6 (n=2); error bars show the standard deviation between these independent repeats. For iGluR2 binding glu-azo and the control with the saturated amount of glutamate and with the labeled protein n=1. In these cases the error was estimated by the noise of the fluorescence detection.

3 Exact error estimations for values given as an upper limit

The fitting procedure assumes a Gaussian, symmetric error distribution. Due to this approximation, the distribution reached negative values in three cases. The corresponding values are given as upper limits of affinity in the manuscript. The exact error estimations are listed in Table S-1.

Table S-1. In three cases an upper limit of affinity is given. The exact error estimations are listed below.

Binding event	Upper limit given in manuscript	Exact values derived from data fit
iGluR6		
glutamate	$\leq 359 \text{ nM}^{[a]}$	$153 \pm 206 \text{ nM}$
p38 α		
PD169316	$\leq 33 \text{ nM}^{[a]}$	18 ± 15
SB239063	$\leq 20 \text{ nM}^{[a]}$	8 ± 12

4 Additional iGluR binding curves

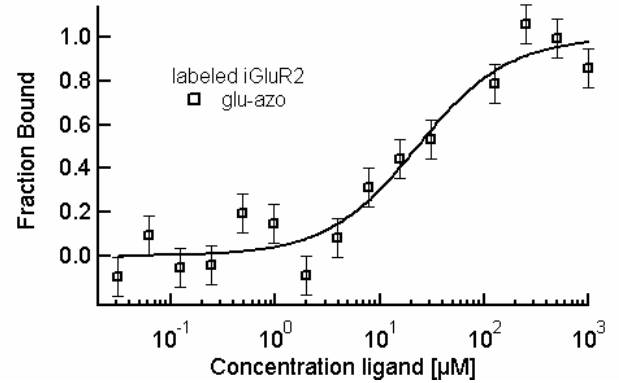


Figure S-1. Standard MST control for the binding of the iGluR2-LBD to glu-azo. The protein was fluorescently labeled and used in a concentration of 200 nM. The measured K_D of $22 \pm 8 \mu\text{M}$ verifies the label free result ($19 \pm 5 \mu\text{M}$) thus excluding disturbances by autofluorescence.

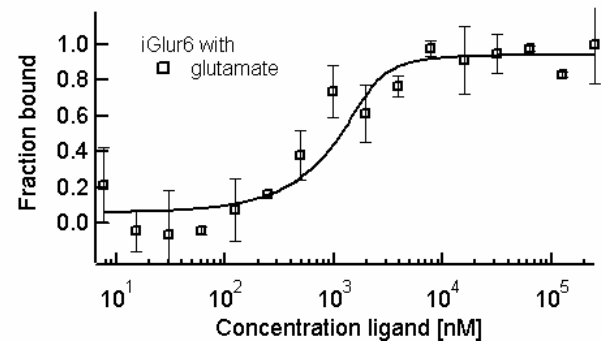


Figure S-2. Label free MST measurement of glutamate binding the iGluR6-LBD ($c=2 \mu\text{M}$). An upper limit of affinity of 359 nM was derived.

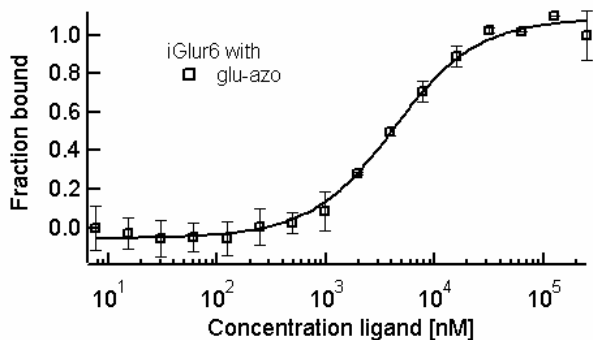


Figure S-3. Label free MST measurement of glu-azo binding the iGluR6-LBD ($c=2 \mu\text{M}$). The determined K_D is $3.2 \pm 0.4 \mu\text{M}$.

5 Additional experiments

5.1 Aptamer binding to thrombin

Despite their much simpler production and higher stability, DNA aptamers resemble the binding behavior of antibodies. We demonstrate the applicability of label-free MST to monitor the binding of these valuable molecular tools using the example of human α -thrombin (36.7 kDa; 9 Trp residues). This serine protease is part of the human coagulation cascade. In 1992 Bock et al. designed a single stranded 15mer DNA aptamer binding to the fibrinogen recognition exosite.^[1] Five years later Tasset et al. reported on a 29mer binding to the heparin exosite.^[2]

For our label-free MST analysis of these aptamers, we used a constant thrombin concentration of 200 nM (Fig. S-4). The measured K_D of $32 \pm 15 \text{ nM}$ for the 15mer reproduces the previously reported standard MST result with 5'-fluorescently labeled 15mer ($K_D=30 \pm 19 \text{ nM}$).^[3] It is in good agreement with literature values specifying the affinity as 25 to 100 nM based on filter binding assays.^[1,2,4] For the 29mer, label-free MST reported an affinity of $133 \pm 42 \text{ nM}$. This is much higher than the K_D of 0.5 nM, reported by Tasset et al.^[2] However, SPR measurements could not confirm the very high affinity of the 29mer either and instead reported a K_D in the range of 100 nM.^[5] Tang et al. even found an affinity lower than for the 15mer consistent with our results.^[6] Apart from the specific aptamers a 15mer dinucleotide mutant was measured. The mutant did not show binding, thus proving specificity.

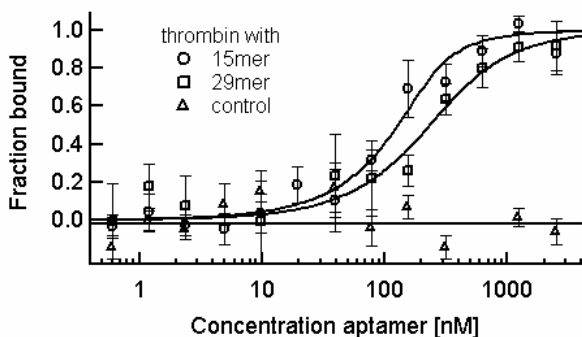


Figure S-4. Thrombin interaction with aptamers. Specific 15mer and 29mer DNA aptamers bind to the fibrinogen and heparin exosites of human α -thrombin ($c=200 \text{ nM}$). We measured a K_D of $32 \pm 15 \text{ nM}$ for the 15mer and a K_D of $133 \pm 42 \text{ nM}$ for the 29mer and. A 15mer dinucleotide mutant did not bind to thrombin (control).

5.2 Ca^{2+} -ion-binding to synaptotagmin 1

As previously reported protein binding to ions can be measured with standard MST.^[7] This type of binding events is also accessible via label-free MST. We analyzed the interaction of the synaptic vesicle protein synaptotagmin 1 (Syt1) with Ca^{2+} . The cytoplasmic C-terminal part of the protein consists of two C2 domains, C2A and C2B. NMR suggests that three and two Ca^{2+} bind to C2A and C2B, respectively. Upon binding, the C2 domains mediate membrane translocation. Hence synaptotagmin can act as a neuronal Ca^{2+} sensor triggering exocytosis of neurotransmitters into the synaptic cleft.^[8]

We used Syt1's C2AB fragment in a constant concentration of $1 \mu\text{M}$ and titrated CaCl_2 . Label-free MST yielded an overall Ca^{2+} affinity of $326 \pm 26 \mu\text{M}$ (Fig. S-5). A standard MST control with fluorescently labeled C2AB confirmed this affinity (see Supporting information Fig. S-6). Our results are in good agreement with ITC measurements by Radhakrishnan et al.^[9] Assuming quintuple binding, the group extracted K_D s of 48, 142 and $3120 \mu\text{M}$ for C2A and $490 \mu\text{M}$ for both Ca^{2+} binding to C2B. To obtain distinct K_D s for the different binding sites, MST measurements of selective Ca^{2+} binding mutants of C2AB seem to be very suitable.^[10] Titrating MgCl_2 did not result in a change in thermophoresis, demonstrating the specificity of the label free MST analysis (Fig. S-5). Standard MST experiments on cooperative Ca^{2+} and phosphatidylinositol 4,5-bisphosphate binding to Syt1 have already been performed successfully, suggesting that label free MST could also be used for extensive studies of Syt1 function.^[11]

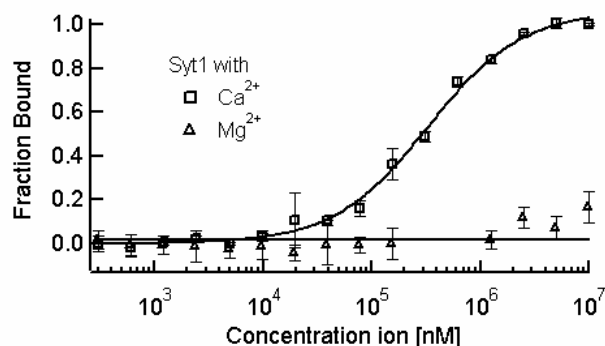


Figure S-5. Synaptotagmin 1 binds Ca^{2+} ions. Syt1's C2AB fragment was used in a constant concentration of $1 \mu\text{M}$. CaCl_2 titration alters the thermophoretic mobility. An overall binding affinity of $326 \pm 26 \mu\text{M}$ was derived. In contrast, MgCl_2 does not have an influence on thermophoresis, documenting specificity.

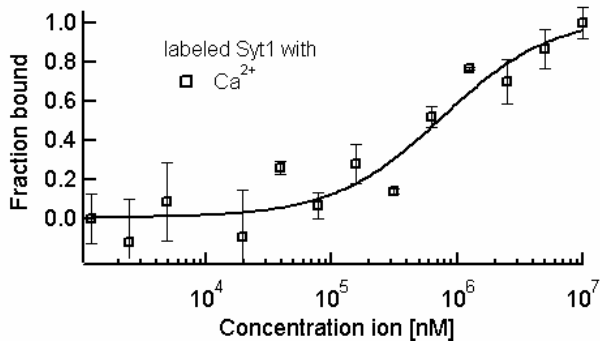


Figure S-6. Standard MST control for the binding of Syt1-C2AB to glu-azo. The protein was fluorescently labeled and used in a concentration of 40 nM. The measured K_D of 757 ± 299 μM verifies the label free result (326 ± 26 μM) thus excluding disturbances by autofluorescence.

5.3 Additional experimental section

Human α -thrombin was purchased from Haematologic Technologies Inc. (Essex Junction, USA). DNA oligonucleotides were synthesized by Metabion (Martinsried, Germany). The sequences of the oligonucleotides, with mutations as small letters, are: 15mer 5'-GGT TGG TGT GGT TGG-3'; 29mer: 5'-AGT CCG TGG TAG GGC AGG TTG GGG TGA CT-3'; f 15mer dinucleotide mutant: 5'-GGT TGT TGT GGT TtG-3'. The aptamers were denatured and re-natured prior to the experiments to ensure that they reached their active conformation. The Syt1 C2AB construct from

R. norvegicus was cloned into a pET28a expression vector. The purified protein was kindly provided by Geert van den Boogaart.

For the standard MST control Syt1-C2AB was labeled using the Monolith NT Protein Labeling Kit RED according to the supplied protocol.

Measurements were conducted in the following buffers: Thrombin selection buffer: 20 mM Tris-HCl pH 7.4, 150 mM NaCl, 5 mM KCl, 1 mM CaCl₂, 1 mM MgCl₂, 0.1% TWEEN20;^[1] Syt1: 20 mM HEPES pH 7.4, 150 mM KCl, for the labeled control additionally 0.5 mg/ml BSA. All solutions were incubated at RT for 1h after the proteins had been mixed with the different target molecules.

- [1] L. C. Bock, L. C. Griffin, J. A. Latham, E. H. Vermaas, J. J. Toole, *Nature* **1992**, 355, 564–566.
- [2] D. M. Tasset, M. F. Kubik, W. Steiner, *J Mol Biol* **1997**, 272, 688–698.
- [3] P. Baaske, C. J. Wienken, P. Reineck, S. Duhr, D. Braun, *Angew. Chem. Int. Ed. Engl.* **2010**, 49, 2238–2241.
- [4] M. C. R. Buff, F. Schäfer, B. Wulffen, J. Müller, B. Pötzsch, A. Heckel, G. Mayer, *Nucleic Acids Res.* **2010**, 38, 2111–2118.
- [5] P.-H. Lin, R.-H. Chen, C.-H. Lee, Y. Chang, C.-S. Chen, W.-Y. Chen, *Colloids Surf B Biointerfaces* **2011**, 88, 552–558.
- [6] Q. Tang, X. Su, K. P. Loh, *J Colloid Interface Sci* **2007**, 315, 99–106.
- [7] C. J. Wienken, P. Baaske, U. Rothbauer, D. Braun, S. Duhr, *Nat Comms* **2010**, 1, 100.
- [8] H. Tokuoka, Y. Goda, *Neuron* **2003**, 38, 521–524.
- [9] A. Radhakrishnan, A. Stein, R. Jahn, D. Fasshauer, *Journal of Biological Chemistry* **2009**, 284, 25749–25760.
- [10] A. Stein, A. Radhakrishnan, D. Riedel, D. Fasshauer, R. Jahn, *Nat. Struct. Mol. Biol.* **2007**, 14, 904–911.
- [11] G. van den Bogaart, K. Meyenberg, U. Diederichsen, R. Jahn, *Journal of Biological Chemistry* **2012**, 287, 16447–16453.

A Monoclonal Antibody (MCPR3-7) Interfering with the Activity of Proteinase 3 by an Allosteric Mechanism*

Received for publication, June 25, 2013. Published, JBC Papers in Press, July 31, 2013, DOI 10.1074/jbc.M113.495770

Lisa C. Hinkofer[‡], Susanne A. I. Seidel[§], Brice Korkmaz^{‡¶}, Francisco Silva^{||**1}, Amber M. Hummel^{||}, Dieter Braun[§], Dieter E. Jenne^{‡¶¶2}, and Ulrich Specks^{||}

From the [‡]Comprehensive Pneumology Center, Institute of Lung Biology and Disease (iLBD), University Hospital, Ludwig Maximilians University and Helmholtz Zentrum München, Member of the German Center for Lung Research (DZL), Max-Lebsche-Platz 31, 81377 Munich, Germany, [§]Systems Biophysics and Functional Nanosystems, Ludwig Maximilians University München, Amalienstrasse 54, 80799 Munich, Germany, [¶]Centre d'Etude des Pathologies Respiratoires, INSERM U-1100/EA-6305, 37032 Tours, France, ^{||}Thoracic Diseases Research Unit, Division of Pulmonary and Critical Care Medicine, Mayo Clinic and Foundation, Rochester, Minnesota 55905, ^{**}Departamento de Inmunología Clínica y Reumatología, Facultad de Medicina, Pontificia Universidad Católica de Chile, Marcoleta 352, 8330033 Santiago, Chile, and ^{¶¶}Max Planck Institute of Neurobiology, am Klopferspitz 18, 82152 Planegg-Martinsried, Germany

Background: Proteinase 3 is an abundant serine protease with high similarity to neutrophil elastase and a major autoimmune target in systemic vasculitis.

Results: We identified a monoclonal antibody that inhibits PR3 activity.

Conclusion: PR3-inhibiting antibodies can change its conformation and impair interactions with α_1 -proteinase inhibitor.

Significance: PR3-inhibiting antibodies may play a role in autoimmune vasculitis and could be exploited as highly selective inhibitors.

Proteinase 3 (PR3) is an abundant serine protease of neutrophil granules and a major target of autoantibodies (PR3 anti-neutrophil cytoplasmic antibodies) in granulomatosis with polyangiitis. Some of the PR3 synthesized by promyelocytes in the bone marrow escapes the targeting to granules and occurs on the plasma membrane of naive and primed neutrophils. This membrane-associated PR3 antigen may represent pro-PR3, mature PR3, or both forms. To discriminate between mature PR3 and its inactive zymogen, which have different conformations, we generated and identified a monoclonal antibody called MCPR3-7. It bound much better to pro-PR3 than to mature PR3. This monoclonal antibody greatly reduced the catalytic activity of mature PR3 toward extended peptide substrates. Using diverse techniques and multiple recombinant PR3 variants, we characterized its binding properties and found that MCPR3-7 preferentially bound to the so-called activation domain of the zymogen and changed the conformation of mature PR3, resulting in impaired catalysis and inactivation by α_1 -proteinase inhibitor (α_1 -antitrypsin). Noncovalent as well as

covalent complexation between PR3 and α_1 -proteinase inhibitor was delayed in the presence of MCPR3-7, but cleavage of certain thioester and paranitroanilide substrates with small residues in the P1 position was not inhibited. We conclude that MCPR3-7 reduces PR3 activity by an allosteric mechanism affecting the S1' pocket and further prime side interactions with substrates. In addition, MCPR3-7 prevents binding of PR3 to cellular membranes. Inhibitory antibodies targeting the activation domain of PR3 could be exploited as highly selective inhibitors of PR3, scavengers, and clearers of the PR3 autoantigen in granulomatosis with polyangiitis.

Proteinase 3 (PR3³; EC 3.4.21.76) is one of four neutral serine proteases (elastase, cathepsin G, proteinase 3, and neutrophil serine protease 4) stored as fully processed mature enzymes in azurophil granules of human neutrophils (1–4). Small amounts of PR3 are also expressed on the plasma membrane of resting neutrophils (5, 6). The degree of this constitutive expression is genetically determined (7–9), but the surface exposure and pericellular activity of PR3 around neutrophils is further increased by priming and activation of neutrophils. Autoantibody responses to PR3 have been identified as a central pathogenic feature in patients suffering from granulomatosis with polyangiitis (GPA; formerly called Wegener granulomatosis). PR3-directed autoantibodies are capable of activating cytokine-

* This work was supported, in whole or in part, by National Institutes of Health Grants RO1-AR49806 and RC1-AR58303 (to U. S.) and U54-RR019497 from the Vasculitis Clinical Research Consortium (to F. S.). This work was also supported by European Union Seventh Framework Programme (FP7/2007–2013) under Grant Agreement 261382 (INTRICATE), the Alexander von Humboldt Foundation, a joint grant from the Deutsche Forschungsgemeinschaft (JE194/4-1; BR2152/2-1), the NanoSystems Initiative Munich, the Center for NanoScience, the Ludwig-Maximilians-Universität Munich Initiative Functional Nanosystems, and the Mayo Clinic Monoclonal Antibody Core Facility.

¹ Supported in part by funds from The Mayo Foundation.

² To whom correspondence should be addressed: Comprehensive Pneumology Center, Inst. of Lung Biology and Disease (iLBD), University Hospital, Ludwig Maximilians University and Helmholtz Zentrum München, Member of the German Center for Lung Research (DZL), Max-Lebsche-Platz 31, 81377 Munich, Germany. Tel.: 49-89-3187-4664; Fax: 49-89-3187-4661; E-mail: dieter.jenne@helmholtz-muenchen.de.

³ The abbreviations used are: PR3, proteinase 3; GPA, granulomatosis with polyangiitis; α_1 PI, α_1 -proteinase inhibitor; ANB, 5-amino-2-nitrobenzoic acid; Abz, γ -aminobenzoic acid; EBNA, Epstein-Barr nuclear antigen 1; Abu, δ -aminobutyric acid; DAP(CF), diaminopropionyl fluorescein; SBzl, thio-benzyl ester; nVal or nV, norvaline; For, formyl; Boc, *t*-butoxycarbonyl; TAMRA, tetramethylrhodamine; Ahx, aminohexanoic acid; ONp, *para*-nitrophenyl ester; pNA, *para*-nitroaniline; CMK, chloromethyl ketone; h, human; gib, gibbon; MST, microscale thermophoresis.

Antibodies Interfering with PR3 Activity and Inactivation

primed neutrophils *in vitro* by binding to surface-exposed PR3 and Fc γ receptors (10). In its generalized form, a necrotizing vasculitic process affects and damages the endothelium of small vessels in the lungs and kidneys (11).

Although PR3 has been extensively studied for decades, its biological functions during immune defense responses are poorly understood. Likewise its interaction with anti-neutrophil cytoplasmic antibodies in patients with GPA and their pathogenic role for this relapsing-remitting disease have not been clarified. A large genome-wide association study recently confirmed the genetic association between anti-neutrophil cytoplasmic antibody formation and the PR3 locus on the one hand and the presence of the Z-variant of α_1 -proteinase inhibitor (α_1 PI) on the other hand in GPA (12). This finding suggests that PR3 activity and/or inactivation of PR3 by α_1 PI varies in the human population and contributes to the risk for GPA manifestations either at onset, during relapses, or during systemic progression.

Inhibition of neutrophil elastase and PR3 by α_1 PI is highly dependent on the proper conformation of an exposed reactive center loop, which serves as a pseudosubstrate. Single point mutations, even at distant sites within α_1 PI like a lysine substitution of Glu³⁴² in the Z-variant, can affect the conformation of the reactive center loop and can decrease the association rates with target proteases (13). Once hydrolyzed after the methionine in position 358, the new carboxyl terminus of α_1 PI forms an irreversible covalent acyl-enzyme complex that undergoes a sophisticated conformational rearrangement. These enzyme-serpin complexes are quickly removed from neutrophil membranes, the interstitial fluids, and the circulation by a specific receptor-mediated uptake into endolysosomes (14). The question as to how antibodies can interfere with the activity of PR3 and impair its clearance by the natural plasma inhibitor α_1 PI, however, has not been addressed and answered.

Like other serine proteases of neutrophils, PR3 (15, 16) is synthesized as a proenzyme almost exclusively at the promyelocyte stage. Following cleavage of the signal peptide and translocation into the endoplasmic reticulum, the proenzyme (pro-PR3) egresses from the endoplasmic reticulum and migrates to the Golgi complex. At this stage, it carries a short amino-terminal extension, the dipeptide Ala-Glu. This dipeptide prevents the molecule from assuming its active enzyme conformation prematurely during biosynthesis but is cleaved off by the dipeptidyl aminopeptidase I (cathepsin C) just before storage in primary granules (17–20). After the removal of the amino-terminal dipeptide, the free positively charged amino terminus of Ile¹⁶ (chymotrypsinogen numbering) forms an internal salt bridge with the side chain carboxylate of Asp¹⁹⁴. This rearrangement stabilizes the oxyanion hole and renders the active site cleft fully accessible to substrates. During biosynthesis, some catalytically inactive pro-PR3 escapes granule targeting and is transported to the cellular surface for secretion. As pro-PR3 is a catalytically inactive precursor, it is not cleared by α_1 PI and may be more easily accessible for autoantibodies in GPA.

Although the crystal structure of mature PR3 (without inhibitors bound to it) has been reported (21), inferences about the pro-PR3 structure can be drawn from comparisons with other

closely related zymogen-enzyme pairs for which the structures are known. The best studied zymogen-enzyme pair, bovine cationic trypsinogen and its mature counterpart, bovine cationic trypsin (22), have identical structures for about 85% of the C α chain, but four segments of the main chain are entirely different: the amino terminus (Ile¹⁶–Gly¹⁹), the so-called autolysis loop (Gly¹⁴²–Ala¹⁵²), the Val¹⁸⁵–Gly¹⁹³ loop, and the Val²¹⁶–Leu²²³ loop (22). The latter three loops form the activation domain in the active enzyme in which the free amino terminus is inserted into the so-called activation pocket of the zymogen. All four segments are highly flexible in the zymogen but ordered in the active enzyme. Allosteric regulation of the two segments around residues 190 and 220 essentially switches the molecule from a functionally incompetent zymogen into a catalytically competent state and creates the S1 binding site and oxyanion hole (22, 23). This conformational switch between the proenzyme state and the catalytically active state of the mature enzyme is the well established structural basis for allosteric regulation of trypsin-/chymotrypsin-like enzyme activity (24).

The goal of our studies was to identify a new class of monoclonal antibodies (mAbs) that can discriminate between the catalytically competent state of the activation domain and the enzymatically inactive conformation of the zymogen. To develop such a monoclonal antibody with specificity close to the active site cleft and activity blocking properties, we immunized mice with a stable proform of PR3 carrying the tripeptide Ala-Glu-Pro at the mature amino terminus and selected hybridomas that showed preferential binding to the proform. We describe the binding specificity and activity blocking properties of the newly produced MCPR3-7 in comparison with the commercially available anti-PR3 mAb CLB-12.8. Besides the reduction of the PR3 activity, MCPR3-7 also interferes with the complexation of PR3 and α_1 PI and switches the active enzyme into an inactive, zymogen-like state by altering the autolysis and 190 loops. The antibody can be regarded as a starting point for the development of antibody-based allosteric inhibitors of PR3 that block activity and prevent the binding of neutrophil-activating, pathogenic anti-neutrophil cytoplasmic antibody.

EXPERIMENTAL PROCEDURES

Cells, Proteases, Antibodies, and Substrates—The human embryonic kidney (HEK) cell line 293 was purchased from the American Type Culture Collection (ATCC, Manassas, VA). The human embryonic kidney cell line 293 EBNA was received from Yves Durocher, National Research Council Canada, Montreal, Canada. Human neutrophil PR3 purified from neutrophils of peripheral blood was obtained from DIARECT AG, Freiburg, Germany. The anti-PR3 mAb MCPR3-2, which was used as control in most experiments, binds pro-PR3 and mature PR3 equally well and has been described previously (25). The anti-PR3 mAb CLB-12.8 was purchased from Sanquin, Amsterdam, The Netherlands. The FRET substrate Abz-Tyr-Tyr-Abu-ANB-NH₂ was kindly provided by Adam Lesner, University of Gdansk, Gdansk, Poland and was described previously (26). The FRET substrate 5-TAMRA-VADnVADYQ-diaminopropionyl fluorescein (DAP(CF)) was ordered from EMC Microcollections, Tübingen, Germany. The thiobenzyl ester sub-

strates Boc-Ala-Pro-nVal-SBzl and For-Ala-Ala-Pro-Abu-SBzl were purchased from Bachem AG, Bubendorf, Switzerland, and the substrate Boc-Ala-ONp was from Sigma-Aldrich. The substrate Ahx-PYFA-pNA was obtained from Dr. Francis Gauthier, Tours, France, and α_1 PI was from Athens Research and Technology, Athens, GA.

Expression of Recombinant Pro-PR3 and Mature PR3 Variants—The different recombinant PR3 variants used for the generation, selection, and characterization of mAbs with preferential binding to pro-PR3 are described schematically in Fig. 1A. The development of the cDNA construct coding for recombinant wild-type PR3 (pro-PR3ctp) and the cDNA construct of the active site mutant lacking the codons for the amino-terminal activation dipeptide (Δ PR3ctp-S195A) as well as their expression in HEK 293 cells have been described previously (18, 25). Similarly, the preparation and characterization of the active site mutant carrying a carboxyl-terminal c-myc-His tag (PR3-S195A-cmyc) has been described elsewhere (27). When expressed in HEK 293 cells and secreted into the cell culture supernatant, pro-PR3ctp and PR3ctp-S195A-cmyc have the conformation of pro-PR3, whereas Δ PR3ctp-S195A has the conformation of the mature enzyme (20, 27).

To obtain an immunogen that was not contaminated by traces of amino-terminally processed PR3 (mature PR3), we generated a pro-PR3 variant named proP-PR3ctp, which carries a three-residue-long propeptide ending with proline. This propeptide cannot be cleaved and removed by cathepsin C. The cDNA coding for the insertion of a proline residue between the natural activation dipeptide Ala-Glu and the Ile residue constituting the amino terminus of the mature enzyme was generated using the QuikChange site-directed mutagenesis kit (Stratagene Cloning Systems, La Jolla, CA) with the sense primer US127-5'-GCTGCGGAGCCAATCGTGGGC-3', the anti-sense primer US128-5'-GCCACGATGGCTCCGCAGC-3', and pro-PR3ctp as template. The underlined triplet of nucleotides encodes the inserted proline residue.

Stably transfected proP-PR3ctp-expressing HEK 293 cells were selected and cultured as described previously (20, 27), and proP-PR3ctp was purified from HEK 293 culture supernatant by immunoaffinity chromatography using MCPR3-2 coupled to a cyanogen bromide-activated Sepharose 4B column and 3 M KSCN in 1% NaHCO₃ as elution buffer. ProP-PR3ctp in the eluted fractions was quantified by capture ELISA as described (25), pooled, and concentrated after dialysis.

Production of PR3 Variants in Flip-in HEK 293 and HEK 293 EBNA Cells—The constructs as well as the expression of human pro-PR3 (pro(4DK)-PR3), gibbon pro-PR3, and the two human/gibbon chimeras were produced as described (28). Furthermore, human pro-PR3 was expressed by transient transfection of HEK 293 EBNA cells as described elsewhere (29). The catalytically inactive PR3 variant Δ PR3-S195A (Fig. 1A) was also produced in the HEK 293 EBNA expression system. Purification of His-tagged proteins from cell supernatants was carried out as described previously (29). The PR3 variants, which were produced in their proform, were converted into an active state by enterokinase from calf intestine (Roche Applied Science). After dialysis against 20 mM Tris-HCl, 50 mM NaCl, and

2 mM CaCl₂, pH 7.4, the proteins were cleaved at an enzyme to substrate ratio of 1:40 at room temperature overnight.

Generation of Antibodies and Selection of Hybridomas—For the generation of the mAb MCPR3-7, BALB/c mice were immunized with immunoaffinity-purified proP-PR3ctp following standard immunization protocols. Antibody titers of immunized mice were determined by ELISA. Spleen cells from immunized mice were fused with a FO myeloma cell line of BALB/c origin to generate hybridomas. Animal experimentation for this study was approved by the Institutional Animal Care and Use Committee. Handling and care of animals were in accordance with institutional guidelines.

For the identification and selection of hybridoma antibodies that bind to pro-PR3 but not to mature PR3, the following capture ELISA technique was applied. Immulon I strips were coated with rabbit anti-mouse IgG diluted 1:1000 in 0.5 M NaHCO₃ buffer, pH 9.6 overnight. After blocking with BSA/immunoradiometric assay buffer (50 mM Tris, 0.1 M NaCl, and 2% BSA, pH 7.4), 0.1 μ g of the monoclonal hybridoma antibodies or control antibody (MCPR3-2) was added and incubated at room temperature for 30 min while shaking. Supernatants from [³⁵S]methionine-labeled proP-PR3ctp- or Δ PR3ctp-S195A-expressing HEK 293 cells diluted 1:20 in immunoradiometric assay buffer (50 mM Tris, 0.1 M NaCl, and 0.1% BSA, pH 7.4) were added and incubated at room temperature for 60 min. After removal of unbound PR3 by washing, antibody-bound radioactivity was measured in counts/min for each well. The hybridomas generating the highest signal difference between pro-PR3 and mature PR3 were chosen for all subsequent experiments (MCPR3-7).

Biosynthetic Labeling and Immunoprecipitation—ProP-PR3ctp- and Δ PR3ctp-S195A-expressing HEK 293 cells were cultured in Dulbecco's modified Eagle's medium (DMEM) supplemented with 100 μ Ci/ml [³⁵S]methionine, penicillin, streptomycin, and 10% fetal bovine serum in a 5% CO₂ atmosphere at 37 °C overnight. Unless otherwise stated, all immunoprecipitation steps were performed at 4 °C. Staphylococcal protein A was incubated with rabbit anti-mouse IgG and then with different concentrations of MCPR3-7 (1:100, 1:200, and 1:400 dilutions of a 1.3 mg/ml stock solution) in each case for 1 h. The cell culture supernatants of biosynthetically labeled cells were precleared by incubation with staphylococcal protein A for 30 min followed by centrifugation at 10,000 \times g for 2 min. The precleared culture supernatants were then incubated for 10 min with the staphylococcal protein A/rabbit anti-mouse IgG/MCPR3-7 mixture and washed three times with radioimmune precipitation assay buffer (50 mM Tris, pH 8.0, 0.5% deoxycholate, 1% Triton X-100, 0.1% SDS, and 50 mM NaF in PBS to which 1 μ g/ml leupeptin, 2 μ g/ml aprotinin, and 75 μ g/ml PMSF were freshly added prior to use). The precipitate was resuspended in SDS sample buffer, boiled for 5 min, and centrifuged at 10,000 \times g for 2 min, and the supernatant was collected and stored at -20 °C until analysis by SDS-PAGE and Western blotting.

Bead-based Flow Cytometry—The possible competition between the two mAbs MCPR3-2 and MCPR3-7 in binding to pro-PR3 was analyzed by bead-based flow cytometry using the carboxyl-terminally tagged PR3 variant PR3ctp-S195A-cmyc

Antibodies Interfering with PR3 Activity and Inactivation

(pro-PR3) (30). Stably transfected HEK 293 cells expressing the proforms were grown in serum-free medium for 2 days. Cell culture supernatants were concentrated using an Amicon Centrplus C-10 with a cutoff of 10,000 Da. Imidazole was added to a final concentration of 20 mM, and the concentrate was applied to a HiTrap chelating high performance column (GE Healthcare) according to the manufacturer's instructions. Proteins were eluted with 20 mM phosphate, 500 mM NaCl, and 200 mM imidazole. Imidazole was removed by centrifugation through a spin column equilibrated with 50 mM sodium phosphate, 300 mM NaCl, and 0.01% Tween 20, pH 8.0. Proteins were quantified by Coomassie Plus[®] (Pierce). A total of 2.8×10^6 beads coated with PR3 variants were incubated with 0.25 $\mu\text{g}/100 \mu\text{l}$ MCPR3-2 or MCPR3-7 as described. After washing with PBS, 0.1% BSA, and 0.01% Tween 20, the beads were incubated with 100 μl of a 1:50 dilution of FITC-conjugated MCPR3-2 or FITC-conjugated MCPR3-7 (prepared in our laboratory) for 5 min, washed, and analyzed by FACScan (setting, fluorescence = 1 at 682 nm).

FRET-based Activity Assay—The activity of PR3 variants diluted to 50 nM in Tris-HCl buffer (100 mM Tris, 500 mM NaCl, and 0.01% Brij 39, pH 7.5) was measured over time using the FRET substrate Abz-Tyr-Tyr-Abu-ANB-NH₂ (excitation at 325 nm, emission at 400 nm) at a concentration of 800 nM.

To locate the epitope of MCPR3-7, the activity of human PR3, gibbon PR3, and two gibbon/human chimeras (after activation of the respective pro(4DK) precursors) was determined. The activity of proteases was measured directly after adding a 2-fold molar excess of MCPR3-7. As controls, the emission of the FRET substrate without the enzyme and the activity of the enzyme without the antibody were measured. To detect the inhibitory effect of mAbs, the activity of PR3 was measured in the presence of increasing concentrations (0–750 nM) of MCPR3-7, CLB-12.8, and MCPR3-2. The activity was recorded over time directly after adding the mAbs. The effect of MCPR3-7 on PR3-mediated cleavage of the FRET substrate 5-TAMRA-VADnVADYQ-DAP(CF) (5 μM ; excitation at 485 nm, emission at 520 nm) was measured over time. The activity of a 50 nM PR3 solution in activity buffer (50 mM Tris, 150 mM NaCl, and 0.01% Triton X-100, pH 7.4) was determined directly after adding a 3-fold molar excess of the antibody.

Absorbance-based Activity Assay—To search for conformational changes of PR3 in response to MCPR3-7 binding, the cleavage of different substrates was investigated. The activity of 50 nM PR3 in activity buffer at a 3-fold molar excess of MCPR3-7 was compared with its activity in the absence of antibodies using Ahx-PYFA-pNA, Boc-Ala-ONp, Boc-Ala-Pro-nVal-SBzl, and For-Ala-Ala-Pro-Abu-SBzl (1 mM each) as substrates. For the reaction with the two thiobenzyl ester substrates, 5,5'-dithiobis(2-nitrobenzoic acid) was added to the samples at a concentration of 500 μM .

ELISA—To investigate the differential interactions of mAbs with PR3-inhibitor complexes, two covalent and two canonical complexes were assembled. The covalent complexes were formed with active PR3 (converted pro(4DK)-PR3) and $\alpha_1\text{PI}$ or AAPV-chloromethyl ketone (CMK) (American Peptide Co., Sunnyvale, CA), and the canonical complexes were formed with active PR3 and elafin or catalytically inactive $\Delta\text{PR3-S195A}$ in

association with $\alpha_1\text{PI}$ (PR3* $\alpha_1\text{PI}$). The PR3-inhibitor complexes were coated on nickel plates via the His tag of the PR3, and a capture ELISA was performed as described elsewhere (31). The coating concentration of the PR3 complexes was 2 $\mu\text{g}/\text{ml}$. The dilution of the mAb was 1:1000 for CLB-12.8, 1:5000 for MCPR3-2, 1:200 for MCPR3-7, and 1:50 for the IgG1 control antibody (Mouse IgG1Pure, BD Biosciences). As secondary antibody, goat anti-mouse HRP antibody was used (dilution, 1:2500), and the reaction was developed with a peroxidase substrate. Recognition of PR3 variants was normalized to the signal obtained with pro(4DK)-PR3, which was set to 100%.

Thermophoresis—MCPR3-7 and $\alpha_1\text{PI}$ were labeled with the red fluorescent dye NT647 using the Monolith NT Protein Labeling kit RED (NanoTemper Technologies, Munich, Germany) according to the supplied protocol. This approach is based on covalently attaching NT647 *N*-hydroxysuccinimide ester to primary amines of lysine residues. Prior to thermophoresis experiments, the free dye was removed via dialysis.

To quantify the affinity of MCPR3-7 to different PR3 conformations, a 1:1 dilution series of pro(4DK)-PR3, PR3-CMK, or PR3 was prepared starting at a maximum concentration of 5 μM each. To guarantee constant buffer conditions throughout the dilution, the proteinases were diluted in the exact same buffer as the stock solution: 20 mM sodium phosphate, 300 mM NaCl, and 0.02% Tween 20, pH 6.2 with (PR3-CMK) or without (pro(4DK)-PR3 and PR3) 1.75% DMSO. Each point of the dilution series was mixed 1:1 with MCPR3-7-NT647 in PBS with 0.05% Tween 20 and 2% BSA to yield a constant final antibody concentration of 50 nM and a maximum proteinase concentration of 2.5 μM .

In addition, thermophoresis was used to test whether the mAbs MCPR3-7 and CLB-12.8 have an influence on the formation of canonical $\alpha_1\text{PI}$ -PR3 complexes. Separate 1:1 dilution series of $\Delta\text{PR3-S195A}$ in EB buffer (20 mM sodium phosphate and 500 mM NaCl, pH 7.4) were prepared, starting at a maximum concentration of 12 μM each. 5 μl of each dilution step were mixed with 1 μl of either PBS or 1 μl of a 4 μM stock of MCPR3-7 or CLB-12.8 in PBS, which results in an antibody concentration of 670 nM. After incubating the sample for 1 h at room temperature in the dark, 1 μl of a 6.15 μM $\alpha_1\text{PI}$ -NT647 solution in PBS with 0.05% Tween 20 was added, resulting in a final $\alpha_1\text{PI}$ concentration of 880 nM. To avoid adsorption to the capillary walls during the measurement, BSA was added at a final concentration of 1% (w/v).

Standard treated enhanced gradient capillaries (NanoTemper Technologies) were filled with the samples. Measurements were performed on a Monolith NT.115 system (NanoTemper Technologies) at a constant ambient temperature of 20 °C using 60% light-emitting diode (experiments with MCPR3-7-NT647) or 20% light-emitting diode (experiments with $\alpha_1\text{PI}$ -NT647) and 20% infrared (IR) laser power with laser on and off times of 40 and 20 s.

After bleaching correction, the fluorescence after temperature jump and early thermophoresis was normalized to the fluorescence before laser heating with a LabVIEW routine. Mean F_{norm} values of at least three technical repeats of each measurement were plotted on a linear *y* axis in per mil units (‰) against

the proteinase concentration on a $\log_{10} x$ axis. The standard deviation of the repeats was calculated for each point. To get a better estimate of the error, the mean of all standard deviations of a binding curve was determined. This mean error is visualized as an error bar on all points of the corresponding graph. Using IGOR Pro, a weighted fit to the quadratic solution of the mass action law

$$FB = \frac{[AB]}{[B]} = \frac{[A] + [B] + K_D - \sqrt{([A] + [B] + K_D)^2 - 4[AB]}}{2[B]} \quad (\text{Eq. 1})$$

where FB is the fraction bound, [A] is the concentration of the titrated binding partner, [B] is the concentration of the labeled binding partner, [AB] is the concentration of bound complex of A and B, and K_D is the equilibrium dissociation constant was performed with K_D as the single free fit parameter (32). K_D values are given together with an error estimation from the fit. The fitting procedure assumes a Gaussian, symmetric error distribution. Thus, the error can reach negative values if the sensitivity limit determined by the lowest detectable concentration of fluorescent partner is reached. In these cases, the K_D values are presented as an upper limit. F_{norm} of the unbound state as revealed by the fit was subtracted as a base-line value to yield ΔF_{norm} as depicted on the y axis of the figures.

Possible Interference of mAb with PR3 Complexation—The effect of mAbs on the covalent inactivation reaction of PR3 by $\alpha_1\text{PI}$ was measured over time. A 3-fold molar excess of mAbs was added to an 800 nM solution of active PR3 in Tris-HCl buffer and incubated at room temperature for 1 h. After adding a 5-fold molar excess of $\alpha_1\text{PI}$, the sample was incubated at 37 °C, and 10- μl aliquots were taken after different time points. The reaction was stopped by adding Laemmli buffer and heating to 95 °C for 10 min. Proteins in the samples were then separated by SDS-PAGE under reducing conditions and visualized by silver staining.

Isolation and Priming of Neutrophils—The recognition of PR3 on the neutrophil membrane from one normal donor was evaluated without and after stimulation with TNF α . The neutrophils were isolated from EDTA-anticoagulated blood by centrifugation on PolymorphprepTM (Accurate Chemical and Scientific Corp., Westbury, NY) and hypotonic lysis of erythrocytes with distilled water. Cells were washed with cold Hanks' balanced salt solution without $\text{Ca}^{2+}/\text{Mg}^{2+}$ (Mediatech Inc., Herndon, VA) and resuspended in Hanks' balanced salt solution with $\text{Ca}^{2+}/\text{Mg}^{2+}$ (Mediatech Inc.) to obtain 1×10^7 cells/ml. One-half of the preparation was primed with 2 ng/ml recombinant TNF α (Roche Applied Science) for 15 min at 37 °C before analysis of membrane expression. Non-primed neutrophils were analyzed for membrane expression immediately after isolation.

PR3 on Neutrophil Membranes—The recognition of PR3 on the membrane was evaluated using flow cytometry. All steps were performed on ice. Samples containing 1×10^6 neutrophils were fixed with 0.5% paraformaldehyde for 10 min, washed with PBS and 1% BSA by centrifugation at $1200 \times g$ at 4 °C for 3 min, and incubated with 0.5 mg/ml heat-aggregated goat immunoglobulins (IgG; Sigma) for 15 min to saturate Fc γ

receptors. Next, cells were stained with a saturating dose of mouse monoclonal IgG1 directed against human PR3 (MCPR3-2 and MCPR3-7) and anti-CD32 (AbD Serotec, UK) or with an IgG1 control antibody for 30 min. Unbound antibodies were washed off with PBS and 1% BSA, and the cells were incubated for 30 min with FITC-conjugated goat anti-mouse antibody. After washing, the fluorescence intensity was analyzed on a FACScan flow cytometer (BD Biosciences Immunocytometry Systems).

RESULTS

Identification of New mAbs with Preferential Binding to Pro-PR3—To generate antibodies with preferred specificity for the inactive conformation of pro-PR3, we produced a pro-PR3 variant that was resistant to cathepsin C cleavage and other exopeptidases. Non-hematopoietic cells like HEK 293 cells were found to be devoid of cathepsin C and could not properly convert recombinant neutrophil serine protease precursors to mature enzymes. Nevertheless, minimal amounts of amino-terminally processed active recombinant PR3 have been noticed in cell lysates of HEK 293 cells transfected with wild-type PR3 cDNA.⁴ Therefore, a PR3 variant with an amino terminus that cannot be trimmed by exo- and endopeptidases was constructed and expressed in a stable HEK 293 cell line. The cDNA construct proP-PR3ctp codes for the insertion of a proline residue between the natural propeptide Ala-Glu and the amino terminus of mature PR3. The resulting pro-PR3 variant (Fig. 1A) with the amino-terminal sequence Ala-Glu-Pro-Ile-Val-Gly-Gly cannot be processed by cathepsin C or other exodipeptidases. This was verified by radiosequencing of supernatants and lysates from [³H]isoleucine pulse-labeled HEK 293 cells expressing proP-PR3ctp (data not shown). ProP-PR3ctp was purified via immunoaffinity chromatography from cell culture supernatants of HEK 293 cells.

Splenocytes from BALB/c mice immunized with this pro-PR3 variant were fused with FO myeloma cells. The resulting hybridoma cell clones were screened for anti-PR3 IgG secretion via capture ELISA as described under "Experimental Procedures." Supernatants from 43 cell clones that reacted with pro-PR3 in the initial capture ELISA were retested in parallel for reactivity with pro-PR3 and mature PR3. Nineteen of these showed between 0 and 30% difference in reactivity (group A) with the two antigens, 13 showed a 31–60% difference (group B), and 11 displayed a 61–96% difference (group C). Four clones from group A, five from group B, and nine from group C were subjected to another round of dilution subcloning and retested for differential binding to pro-PR3 and mature PR3. Only six clones with persistent pro-PR3 reactivity emerged. Four of these showed similar reactivity with both antigens, and two had a 75% greater reactivity with pro-PR3 compared with mature PR3. Clone MCPR3-7, generating the highest signal difference between pro-PR3 and mature PR3 in the capture ELISA (Fig. 1B), was chosen for further characterization.

To demonstrate the differential binding of MCPR3-7 to pro-PR3 and mature PR3, rabbit anti-mouse IgG bound to *Staphylococcus aureus* protein A was incubated with dilutions (rang-

⁴ U. Specks, unpublished data.

Antibodies Interfering with PR3 Activity and Inactivation

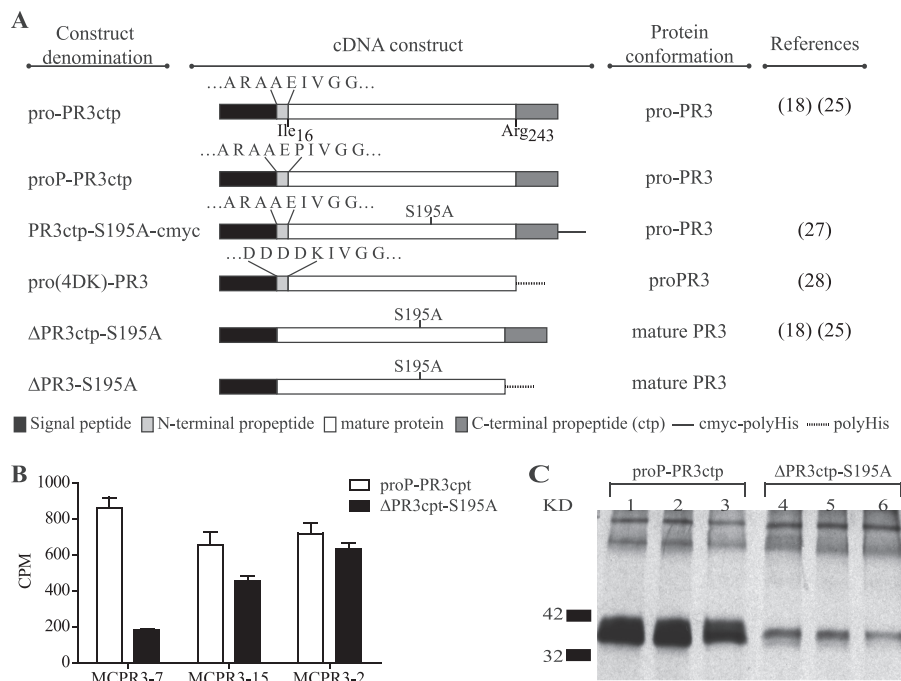


FIGURE 1. Schematic diagram of cDNA constructs and identification of pro-PR3-binding monoclonal antibodies. *A*, the PR3 variants pro-PR3ctp, proP-PR3ctp, PR3ctp-S195A-cmyc, and pro(4DK)-PR3 are secreted by HEK 293 cells as an unprocessed zymogen (pro-PR3). ΔPR3ctp-S195A and ΔPR3-S195A do not contain the amino-terminal activation dipeptide AE and are secreted as mature but catalytically inactive PR3. Ile¹⁶ and Arg²⁴³ represent the amino-terminal and carboxyl-terminal residue, respectively, of mature PR3 and are numbered as in Protein Data Bank code 1FUJ according to chymotrypsinogen. Except proP-PR3ctp and ΔPR3-S195A, all constructs have been described previously (see references for more details). ProP-PR3ctp carries an additional proline residue between the natural dipeptide AE (*light gray* segment) and the amino terminus of mature PR3 (*white bar*). The resulting amino-terminal amino acid sequence of proP-PR3ctp is AEPIVGG. The insertion of this proline residue precludes the activation by cathepsin C and prevents any contamination by intracellularly processed (mature) PR3 in HEK 293 cells. The mutation S195A of the catalytic triad in mature PR3 eliminates the catalytic activity of the molecule, which was required to avoid autodigestion and damage of HEK 293 cells during biosynthesis of PR3. *B*, monoclonal antibodies from hybridoma supernatants were screened by capture ELISA with goat anti-mouse IgG. Subsequently, 0.025 μg of radiolabeled pro-PR3 (proP-PR3ctp) or mature PR3 (ΔPR3ctp-S195A) was added. The captured PR3 is quantified in counts/min (CPM). MCPR3-2 is known to recognize pro-PR3 and mature PR3 equally well and served as a control. MCPR3-7 displayed the largest difference in the binding to pro-PR3 and mature PR3. All other hybridomas (one example shown) discriminated less well between the two antigens. *C*, rabbit anti-mouse IgG bound to *S. aureus* protein A was incubated with various dilutions of MCPR3-7 (1.3 mg/ml stock solution) and used to immunoprecipitate radiolabeled pro-PR3 (proP-PR3ctp) or mature PR3 (ΔPR3ctp-S195A) from transfected HEK 293 cell supernatants. Immunoprecipitated proteins were then separated by SDS-PAGE (lanes 1–3, pro-PR3; lanes 4–6, mature PR3) and visualized by autoradiography (3 days of exposure). All dilutions of MCPR3-7 showed intense binding of pro-PR3 and weak recognition of mature PR3. Error bars represent S.E.

ing from 1:100 to 1:400 of a 1.3 mg/ml stock solution) of MCPR3-7 and was used to precipitate 500 ng/ml radiolabeled pro-PR3 and mature PR3 from stably transfected HEK 293 cell culture supernatants. Immunoprecipitated proteins were separated by SDS-PAGE (12% gels) under reducing conditions (Fig. 1C). The preferential recognition of pro-PR3 by MCPR3-7 was observed at all mAb concentrations tested. These findings confirmed that MCPR3-7 preferentially bound pro-PR3 but that there was some cross-reactivity with mature PR3.

Characterization of the MCPR3-7 Binding Site—To determine whether MCPR3-7 and MCPR3-2, which is known to bind pro-PR3 and mature PR3 equally well, recognize non-overlapping PR3 surface structures, we modified the bead-based capture assay. Pro-PR3 (PR3ctp-S195A-cmyc) was attached to the beads as an antigen because both mAbs bound to it with similar affinity. Fig. 2A shows that each unlabeled mAb inhibited the binding of its FITC-labeled derivative by more than 90% (*upper left and lower right panels*). In contrast, unlabeled MCPR3-7 did not interfere with the binding of FITC-conjugated MCPR3-2 (*lower left panel*), and unlabeled MCPR3-2 inhibited the binding of FITC-conjugated MCPR3-7 by only 21% (*upper right panel*). These findings

corroborated previous data (30), clearly indicating that MCPR3-7 recognized a unique epitope on pro-PR3 that is different from that of MCPR3-2 and all other mAbs. The precise binding site of MCPR3-7, however, remained uncertain as the epitope on human PR3 was not lost after replacing Ala¹⁴⁶, Trp²¹⁸, and Leu²²³ with the respective residues of murine PR3.

To map the interaction of MCPR3-7 in closer detail, we studied its effects on the activity of mature human PR3 in a FRET-based activity assay. In contrast to CLB-12.8 and MCPR3-2, MCPR3-7 inhibited the activity of human PR3 (Fig. 2B). This inhibitory effect was already observed at a 1:1 ratio of PR3 and MCPR3-7. PR3 was completely inhibited at a 3-fold molar excess of MCPR3-7, whereas CLB-12.8 and MCPR3-2 did not show any effect on PR3 activity even at a 15-fold molar excess over PR3. This inhibitory effect of MCPR3-7 was sequence-dependent as it was much less pronounced for the closely related PR3 homolog of a gibbon species (Fig. 2C, *second panel*). The activity of a chimeric PR3 variant composed of the amino-terminal subdomain of gibbon PR3 and the carboxyl-terminal subdomain of human PR3 (gib/hPR3) was also suppressed by MCPR3-7 (Fig. 2C, *right panel*). Conversely, MCPR3-7 had a much smaller effect on the activity of an h/gibPR3 chimera with

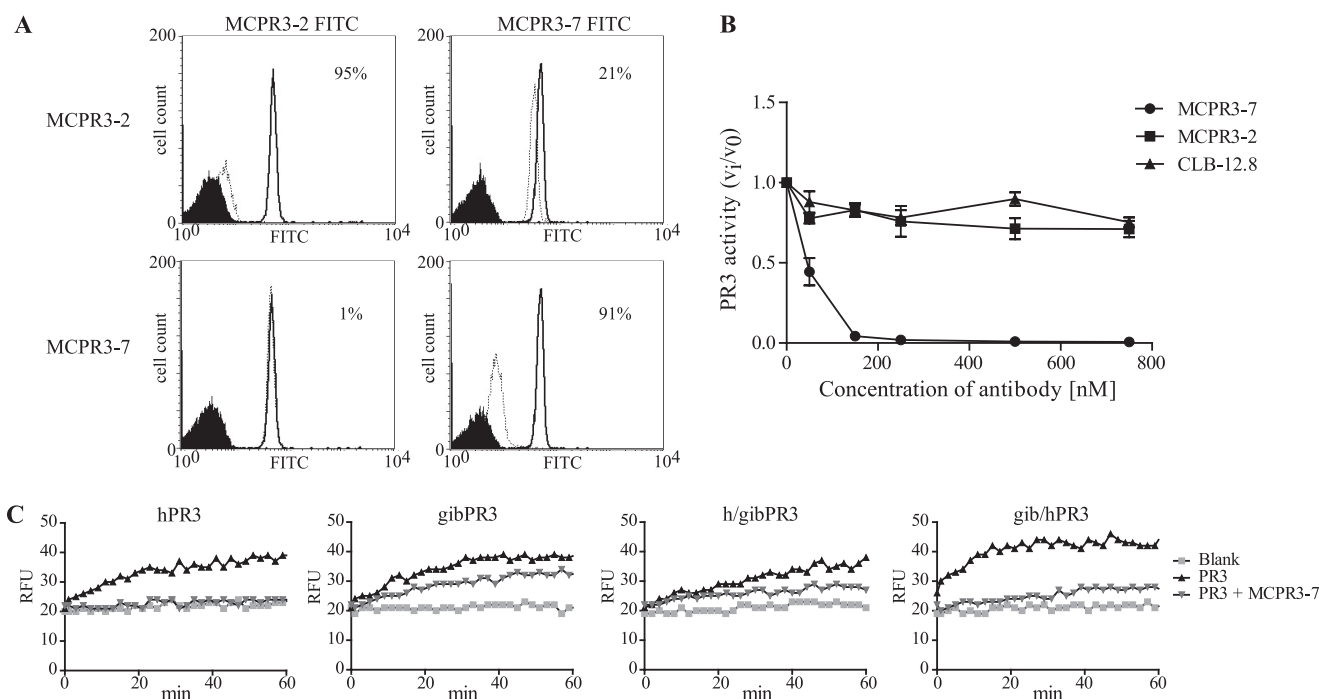


FIGURE 2. Characterization of the MCPR3-7 binding site. A, pairwise competition between the unlabeled PR3-specific mAbs MCPR3-2 and MCPR3-7 and FITC-conjugated MCPR3-2 and MCPR3-7 using a bead-based FACS assay. Unlabeled MCPR3-2 and MCPR3-7 (on the left) served as inhibitors for the binding of the respective FITC-tagged mAbs (on the top) to immobilized pro-PR3. Pro-PR3 was chosen as it binds equally well to both mAbs. The continuous lines represent the binding of FITC-conjugated mAbs to pro-PR3-coated beads in the absence of a competing mAb; black reference histograms indicate the lack of binding to uncoated beads; the dashed lines refer to the binding of FITC-conjugated mAbs after preincubation of the pro-PR3-coated beads with unlabeled mAbs. The degree of inhibition of the FITC-conjugated mAb after preincubation with unlabeled antibodies is expressed in percent. Using the same mAb as unlabeled competitor, inhibition was 95% for MCPR3-2 (A, upper left panel) and 91% for MCPR3-7 (A, lower right panel). Unlabeled MCPR3-7 did not interfere with the binding of FITC-conjugated MCPR3-2 (A, lower left panel), and the binding of FITC-conjugated MCPR3-7 was only inhibited by 21% due to unlabeled MCPR3-2 (A, upper right panel). These findings indicate that the two mAbs recognize distinct and non-overlapping epitopes. B, PR3 activity was measured in the presence of three mAbs at different concentrations to study their differential inhibitory capacity ($n = 3$; \pm S.E.). The activity of PR3 (50 nM) was measured with 800 nM Abz-Tyr-Tyr-Abu-ANB-NH₂. MCPR3-2 and CLB-12.8 did not have any effect on the PR3 activity. By contrast, MCPR3-7 completely inhibited PR3 at a 3-fold molar excess and above. C, the activity of gibbon PR3, human PR3, and two gibbon/human chimeras was determined in the presence of a 2-fold molar excess of MCPR3-7. The h/gibPR3 variant consists of the human amino-terminal β -barrel and the gibbon carboxyl-terminal β -barrel, whereas the gib/hPR3 variant contains the human carboxyl-terminal β -barrel. The activity of PR3 variants in the presence or absence of MCPR3-7 was measured utilizing a highly sensitive FRET substrate, Abz-Tyr-Tyr-Abu-ANB-NH₂, and is shown in relative fluorescence units (RFU) as an example of three technical repeats. MCPR3-7 strongly inhibited hPR3 and gib/hPR3 but not h/gibPR3. Accordingly, the epitope of MCPR3-7 is located on the carboxyl-terminal β -barrel. Error bars represent S.E.

a humanized amino terminus and a carboxyl-terminal gibbon subdomain (Fig. 2C, third panel). As MCPR3-7 completely inhibited the activity of the gibbon/human PR3 but not that of the human/gibbon PR3 chimera, we conclude that its major binding region is located within the carboxyl-terminal subdomain (barrel) of human PR3.

Binding Affinity of MCPR3-7 for Different PR3 Conformations—To quantify the differences in binding affinities of MCPR3-7 to either pro(4DK)-PR3, active PR3, or PR3 in a complex with AAPV-CMK (see below for details), microscale thermophoresis (MST), the directed movement of molecules along a microscopic temperature gradient, was utilized. MST can be used to determine biomolecular binding affinities in free solution as it probes any binding-induced changes in size, charge, or conformation (33). In an all-optical, free solution-based approach, thermophoresis of the samples inside a glass capillary was induced via IR laser heating and observed via detection of a red fluorescent label covalently attached to MCPR3-7. When the IR laser is turned on, the fluorescence signal drops for two reasons: first, because of an intrinsic temperature effect on the fluorophore (100-ms time scale), the so-called temperature jump, and second, because of thermophoretic depletion (several seconds). Pro(4DK)-PR3, CMK-in-

hibited PR3, and PR3 were titrated against a fixed concentration of labeled MCPR3-7. Binding induced a change in both temperature jump and thermophoresis. As the thermophoretic depletion is linear to the bound fraction, the dissociation constant K_D was determined by fitting the data points to the quadratic solution of the mass action law. MST revealed a high binding affinity of MCPR3-7 to the proform with a $K_D \leq 10$ nM. By contrast, we were not able to detect any binding of MCPR3-7 to the active conformation of PR3 stabilized by complexation with CMK, an irreversible, mechanism-based small molecule inhibitor of PR3 (Fig. 3A). This clearly indicated that MCPR3-7 selectively recognized the zymogen conformation of PR3. Using active PR3, however, we noticed that MCPR3-7 was indeed able to interact with mature PR3 but with a much lower affinity in comparison with pro(4DK)-PR3 (Fig. 3B). This is probably due to a reversible allosteric switch from the active form of PR3 to a more zymogen-like conformation in free solution that is recognized by MCPR3-7. A K_D of 0.4 ± 0.2 μ M could be inferred from the data. This means that the affinity of MCPR3-7 for the free active form is \sim 40-fold lower than for its proform.

Interaction of mAbs with Different PR3-Inhibitor Complexes—To test the differential binding capabilities of mAbs to PR3-inhibitor complexes, complexes were formed by adding a

Antibodies Interfering with PR3 Activity and Inactivation

10-fold molar excess of each inhibitor to PR3 and incubating these mixtures at 37 °C for 1 h. To generate covalently linked complexes, natural α_1 PI or AAPV-CMK was added to active His-tagged PR3 (activated pro(4DK)-PR3). In the case of α_1 PI, the resulting complexes were purified over a nickel column and checked for complete complexation on a polyacrylamide gel (data not shown). Free, uncomplexed PR3 was excluded in this way. The canonical PR3-elafin complexes were also made with active enzyme, whereas the catalytically inactive Δ PR3-S195A

variant was used to assemble the so-called canonical encounter complex between PR3 and α_1 PI (PR3* α_1 PI). These PR3 complexes were immobilized on nickel plates. MCPR3-7 (Fig. 4A) only showed weak binding to active PR3, PR3-elafin, CMK-inhibited PR3, and the encounter complex. By contrast, MCPR3-7 strongly bound to pro(4DK)-PR3. Most surprisingly, MCPR3-7 also showed strong binding to the covalent PR3* α_1 PI complex although, as mentioned before, not to the PR3*AAPV-CMK complex. The structural background for its differential binding to serpin-inactivated PR3 and canonical PR3 complexes is the precursor-like conformation of PR3 in the covalent serpin complex, whereas complexation of active PR3 with AAPV-CMK and elafin as well as complexation of catalytically inactive PR3 to α_1 PI does not alter the mature conformation of PR3. Conversely, CLB-12.8 was able to bind all PR3 variants and inhibitor complexes except for the covalent PR3* α_1 PI complex (Fig. 4B). The epitope of CLB-12.8 lies close to the active site cleft and may become inaccessible after binding and rearrangement of α_1 PI (30). MCPR3-2 was chosen as an appropriate coating control (Fig. 4C) as it could bind to all PR3 variants. Thus, equal coating of wells with different variants was ascertained. No interaction between PR3 complexes and an isotype control antibody was observed.

Inhibitory Effect of mAbs on Serpin Complexation—To assess the impact of the antibodies on the interaction between PR3 and α_1 PI, we monitored the covalent complexation in the presence of a 3-fold molar excess of mAbs after different incubation times by SDS-PAGE. The reaction of PR3 with α_1 PI in the absence of antibodies at different time points is shown in Fig. 5A. The complexes occurred immediately after mixing the two components, and the reaction was already completed within 5 s of incubation. In contrast, preincubation of PR3 with MCPR3-7 led to a delay of complexation (Fig. 5B). At the early time points until 15 s, hardly any complexes could be detected. Complex formation was only completed within a time span of 3 min. By comparison, CLB-12.8 (Fig. 5C) and MCPR3-2 (Fig. 5D) did not show any effect on PR3* α_1 PI complexation. Under these assay conditions, complexes were formed within the first 5 s as seen without antibodies, and it took only 15 s until all PR3 was covalently attached to α_1 PI. These findings clearly indicate that the binding of MCPR3-7 to PR3 affects the covalent complexation with α_1 PI and delays the irreversible inhibition of PR3.

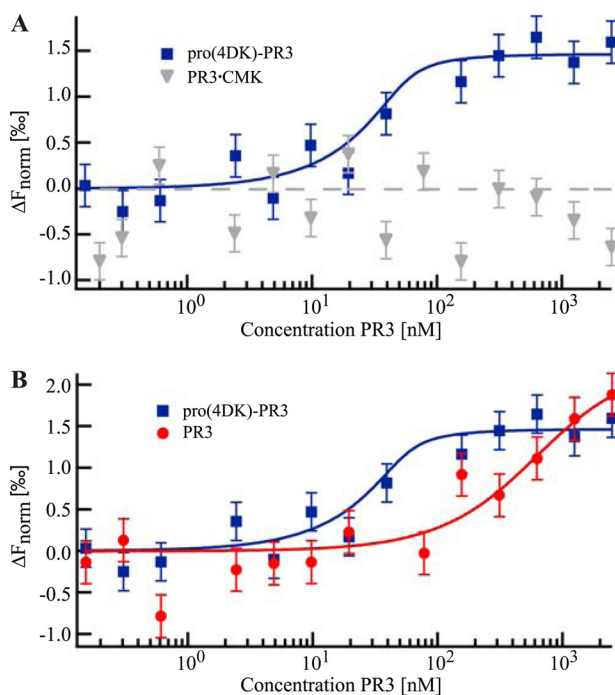


FIGURE 3. Thermophoretic quantification of MCPR3-7 binding affinity. Starting at a maximum concentration of 2.5 μ M, pro(4DK)-PR3, active PR3, and PR3 complexed with AAPV-CMK (PR3.CMK) were titrated against a constant concentration of fluorescently labeled MCPR3-7 (50 nM). The biophysical method of MST allows an absolute affinity quantification by fitting the thermophoretic depletion to the quadratic solution of the mass action law with the dissociation constant K_D as the single free fit parameter. Data points represent the mean value of at least three technical repeats; the error bars represent the mean of the S.D. K_D values are given with an error estimation from the fit. **A**, MST revealed a strong binding affinity of MCPR3-7 to pro-PR3 ($K_D \leq 10$ nM; blue rectangles). In contrast, MCPR3-7 did not show binding to the mature conformation of the PR3-CMK complex (gray triangles). **B**, active PR3 was bound with a much lower affinity ($K_D = 0.4 \pm 0.2$ μ M) corresponding to a 40-fold weaker binding compared with pro-PR3 (red circles).

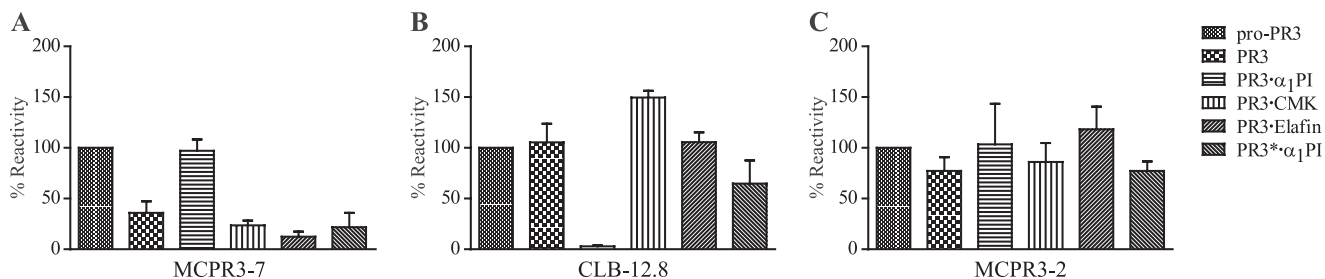


FIGURE 4. Interaction of monoclonal antibodies with different PR3-inhibitor complexes. Inhibitors were added to PR3 in solution at a 10-fold molar excess relative to PR3 and incubated at 37 °C for 1 h. His-tagged pro-PR3 (pro(4DK)-PR3), active PR3 (activated pro(4DK)-PR3), and PR3 complexes were immobilized on nickel plates. Binding of the monoclonal antibodies was analyzed via ELISA using a secondary anti-mouse HRP-conjugated polyclonal antibody. Recognition of PR3 variants of three technical repeats was normalized to the signal obtained with pro-PR3, which was set to 100% ($n = 3$; \pm S.E.). **A**, MCPR3-7 was able to bind strongly to pro-PR3 and covalent PR3* α_1 PI complexes but failed to bind to active PR3 or other complexes. **B**, no binding of CLB-12.8 to the covalent PR3* α_1 PI complex was observed, whereas all other variants were bound similarly. **C**, binding of MCPR3-2 was used as a coating control and showed similar binding to all complexes. Error bars represent S.E.

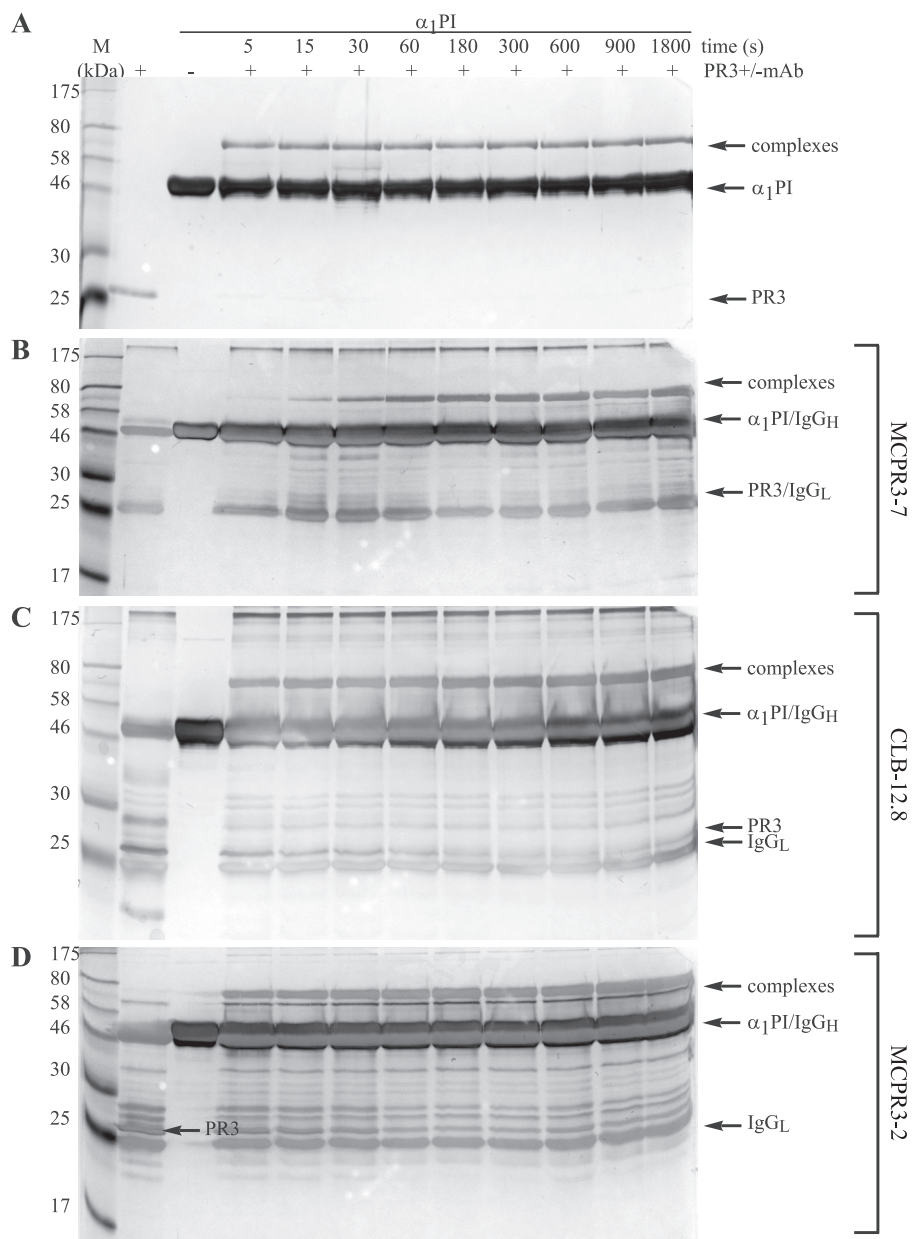


FIGURE 5. **Interference of monoclonal antibodies with PR3-serpin complexation.** A, covalent complexation of PR3 (800 nm) with α_1 PI was measured over time by adding a 5-fold molar excess of α_1 PI at 37 °C. B–D, after preincubation of PR3 with a 3-fold molar excess of the different antibodies, the effects of MCPR3-7 (B), CLB-12.8 (C), and MCPR3-2 (D) on this reaction were measured. Examples of three technical repeats are shown. The covalent binding of α_1 PI to PR3 was delayed by MCPR3-7, whereas CLB-12.8 and MCPR3-2 did not affect this complexation. *mAb*, monoclonal antibody; *IgG_H*, IgG heavy; *IgG_L*, IgG light.

Effects of mAbs on Noncovalent Complex Formation via Thermophoresis—To find out whether the mAbs MCPR3-7 and CLB-12.8 interfere with the formation of the canonical PR3- α_1 PI complex, thermophoretic competition experiments were performed. To this end, the binding of NT647-labeled α_1 PI to Δ PR3-S195A was quantified in the presence or absence of mAbs (Fig. 6). To form the PR3-mAb complexes, the components were preincubated for 1 h before adding labeled α_1 PI and measuring the binding affinity.

Δ PR3-S195A and α_1 PI bound with a K_D of $1.9 \pm 1.1 \mu\text{M}$ in the absence of mAbs. In the competition experiments, we were not able to use saturating amounts of MCPR3-7 as this antibody could not be concentrated to very high levels. We instead used a relatively low MCPR3-7 concentration of 570 nM. Thus, not

only MCPR3-7- Δ PR3-S195A complexes but also free Δ PR3-S195A is present in solution. This reduces the putative overall effect of the antibody on the binding curve and leads to a more complex binding behavior. The thermophoresis signal corresponds to the binding of α_1 PI to free and MCPR3-7-bound Δ PR3-S195A, which is most likely characterized by two different K_D constants. The data could not be fitted to a more complex binding model as saturation was not reached in the binding curve, and data points for higher MCPR3-7 concentrations were limited.

We instead chose to fit the data to the simple model according to the mass action law, which in this case revealed an apparent K_D of $5.6 \pm 1.0 \mu\text{M}$. This apparent K_D corresponds not only to the binding of α_1 PI to MCPR3-7- Δ PR3-S195A complexes

Antibodies Interfering with PR3 Activity and Inactivation

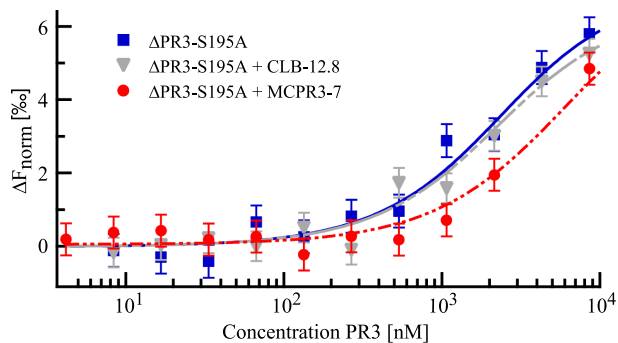


FIGURE 6. Evaluation of the interference of mAbs with the noncovalent PR3· α_1 PI complex formation via thermophoresis. Starting with a maximum concentration of 12 μM , dilution series of $\Delta\text{PR3-S195A}$ were prepared. Each sample of the dilution was mixed 6:1 with either PBS, MCPR3-7 in PBS, or CLB-12.8 in PBS to yield a mAb concentration of 670 nM. After preincubation for 1 h at room temperature, $\alpha_1\text{PI-NT647}$ was added to yield a final concentration of 880 nM. Thermophoresis revealed a K_D of $1.9 \pm 1.1 \mu\text{M}$ in the absence of mAbs (blue rectangles). Preincubation with CLB-12.8 did not have a significant effect on the affinity ($K_D = 1.8 \pm 0.8 \mu\text{M}$; gray triangles). In contrast, preincubation with MCPR3-7 led to a right shift of the binding curve corresponding to a 3-fold decrease in the apparent affinity to $\alpha_1\text{PI}$ ($K_D = 5.6 \pm 1.0 \mu\text{M}$; red circles). Error bars represent S.D.

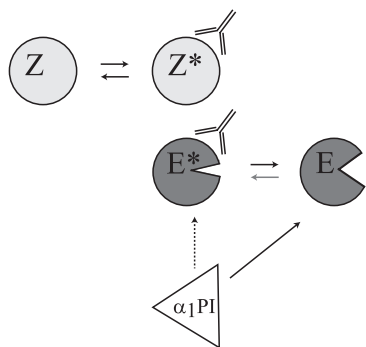


FIGURE 7. Impact of MCPR3-7 on PR3 activity and $\alpha_1\text{PI}$ inhibition. Binding of MCPR3-7 to the proform of PR3 (Z) leads to slight conformational changes of the zymogen (Z^*). The mature form of PR3 occurs in an equilibrium between a highly favored active (E) and an inactive (E^*) conformation. Binding of the antibody shifts this equilibrium between E and E^* toward the inactive E^* . The antibody interaction stabilizes an altered conformation of E (modified substrate binding left; left shape) and changes activity and substrate specificity of PR3 (open substrate binding left; right shape). It also has an inhibitory effect (dotted arrow) on the complexation with $\alpha_1\text{PI}$.

but also to $\alpha_1\text{PI}$ binding to free $\Delta\text{PR3-S195A}$ still present in solution. Taking into account the rather high affinity between $\alpha_1\text{PI}$ and $\Delta\text{PR3-S195A}$ ($1.9 \mu\text{M}$), the actual binding affinity of $\alpha_1\text{PI}$ for MCPR3-7- $\Delta\text{PR3-S195A}$ complexes can be expected to be lower than the measured apparent affinity (K_D of $5.6 \pm 1.0 \mu\text{M}$). The competition experiment demonstrates the inhibiting impact of MCPR3-7 on PR3· $\alpha_1\text{PI}$ noncovalent complex formation: preincubation with MCPR3-7 reduced the apparent affinity by a factor of 3. This inhibitory effect was already observed despite a relatively low MCPR3-7 concentration. Preincubation of $\Delta\text{PR3-S195A}$ with a higher MCPR3-7 concentration can be expected to lead to a much more pronounced decrease of the apparent affinity to $\alpha_1\text{PI}$. This finding clearly indicates that binding of MCPR3-7 leads to a conformational change of the free active PR3 and impairs the canonical interaction of PR3 and $\alpha_1\text{PI}$ (Fig. 7).

In contrast to this pronounced impact of MCPR3-7, preincubation of $\Delta\text{PR3-S195A}$ with CLB-12.8 did not have an effect

on its affinity to $\alpha_1\text{PI}$. The fitted binding curve depicted a nearly perfect overlay of the curve without mAbs, and the K_D of $1.8 \pm 0.8 \mu\text{M}$ did not significantly differ from the K_D without mAbs ($1.9 \pm 1.1 \mu\text{M}$). The affinity of CLB-12.8 to $\Delta\text{PR3-S195A}$ is expected to be much higher than the affinity of MCPR3-7 to $\Delta\text{PR3-S195A}$. Thus, when adding the same concentration of CLB-12.8 and MCPR3-7, a much higher amount of CLB-12.8-PR3· $\alpha_1\text{PI}$ complexes is present in solution. Nevertheless, CLB-12.8 did not have any effect on the canonical $\Delta\text{PR3-S195A}$ · $\alpha_1\text{PI}$ complexation.

Activity Changes of PR3 Induced by MCPR3-7—To determine which subsites of PR3 are affected by conformational changes upon MCPR3-7 binding, the activity of PR3 toward different substrates was tested in the presence and absence of MCPR3-7. We used substrates with different amino acids at the P1 site and different leaving groups at the P1' site. The cleavage of the substrate Abz-Tyr-Tyr-Abu-ANB-NH₂ with the best fitting non-natural residue in P1 was strongly inhibited after binding of MCPR3-7 to PR3 (Fig. 8A). Likewise, the substrates 5-TAMRA-VADnVADYQ-DAP(CF) (Fig. 8B), an optimized extended peptide substrate, and Ahx-PYFA-pNA (Fig. 8C), a substrate with a relatively big leaving group in the P1' position, could no longer be cleaved by PR3-MCPR3-7 complexes. In contrast, the substrates Boc-Ala-ONp (Fig. 8D) and Boc-Ala-Pro-nVal-SBzl (Fig. 8E), which carry residues of different sizes in their P1 position but have relatively small leaving groups in the P1' position, were efficiently cleaved by PR3 even after binding of MCPR3-7. The cleavage of For-Ala-Ala-Pro-Abu-SBzl was partly inhibited by the binding of MCPR3-7 to PR3 (Fig. 8F), but PR3 still showed activity toward this substrate at a lower rate of about 50%. These findings strongly suggest that the conformation of the S1 pocket is not changed significantly after binding of MCPR3-7, but rather the S1' subsite of PR3 is changed. Smaller leaving groups can still interact with PR3-MCPR3-7 complexes, whereas substrates with larger leaving groups could not be cleaved.

Detection of PR3 Expression on Neutrophil Membranes—After biochemical characterization of MCPR3-7 and MCPR3-2, we explored these as potential tools to determine PR3 expression on the membranes of non-stimulated neutrophils. A bimodal expression pattern of PR3 representing a large population of PR3-positive and a small subpopulation of PR3-negative neutrophils from peripheral blood was observed using MCPR3-2 for the recognition of membrane-bound PR3 (Fig. 9A, continuous black line). The majority of cells expressed PR3 on their surface, and a much smaller number of cells had no detectable membrane PR3 (Fig. 9A). After TNF α priming, the membrane-bound PR3 fraction increased, and essentially all PMNs expressed PR3 on their surface (Fig. 9B). CD32 staining served as a positive control and is indicated by the dotted line.

When MCPR3-7 was used for the detection of membrane-bound PR3 on unstimulated neutrophils, the vast majority of cells did not display any membrane PR3, and only a tiny second population (arrow) with marginal MCPR3-7 reactivity was observed (Fig. 9C). After TNF α stimulation, a strong increase of membrane-bound PR3 was observed using MCPR3-2, and again this increase was not discernible with MCPR3-7; in fact,

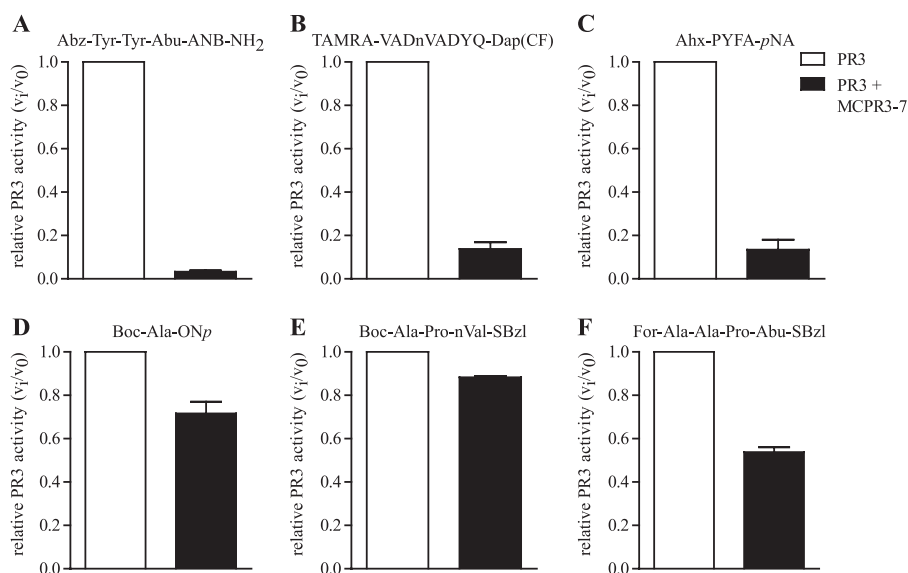


FIGURE 8. Binding of MCPR3-7 leads to an alteration in the S1' subsite of PR3. The effect of MCPR3-7 binding on the cleavage of different PR3 substrates was obtained in three technical repeats (\pm S.E.) with a 50 nM PR3 solution (A–E) or a 100 nM PR3 solution (F). A 3-fold molar excess of MCPR3-7 hindered the binding and cleavage of 800 nM Abz-Tyr-Tyr-Abu-ANB-NH₂ (A), 5 μ M 5-TAMRA-VADnVADYQ-DAP(CF) (B), and 1 mM Ahx-PYFA-pNA (C), whereas the cleavage of 1 mM Boc-Ala-ONp (D) and 1 mM Boc-Ala-Pro-nVal-SBzl (E) was not affected by the binding of MCPR3-7. For-Ala-Ala-Pro-Abu-SBzl (F) at a 1 mM concentration was still cleaved by PR3-MCPR3-7 complexes but at a lower rate of about 50%. The relative activity was determined by normalizing the activity of PR3 in the absence of antibodies to 1. Error bars represent S.E.

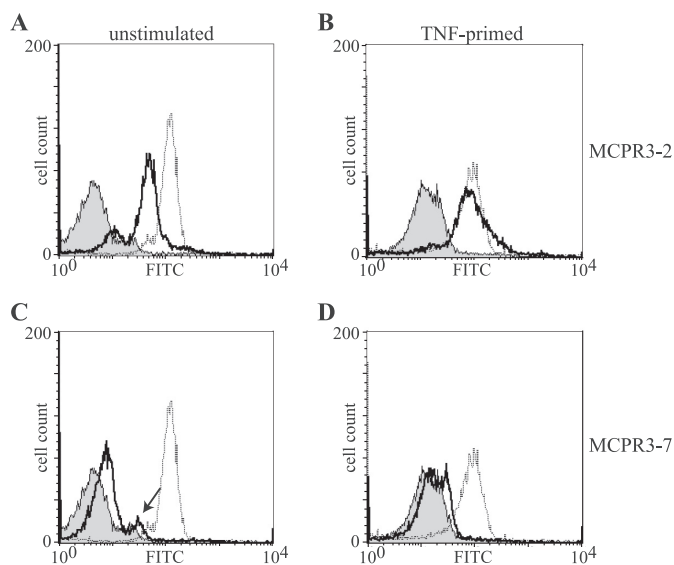


FIGURE 9. Differential recognition of PR3 on neutrophil membrane. Membrane expression of PR3 (continuous black line) in non-stimulated (A and C) and TNF α -primed neutrophils (B and D) was detected with MCPR3-2 (A and B) and MCPR3-7 (C and D). The gray peak represents an isotype control, and CD32 expression is represented by the dotted line. Non-stimulated neutrophils from this individual donor showed a bimodal distribution of PR3 membrane expression (A). PR3 membrane expression increased with priming of the neutrophils, and essentially all neutrophils expressed PR3 detectable with MCPR3-2 (B). By contrast, only a small fraction of unprimed neutrophils (arrow) expressed membrane PR3 using MCPR3-7 (C); PR3 expressed on primed neutrophils was essentially undetectable by MCPR3-7 (D).

essentially none of the cells displayed PR3 binding to MCPR3-7 (Fig. 9D).

The likely reason for these disparate findings is that human PR3 is attached to membranes specifically and forms complexes with CD177 and/or lipid bilayers with its active conformation. Under these conditions, it cannot present the structural determinants recognized by MCPR3-7. These obser-

vations are fully consistent with the idea that MCPR3-7 interacts with hydrophobic patches of the activation domain that are not accessible in membrane-bound PR3.

DISCUSSION

The initial goal of this study was to identify a mAb that preferentially recognized the inactive proform of human PR3. As the proform sequence of PR3 is only two residues longer than the mature enzyme and the amino-terminal sequence of serine proteases is highly conserved, a unique amino-terminal peptide as a proform-specific immunogen cannot be designed. We therefore aimed at identifying a conformation-specific antibody that discriminates between the two principal conformations of mature and catalytically inactive PR3 (23). To prevent any spurious amino-terminal processing during synthesis of the recombinant pro-PR3 as well as subsequent *in vivo* modifications of the immunogen after injection, we inserted a proline residue between the natural propeptide and the amino terminus of mature PR3 (Fig. 1A). Most proteases including exoaminopeptidases even in combination with dipeptidyl aminopeptidase I cannot remove this tripeptide after a proline residue (34, 35). Moreover, endogenous PR3 inhibitors cannot associate with the proform of PR3, which would restrict the surface-accessible area for antibody responses.

The challenge of this strategy, however, was the high structural similarity between the proform (Z) and the mature form of PR3 (E) whose conformations only differ in one subregion, the so-called activation domain (22). The activation domain of mature PR3 can adopt a zymogen-like conformation (E*) even after propeptide removal although with low probability (24). Binding of an antibody could forcefully induce this zymogen-like, catalytically inactive state even in mature, amino-terminally processed PR3, resulting in a loss of the S1 binding site and oxyanion hole. In view of these circumstances, it was not too

Antibodies Interfering with PR3 Activity and Inactivation

surprising that most mAbs generated failed to discriminate these two conformational states and showed very similar binding to both PR3 preparations.

Therefore, we selected a mAb on the basis of its differential affinities to both conformational states. To this end, we tested the direct binding of radioactively labeled pro-PR3 and PR3 to immobilized hybridoma IgG in an ELISA and to IgGs in solution followed by a single immunoprecipitation step (Fig. 1, B and C) and decided to use MCPR3-7, which showed the best discrimination between the two forms, for further analysis. To stabilize the activation domain in its active conformation, we used a mechanism-based small molecule inhibitor, Ala-Ala-Pro-Val-CMK, which forms a stable covalent complex with the transition state of PR3 (E) during catalysis, and tested the binding capability of this antibody to the active conformation. Indeed, this covalent complex displayed no detectable affinity toward MCPR3-7 as determined by ELISA (Fig. 4A) and by thermophoresis in free homogenous solution (Fig. 3A). In contrast, free active PR3 in solution showed some affinity for MCPR3-7 as revealed by thermophoresis, although it was ~40-fold lower than that of pro-PR3. This weak interaction with free mature PR3 was also detectable by ELISA. Consistent with this finding, MCPR3-7 showed minimal binding to the so-called canonical complexes in which PR3 is constrained to adopt its active conformation (Fig. 4A). Covalently linked complexes between α_1 PI and PR3, however, exposed the epitope for MCPR3-7 (Fig. 4A). Two studies reporting covalent serpin structures between pancreatic elastase and α_1 PI (36) and trypsin with an arginine mutant of α_1 -antitrypsin (37) point out that the P1 residue of the reactive center loop is no longer buried in the S1 pocket of the protease and that the so-called autolysis loop 142–149, the 186–190 loop, and the amino-terminal four residues are disordered. Within this covalent complex, the protease adopts a zymogen-like conformation (E*) that carries the target epitope of MCPR3-7 on the accessible surface.

The MCPR3-7 epitope was mapped to the carboxyl-terminal half of PR3 using human/gibbon chimera (Fig. 2C). Non-conservative residue substitutions are found on all three loops of the so-called activation domain: a Lys to Gly change at position 187, a Trp to Arg substitution at 218, and an Ala to Thr switch at position 146 within the autolysis loop (31). MCPR3-7, which is able to interact with free active PR3 in solution, showed a strong inhibitory effect toward human PR3 and most significantly inhibited the activity of the chimera with the human sequence in the carboxyl-terminal half, which makes up the activation domain. This differential inhibitory effect on the gibbon/human *versus* the human/gibbon chimera (Fig. 2C) clearly indicates that the major binding site of MCPR3-7 is on the carboxyl-terminal half of PR3. These functional data are fully consistent with our previous observation that the epitope of MCPR3-7 could be reconstructed at least in part by a murine to human residue swap in the carboxyl-terminal half of murine PR3 (T146A,R218W,Q223L) (30).

Two other mAbs tested in this study (Fig. 2B) did not show any effect on the activity of human PR3 and also did not interfere with the inhibitory effect of MCPR3-7, indicating that the antibody binding site of MCPR3-7 is unique and does not overlap with the epitopes of the other mAbs (Fig. 2A). The strong

inhibitory effect of MCPR3-7 was detected with an internally quenched substrate that occupies the S3 to S1 subsites of PR3 (Tyr-Tyr-Abu) and interacts with the S4 and S1' pockets by virtue of its quencher ANB-NH₂ and fluorogen Abz, respectively (Fig. 2B).

Substrates with other P1' leaving groups, *e.g.* 5-amino-2-nitrobenzoic acid (ANB-OH), *para*-nitroaniline (*p*NA), the benzyl mercaptan from thiobenzyl esters, the *para*-nitrophenol from Boc-L-Ala-ONp, do not interact with the S1' subsite of PR3 as efficiently as ANB-NH₂ substrates (26). Indeed, we found that cleavage of the small ester substrate Boc-L-Ala-ONp and the thioester substrate Boc-Ala-Pro-nVal-SBzl (Fig. 8, D and E) was not significantly affected by MCPR3-7, suggesting that the shape and/or access to the S1' pocket is primarily altered in the MCPR3-7-PR3 enzyme complex. Although the S1 pocket can accept P1 residues like Ala and nor-Val, which are shorter and longer than Abu, respectively, the S1' pocket appears to accept only smaller and less polar leaving groups after MCPR3-7 binding. Extended peptide substrates that have to be optimally aligned with the S1, S1', and S2' pockets were most strongly affected by MCPR3-7 binding (Fig. 8B). Moreover, binding of this antibody to active PR3 reduced canonical interactions with the reactive center loop of α_1 PI (Fig. 6) and subsequent covalent complex formation (Fig. 5). Taken together, all these characteristics qualify MCPR3-7 as a first prototype of a PR3-directed conformation-specific mAb with inhibitory properties. Inhibition is most likely due to an allosteric effect changing the autolysis and 187–190 loops. Both loops shape the size and physical character of adjacent subsites around the cleaved peptide bond, namely S1, S1', and S2'. The autolysis loop (Gly¹⁴⁵–Ala¹⁵²) shows the highest temperature factor of the main chain and is completely disordered in all four PR3 molecules of the asymmetric unit (21). A second region with a high temperature factor maps to the 187–190 loop (21). Such regions are in general preferred target sites for antibody interactions and are good targets for allosteric regulation of enzyme activities. Capture of partially altered loop conformations of PR3 by MCPR3-7 most likely changes substrate recognition and impairs the interaction of PR3 with the reactive center loop of α_1 PI.

Antibodies that can interfere with the catalytic activity of serine proteases are classified in two groups according to their mode of action as reviewed recently (38). Antibodies like MCPR3-7 induce an allosteric switch in the target antigen. This first group of antibodies does not directly compete with substrates for the active site cleft but rather interacts with a region at the periphery of the substrate binding region. Upon binding to the enzyme, antibodies of this group induce a significant conformational switch in surface loops that determine the shape and size of substrate binding pockets. The epitopes of these antibodies can be regarded as regulatory hot spots that are connected to mobile surface structures around the active site cleft. The altered conformation of loops surrounding the substrate binding pockets reduces, alters, or suppresses catalytic activity.

The second group can bind to the catalytic domain of a serine protease in a way that substrate access to the catalytic cleft is partially or fully occluded. Some complementarity-determin-

ing region loops of these antibodies directly insert into substrate binding pockets and occupy the substrate binding regions with high affinity. The latter type of antibodies, however, is rarely found in mammals and is hardly induced by immunizations as the antigen binding surface of mammalian antibodies mostly interacts with convex, protruding surfaces or a flat surface of an antigen. Directly inhibiting antibodies, however, have been produced in camelids. These antibodies represent unusual homodimers of a single heavy chain but are immunogenic in humans. Hence, camelid antibodies so far have found little application in preclinical (animal) and clinical studies.

Identification of monoclonal antibodies with similar properties and epitope specificity as MCPR3-7 but a higher affinity for mature PR3 should be of medical impact for two reasons. Antibodies of this type would not only block the binding of secreted soluble PR3 to neutrophils membranes but also could serve as selective PR3 inhibitors and clearers of PR3. Application of these antibodies in GPA patients may reduce the extent of neutrophil activation by anti-neutrophil cytoplasmic antibody via membrane-bound PR3 and Fc γ receptors and other tissue-damaging effects of secreted PR3.

Acknowledgments—The expert technical assistance of Heike Kittel is gratefully acknowledged. In addition, the authors thank Oliver Eickelberg for continuous interest in the project and Karl-Heinz Wiesmüller, EMC Microcollections for the design and synthesis of FRET substrates.

REFERENCES

- Korkmaz, B., Horwitz, M. S., Jenne, D. E., and Gauthier, F. (2010) Neutrophil elastase, proteinase 3, and cathepsin G as therapeutic targets in human diseases. *Pharmacol. Rev.* **62**, 726–759
- Perera, N. C., and Jenne, D. E. (2012) Perspectives and potential roles for the newly discovered NSP4 in the immune system. *Expert Rev. Clin. Immunol.* **8**, 501–503
- Pham, C. T. (2006) Neutrophil serine proteases: specific regulators of inflammation. *Nat. Rev. Immunol.* **6**, 541–550
- Heutinck, K. M., ten Berge, I. J., Hack, C. E., Hamann, J., and Rowshani, A. T. (2010) Serine proteases of the human immune system in health and disease. *Mol. Immunol.* **47**, 1943–1955
- Csernok, E., Lüdemann, J., Gross, W. L., and Bainton, D. F. (1990) Ultrastructural localization of proteinase 3, the target antigen of anti-cytoplasmic antibodies circulating in Wegener's granulomatosis. *Am. J. Pathol.* **137**, 1113–1120
- Witko-Sarsat, V., Cramer, E. M., Hieblot, C., Guichard, J., Nusbaum, P., Lopez, S., Lesavre, P., and Halbwachs-Mecarelli, L. (1999) Presence of proteinase 3 in secretory vesicles: evidence of a novel, highly mobilizable intracellular pool distinct from azurophil granules. *Blood* **94**, 2487–2496
- Csernok, E., Ernst, M., Schmitt, W., Bainton, D. F., and Gross, W. L. (1994) Activated neutrophils express proteinase 3 on their plasma membrane *in vitro* and *in vivo*. *Clin. Exp. Immunol.* **95**, 244–250
- Halbwachs-Mecarelli, L., Bessou, G., Lesavre, P., Lopez, S., and Witko-Sarsat, V. (1995) Bimodal distribution of proteinase 3 (PR3) surface expression reflects a constitutive heterogeneity in the polymorphonuclear neutrophil pool. *FEBS Lett.* **374**, 29–33
- Schreiber, A., Busjahn, A., Luft, F. C., and Kettritz, R. (2003) Membrane expression of proteinase 3 is genetically determined. *J. Am. Soc. Nephrol.* **14**, 68–75
- Kallenberg, C. G. (2011) Pathogenesis of ANCA-associated vasculitis, an update. *Clin. Rev. Allergy Immunol.* **41**, 224–231
- Hoffman, G. S., and Specks, U. (1998) Antineutrophil cytoplasmic antibodies. *Arthritis Rheum.* **41**, 1521–1537
- Lyons, P. A., Rayner, T. F., Trivedi, S., Holle, J. U., Watts, R. A., Jayne, D. R., Baslund, B., Brenchley, P., Bruchfeld, A., Chaudhry, A. N., Cohen-Tervaert, J. W., Deloukas, P., Feighery, C., Gross, W. L., Guillevin, L., Gunnarsson, I., Harper, L., Hrušková, Z., Little, M. A., Martorana, D., Neumann, T., Ohlsson, S., Padmanabhan, S., Pusey, C. D., Salama, A. D., Sanders, J.-S., Savage, C. O., Segelmark, M., Stegeman, C. A., Tesaf, V., Vaglio, A., Wiczorek, S., Wilde, B., Zwerina, J., Rees, A. J., Clayton, D. G., and Smith, K. G. (2012) Genetically distinct subsets within ANCA-associated vasculitis. *N. Engl. J. Med.* **367**, 214–223
- Ogushi, F., Fells, G. A., Hubbard, R. C., Straus, S. D., and Crystal, R. G. (1987) Z-type α 1-antitrypsin is less competent than M1-type α 1-antitrypsin as an inhibitor of neutrophil elastase. *J. Clin. Investig.* **80**, 1366–1374
- Gettins, P. G. (2002) Serpin structure, mechanism, and function. *Chem. Rev.* **102**, 4751–4804
- Campanelli, D., Melchior, M., Fu, Y., Nakata, M., Shuman, H., Nathan, C., and Gabay, J. E. (1990) Cloning of cDNA for proteinase 3: a serine protease, antibiotic, and autoantigen from human neutrophils. *J. Exp. Med.* **172**, 1709–1715
- Zimmer, M., Medcalf, R. L., Fink, T. M., Mattmann, C., Lichter, P., and Jenne, D. E. (1992) Three human elastase-like genes coordinately expressed in the myelomonocyte lineage are organized as a single genetic locus on 19pter. *Proc. Natl. Acad. Sci. U.S.A.* **89**, 8215–8219
- Rao, N. V., Rao, G. V., Marshall, B. C., and Hoidal, J. R. (1996) Biosynthesis and processing of proteinase 3 in U937 cells. Processing pathways are distinct from those of cathepsin G. *J. Biol. Chem.* **271**, 2972–2978
- Specks, U., Fass, D. N., Fautsch, M. P., Hummel, A. M., and Viss, M. A. (1996) Recombinant human proteinase 3, the Wegener's autoantigen, expressed in HMC-1 cells is enzymatically active and recognized by c-ANCA. *FEBS Lett.* **390**, 265–270
- Garwicz, D., Lindmark, A., Hellmark, T., Gladh, M., Jögi, J., and Gullberg, U. (1997) Characterization of the processing and granular targeting of human proteinase 3 after transfection to the rat RBL or the murine 32D leukemic cell lines. *J. Leukoc. Biol.* **61**, 113–123
- Sun, J., Fass, D. N., Viss, M. A., Hummel, A. M., Tang, H., Homburger, H. A., and Specks, U. (1998) A proportion of proteinase 3 (PR3)-specific anti-neutrophil cytoplasmic antibodies (ANCA) only react with PR3 after cleavage of its N-terminal activation dipeptide. *Clin. Exp. Immunol.* **114**, 320–326
- Fujinaga, M., Chernaia, M. M., Halenbeck, R., Kothe, K., and James, M. N. (1996) The crystal structure of PR3, a neutrophil serine proteinase antigen of Wegener's granulomatosis antibodies. *J. Mol. Biol.* **261**, 267–278
- Fehlhammer, H., Bode, W., and Huber, R. (1977) Crystal structure of bovine trypsinogen at 1.8 Å resolution. II. Crystallographic refinement, refined crystal structure and comparison with bovine trypsin. *J. Mol. Biol.* **111**, 415–438
- Jenne, D. E., and Kuhl, A. (2006) Production and applications of recombinant proteinase 3, Wegener's autoantigen: problems and perspectives. *Clin. Nephrol.* **66**, 153–159
- Pozzi, N., Vogt, A. D., Gohara, D. W., and Di Cera, E. (2012) Conformational selection in trypsin-like proteases. *Curr. Opin. Struct. Biol.* **22**, 421–431
- Sun, J., Fass, D. N., Hudson, J. A., Viss, M. A., Wieslander, J., Homburger, H. A., and Specks, U. (1998) Capture-ELISA based on recombinant PR3 is sensitive for PR3-ANCA testing and allows detection of PR3 and PR3-ANCA/PR3 immune complexes. *J. Immunol. Methods* **211**, 111–123
- Wysocka, M., Lesner, A., Guzow, K., Mackiewicz, L., Legowska, A., Wiczek, W., and Rolka, K. (2008) Design of selective substrates of proteinase 3 using combinatorial chemistry methods. *Anal. Biochem.* **378**, 208–215
- Capizzi, S. A., Viss, M. A., Hummel, A. M., Fass, D. N., and Specks, U. (2003) Effects of carboxy-terminal modifications of proteinase 3 (PR3) on the recognition by PR3-ANCA. *Kidney Int.* **63**, 756–760
- Korkmaz, B., Kuhl, A., Bayat, B., Santoso, S., and Jenne, D. E. (2008) A hydrophobic patch on proteinase 3, the target of autoantibodies in Wegener granulomatosis, mediates membrane binding via NB1 receptors. *J. Biol. Chem.* **283**, 35976–35982
- Perera, N. C., Schilling, O., Kittel, H., Back, W., Kremmer, E., and Jenne, D. E. (2012) NSP4, an elastase-related protease in human neutrophils with

Antibodies Interfering with PR3 Activity and Inactivation

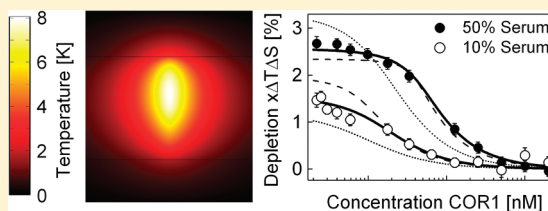
- arginine specificity. *Proc. Natl. Acad. Sci. U.S.A.* **109**, 6229–6234
30. Silva, F., Hummel, A. M., Jenne, D. E., and Specks, U. (2010) Discrimination and variable impact of ANCA binding to different surface epitopes on proteinase 3, the Wegener's autoantigen. *J. Autoimmun.* **35**, 299–308
 31. Kuhl, A., Korkmaz, B., Utecht, B., Kniepert, A., Schönermarck, U., Specks, U., and Jenne, D. E. (2010) Mapping of conformational epitopes on human proteinase 3, the autoantigen of Wegener's granulomatosis. *J. Immunol.* **185**, 387–399
 32. Seidel, S. A., Dijkman, P. M., Lea, W. A., van den Bogaart, G., Jerabek-Willemsen, M., Lazic, A., Joseph, J. S., Srinivasan, P., Baaske, P., Simeonov, A., Katritch, I., Melo, F. A., Ladbury, J. E., Schreiber, G., Watts, A., Braun, D., and Duhr, S. (2013) Microscale thermophoresis quantifies biomolecular interactions under previously challenging conditions. *Methods* **59**, 301–315
 33. Seidel, S. A., Wienken, C. J., Geissler, S., Jerabek-Willemsen, M., Duhr, S., Reiter, A., Trauner, D., Braun, D., and Baaske, P. (2012) Label-free microscale thermophoresis discriminates sites and affinity of protein-ligand binding. *Angew. Chem. Int. Ed. Engl.* **51**, 10656–10659
 34. Lindley, H. (1972) The specificity of dipeptidyl aminopeptidase I (cathepsin C) and its use in peptide sequence studies. *Biochem. J.* **126**, 683–685
 35. Lone, A. M., Nolte, W. M., Tinoco, A. D., and Saghatelian, A. (2010) Peptidomics of the prolyl peptidases. *AAPS J.* **12**, 483–491
 36. Huntington, J. A., Read, R. J., and Carrell, R. W. (2000) Structure of a serpin-protease complex shows inhibition by deformation. *Nature* **407**, 923–926
 37. Dementiev, A., Dobó, J., and Gettins, P. G. (2006) Active site distortion is sufficient for proteinase inhibition by serpins: structure of the covalent complex of α 1-proteinase inhibitor with porcine pancreatic elastase. *J. Biol. Chem.* **281**, 3452–3457
 38. Ganesan, R., Eigenbrot, C., and Kirchhofer, D. (2010) Structural and mechanistic insight into how antibodies inhibit serine proteases. *Biochem. J.* **430**, 179–189

Direct Detection of Antibody Concentration and Affinity in Human Serum Using Microscale Thermophoresis

Svenja Lippok,[†] Susanne A. I. Seidel,[†] Stefan Duhr,[‡] Kerstin Uhland,[§] Hans-Peter Holthoff,[§] Dieter Jenne,^{||} and Dieter Braun^{*†}[†]Systems Biophysics, Center for Nanoscience, Physics Department, Ludwig Maximilians Universität München, Amalienstrasse 54, 80799 München, Germany[‡]NanoTemper Technologies GmbH, Flössergasse 4, 81369 München, Germany[§]Corimmun GmbH, Lochhamer Strasse 29, 82152 Martinsried, Germany^{||}Max Planck Institute of Neurobiology, Am Klopferspitz 18, 82152 Martinsried, Germany

S Supporting Information

ABSTRACT: The direct quantification of both the binding affinity and absolute concentration of disease-related biomarkers in biological fluids is particularly beneficial for differential diagnosis and therapy monitoring. Here, we extend microscale thermophoresis to target immunological questions. Optically generated thermal gradients were used to deplete fluorescently marked antigens in 2- and 10-fold-diluted human serum. We devised and validated an autocompetitive strategy to independently fit the concentration and dissociation constant of autoimmune antibodies against the cardiac β 1-adrenergic receptor related to dilated cardiomyopathy. As an artificial antigen, the peptide COR1 was designed to mimic the second extracellular receptor loop. Thermophoresis resolved antibody concentrations from 2 to 200 nM and measured the dissociation constant as 75 nM. The approach quantifies antibody binding in its native serum environment within microliter volumes and without any surface attachments. The simplicity of the mix and probe protocol minimizes systematic errors, making thermophoresis a promising detection method for personalized medicine.



Only a few physical forces are strong enough to induce translational motion of molecules in their native environment. Light fields or magnetic fields, for example, are not sufficient. Electrophoresis is the dominant technique to separate biomolecules on the basis of their size and structure. Unexpectedly, focused temperature fields can move biomolecules, an effect termed “thermophoresis”. Temperature cannot drive molecules over large length scales as electrophoresis does. Thermophoresis merely leads to a 20% concentration depletion over tens of micrometers when moderate temperature differences on the 5 K scale are applied. However, this small depletion is easily detectable with fluorescence and provides detailed information on the molecule’s interface.

We devised a strategy to probe both the concentration and affinity of biomolecules in bulk blood serum applying microscale temperature gradients. In the recent past, thermophoresis has been used successfully to detect close to literature binding constants for nucleotide aptamers as well as proteins binding to small molecules.^{1–3}

Here, we established a combined dilution and autocompetition protocol to tackle immunological problems in blood serum as the according native environment. Unlike methods depending on molecule immobilization to surfaces, microscale thermophoresis (MST) to measure binding affinity in bulk fluid requires only a single unspecific fluorescent probe. Fluorescence reports a change in thermophoretic depletion upon

binding, thus quantifying the latter within tens of seconds per sample. We focused on the increasingly important group of autoimmune diseases which are difficult to classify and treat using standard immunological methods.

Dilated cardiomyopathy (DCM) is a nonischemic heart muscle disease characterized by dilation and impaired contraction of the left or both ventricles. With a prevalence of 300–400 patients per million, DCM belongs to the main causes of severe heart defects.⁴ Moreover, it is the prime reason for heart transplantations.⁵ Besides genetic, toxic, and infectious factors, autoimmune reactions are discussed as a putative trigger for its appearance. In a notable number of DCM patients, increased concentrations of autoantibodies against several cardiac antigens, including membrane proteins such as cell surface adrenergic receptors, are found.^{6–8} Some of these autoantibodies seem to injure the myocardium directly or indirectly.⁹ The β 1-adrenergic receptor regulating heart activity represents a major autoimmune target in DCM (Figure 1a). Agonist-like antibodies found in DCM patients have been shown to be associated with severe ventricular arrhythmias.^{7,12–14} The prevalence of these antibodies varies from 30% to 95% in DCM sera and from 0% to 13% in sera from

Received: November 4, 2011

Accepted: March 7, 2012

Published: March 7, 2012

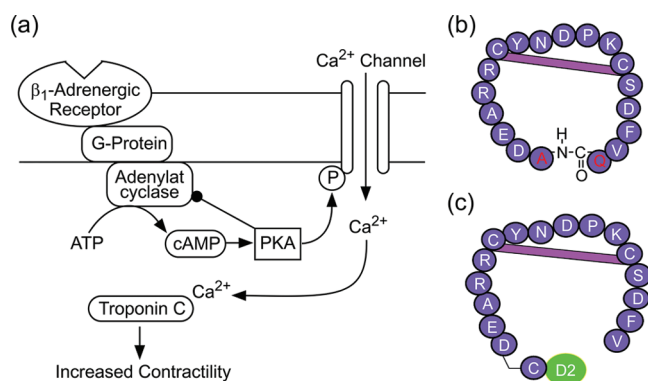


Figure 1. Target pathway. (a) Activation of the β_1 -adrenergic receptor via a β -adrenoceptor–adenylyl cyclase protein kinase A cascade. The cAMP-dependent PKA phosphorylates Ca^{2+} channels, and the resulting calcium influx increases the contractility of the myocard. (b) The extracellular loop of the β_1 -adrenergic receptor is mimicked by the peptide sequence COR1. (c) The labeled COR1 variant is used to detect binding with thermophoresis.

unaffected controls.^{15,16} It is widely accepted that, in many patients suffering from heart failure, a chronic adrenergic overexcitation plays a harmful role.¹⁷ Permanent stimulation of β_1 -adrenoceptors due to elevated levels of circulating catecholamines in combination with autoantibodies could change the Ca^{2+} homeostasis of cardiomyocytes, resulting in metabolic and electrophysiological disturbances which are responsible for tachyarrhythmia and sudden death.¹⁸ It was also shown that DCM autoantibodies against β_1 -adrenergic receptors increase the activity of cyclic adenosine monophosphate (cAMP)-dependent protein kinase A (PKA).¹⁹ Therefore, the detection of β_1 -adrenergic receptor autoantibodies in human serum as an indicator for dilated cardiomyopathy and the development of specific antigens are important steps toward reliable diagnostics and treatment of the disease. The autoimmune antibodies' target, the second extracellular receptor loop,^{10,11} is mimicked by the candidate peptide drug COR1 (Figure 1b). Thus, COR1 competes with the binding of autoimmune antibodies to the receptor. In animal models, COR1 was shown to prevent heart failure and reverse existing cardiac insufficiency (manuscript in preparation).

Although quantitative autoantibody analysis is crucial to characterize and discriminate different autoimmune disease types and optimize their treatment, it still remains challenging. Enzyme-linked immunosorbent assays (ELISAs) are widely used to detect and quantify disease-related biomarkers, but display several disadvantages. Surface immobilization, initial strong dilution as well as tedious washing steps, enzymatic signal amplification, and normalization to a standard curve often cannot be avoided, resulting in unpredictable influences on the results. The optimization of surfaces and linkers has improved the binding protocols of ELISA; however, it is time-consuming and often depends on the studied binding reaction. Linking small peptides to surfaces in a way that all binding epitopes are presented in the same manner as in solution remains a pertinent obstacle.^{20,21} The surface density of the captured proteins is hard to predict.^{22,23} Additionally, the nonspecific binding of molecules of interest and plasma/serum poses a challenge. Thus, absolute biomarker quantification via ELISA remains difficult. Despite these limitations and pitfalls, the popularity and application depth of ELISA are enormous.

Only a few solution-phase alternatives to ELISA are being utilized. As radioimmunoassays (RIAs) fulfilled these principles very closely, they were popular until the 1970s. However, the need for radioactive labeling and purification of the analyte–probe complexes from the free radioactive probe by a secondary reagent is a significant disadvantage compared to the later developed ELISA.

A number of recent approaches are based on fluorescence resonance energy transfer (FRET) between two labeled ligands to detect binding in biological fluids or inside cells.²⁴ For example, homogeneous time-resolved fluorescence (HTRF)²⁵ detects binding by proximity in bulk fluids, while in the bead-based alphascreen²⁶ singlet oxygen is used as a chemical proximity signal.

In contrast to the above methods, microscale thermophoresis is much simpler to set up, as only one binder is labeled and the measurement follows a straightforward mix and read protocol. It is sample-efficient and immobilization-free and allows measurements in bulk fluids. As shown here, it can be used for simultaneous and quantitative analysis of antibody concentration and affinity, making it a promising alternative to the commonly used techniques.

EXPERIMENTAL SECTION

Setup. A fluorescence microscope (AxioScope Vario, Carl Zeiss GmbH, Germany) was modified by a 1480 nm infrared heating laser (Fibotec Fiberoptics, Germany) generating local temperature gradients in solution (Figure 2a and Supporting Information).^{1,2} Most of the laser power is absorbed by the probe volume. Back-reflected light is absorbed by an IR filter placed above the fluorescence emission filter, and stray light is blocked by housing the capillaries. The maximal temperature increase was measured to be 8 K in the beam center using BCECF (2'-7'-bis(carboxyethyl)-5(6)-carboxyfluorescein) and finite element calculations (Figure 2b).^{27,28} With the initial temperature jump set at time $t = 0$ s, the cold fluorescence signal F^I was averaged from -6 to -2 s, while the warm fluorescence signal F^{II} was between 1.2 and 3.7 s (Figure 2c). Error bars of fluorescence F are the result of at least four measurements.

Peptides. The dominant epitope in the second extracellular domain of the β_1 -adrenergic receptor is the sequence ARRCYND forming a disulfide bridge with the cysteine of the first extracellular loop.^{11,34} COR1, an 18-mer cyclic peptide with the sequence ADEARRCYNDPKCSDFVQ and the N- and C-termini linked via a peptide bond, represents this second extracellular loop. COR1 was labeled with a red dye, D2 (Figure 1c, Cisbio Bioassays, France).

Sample Preparation. Measurements were conducted in phosphate-buffered saline (PBS) with 0.1% Tween 20 and human serum. Serum from unaffected donors was collected in S-monovettes (Sarstedt, Germany), incubated at room temperature (30 min), and centrifuged (10 min, 12000g). The supernatant was aliquoted and stored at -20 °C.

Measurement Protocols. For measurements with varying antibody concentration, titration series of antibodies in PBS were prepared using Quali-PCR-Tubes (Kisker, Germany). A serial dilution was set up, starting with a concentration of 2.6 μM polyclonal antibody (pAB), with a 2-fold dilution down to 2.6 nM. Separately, a 40 nM COR1-D2 stock was prepared in PBS with 0.2% Tween 20 or blood serum. The monoclonal antibody concentration ranged from 4000 to 1.6 nM with 200 nM COR1-D2. The antibody and COR1 dilution series were

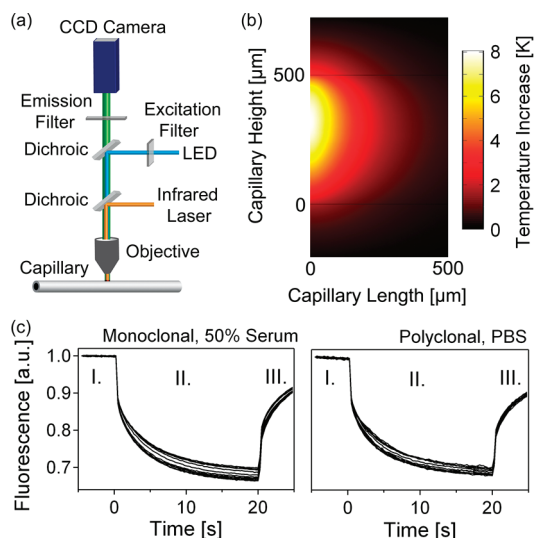


Figure 2. Microscale thermophoresis. (a) Experimental setup. An infrared laser for heating is coupled into the microscope light path using a dichroic mirror. It is focused into the fluid with the standard epifluorescence microscope objective. Bright-field illumination is provided with a high-power light-emitting diode (LED), fluorescence detection with a charge-coupled device (CCD) camera. (b) Temperature profile based on finite element calculations and temperature-dependent fluorescence measurements. The inhomogeneous heating does not affect the analysis in the linear regime, shown in eqs 3–7. (c) Trace of the COR1 fluorescence intensity in the heated center. The cold baseline fluorescence before heating (I) drops by outward thermophoresis and the temperature dependence of the dye (II) and recovers by back-diffusion after the laser heating is switched off (III). The measured signal is the fluorescence depletion between the warm regime (II) and the cold baseline (I). The thermophoretic depletion shifts depending on the concentration of binder. As an example, we show the raw data of the measurements presented in Figure 4b, c which quantify the affinity against COR1 for the monoclonal antibody in serum and the polyclonal antibody in PBS.

mixed 1:1 to obtain final measurement samples. For the autocompetition assay, a serial dilution of unlabeled COR1 from 4000 to 42 nM was set up in PBS. Separately, a stock solution containing 40 nM labeled COR1-D2 was mixed with twice the final pAB concentration in human serum at a 1:1 ratio, resulting in a total COR1 concentration (labeled and unlabeled) from 2000 to 21 nM. For the measurements in 10% human serum, the stock solutions of COR1-D2 and pAB were set up in 20% human serum and 80% PBS. After 2 h of incubation at room temperature, about 5 μ L of each sample was filled into capillaries, which were then closed with sealing wax (NanoTemper, Germany).

RESULTS AND DISCUSSION

Thermophoresis. The movement of molecules in a temperature gradient^{27–29} is modeled phenomenologically by the drift velocity $v = -D_{T,i} \text{grad } T$ with temperature gradient $\text{grad } T$. The proportionality constant $D_{T,i}$ is termed the “thermal diffusion coefficient” or “thermophoretic mobility”. The index i distinguishes between the bound and unbound states of the molecule. The drift is counterbalanced by mass diffusion:

$$j_i = -c_i D_{T,i} \text{grad } T - D_i \text{grad } c_i \quad (1)$$

with diffusion coefficient D_i and molecule concentration c_i . Integration with a temperature-independent $D_{T,i}$ and D_i yields a steady-state concentration of $c_{T,i} = c_i \exp(-S_{T,i} \Delta T)$ at the position where the temperature is increased by ΔT . The Soret coefficient $S_{T,i}$ is defined by the ratio $S_{T,i} = D_{T,i}/D_i$. A number of ways to measure thermophoresis have been devised in the past.^{30–32} Typically, the depleted concentration is lower, $c_{T,i} < c_i$; i.e., the Soret coefficient is positive.

Linearity of Detection. In the presented measurements, the depletion is kept small ($\sim 15\%$) and changes only slightly upon binding (2–4%). This is ensured by small applied temperature differences ($\Delta T \approx 5\text{--}10$ K). As a result, the linearization $c_{T,i} = c_i(1 - S_{T,i} \Delta T)$ introduces only small systematic errors:

$$\Delta c_i = c_{T,i} - c_i = -S_{T,i} c_i \Delta T \quad (2)$$

The temperature increase $\Delta \tilde{T}(x,y,z)$ in the capillary has a rather complex shape (Figure 2b). Additionally, the efficiency $\varphi(x,y,z)$ to detect a photon from position x,y,z by the objective is nontrivial. Interestingly, due to the above linearization, exact knowledge of both functions is not required.

The quantum efficiency $f_{T,i}$ of the fluorescent dye attached to the molecule in binding state i is given by a linear function, $f_{T,i}(\Delta \tilde{T}) = f_i + \Delta \tilde{T}(\partial f_i / \partial T)$, for the small temperature range used (5–10 K). Typical values are $\partial f_i / \partial T \approx -1\%/K$.²⁷ The molecule concentration in the steady state at position x,y,z is given by eq 2 with $c_{T,i}(\Delta \tilde{T}) = c_i(1 - S_{T,i} \Delta \tilde{T}(x,y,z))$. The cold fluorescence intensity flux F^I at $\Delta \tilde{T} = 0$ can be linearly integrated:

$$\begin{aligned} F^I &= \sum_i \int f_{T,i}(\Delta \tilde{T}) c_{T,i}(\Delta \tilde{T}) \varphi(x,y,z) dx dy dz \\ &= \sum_i f_i c_i \int \varphi(x,y,z) dx dy dz \end{aligned} \quad (3)$$

The fluorescence in the heated steady state

$$F^{II} = \sum_i \int [f_i + \Delta \tilde{T}(\partial f_i / \partial T)] c_i [1 - S_{T,i} \Delta \tilde{T}] \varphi(x,y,z) dx dy dz \quad (4)$$

can be expanded to first order in $\Delta \tilde{T}$:

$$F^{II} = F^I + \Delta T \sum_i c_i f_i \left[\frac{\partial f_i}{f_i \partial T} - S_{T,i} \right] + O(\Delta \tilde{T}^2) \quad (5)$$

with the averaged temperature increase ΔT defined by $\int \Delta \tilde{T}(x,y,z) \varphi(x,y,z) dx dy dz = \Delta T \int \varphi(x,y,z) dx dy dz$. As a result the relative depleted fluorescence signal $\Delta F/F$, subtracted and normalized to the initial cold fluorescence F^I , is given by

$$\frac{\Delta F}{F} = \frac{F^{II} - F^I}{F^I} = \frac{\Delta T \sum_i c_i f_i S_i}{\sum_i c_i f_i} + O(\Delta \tilde{T}^2) \quad (6)$$

Above, we defined an apparent Soret coefficient by the combined temperature dependence of the dye and thermophoretic depletion into

$$S_i = \left[\frac{\partial f_i}{f_i \partial T} - S_{T,i} \right] \quad (7)$$

The fluorescence signal becomes a linear function of the apparent Soret coefficient S_i even for a spatially varying temperature increase $\Delta\tilde{T}$ and fluorescence detection field φ .

Depletion Reports Fraction of Bound Molecules. Let us consider the chemical binding equilibrium between ligand L and fluorescently labeled binder B:



The binding is reported by the difference in the thermophoretic depletion of molecule B in the free state B^{free} and the bound state LB with state index $i = \{B^{\text{free}}, LB\}$. The fraction x of bound concentration against all labeled concentrations $x = c_{LB}/(c_B + c_{LB})$ is a linear function of the depleted fluorescence $\Delta F/F$. From eq 6 follows that the fluorescence depletion is given by

$$\frac{\Delta F}{F} = \Delta T \frac{c_B f_B S_B + c_{LB} f_{LB} S_{LB}}{c_B f_B + c_{LB} f_{LB}} \quad (9)$$

We will focus on the likely case that the fluorescence quantum efficiencies $f_B = f_{LB}$ are equal. Otherwise the binding between B and L could be reported directly by absolute fluorescence. However, no change in absolute intensity under variation of the ligand concentration was found. We find

$$\begin{aligned} \frac{\Delta F}{F} &= \frac{F^{\text{II}} - F^{\text{I}}}{F^{\text{I}}} \\ &= \Delta T \frac{(1-x)f_B S_B + x f_{LB} S_{LB}}{(1-x)f_B + x f_{LB}} = \Delta T [S_B + x \Delta S] \end{aligned} \quad (10)$$

with $\Delta S = S_{LB} - S_B$ the difference between the apparent Soret coefficients of the bound and unbound states. Only the total concentrations of binder, $c_{B0} = c_B + c_{LB}$, and ligand, $c_{L0} = c_L + c_{LB}$, are known. The mass action law with dissociation constant K_D reads

$$K_D = \frac{c_L c_B}{c_{LB}} = \frac{(c_{L0} - c_{LB})(c_{B0} - c_{LB})}{c_{LB}} \quad (11)$$

Solving for the fraction of occupied binder B yields

$$\begin{aligned} x &= \frac{c_{LB}}{c_{B0}} \\ &= \frac{c_{L0} + c_{B0} + K_D - \sqrt{(c_{L0} + c_{B0} + K_D)^2 - 4c_{L0}c_{B0}}}{2c_{L0}} \end{aligned} \quad (12)$$

To conclude, the minimal and maximal levels of depleted fluorescence are given by S_B (no ligand bound) and $S_B + \Delta S$ (all ligands bound). In between, the depletion linearly reports the fraction x of bound states according to eq 10. The fraction x is modeled by the mass action law and fitted to the experimental results to reveal the dissociation constant K_D and the unlabeled ligand concentration c_{L0} .

Figure 3 shows that the dissociation coefficient K_D and ligand concentration c_{L0} of the antibody can be fitted independently. An increasing ligand concentration shifts the binding curve along the c_{B0} axis toward higher binder concentrations (Figure 3a). Contrary to intuition, the dissociation constant changes the amplitude of the fraction of bound ligand L (antibody) (Figure 3b) as a higher percentage of the constant amount of ligands is captured by the binder B (COR1). Only when the ligand

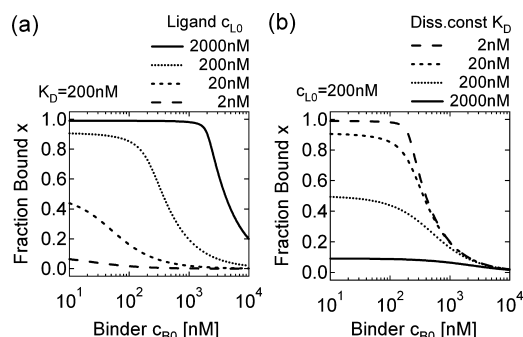


Figure 3. Concentration and affinity inferred independently. The fraction x of binder B (COR1) bound to ligand L (antibody) is plotted against the binder concentration c_{B0} according to eq 12. The fraction x is a linear function of thermophoretic depletion (eq 10). Thus, a rescaled plot of the measured fluorescence ratio $\Delta F/F$ will show the same behavior. (a) A change of the ligand concentration shifts the thermophoretic depletion along the binder concentration axis under a fixed dissociation constant, $K_D = 200$ nM. (b) A change in the dissociation constant modulates the amplitude of thermophoretic depletion under constant ligand concentration $c_{L0} = 200$ nM. The depletion is changed differently by both parameters and thus can be fitted independently.

concentration is lower than the dissociation constant, $c_{L0} \leq K_D$, do the above shift and amplitude change of the binding curve become very similar. At low concentrations, $4c_{B0}c_{L0}/(c_{B0} + c_{L0} + K_D) \ll 1$, the bound fraction can be approximated by $x \approx c_{B0}/(c_{B0} + c_{L0} + K_D)$.

Assay Sensitivity. What concentration of labeled ligand COR1 should be used? When the concentrations reach K_D , the amplitude signal saturates and reduces the sensitivity. At lower concentrations, the fluorescence signal diminishes. We assume that the fluorescence intensity is photon shot noise limited, scaling with the number of chromophores $F \propto c_{B0}$ and yielding a relative error of $\Delta F_{\text{err}}/F \propto 1/c_{B0}^{1/2}$. With eq 10, the signal-to-noise ratio (SNR) of fluorescence depletion $\Delta F/F$ is $\text{SNR} \propto \Delta T \Delta S x c_{B0}^{1/2}$. The temperature increase ΔT is typically limited by the temperature dependence of the binding reaction, the linearity of thermophoresis, and artifacts by thermal convection. The change of apparent Soret coefficient upon binding ΔS is a function of the molecules and might only be increased by optimizing buffers or reducing the temperature dependence of the chromophore. This leaves the product $\text{SNR} \propto x c_{B0}^{1/2}$ for optimization (Supporting Information, Figure S-1). The maximal signal-to-noise ratio $\partial(\text{SNR})/\partial c_{B0} = 0$ enforces that the concentration of labeled binder

$$c_{B0}^{\text{optimal}} = K_D + c_{L0} \quad (13)$$

is given by the sum of the dissociation constant and concentration of the ligand. Two regimes for a maximal signal-to-noise ratio are thus found. The labeled binder should be near the ligand concentration $c_{B0} \approx c_{L0}$ for highly affine ligands ($c_{B0} \geq K_D$). However, for less affine ligands ($c_{L0} \leq K_D$), the binder concentration should equal the dissociation constant with $c_{B0} \approx K_D$. Only high-affinity binders with low K_D lead to a high SNR (Supporting Information, Figure S-1).

Affinity Measurement. In Figure 4, we initially measured the affinity of COR1 to monoclonal and polyclonal antibodies with the established spiking protocol in which both concentrations are known.¹⁻³ Monoclonal antibodies (mABs) are produced by genetically identical lymphocytes, while pABs

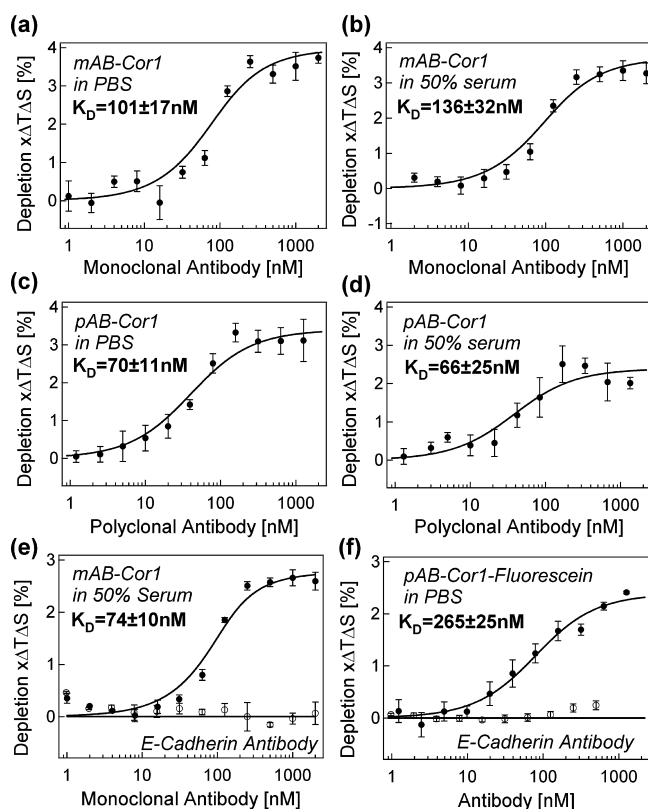


Figure 4. Affinity. The affinity of labeled COR1 to monoclonal and polyclonal autoantibodies was quantified in buffer and 50% human serum. In contrast to the autocompetition assay described in Figure 3, we first performed microscale thermophoresis without autocompetition: with fixed labeled COR1 concentration c_{B0} , the antibody concentration c_{L0} was varied. Again, eqs 10 and 12 were used for fitting, but the traditional usage of the concentrations resulted in inverted characteristics as compared to those of the autocompetition described in Figure 3. (a, b) Binding of COR1 to monoclonal antibody yielded a dissociation constant of $K_D = 101 \pm 17$ nM in PBS buffer and $K_D = 136 \pm 32$ nM in 50% untreated human serum. (c, d) Measurements of polyclonal antibody showed $K_D = 70 \pm 11$ nM for PBS and $K_D = 66 \pm 25$ nM in 50% serum. The dissociation constant is considered as per antibody molecule. Affinities per antigen binding site would have yielded half of the above K_D values. (e) The specificity of binding was confirmed in serum by control experiments with an unspecific monoclonal anti-E-cadherin antibody. A constant thermophoretic depletion signal was found, indicating no binding. (f) Measurements using a COR1 which was labeled with fluorescein show the same specific binding signal; however, they yield a slightly lower affinity.

are produced by various lymphocyte clones and directed against one or several epitopes of a specific antigen. The autoantibodies found in patients' sera are polyclonal.

We titrated either monoclonal or polyclonal antibodies (see the Supporting Information) against labeled COR1 to infer the dissociation constant in a spiked experimental setting. The indexing for eqs 10 and 12 was $i = \{L, B\} = \{\text{antibody}, \text{COR1}\}$ with the binder B as the labeled species. The antibody has two binding sites, and we used the assignment $c_{L0} = 2c_{L0}^{AB}$ with c_{L0}^{AB} denoting the antibody concentration. The experiment reports $\Delta F/F$ with varying concentration of c_{L0} and a constant c_{B0} . We fitted the thermophoretic depletion for a fixed labeled COR1 concentration, $c_{B0} = 20$ nM ($c_{B0} = 100$ nM for the monoclonal antibody), and varied antibody concentration c_{L0} . The baseline depletion was $\Delta TS_B = 78.8\%$ (79.2%) for monoclonal

(polyclonal) antibodies in buffer and 82.9% (80.6%) for monoclonal (polyclonal) antibodies in 50% serum. Minor discrepancies probably stem from differences in the heating focus ΔT between runs and a slightly different thermophoretic depletion in blood serum and PBS. The depletion amplitude upon binding was $\Delta T\Delta S = 3.72\%$ and 3.58% (3.49% and 2.39%) for mAB and pAB in PBS (and serum). With the exception of the polyclonal antibody in serum, the depletion amplitudes showed comparable values. The inverted measurement protocol of detecting the change in thermophoretic depletion of the antibody (150 kDa) upon binding to the much smaller COR1 peptide (3 kDa) was not successful, most probably due to the small size change upon binding in this configuration.

The fitted dissociation constants K_D of the COR1–antibody binding are similar to each other and all within the range of 70–140 nM. We found $K_D = 101 \pm 17$ nM for the monoclonal antibodies in PBS and $K_D = 136 \pm 32$ nM in serum. The polyclonal antibody preparation showed comparable affinities, $K_D = 70 \pm 11$ nM in PBS and $K_D = 66 \pm 25$ nM in serum. Error bars are the result of the fitting procedure. Experiments were performed at least three times, confirming the error bars of a single measurement. We found a slightly higher affinity for the polyclonal antibody compared to the monoclonal antibody. No significant difference between measurements in buffer and serum could be concluded from the data. It should be noted that the depletion mostly stems from the size difference between COR1 and COR1 + antibody. An additional increase of thermophoretic depletion due to binding of COR1 to the second arm of the antibody is not expected. Indeed, the measurements show that a two-state model is sufficient to describe the binding curves.

The specificity of binding is checked in Figure 4e, f. We performed measurements with an unspecific antibody for COR1, namely a monoclonal antibody against E-cadherin. While the control shows no binding signal, the binding is reproduced for the specific antibody (Figure 4e). The 2-fold reduction in binding affinity as compared to the measurement in Figure 4b could be the result of a new serum stock. In Figure 4f, COR1 was labeled with fluorescein to check for possible interactions of the dye D2 with the antibody. Again specific binding is detected, and we find no thermophoretic depletion for the E-cadherin antibody. The binding with COR1–fluorescein is slightly less affine as compared to that with COR1. This could be due to the fluorescence correction which was required for fluorescein (Supporting Information, S-7).

Autocompetition Assay. To determine both affinity and concentration, a strategy to mix labeled and unlabeled COR1 was successful. Perturbations of the thermophoretic measurement signal are minimal if both the labeled COR1 concentration and serum dilution are held constant. The total concentration of COR1 was changed by adding unlabeled COR1 in a protocol we termed “autocompetition”. The assumption that both COR1 species bind to the antibody with equal affinity was later tested successfully by model fits. We thus assign the index $i = \{L, B\} = \{\text{antibody}, \text{COR1}^{\text{labeled}} + \text{COR1}^{\text{unlabeled}}\}$ with c_{L0} unknown and $c_{B0} = c_{B0}^{\text{labeled}} + c_{B0}^{\text{unlabeled}}$ at a fixed concentration of c_{B0}^{labeled} . Again, the concentration of binding sites of the antibody was quantified using $c_{L0} = 2c_{L0}^{AB}$. We started with $c_{B0}^{\text{labeled}} = 20$ nM to ensure maximal sensitivity also for low antibody concentrations. We first tested the approach by spiking polyclonal antibody with concentrations between 2 and 200 nM into 50% human serum. The goal was

to recover both the K_D and the concentration of the antibodies from the experiment.

In Figure 5, we present the results with fitted theoretical curves. In the inset, the fitted antibody concentrations are

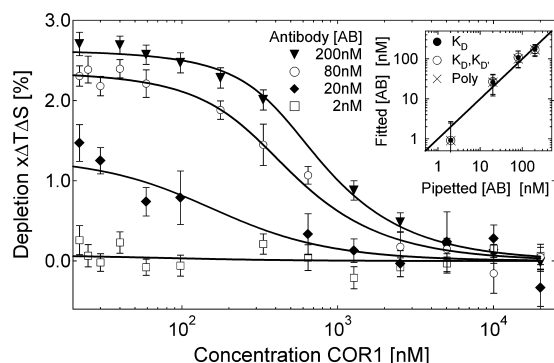


Figure 5. Autocompetition assay. In 50% human serum, the concentration of total COR1 is increased by adding unlabeled COR1 to 20 nM labeled COR1. Thermophoresis only records the depletion of the labeled species. Autocompetition reduces the thermophoretic depletion as less labeled COR1 is bound to the antibody. Four binding curves are recorded for antibody concentrations of 2, 20, 80, and 200 nM. We recover the concentrations from the fit with 0.9 ± 1.5 , 26 ± 3.4 , 108 ± 20 , and 176 ± 21 nM (SD), well within the pipetting errors. Independently, the dissociation constant was inferred to be 74 ± 11 nM. Inset: More complex binding models assuming label-dependent affinity or polyclonal binding did not change the fitted concentrations noticeably, confirming the simple binding assumption.

plotted against the experimentally added concentrations for three different fitting scenarios: the simple binding assumption with one K_D (eqs 10 and 12), label-dependent affinity with two differing K_D values for the labeled and unlabeled COR1 (Supporting Information, eqs S2–S4), and polyclonal binding where we assume two different antibody subpopulations (Supporting Information, eqs S5–S7).

For the simple binding assumption, the fitted antibody concentrations were 0.9 ± 1.5 , 26 ± 3.4 , 108 ± 19 , and 176 ± 21 nM, confirming within statistical errors the pipetted values of 2, 20, 80, and 200 nM. Furthermore, the fit resulted in a dissociation constant of $K_D = 74 \pm 11$ nM, matching the previously measured value of 66 nM in 50% serum (Figure 4). The thermophoretic depletion amplitude $\Delta T\Delta S$ was globally fitted, but held constant for all four concentrations. Baselines $\Delta T\Delta S_B$ were fitted individually for each run as they showed a minor variability of about 0.5%.

The label-dependent binding model assumes different affinities of labeled and unlabeled probes. It did not describe the measurements better and reported statistically indistinguishable values for the unlabeled COR1 of $K_D' = 73.9 \pm 25$ nM and the labeled COR1 of $K_D = 75.8 \pm 73$ nM with very similar antibody concentration values of 0.91 ± 1.8 , 27 ± 14 , 110 ± 49 , and 170 ± 55 nM. The unlabeled COR1 and labeled COR1 probes did not show a difference in binding, confirming our initial assumption in performing a competitive assay with unlabeled COR1 while keeping the labeled COR1 concentration constant.

Similarly, the polyclonal labeling model did not improve the description of the measurements. By assuming a polyclonal distribution consisting of half more affine (K_D) and less affine (K_D') antibodies, the analysis could not distinguish statistically

between the fitted $K_D = 72.6 \pm 3$ nM and $K_D' = 73.7 \pm 4$ nM. The determined concentrations, 0.9 ± 1.6 , 26 ± 5 , 100 ± 19 , and 170 ± 32 nM, were also very similar to the above simple fit results. Thus, no evidence for polyclonal binding was found.

To conclude, we measured the antibody concentration down to 2 nM. At such low concentrations, significant errors arise as the thermophoretic depletion amplitude approaches the instrumentation error. Otherwise, the affinity and concentration of the antibody were measured with errors on the 20% scale.

Concentration and Affinity Approach. In Figure 6, we combine the autocompetition assay of Figure 5 with a moderate

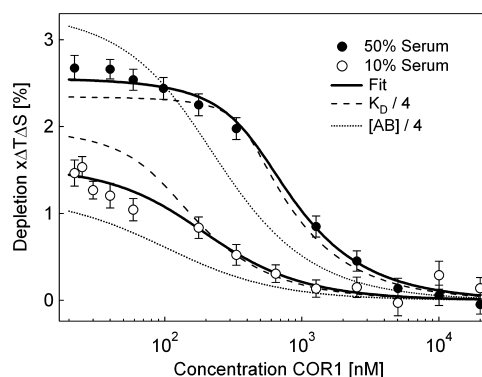


Figure 6. Concentration and affinity assay. Two autocompetition assays are performed in 50% human serum and the 5-fold dilution to 10% serum. This protocol allows the determination of both the concentration and affinity of antibodies. We find an antibody concentration of 187 ± 26 nM with a dissociation constant of $K_D = 73 \pm 18$ nM. The theoretical predictions for a 4-fold lower antibody concentration (dotted line) and a 4-fold smaller dissociation constant (dashed line) differ significantly from the measurements.

5-fold dilution of the serum. As a result, we can fit both the concentration and affinity of the antibody without any prior knowledge. Two autocompetition curves were measured with thermophoresis for a 50% serum dilution and a 10% serum dilution. Both binding curves were fitted with an equal, but unknown, dissociation coefficient and a common depletion amplitude, $\Delta T\Delta S$, considering the 5-fold concentration dilution of the ligand. We found an antibody concentration of 187 ± 26 nM with a dissociation constant of $K_D = 73 \pm 18$ nM.

The combined dilution and autocompetition strategy reports the pipetted concentration of 200 nM and the previously measured dissociation constant of 66 nM (Figure 4) with a 13% error in concentration and 25% error in affinity. For example, a 4-fold lower antibody concentration or 4-fold smaller affinity shows a strongly differing autocompetition and dilution response, although we treated the depletion amplitude $\Delta T\Delta S$ as a fitted free parameter. This shows that thermophoresis allows the concurrent determination of the affinity and concentration of antibodies in 50% serum, under close to in vivo conditions.

Discussion. The results show that thermophoresis, using an autocompetition and dilution protocol, bodes well to detect autoimmune antibody profiles directly in serum. We could detect concentrations up to 35-fold below the affinity of the antibody. The major limitation to detect antibodies in patient samples is the affinity of the probe. As the antibody concentrations in patient sera are estimated to be within the low nanomolar range, a decrease of the dissociation constant by an order of magnitude is necessary for any direct detection

scheme. A dimeric peptide probe should make this possible as the avidity of binding with both antibody arms enhances the affinity.³³ In such a scenario, the signal-to-noise ratio is optimal near the K_D of the binder (Supporting Information, Figure S-1); thus, sensitivity is increased with a parallel reduction of the labeled antigen's concentration. On the basis of the low noise of the fluorescence signal (Figure 2c), a further reduction of labeled antigen concentration to 1 nM is feasible. With both improvements, the detection of antigen concentrations below 100 pM is expected to be achieved.

Such an improved sensitivity would facilitate screening for binding and concentration profiles of antibody interactions with labeled antigen libraries. Moreover, while the measurements were conducted in a capillary, extensions of the approach to specially designed multiwell plates appear realistic and would allow for a highly increased throughput rate. This paves the way toward probing for a large class of disease-related, elevated levels of autoimmune antibodies which have been hard to detect reliably up to now. Especially the possibility to probe not only concentration but also affinity would allow us to obtain a very quantitative picture.

From a more fundamental perspective, the shown experiments could be scaled down to the single-molecule regime. With optimized optics, a single chromophore might emit $N = 100\,000$ photons. The fundamental photon noise limit would allow the depletion to be detected with $1/\sqrt{N} \approx 0.3\%$ accuracy, well below the typical thermophoretic amplitude upon binding of 2–3% reported here. Given low background levels, single-molecule thermophoresis appears feasible.

Recently, we have shown that thermophoresis is capable of measuring the binding of pharmaceutically interesting small molecules to proteins.¹ While we have chosen to label the small antigen here, the opposite protocol would also be feasible, although it would lead to smaller depletion amplitudes. However, with the protocols presented here, screening for pharmaceutically relevant molecules in complex biological liquids would reveal the affinity and concentration of the binders in their native environment.

The thermophoretic approach does not include an amplification step such as ELISA which concentrates the initially diluted probes on the surface. However, amplification steps are often problematic in that they introduce nonlinear characteristics into the detection signal. Thermophoresis solely relies on the mass action law in bulk fluid. Until now only expensive and complex labeling methods using radioactive labeling could give a similar straightforward prospect. We expect that the closer the detection scheme to the natural setting, the smaller the risk of introducing systematic errors.

CONCLUSION

We demonstrated that thermophoresis allows direct measurements of antibody affinity and concentration in 50% serum. Sensitivity was limited by the suboptimal affinity of the antibody ($K_D = 70$ nM), yielding a concentration detection limit of 2–5 nM. Typical error bars for affinity and concentration are on the order of 20%. The limited affinity of the used monomeric antigen does not yet allow for the screening of patient sera. The analysis, however, shows that with an improved affinity, obtained, for example, by using a dimeric probe, concentrations well below 1 nM should be readily detected.

The advantage of the method is to detect both affinity and concentration in the bulk volume of a biologically complex

liquid. Furthermore, it is not at the risk of possible surface artifacts and requires only microliter sample volumes. Notably, the approach developed here not only is applicable to serum-based immunology, but also can detect concentration and affinity in more complex biological fluids such as cell lysates.¹ As biology becomes more quantitative in the future, our approach is likely to find interesting applications.

ASSOCIATED CONTENT

Supporting Information

Additional information as noted in text. This material is available free of charge via the Internet at <http://pubs.acs.org>.

AUTHOR INFORMATION

Corresponding Author

*E-mail: dieter.braun@lmu.de.

Notes

S.D. is one of the founders of the LMU spin-off company NanoTemper Technologies GmbH, which provides services and devices based on thermophoresis. The remaining authors declare no competing financial interest.

ACKNOWLEDGMENTS

We thank Marlon Hinner for discussions and Maren Funk and Natan Osterman for reading the manuscript. Financial support from the NanoSystems Initiative Munich (NIM) and the Ludwig Maximilians Universität München (LMU) Initiative Functional Nanosystems is gratefully acknowledged. This work was supported with seed funds from the Center for Nanoscience and a joint grant of the Deutsche Forschungsgemeinschaft.

REFERENCES

- (1) Wienken, C. J.; Baaske, P.; Rothbauer, U.; Braun, D.; Duhr, S. *Nat. Commun.* **2010**, *1*, 100.
- (2) Baaske, P.; Wienken, C. J.; Reineck, P.; Duhr, S.; Braun, D. *Angew. Chem., Int. Ed.* **2010**, *49*, 2238–2241.
- (3) Jerabek-Willemsen, M.; Wienken, C. J.; Braun, D.; Baaske, P.; Duhr, S. *ASSAY Drug Dev. Technol.* **2011**, *9*, 342–353.
- (4) Rosamond, W.; Flegel, K.; Friday, G.; Furie, K.; Go, A.; Greenlund, K.; Haase, N.; Ho, M.; Howard, V.; Kissela, B.; Kittner, S.; Lloyd-Jones, D.; Meigs, J.; Moy, C.; Nichol, G.; , C. J.; Roger, V.; Rumsfeld, J.; Sorlie, P.; Steinberger, J.; Thom, T.; Wasserthiel-Smoller, S.; Hong, Y. *Circulation* **2007**, *115*, e69–e171.
- (5) Fu, M.; Matsui, S. *Keio J. Med.* **2002**, *51*, 208–212.
- (6) Fu, L. X.; Magnusson, Y.; Bergh, C. H.; Liljeqvist, J. A.; Waagstein, F.; Hjalmarsen, A.; Hoebeke, J. *J. Clin. Invest.* **1993**, *91*, 1964–1968.
- (7) Jahns, R.; Boivin, V.; Siegmund, C.; Inselmann, G.; Lohse, M. J.; Boege, F. *Circulation* **1999**, *99*, 649–654.
- (8) Matsui, S.; Fu, M. L.; Shimizu, M.; Fukuoka, T.; Teraoka, K.; Takekoshi, N.; Murakami, E.; Hjalmarsen, A. *Autoimmunity* **1995**, *21*, 85–88.
- (9) Jahns, R.; Boivin, V.; Schwarzbach, V.; Ertl, G.; Lohse, M. *Autoimmunity* **2008**, *41*, 454–461.
- (10) Dixon, R. A.; Sigal, S.; Candelore, M. R.; Register, R. B.; Scattergood, W.; Rands, E.; Strader, C. D. *EMBO J.* **1987**, *6*, 3269–3275.
- (11) Wallukat, G.; Wollenberger, A.; Morwinski, R.; Pitschner, H. *J. Mol. Cell. Cardiol.* **1995**, *27*, 397–406.
- (12) Christ, T.; Schindelbauer, S.; Wettwer, E.; Wallukat, G.; Ravens, U. *J. Mol. Cell. Cardiol.* **2006**, *41*, 716–723.
- (13) Iwata, M.; Yoshikawa, T.; Baba, A.; Anzai, T.; Mitamura, H.; Ogawa, S. *J. Am. Coll. Cardiol.* **2001**, *37*, 418–424.
- (14) Khojenezhad, A. *Eur. J. Heart Failure* **2007**, *9*, 120–123.

- (15) Limas, C.; Goldenberg, I.; Limas, C. *Am. Heart J.* **1992**, *123*, 967–970.
- (16) Wallukat, G.; Morwinski, M.; Kowal, K.; Förster, A.; Boewer, V.; Wollenberger, A. *Eur. Heart J.* **1991**, *12*, 178–181.
- (17) Francis, G. *Am. J. Cardiol.* **1985**, *55*, 15A–21A.
- (18) Wallukat, G. *Herz* **2002**, *27*, 683–690.
- (19) Krause, E.; Bartel, S.; Beyerdörfer, I.; Wallukat, G. *Blood Pressure, Suppl.* **1996**, *3*, 37–40.
- (20) Butler, J. E.; Weber, P.; Sinkora, M.; Sun, J.; Ford, S. J.; Christenson, R. K. *J. Immunol.* **2000**, *165*, 6999–7010.
- (21) Klinger, H. *Frankf. Z. Pathol.* **1931**, *42*, 455–480.
- (22) Wegener, F. *Verh. Dtsch. Pathol. Ges.* **1936**, *29*, 202–210.
- (23) Butler, J. E. *Methods Mol. Med.* **2004**, *94*, 333–372.
- (24) Pollitt, S. K.; Pallos, J.; Shao, J.; Desai, U. A.; Ma, A. A.; Thompson, L. M.; Marsh, J. L.; Diamond, M. I. *Neuron* **2003**, *40*, 685–694.
- (25) Park, Y.-W.; Cummings, R. T.; Wu, L.; Zheng, S.; Cameron, P. M.; Woods, A.; Zaller, D. M.; Marcy, A. I.; Hermes, J. D. *Anal. Biochem.* **1999**, *269*, 94–104.
- (26) Beaudet, L.; Bédard, J.; Breton, B.; Mercuri, R. J.; Budarf, M. L. *Genome Res.* **2001**, *11*, 600–608.
- (27) Duhr, S.; Braun, D. *Phys. Rev. Lett.* **2006**, *96*, 168301.
- (28) Duhr, S.; Braun, D. *Proc. Natl. Acad. Sci. U.S.A.* **2006**, *103*, 19678–19682.
- (29) Ludwig, C. *Sitzungsber.-Bayer. Akad. Wiss. Wien, Math.-Naturwiss. Kl.* **1856**, *20*, 539.
- (30) Köhler, W. *J. Chem. Phys.* **1993**, *98*, 660–668.
- (31) Wiegand, S.; Ning, H.; Kriegs, H. *J. Phys. Chem. B* **2007**, *111*, 14169–14174.
- (32) Piazza, R.; Iacopini, S.; Triulzi, B. *Phys. Chem. Chem. Phys.* **2004**, *6*, 1616–1622.
- (33) Randle, B. J.; Scoltock, S. J.; Scott, D. K. *Biochem. Biophys. Res. Commun.* **2004**, *324*, 504–510.
- (34) Wallukat, G.; Kayser, A.; Wollenberger, A. *Eur. Heart J.* **1995**, *16*, 85–88.

Supporting Information for

Direct Detection of Antibody Concentration and Affinity in Human Serum using Microscale Thermophoresis

Svenja Lippok,[‡] Susanne A.I. Seidel,[‡] Stefan Duhr,[†] Kerstin Uhland,[‡]
Hans-Peter Holthoff,[‡] Dieter Jenne,[¶] and Dieter Braun^{‡*}

[‡] Systems Biophysics, Center for Nanoscience, Physics Department, Ludwig Maximilians Universität München, Amalienstr. 54, 80799 München, Germany;

[†] NanoTemper Technologies GmbH, Flößergasse 4, 81369 München, Germany;

[‡] Corimmun GmbH, Lochhamer Str. 29, 82152 Martinsried, Germany;

[¶] Max Planck Institute of Neurobiology, Am Klopferspitz 18, 82152 Martinsried, Germany

Address reprint requests and inquiries to dieter.braun@lmu.de

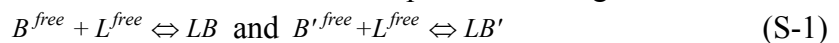
S1. Antibodies. The mouse monoclonal antibody 23-6-7, batch KD-250208-001 was produced by Biogenes GmbH, Germany by immunizing 8-week old BALB/c female mice subcutaneously over a period of 39 days with a GST fusion protein carrying the complete second extracellular domain (ARAES DEARR CYNDP KCCDF VTNRQ). The antibody produced from hybridoma cell clone 23-6-7 was purified by Protein A affinity chromatography and dissolved as 2 mg/ml stock solution in PBS. The goat polyclonal antibody (Lot: 28498) was generated by Biogenes GmbH, Germany. The immunization of the goat was carried out by six boosts over a period of 23 weeks with above GST fusion protein. The antibody containing serum was purified by affinity chromatography. The antibody was dissolved in Glycine buffer, pH 7.5, 250 mM NaCl, 0.02% Thimerosal as a 377 µg/ml stock solution. For control measurements a monoclonal antibody to Mouse E-cadherin from TaKara Bio Inc. (Otsu, Shiga, Japan) was used.

S2. Imaging and Setup. Excitation was provided by a red high power LED (627 nm, Thorlabs, United Kingdom). For measurements in serum, D2 dyes were used to bypass the autofluorescence interference from serum at shorter wavelengths. A Cy5 filter set with an excitation range of 590-650 nm and emission range of 663-738 nm (F46-006, AHF-Analysetechnik, Germany) was used. The infrared laser was coupled into the imaging path with an infrared dichroic mirror and focused into the fluid with the microscope objective (20x Plan-Apochromat, NA=0.8, Carl Zeiss, Germany) which was also used for epifluorescence imaging with a CCD camera (Sensicam UV, PCO AG, Germany). A region of 20 x 20 µm around the center of heating was used for analysis. The images were corrected for constant background fluorescence.

Glass capillaries with low diameter variation and standardized surface condition (NanoTemper, Germany) were used with an inner diameter of 500 µm, an outer diameter of 1 mm and a length of 50 mm. All measurements were performed twice at room temperature, error bars indicate the difference between measurements.

S3. Temperature. According to the Lambert-Beer-Bouguer law $I/I_0 = \exp(-\alpha d)$ and an absorption coefficient of $\alpha = 2850 \text{ m}^{-1}$ at 1480 nm, the intensity decreases to 1/e after $d = 350 \text{ µm}$. The temperature profile was imaged by the temperature dependence of the fluorescence dye BCECF in 10 mM Tris-HCl buffer [17]. Measurements confirmed that due to the fixed capillary thickness and constant infrared laser power, the temperature increase was reproducibly generated with a precision of <0.1 K.

S4. Label dependent affinity. Let us assume that labeled and unlabeled binder (B , B') differ in their affinity. Since we use a mixed protocol where we titrate the binder that is a mixture of labeled and unlabeled elements ($c_{B0} = c_{B0}^{\text{labeled}} + c_{B0}^{\text{unlabeled}}$) as a mixture of both labeled and unlabeled binder, it is important to check experimentally that both binders have the same dissociation constant. We extend the mass action law to two parallel binding reactions



with dissociation constants K_D and K'_D . With the fraction of bound ligand $\chi = (c_{LB} + c_{LB'}) / c_L$ both equilibria are given by

$$\begin{aligned}
K_D &= \frac{(c_{L0} - c_{LB} - c_{LB'})(c_{B0} - c_{LB})}{c_{LB}} \\
&= c_{L0}(1 - \chi) \left(\frac{c_{B0}}{c_{LB}} - 1 \right)
\end{aligned}$$

(S-2)

and

$$\begin{aligned}
K'_D &= \frac{(c_{L0} - c_{LB} - c_{LB'})(c_{B0'} - c_{LB'})}{c_{LB'}} \\
&= c_{L0}(1 - \chi) \left(\frac{c_{B0'}}{\chi c_{L0} - c_{LB}} - 1 \right)
\end{aligned}$$

(S-3)

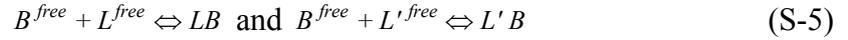
Solving for χ and inserting it into equation (S-2) gives a fraction of occupied labeled binder

$$x = \frac{c_{LB}}{c_{B0}} = \left[\frac{K_D}{c_{L0}(1 - \chi)} + 1 \right]^{-1}$$

(S-4)

which can be then inserted into equation (10) to evaluate the experiments. On a numerical level, this means we have to solve a cubic equation. However, fitting the data with this approach did not lead to statistically significant differences in both affinities.

S5. Polyclonal binding. For the case of polyclonal antibodies, the possibility of a broad distribution of binding affinities has to be considered. To explore this, we assume as a first approximation that the two ligands L and L' are of differing dissociation constants K_D and K'_D , respectively. We extend the mass action law to two parallel binding reactions



(S-5)

With the fraction of bound ligand $\zeta = (c_{LB} + c_{L'B})/c_L$ both equilibria are given by

$$\begin{aligned}
K_D &= \frac{(c_{B0} - c_{LB} - c_{L'B})(c_{L0} - c_{LB})}{c_{LB}} \\
&= c_{B0}(1 - \zeta) \left(\frac{c_{L0}}{c_{LB}} - 1 \right)
\end{aligned}$$

(S-6)

and

$$\begin{aligned}
K'_D &= \frac{(c_{B0} - c_{LB} - c_{L'B})(c_{L0'} - c_{L'B})}{c_{L'B}} \\
&= c_{B0}(1 - \zeta) \left(\frac{c_{L0'}}{\zeta c_{B0} - c_{LB}} - 1 \right)
\end{aligned}$$

(S-7)

Solving for ζ and inserting it into equation (S-7) gives a fraction of occupied labeled binder $x = (c_{LB} + c_{L'B})/c_{B0}$ that can be inserted into equation (10). On a numerical level, this means we have to solve a cubic equation. As before, fitting the data with the more complex binding model did not yield differences in the respective affinities.

S6. Signal to Noise

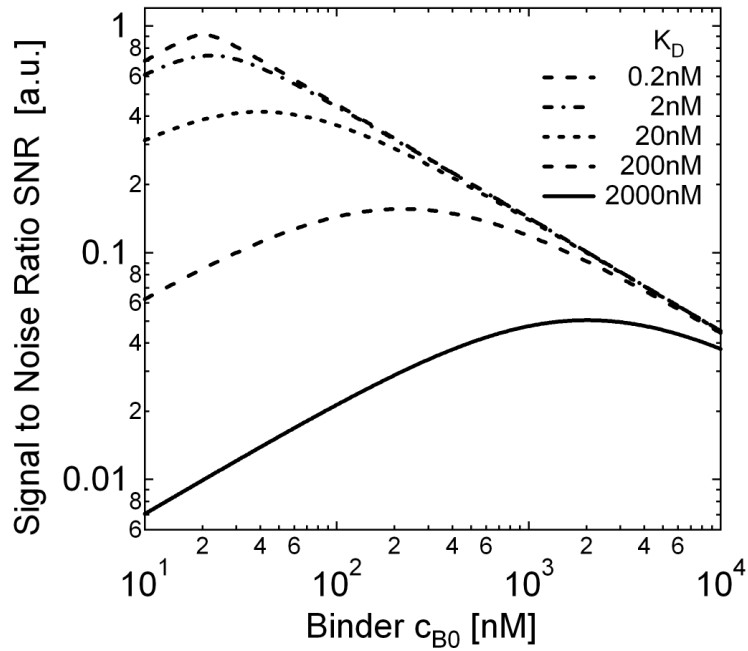


*Figure S-1. **Signal to noise ratio.** The signal to noise ratio for detection is optimal at $c_{B0} = K_D + c_{L0}$. Thus detection is optimal at $c_{B0} = c_{L0}$ for highly affine binding reactions ($c_{B0} \geq K_D$). For less affine binders ($c_{L0} \leq K_D$), detection is optimal for $c_{B0} = K_D$. The shown curves were calculated with $c_{L0} = 20\text{nM}$.*

S7. Correction of concentration dependent Fluorescein fluorescence. For a control measurement with a fluorescein-labeled COR1 peptide (Figure 4f), we observed a consistent fluorescence drop in the raw depletion signal with increasing antibody concentration (Figure S-2a). A similar drop was not found for the D2-labeled COR1 used throughout the manuscript and therefore no correction for the measurements with the D2 chromophore was needed. We attribute this effect to changes in the temperature dependent fluorescence of fluorescein depending on the antibody concentration - similar effects of proximity enhanced fluorescence are known in literature.

For account for this, we base both the warm and cold fluorescence F^{II} and F^{I} of fluorescein-COR1 on the respective measurement F^{II}_{R} and F^{I}_{R} using fluorescein without peptide. The

fluorescence change $\frac{\Delta F}{F} = \frac{F^{\text{II}} - F^{\text{I}}}{F^{\text{I}}}$ is now normalized to

$$\frac{\Delta F}{F} = \frac{F^{\text{II}} / F^{\text{II}}_{\text{R}} - F^{\text{I}} / F^{\text{I}}_{\text{R}}}{F^{\text{I}} / F^{\text{I}}_{\text{R}}} = \frac{F^{\text{II}}}{F^{\text{I}}} \cdot \frac{F^{\text{I}}_{\text{R}}}{F^{\text{II}}_{\text{R}}} - 1. \text{ In other words, the depletion signal of the}$$

binding measurement $F^{\text{II}} / F^{\text{I}}$ is divided by the depletion ratio measurement of the chromophore $F^{\text{I}}_{\text{R}} / F^{\text{II}}_{\text{R}}$. This results in a depletion binding curve which reveals the typical 3%

thermophoretic depletion known from the D2-Cor1 labeling. Interestingly, we did not observe a similar fluorescence drop in the presence of the E-Cadherin antibody used to control the specificity of the binding of both the COR1-D2 and COR1-fluorescein peptide (Figure S-2b). Data correction for both antibodies demonstrates the specificity of binding to Cor1 pAB (Figure S-2c).

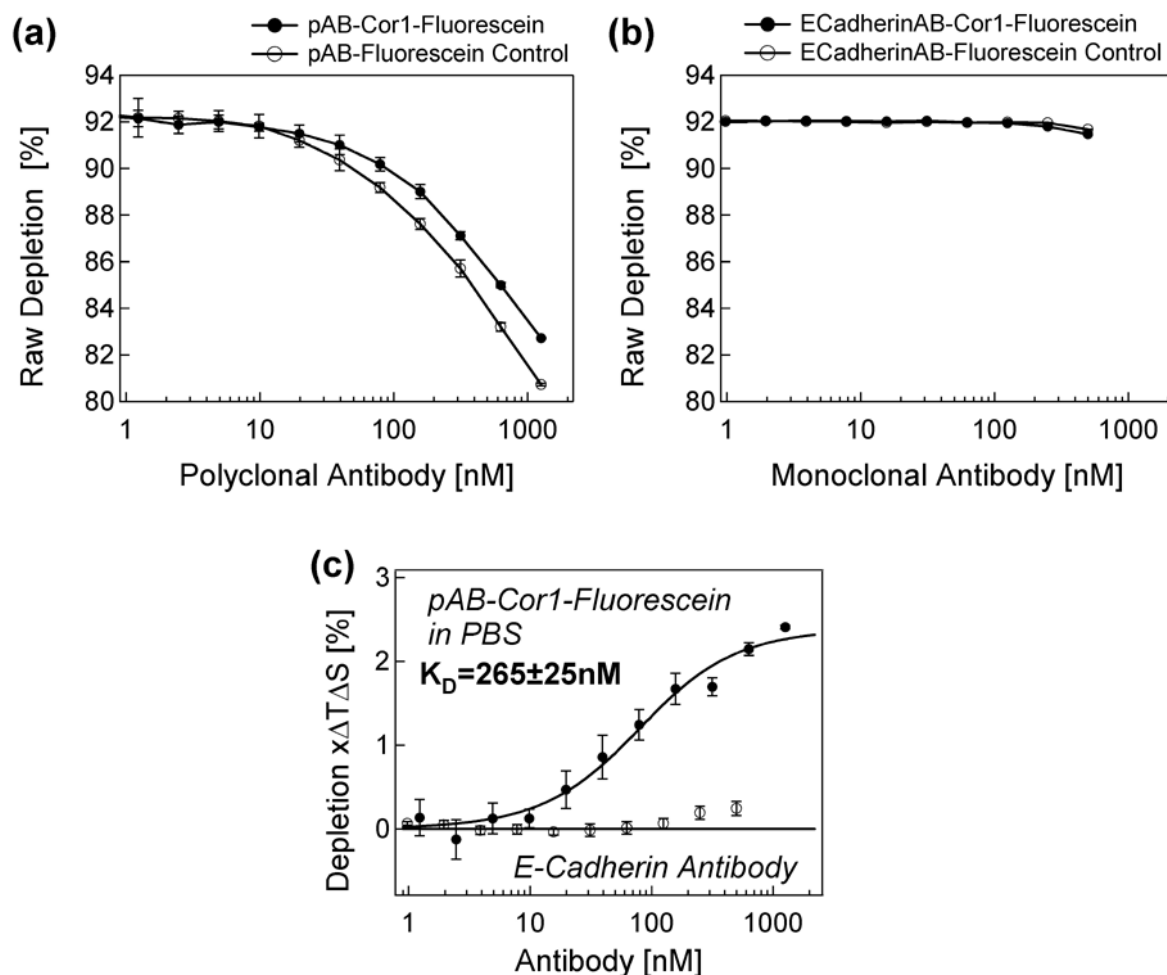


Figure S-2. Correction of Fluorescein concentration dependence. The fluorescence signal of fluorescein-COR1 varies with the concentration of the polyclonal antibody. Thermophoretic depletion of (a) titrated COR1-Polyclonal Antibody and (b) E-Cadherin Antibody with fluorescein-labeled COR1 (filled circles) and fluorescein (open circles) are used to correct the concentration dependence of the chromophore. (c) Corrected data shows the specificity of binding to Cor1 pAB (see Figure 4f).